QA: QA

MDL-NBS-HS-000016 REV 01

September 2004

Drift-Scale Radionuclide Transport

Prepared for:
U.S. Department of Energy
Office of Civilian Radioactive Waste Management
Office of Repository Development
1551 Hillshire Drive
Las Vegas, Nevada 89134-6321

Prepared by:
Bechtel SAIC Company, LLC
1180 Town Center Drive
Las Vegas, Nevada 89144

Under Contract Number
DE-AC28-01RW12101

DISCLAIMER

This report was prepared as an account of work sponsored by an agency of the United States Government. Neither the United States Government nor any agency thereof, nor any of their employees, nor any of their contractors, subcontractors or their employees, makes any warranty, express or implied, or assumes any legal liability or responsibility for the accuracy, completeness, or any third party's use or the results of such use of any information, apparatus, product, or process disclosed, or represents that its use would not infringe privately owned rights. Reference herein to any specific commercial product, process, or service by trade name, trademark, manufacturer, or otherwise, does not necessarily constitute or imply its endorsement, recommendation, or favoring by the United States Government or any agency thereof or its contractors or subcontractors. The views and opinions of authors expressed herein do not necessarily state or reflect those of the United States Government or any agency thereof.

QA: QA

Drift-Scale Radionuclide Transport

MDL-NBS-HS-000016 REV 01

September 2004

OCRWM	MODEL SIGNATURE PAGE/CHANGE HISTORY	Page iii 1. Total Pages: ~~224~~ 224 (19) 9/27/04

2. Type of Mathematical Model

☒ Process Model ☐ Abstraction Model ☐ System Model

Describe Intended Use of Model

Provide an alternative model for validation of the EBS Radionuclide Transport Model

3. Title

Drift-Scale Radionuclide Transport

4. DI (including Rev. No., if applicable):

MDL-NBS-HS-000016 REV 01

5. Total Appendices	6. No. of Pages in Each Appendix (18) 9/27/04
12	A-6, B-4, C-4, D-8, E-8, F-6, G-12, H-6, I-10, J-12, K-6, L-18

	Printed Name	Signature	Date
7. Originator	J. Houseworth	James E Houseworth	9/22/04
8. Independent Technical Reviewer	R. Andrews	R. Andrews	9/22/04
9. Checker	P. Persoff	Peter Persoff	9/22/04
10. QER	S. Harris	Stephen Harris	9/22/04
11. Responsible Manager/Lead	J. Houseworth	James E. Houseworth	9/22/04
12. Responsible Manager	M. Zhu	M. Zhu	9/22/04

13. Remarks

Change History

14. Revision No.	15. Description of Change
REV 00	Initial Issue
REV 00 Errata 001	Errata in response to CR-1100
REV 01	Entire model document revised. Changes too extensive to use Step 5.8f)1) from AP-SIII.10Q Rev 2 ICN 7.

CONTENTS

Page

CONTENTS (Continued)

Page

CONTENTS (Continued)

Page

INTENTIONALLY LEFT BLANK

FIGURES

Page

FIGURES (Continued)

Page

TABLES

Page

TABLES (Continued)

Page

ACRONYMS

EBS	engineered barrier system
FEPs	features, events, and processes
TSPA	Total System Performance Assessment
UZ	unsaturated zone
YMRP	*Yucca Mountain Review Plan*

INTENTIONALLY LEFT BLANK

1. PURPOSE

The purpose of this model report is to document the drift scale radionuclide transport model, taking into account the effects of emplacement drifts on flow and transport in the vicinity of the drift, which are not captured in the mountain-scale unsaturated zone (UZ) flow and transport models *UZ Flow Models and Submodels* (BSC 2004 [DIRS 169861), *Radionuclide Transport Models Under Ambient Conditions* (BSC 2004 [DIRS 164500]), and *Particle Tracking Model and Abstraction of Transport Process* (BSC 2004 [DIRS 170041]). The drift scale radionuclide transport model is intended to be used as an alternative model for comparison with the engineered barrier system (EBS) radionuclide transport model *EBS Radionuclide Transport Abstraction* (BSC 2004 [DIRS 169868]). For that purpose, two alternative models have been developed for drift-scale radionuclide transport. One of the alternative models is a dual-continuum flow and transport model called the drift shadow model. The effects of variations in the flow field and fracture-matrix interaction in the vicinity of a waste emplacement drift are investigated through sensitivity studies using the drift shadow model (Houseworth et al. 2003 [DIRS 164394]). In this model, the flow is significantly perturbed (reduced) beneath the waste emplacement drifts. However, comparisons of transport in this perturbed flow field with transport in an unperturbed flow field show similar results if the transport is initiated in the rock matrix. This has led to a second alternative model, called the fracture-matrix partitioning model, that focuses on the partitioning of radionuclide transport between the fractures and matrix upon exiting the waste emplacement drift. The fracture-matrix partitioning model computes the partitioning, between fractures and matrix, of diffusive radionuclide transport from the invert (for drifts without seepage) into the rock water. The invert is the structure constructed in a drift to provide the floor of the drift.

The reason for introducing the fracture-matrix partitioning model is to broaden the conceptual model for flow beneath waste emplacement drifts in a way that does not rely on the specific flow behavior predicted by a dual continuum model and to ensure that radionuclide transport is not underestimated. The fracture-matrix partitioning model provides an alternative method of computing the partitioning of radionuclide releases from drifts without seepage into rock fractures and rock matrix. Drifts without seepage are much more likely to have a significant fraction of radionuclide releases into the rock matrix, and therefore warrant additional attention in terms of the partitioning model used for TSPA.

The fracture-matrix partitioning model is intended to be used as the alternative model for comparison with the EBS radionuclide transport model (BSC 2004 [DIRS 169868]). This comparison is limited to waste emplacement drifts without seepage. The EBS radionuclide transport model is used in TSPA calculations to establish the radionuclide partitioning between fractures and matrix upon exiting the drifts, as well as the radionuclide mass flux from the drifts, under all drift seepage conditions. Following release from the drifts, subsequent TSPA transport calculations are conducted using mountain-scale flow and transport models that do not account for the presence of waste emplacement drifts or drift-shadow flow phenomena.

The following analysis and model reports are the sources of DTNs that provide direct inputs to this report:

- *Analysis of Hydrologic Properties Data* (BSC 2004 [DIRS 170038])
- *Calibrated Properties Model* (BSC 2004 [DIRS 169857])
- *UZ Flow Models and Submodels* (BSC 2004 [DIRS 169861])
- *Saturated Zone Flow and Transport Model Abstraction* (BSC 2004 [DIRS 170042])
- *Seepage Model for PA Including Drift Collapse* (BSC 2004 [DIRS 167652]).

The principal output of the fracture-matrix partitioning model is the distribution of radionuclide releases between the fractures and rock matrix from drifts with diffusive-dominated transport into the rock. Uncertainty in the fracture-matrix partitioning model is evaluated through the development of results over a suitable range of parameters that affect release fractions to the rock matrix and fractures. The distribution of radionuclide releases between fractures and matrix from drifts with advective-dominated transport into the rock is also provided. Data developed as inputs for the fracture-matrix partitioning model may also be used as input for the EBS radionuclide transport model (BSC 2004 [DIRS 169868]).

The phenomenon of flow and transport in the vicinity of the waste emplacement drift are evaluated in this model report under ambient thermal, chemical, and mechanical conditions. This includes the effects of water diversion around an emplacement drift and the flow and transport behavior expected in a fractured rock below the drift. Model limitations for the fracture-matrix partitioning model include the following approximations:

1. Fracture flow occurs beneath a waste emplacement drift within a distance less than the fracture spacing. Given fracture spacings that are, on average, less than one meter, the zone of reduced flow in the fracture-matrix partitioning model is much smaller than with the drift shadow model.

2. The model is restricted to steady-state conditions (see Section 6.4). Therefore, the initial transient period is not treated, which is initially dominated by diffusive transfer into the rock. This initial radionuclide partitioning ratio will be approximately equal to the water content ratio of the fractures and matrix and will only asymptotically approach the partitioning ratio predicted by the fracture-matrix partitioning model.

3. The effects of dryout during the boiling and re-wetting periods are ignored, during which fracture water saturations are disproportionately reduced in comparison with the matrix. This will lead to preferential entry of radionuclides to the matrix during the thermally-perturbed period.

4. All fractures are flowing in the fracture-matrix partitioning model as opposed to the active fracture model, where only a subset of the fractures is flowing. This leads to greater contact between the invert and flowing fractures and, therefore, greater releases from the invert to the rock fractures.

All of these limitations lead to a conservative prediction for fracture-matrix partitioning of radionuclide releases from drifts without seepage.

This report has been developed in accordance with *Technical Work Plan for: Unsaturated Zone Transport Model Report Integration* (Bechtel SAIC Company, LLC (BSC) 2004 [DIRS 171282]), which includes planning documents for the technical work scope, content, and management of this Model Report in Section 1.2.3. The technical work scope for this Model Report calls for development of a process-level model representing diffusive release from the invert to the rocks, partitioned between fracture and matrix, as compared to the fracture-release approach used in the Site Recommendation. The plan for validation of the models documented in this Model Report is given in Section 2.2.4 (BSC 2004 [DIRS 171282]). See Section 7 for additional discussion.

INTENTIONALLY LEFT BLANK

2. QUALITY ASSURANCE

Development of this model report and the supporting modeling activities have been determined to be subject to the Yucca Mountain Project's quality assurance program, as indicated in *Technical Work Plan for: Unsaturated Zone Transport Model Report Integration* (BSC 2004 [DIRS 171282], Section 8.1). Approved quality assurance procedures identified in the TWP (BSC 2004 [DIRS 171282], Section 4) have been used to conduct and document the activities described in this model report. The TWP also identifies the methods used to control the electronic management of data (BSC 2004 [DIRS 171282], Section 8.4, WP ARTM01) during the modeling and documentation activities.

This model report provides two models of drift-scale radionuclide transport in the unsaturated zone (UZ) below the repository. This natural barrier is classified in the *Q-List* (BSC 2004 [DIRS 168361]) as "Safety Category" because it is important to waste isolation, as defined in AP-2.22Q, *Classification Analyses and Maintenance of the Q-List*. The report contributes to the analysis and modeling data used to support performance assessment (PA); the conclusions do not directly impact engineered features important to safety, as defined in AP-2.22Q.

INTENTIONALLY LEFT BLANK

3. USE OF SOFTWARE

The major software codes and software routines used in this study are listed in Table 3-1. The superceded procedure AP-SI.1Q, *Software Management*, was used because this procedure governing the used of software was in effect at the time revision 00 was completed. There has been no additional use of software in the preparation of this revision 01. The software have been baselined in accordance with AP-SI.1Q, *Software Management*, are appropriate for the intended use, have been used strictly in the range of validation, and were obtained from Software Configuration Management. The iTOUGH2 V4.0 (LBNL 1999 [DIRS 139918]) and TOUGH2 V1.11MEOS9NTV1.0 (LBNL 1999 [DIRS 113943]) programs are the primary software used to represent physical processes for the Drift-Scale Radionuclide Transport models. Flow simulations were performed with iTOUGH2 V4.0 (LBNL 1999 [DIRS 139918]) and flow and transport calculations were performed using TOUGH2 V1.11MEOS9NTV1.0 (LBNL 1999 [DIRS 113943]). The range of use for iTOUGH2 V4.0 and TOUGH2 V1.11MEOS9NTV1.0 is for unsaturated, isothermal flow and tracer transport through fractured, porous rock. The routine CutDrift V1.0 (LBNL 2000 [DIRS 152816]) was used to cut a cylindrical drift shape into the rectangular grid. The routine AddBound V1.0 (LBNL 2000 [DIRS 152823]) was used to generate boundary grids for water and tracers to enter and leave the model grid. The routine EXT V1.0 (LBNL 1999 [DIRS 134141]) was used to postprocess the results of iTOUGH2 V4.0 (LBNL 1999 [DIRS 139918]) for graphical display of the flow field results. The range of use for software CutDrift V1.0, AddBound V1.0, and EXT V1.0 are to pre-process the numerical grid and post-process the flow field output for graphical display. No software was used prior to qualification.

The flow model calibration has been performed using the TOUGH family of software (BSC 2001 [DIRS 161316]), thus the compatibility of the parameters between the parameter development and their implementation in this report lead to the selection of the iTOUGH2 V4.0 software over other possible software and computational methods. Transport calculations are then performed for steady-state flow conditions using the EOS9nT module of TOUGH2 (TOUGH2 V1.11MEOS9NTV1.0 in Table 3-1) (Moridis et al. 1999 [DIRS 123093]). Compatibility between the flow calculations with iTOUGH2 V4.0 and the transport calculations with TOUGH2 V.11MEOS9NTV1.0 lead to the selection of the iTOUGH2 V4.0 software over other possible software and computational methods. Other direct finite difference approaches for treating the time dependence of the transport problem were not used because the Laplace transform method provides a semi-analytical treatment of the time derivatives that eliminates the need for time discretization or any restrictions on time-step size. The software CutDrift V1.0, AddBound V1.0, and EXT V1.0 pre- and post-processing software are commonly used with the TOUGH family of codes. There are no limitations on the use of this software within the range of use identified above.

Table 3-1. Qualified Software Used in this Report

Software Name	Version	Software Tracking Number	DIRS	Platform/Operating System
iTOUGH2	4.0	10003-4.0-00	139918	SUN / SUNOS 5.5.1
CutDrift	1.0	10375-1.0-00	152816	SUN / SUNOS 5.5.1

Table 3-1. Qualified Software Used in this Report (Continued)

Software Name	Version	Software Tracking Number	DIRS	Platform/Operating System
AddBound	1.0	10357-1.0-00	152823	SUN / SUNOS 5.5.1
EXT	1.0	10047-1.0-00	134141	SUN / SUNOS 5.5.1
TOUGH2	1.11MEOS9NTV1.0	10065-1.11MEOS9NTV1.0-00	113943	SUN / OSF1 V4.0

Excel (v. 97-SR-1) and Mathcad (v. 11.0) spreadsheets and visual display graphics programs (Tecplot v. 7.0-4.0 for MS-WINDOWS) were also used. Tecplot was used to create Figures 6-1 through 6-8, 6-13 through 6-20, 7-1, and 7-2. All information needed to reproduce the work using these standard software programs, including the input, computation, and output, is included in this report. Excel calculations are documented in Appendices A through I, and L. Mathcad calculations are discussed in Sections 6.4.3, 6.4.4, 6.4.6, and Appendices J and L.

4. INPUTS

4.1 DIRECT INPUTS

This section provides documentation for direct inputs to the Model Report. Other inputs are identified in the sections where they are used. Data input to the Model Report are referred to by Data Tracking Number (DTN). This format allows for all data of similar use in the Model Report to be kept in a single location, for readability of the document and simplicity for downstream users.

Source DTNs for the hydrological and transport properties used in the calculations that are intended as an alternative model for the EBS Radionuclide Transport Model [*EBS Radionuclide Transport Abstraction* (BSC 2004 [DIRS 169868])] (see Section 6.4) are listed in Table 4-1. These data are summarized in Tables 4-2 through 4-6 for the repository UZ model layers tsw33 (Topopah Spring Tuff upper lithophysal), tsw34 (Topopah Spring Tuff middle nonlithophysal), tsw35 (Topopah Spring Tuff lower lithophysal), and tsw36 (Topopah Spring Tuff lower nonlithophysal).

4.1.1 Fracture Frequency and Fracture Porosity

Data for the mean and standard deviation of fracture frequency and fracture porosity for the tsw33, tsw34, tsw35, and tsw36 (see Table 4-2) are given in Table 6-5 of the report, *Analysis of Hydrologic Properties Data* (BSC 2004 [DIRS 170038] (indirect input); DTN: LB0205REVUZPRP.001 [DIRS 159525]). Fracture frequency is determined from qualified fracture property data developed from field data (BSC 2004 [DIRS 170038], Section 6.1). These include Detailed Line Survey (DLS) fracture data (collected from the Exploratory Studies Facility North and South Ramps, Main Drift, and Enhanced Characterization of the Repository Block (ECRB) Cross Drift, providing spatially varying frequency, length, and fracture dips and strikes) and fracture frequency data from boreholes. A combination of fracture porosity data derived from gas tracer tests in the Exploratory Studies Facility, fracture frequency data, fracture aperture estimates, and the geometry of fracture networks are used to develop representative fracture porosities for the UZ Model layers (BSC 2004 [DIRS 170038] (indirect input), Section 6.1). See Section 6.4.5 for a complete discussion of the uncertainty treatment for fracture frequency and fracture porosity. Fracture frequency data in the repository host rock provides estimates for the standard deviation of fracture frequency for the tsw33 and tsw34 model units, but not for the tsw35 or tsw36. Data from other units shown in Table 4-3 are used to develop uncertainty data for the tsw35 and tsw36.

Table 4-1. Inputs

Input	Type	Description
LB0205REVUZPRP.001 [DIRS 159525]	Data	Fracture frequency and porosity
LB0208UZDSCPLI.002 [DIRS 161788]	Data	Matrix permeabilities, fracture van Genuchten *m*, and fracture residual saturation – lower infiltration scenario.
LB0208UZDSCPMI.002 [DIRS 161243]	Data	Matrix permeabilities, fracture van Genuchten *m*, and fracture residual saturation – mean infiltration scenario.

Table 4-1. Inputs (Continued)

Input	Type	Description
LB0302UZDSCPUI.002 [DIRS 161787]	Data	Matrix permeabilities, fracture van Genuchten *m*, and fracture residual saturation – upper infiltration scenario.
LB03023DSSCP9I.001 [DIRS 163044]	Data	Fracture and matrix flux and saturation, and matrix relative permeability (glacial transition climate, all infiltration scenarios)
LB0406U0075FCS.002 [DIRS 170712]	Data	Flow focusing factor correlation
LB0207REVUZPRP.002 [DIRS 159672]	Data	Matrix porosity, standard deviation for matrix porosity
Weast and Astle 1979 [DIRS 102865]	Established Fact	Diffusion coefficients in aqueous solution
SN0306T0502103.006 [DIRS 163944]; BSC (2004 [DIRS 170042], Section 6.5.2.6, Equation 6-19)	Data	Diffusion coefficient in rock matrix
BSC 2001 [DIRS 156700], pp. 23–25 Equation 37.	Data	Correlation for diffusion coefficient in invert materials
Hilf 1975 [DIRS 169699], p. 257	Established Fact	Intergranular porosity of invert
BSC 2003 [DIRS 164101] 800-IED-WIS0-00302-000-00A	Design information	Emplacement drift committed materials
BSC 2004 [DIRS 168370] 800-IED-WIS0-00103-000-00A	Design Information	Repository design layout information
BSC 2004 [DIRS 168489], 800-IED-MGR0-00201-000-00B	Design Information	Emplacement drift configuration

Table 4-2. Fracture Frequency and Porosity Data for the Repository Host Rock

UZ Model Layer	Frequency (m^{-1})		Porosity	
	F	σ_f	Mean (-)	Std (-)
tsw33	0.81	1.03	5.8E-3	-
tsw34	4.32	3.42	8.5E-3	2.50E-03
tsw35	3.16	-	9.6E-3	-
tsw36	4.02	-	1.3E-2	-

DTN: LB0205REVUZPRP.001 [DIRS 159525], BSC 2004 [DIRS 170038] (indirect input).

NOTE: Fracture properties developed from field data (Std refers to standard deviation for porosity). Note also that BSC 2004 [DIRS 170038] is supporting documentation for the direct input DTN: LB0205REVUZPRP.001 [DIRS 159525].

Table 4-3. Fracture Frequency for Rock Units with Data on Standard Deviation

Fracture frequency data		
UZ Model Layer	Frequency (m^{-1})	
	F	σ_f
tcw11	0.92	0.94
tcw12	1.91	2.09
tcw13	2.79	1.43
ptn21	0.67	0.92
ptn24	0.46	0.45
ptn25	0.52	0.6
ptn26	0.97	0.84
tsw31	2.17	2.37
tsw32	1.12	1.09
tsw33	0.81	1.03
tsw34	4.32	3.42

DTN: LB0205REVUZPRP.001 [DIRS 159525].

BSC 2004 [DIRS 170038] (indirect input).

4.1.2 Unsaturated Zone Flow

Data on UZ flow in the repository were developed using the UZ Flow Model. The site-scale model incorporates the entire Yucca Mountain UZ; it accounts for the main stratigraphic units using layer-averaged rock properties and represents the major faults. Relevant rock properties of each hydrogeologic unit (for fractures, matrix, and fault zones) have been calibrated against saturation data, water-potential data, pneumatic-pressure data, perched-water data, temperature data, and geochemical data [*Calibrated Properties Model* (BSC 2004 [DIRS 169857] (indirect input), Section 6.1 and BSC 2004 [DIRS 169861] (indirect input), Sections 6.2 through 6.5)]. The flow results also include the effects of preferential flow in the fracture network as implemented in the active fracture model (BSC 2004 [DIRS 169861] (indirect input), Section 6.1.2). The calibrations are conducted for lower, mean, and upper infiltration scenarios for the present-day climate to include this key uncertainty in the parameterization. The flow data used are for the lower, mean, and upper bound flow fields for the glacial transition climate. These data, which include the fracture and matrix flux and the fracture and matrix water saturations, are available in DTN: LB03023DSSCP9I.001 [DIRS 163044] and (BSC 2004 [DIRS 169861] (indirect input)). The glacial transition lower, mean, and upper infiltration scenarios cover a range of conditions that encompass all of the monsoon scenarios and all but the present-day lower infiltration scenario. Furthermore, the majority of the compliance period (2,000 to 10,000 years) is modeled as being under glacial transition climate. Because of the predominance in time and wide range of the glacial transition infiltration scenarios, these three cases are used as representative for the low, mean, and high scenarios for the entire compliance period. In conjunction with the mountain-scale flow model results, a distribution for flow

focusing in the fracture continuum is also used to account for sub gridblock scale heterogeneity for the mountain-scale flow fields.

4.1.3 Flow Focusing and Fracture Hydrologic Characteristics

A flow focusing factor is included in the model to account for the effects of heterogeneity on flow at length scales relevant to drift-scale flow. These effects are not accounted for at the drift-scale (on the order of 10 m) because the horizontal dimensions of the mountain-scale numerical grid are on the order of 100m. The treatment of flow focusing is restricted to fracture flow because the effects are expected to be larger in the fractures, which are found to carry in excess of 90 percent of the total water flux in the UZ flow model results. Measurements of flow focusing are not available; therefore, models are used to describe the effects of the drift-scale heterogeneity on flow. The models used to investigate these effects were restricted to 2D and 3D domains for the upper portion Topopah Spring welded units, between the base of the Paintbrush non-welded (vitric tuff) PTn and the repository horizon. This domain was selected due to the more homogeneous, matrix-dominated, flow that is expected in the Paintbrush non-welded (vitric tuff) versus the strongly fracture-dominated flow expected in the Topopah Spring welded units. The model domains were on the order of 100 m in extent in all directions, with model grid spacing of less than 1 m (BSC 2004 [DIRS 167652] (indirect input), Section 6.8.1).

The flow-focusing effect is represented in the fracture fluxes and water saturations, requiring the van Genuchten pore size distribution factor (m) shown in Table 4-4. This parameter is not treated as uncertain because of the uncertainty already investigated through flow model calibration (BSC 2004 [DIRS 169857] (indirect input) and BSC 2004 [DIRS 169861] (indirect input)). These investigations found that the same van Genuchten m could be used for all flow fields (low, mean, and high infiltration conditions) and match field data. Therefore, a constant value appears to be appropriate. Fracture residual water saturation (Table 4-4) is needed to define the effective saturation used in the van Genuchten relative permeability model and is treated as an uncertain parameter. The flow-focusing correlation, documented in BSC (2004 [DIRS 167652] (indirect input), Section 6.8; DTN: LB0406U0075FCS.002 [DIRS 170712]), is given by the following:

$$P = -0.3137F^4 + 5.4998F^3 - 35.66F^2 + 102.3F - 11.434$$

where F is the flow-focusing factor and P is the cumulative probability for the value of F (BSC 2004 [DIRS 167652](indirect input), Figure 6-26). See Section 6.4.5 for a complete discussion of the uncertainty treatment for water flux, residual saturation, and flow focusing.

Table 4-4. Fracture van Genuchten *m* and Residual Saturation, All Infiltration Cases

UZ Model Layer	Hydrogeologic Units	Fracture van Genuchten m	Fracture Residual Saturation
tsw33	TUL	0.633	0.01
tsw34	TMN	0.633	0.01

Table 4-4. Fracture van Genuchten *m* and Residual Saturation, All Infiltration Cases (Continued)

UZ Model Layer	Hydrogeologic Units	Fracture van Genuchten m	Fracture Residual Saturation
tsw35	TLL	0.633	0.01
tsw36	TM2 & TM1	0.633	0.01

DTNs: LB0208UZDSCPLI.002 [DIRS 161788], LB0208UZDSCPMI.002 [DIRS 161243], and LB0302UZDSCPUI.002 [DIRS 161787].

NOTE: The fourth character of model layer is replaced by F or M in these DTNs, indicating fracture or matrix, respectively.

4.1.4 Matrix Hydrologic Characteristics

Data for matrix porosity and permeability (Table 4-5 and Table 4-6) are also used to evaluate matrix diffusion. Matrix porosity is taken from the hydrologic parameter set presented in Table 6-6 of *Analysis of Hydrologic Properties Data* (BSC 2004 [DIRS 170038] (indirect input); LB0207REVUZPRP.002 [DIRS 159672]). Note that the porosity data set selected for use in TSPA is thermal properties data set presented in LB0210THRMLPRP.001 [DIRS 160799] (indirect input). However, the values within the repository model units are (tsw33, tsw34, tsw35, and tsw36) are nearly identical. The reason for using the alternative data set is because this data set provides an estimate of the variance of the porosity, which is used to statistically sample matrix porosity. See Section 6.4.5 for a complete discussion of the uncertainty treatment.

Table 4-5. Matrix Porosity Average and Standard Deviation, All Infiltration Cases

UZ Model Layer	Hydrogeologic Units	Average Matrix Porosity	Standard Deviation for Matrix Porosity
tsw33	TUL	0.155	0.030
tsw34	TMN	0.111	0.020
tsw35	TLL	0.131	0.031
tsw36	TM2 & TM1	0.103	0.025

DTN: LB0207REVUZPRP.002 [DIRS 159672], BSC 2004 [DIRS 170038] (indirect input).

Table 4-6. Matrix Permeability, All Infiltration Cases

UZ Model Layer	Hydrogeologic Units	Average Matrix Permeability (m^2) – lower infiltration case	Average Matrix Permeability (m^2) – mean infiltration case	Average Matrix Permeability (m^2) – upper infiltration case
tsw33	TUL	1.60E-18	6.57E-18	2.39E-17
tsw34	TMN	1.38E-19	1.77E-19	2.96E-19
tsw35	TLL	2.33E-18	4.48E-18	8.55E-18
tsw36	TM2 & TM1	5.58E-19	2.00E-19	7.41E-19

DTNs: LB0208UZDSCPLI.002 [DIRS 161788], LB0208UZDSCPMI.002 [DIRS 161243], and LB0302UZDSCPUI.002 [DIRS 161787].

Matrix permeability is taken from the drift-scale calibrated property sets (BSC 2004 [DIRS 169857] (indirect input), Tables 6-8, 6-9, and 6-10; DTNs: LB0208UZDSCPLI.002 [DIRS 161788]; LB0208UZDSCPMI.002 [DIRS 161243]; and LB0302UZDSCPUI.002 [DIRS 161787]). These permeability values are calibrated against water saturation and water potential values for the lower, mean, and upper bound infiltration cases using one-dimensional models and inverse modeling methods (BSC 2004 [DIRS 169857] (indirect input), Section 6.3.2). These cases represent the uncertainty in flux through the UZ and therefore the property sets calibrated to these different infiltration cases represent the uncertainty in the properties that are consistent with the calibration. The subsequent calibrations with the site-scale 3D model did not affect the values of matrix permeability (BSC 2004 [DIRS 169861] (indirect input), Appendix A, Tables A-1, A-2, and A-3).

4.1.5 Diffusion in Fractured Rock

Mass transport in the rock fractures immediately in contact with the drift is treated as a steady-state diffusion process, as described in Section 6.4.1. Diffusion will occur through rock fractures immediately adjacent to a drift due to the residual water content (or greater) that is present in all fractures. Due to the limited direct information available concerning diffusion coefficients in partially saturated fractures, diffusion coefficients determined for the rock matrix are used as the expected values for diffusion coefficients in the neighboring partially saturated fractures. See Assumption 1 and Section 6.4.5 for a discussion of the justification for this approximation.

Site-specific diffusion cell data were used to develop a correlation between the matrix diffusion coefficient, and the porosity and permeability of the rock matrix under saturated conditions, as discussed in *Diffusive and Advective Transport of ^{3}H, ^{14}C, and ^{99}Tc in Saturated, Fractured Volcanic Rocks from Pahute Mesa, Nevada* (Reimus et al. 2002 [DIRS 163008] (indirect input) and *Saturated Zone Flow and Transport Model Abstraction* BSC 2004 [DIRS 170042], Section 6.5.2.6, Equation 6-19).

The diffusing species ^{3}HHO, Br^{-}, and I^{-} were used in the experiments to define the correlation. Samples of welded and nonwelded volcanic tuffs were taken from Pahute Mesa and the C-holes near Yucca Mountain. The ranges in porosity and permeability of these samples are approximately 0.05 to 0.3 and 10^{-18} m^2 to 10^{-14} m^2, respectively. The porosity and permeability of rock units in the repository horizon are in approximately the same range (porosity ranges from 0.11 to 0.15 (BSC 2004 [DIRS 170038] (indirect input), Table 6-6) and permeability from 10^{-19} m^2 to 10^{-17} m^2 (BSC 2004 [DIRS 169861] (indirect input), Table A-1). Reimus et al. 2002 [DIRS 163008] (indirect input), Section 4, found that differences in rock type account for the largest variability in the effective diffusion coefficients, rather than variability between diffusing species, size, and charge. The highest predictability in determining a value of D_m occurs when both matrix porosity and log permeability are known, with log permeability as the most important predictive variable. The correlation is,

$$\log(D_m) = -3.49 + 1.38\phi_m + 0.165\log_{10}(k_m)$$

where D_m is the effective matrix diffusion coefficient in cm^2/s, ϕ_m is the matrix porosity, and k_m is the matrix permeability in m^2 (BSC 2004 [DIRS 170042], Section 6.5.2.6, Equation 6-19; DTN: SN0306T0502103.006 [DIRS 163944]; Reimus et al. 2002 [DIRS 163008] (indirect input) Equation 2.5). The effects of changes in water saturation on diffusion are included through an adjustment of this correlation to one applicable to unsaturated conditions (see Section 6.4.5).

4.1.6 Diffusion in the Invert

Mass transport in the invert is modeled as a diffusion process. The water-filled pore space is treated as a single continuum. A correlation for the diffusion coefficient is given in the report, *Invert Diffusion Properties Model* (BSC 2001 [DIRS 156700] (indirect input), pp. 23–25). The crushed tuff used for the invert will be "a native material from the development of the emplacement drifts" (refer to design information found in *D&E / PA/C IED Emplacement Drift Configuration and Environment* (BSC 2004 [DIRS 168489]); characteristics of the crushed tuff [*Invert Configuration and Drip Shield Interface* (CRWMS M&O 2000 [DIRS 136255] (indirect input), Section 6.5)]). Therefore, the matrix porosity of the granular material will be the same as the matrix porosity, ϕ_m, from the repository host rock. The matrix porosity characteristics for the invert are taken from the tsw36 (see Table 4-5), as used in *Advection Versus Diffusion in the Invert* (BSC 2003 [DIRS 170881] (indirect input), Sections 5.8 and 6.4). The potential exists that materials from other host rock units may be used for the invert (BSC 2004 [DIRS 169565] (indirect input), Section 5.3.1.2). However, the sensitivity of the results in the fracture-matrix partitioning model to invert diffusion are shown to be very low (Section 6.4.6). Therefore, the use of matrix porosity of the tsw36 is sufficient for the purposes of this model. The expected value and range for the intergranular porosity of the crushed tuff, ϕ_{Ig}, is shown in Table 4-7 (Hilf 1975 [DIRS 169699], p. 257); BSC 2003 [DIRS 170881] (indirect input), Sections 4.1.4 and 6.3). Uncertainty for ϕ_{Ig} is discussed in Section 6.4.5. The uncertainty in the free-water diffusion coefficient is based on data from Weast and Astle (1979 [DIRS 102865]), which provides 38 free-water diffusion coefficients for 19 electrolytes in a range of aqueous solutions (see Table 4-8). These diffusion coefficients range in value from 7.1×10^{-10} m^2/s to 3.87×10^{-9} m^2/s. This is a sufficiently wide range of free-water diffusion coefficients for radionuclides, based on reported values discussed in Section 6.4.5. See Section 6.4.5 for a complete discussion of the uncertainty treatment for diffusive mass transfer in the invert.

Table 4-7. Intergranular Porosity of the Invert

Mean	Range
0.45	0.4 to 0.48

Source: Hilf (1975 [DIRS 169699], p. 257) BSC (2003 [DIRS 170881] (indirect input), Sections 4.1.4 and 6.3).

NOTE: Porosity is computed from the void ratio, e, in this reference as e/(1+e). The "maximum" void ratio for poorly graded sand (SP) is used from this reference to represent uncompacted tuff grains.

The correlation for the diffusive mass transfer coefficient is given by (BSC 2001 [DIRS 156700], pp. 23–25):

$$\log\left(\frac{D_{eI}}{D_0}\right) = 1.849 \log \theta_I$$

where D_{eI} is the invert diffusive mass transfer coefficient, D_0 is the free-water diffusion coefficient, and θ_I is the invert water content. The source document for this correlation is now cancelled, however, this expression is the same as that used in BSC 2004 [DIRS 169868] (indirect input), Eq. 6.3.4.1.1-16 when considering the mean value, except the coefficient, 1.849, differs by 0.8%. This difference is negligible given that the range of uncertainty in the invert diffusion coefficients can exceed an order of magnitude, as shown in Attachment E. Therefore, the correlation in BSC 2004 [DIRS 169868] (indirect input) corroborates the correlation used as suitable for its intended use.

4.1.7 Design Information

Design information on invert characteristics, cited in the in-drift configuration information exchange drawing, are given as follows:

Design data on the dimensions of the drift and invert are presented in the in-drift configuration IED (BSC 2003 [DIRS 164101]), and shown in Figure 4-1 (BSC 2003 [DIRS 164101]). The depth of crushed tuff in the invert varies due to the curvature of the drift wall below the invert (Figure 4-1). The maximum depth of crushed tuff in the invert is 806 mm and the minimum depth is determined by that value, the drift diameter (5.5 m), and the width of the central clear space under the emplacement pallet (1674 mm). BSC 2003 [DIRS 164101] has been superseded. Nevertheless the dimensions shown therein and in Figure 4-1 are appropriate for use, because they are consistent with current IEDs: BSC 2004 [DIRS 168489] (indirect input) confirms the drift diameter value. The maximum depth of crushed tuff (806 mm) is prescribed for use in TSPA by Table 7 of *Postclosure Modeling and Analyses Design Parameters* (BSC 2004 [DIRS 169885]) (indirect input). *D&E/PA/C IED Interlocking Drip Shield and Emplacement Pallet* (BSC 2004 [DIRS 169220]) (indirect input) confirms the nominal width of the emplacement pallet (2150 mm) as shown in Figure 4-1, and therefore is consistent with the clear space dimension of 1674 mm (that is, twice 837 mm).

Information concerning the design layout is also needed. The percentages of each waste emplacement panel (1, 2, 3, and 4) within each of the four rock units (tsw33, tsw34, tsw35, and tsw36) is calculated from information on drift areas by geologic unit in *D&E / PA/C IED Subsurface Facilities* (BSC 2004 [DIRS 168370] 800-IED-WIS0-00103-000-00A). The total drift areas and percentages in each host rock unit are shown in Table 4-9. Note that in the IED geologic lithostratigraphic units are used. The correspondence between these units and the UZ flow model units are as follows: the tptpul is the tsw33, the tptpmn in the tsw34, the tptpll is the tsw35, and the tptpln is the tsw36.

Table 4-8. Free-Water Diffusion Coefficients

Electrolytes	Solute concentration (molarity)		
	0.01	0.1	1
HCl	n.a.	3.05	3.436
HBr	n.a.	3.156	3.87
LiCl	1.312	1.269	1.302
LiBr	n.a.	1.279	1.404
$LiNO_3$	1.276	1.24	1.293
NaCl	1.545	1.483	1.484
NaBr	n.a.	1.517	1.596
NaI	n.a.	1.52	1.662
KCl	1.917	1.844	1.892
KBr	n.a.	1.874	1.975
KI	n.a.	1.865	2.065
KNO_3	1.846	n.a.	n.a.
$KClO_4$	1.79	n.a.	n.a.
$CaCl_2$	1.188	1.11	1.203
$BaCl_2$	1.265	1.159	1.179
Na_2SO_4	1.123	n.a.	n.a.
$MgSO_4$	0.71	n.a.	n.a.
$LaCl_3$	1.105	n.a.	n.a.
$K_4Fe(CN)_4$	1.183	n.a.	n.a.

Source: Weast and Astle 1979 [DIRS 102865], p. F-62.

NOTE: Diffusion coefficient values for strong electrolytes = actual value $\times 10^5$ cm^2/s.

n.a. = data not available

Table 4-9. Drift Areas and Percentage of Each Rock Unit within Waste Emplacement Panels

Panel	Drift Area (m^2)	%tsw33	%tsw34	%tsw35	%tsw36
1	298850	0	40	60	0
2*	1477867	0	5	91	4
3**	1862136	12	22	66	0
4	1344299	0	0	95	5

Source: BSC (2004 [DIRS 168370], 800-IED-WIS0-00103-000-00A) (see also Appendix H).

* including contingency area.
** east and west portions of panel 3.

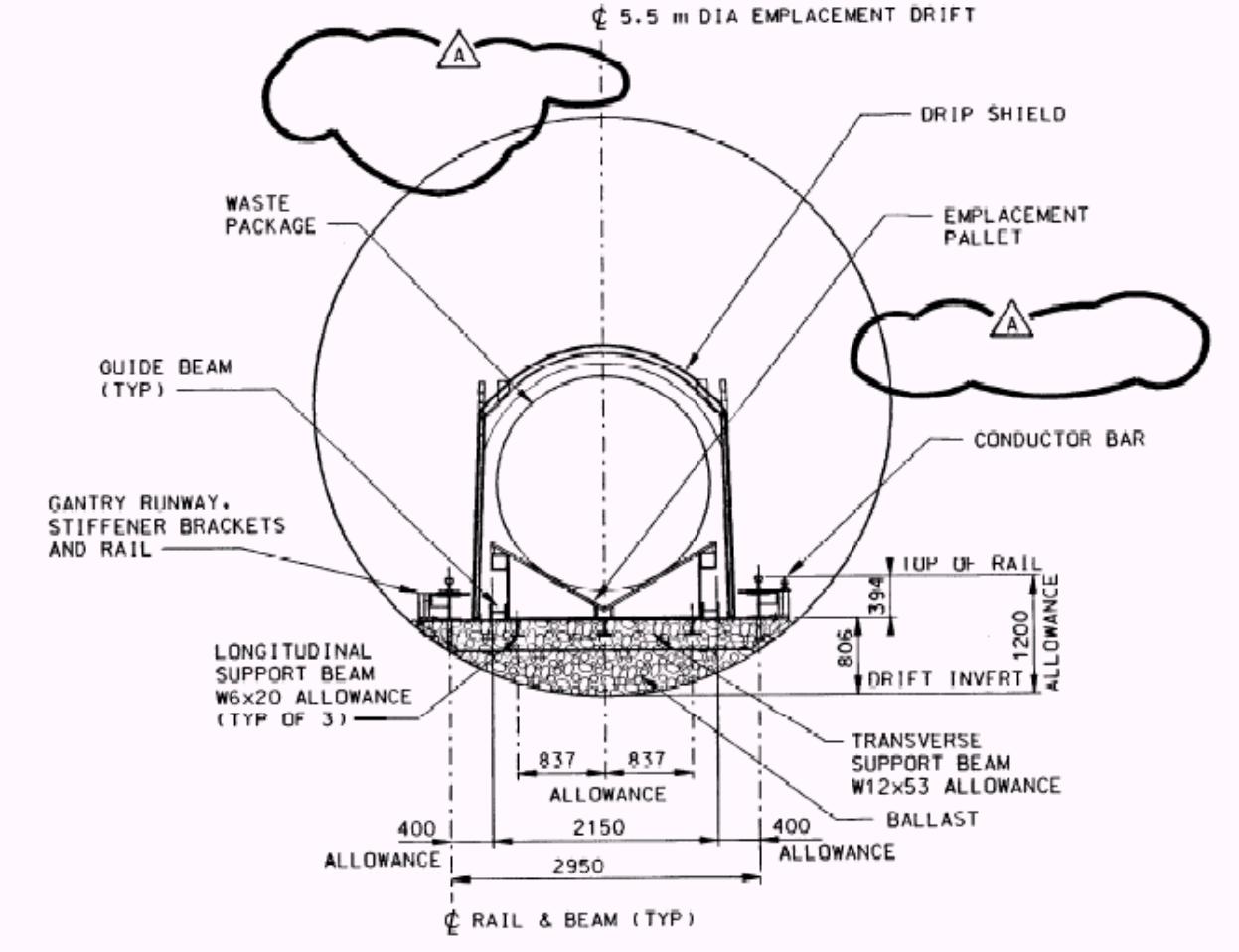

Source: BSC 2003 [DIRS 164101].

NOTE: All dimensions are in mm unless otherwise noted.

Figure 4-1. In-Drift Configuration

4.2 CRITERIA

The licensing criteria for postclosure performance assessment are stated in 10 CFR 63.114 [DIRS 156605]. The requirements to be satisfied by TSPA are identified in the Yucca Mountain *Project Requirements Document* (Canori and Leitner 2003 [DIRS 166275]). The acceptance criteria that will be used by the Nuclear Regulatory Commission (NRC) to determine whether the technical requirements have been met are identified in *Yucca Mountain Review Plan, Final Report* (YMRP; NRC 2003 [DIRS 163274]). The pertinent requirements and criteria for this model report are summarized in Table 4-10.

Table 4-10. Project Requirements and YMRP Acceptance Criteria Applicable to this Model Report

Requirement Number[a]	Requirement Title[a]	10 CFR 63 Link	YMRP Acceptance Criteria
PRD-002/T-015	Requirements for Performance Assessment	10 CFR 63.114(a-c; e-g)	Criteria 1 to 4 for *Radionuclide Transport in the Unsaturated Zone* [b]

[a] from Canori and Leitner (2003 [DIRS 166275]).
[b] from NRC (2003 [DIRS 163274], Section 2.2.1.3.7.3).

The applicable acceptance criteria identified in Section 2.2.1.3.7.3 of the YMRP (NRC 2003 [DIRS 163274]) are given below.

Acceptance Criterion 1, System Description and Model Integration Are Adequate:

(2) The description of the aspects of hydrology, geology, geochemistry, design features, physical phenomena, and couplings, that may affect radionuclide transport in the unsaturated zone, is adequate. For example, the description includes changes in transport properties in the unsaturated zone, from water-rock interaction. Conditions and assumptions in the total system performance assessment abstraction of radionuclide transport in the unsaturated zone are readily identified, and consistent with the body of data presented in the description;

(6) Guidance in NUREG-1297 and NUREG-1298 (Altman et al. 1988 [DIRS 103597] and [DIRS 103750]), or other acceptable approaches, is followed for peer review and data qualification.

Acceptance Criterion 2, Data are Sufficient for Model Justification:

(1) Geological, hydrological, and geochemical values, used in the license application, are adequately justified (e.g., flow-path length, sorption coefficients, retardation factors, colloid concentrations, etc.). Adequate descriptions of how the data were used, interpreted, and appropriately synthesized into the parameters are provided;

Acceptance Criterion 3, Data Uncertainty Is Characterized and Propagated through the Model Abstraction:

(1) Models use parameter values, assumed ranges, probability distributions, and bounding assumptions that are technically defensible, reasonably account for uncertainties and variabilities, and do not result in an under-representation of the risk estimate;

(2) For those radionuclides where the total system performance assessment abstraction indicates that transport in fractures and matrix in the unsaturated zone is important to waste isolation: (i) estimated flow and transport parameters are appropriate and valid, based on techniques that may include laboratory

experiments, field measurements, natural analog research, and process-level modeling studies, conducted under conditions relevant to the unsaturated zone at Yucca Mountain; and (ii) models are demonstrated to adequately reproduce field transport test results. For example, if a sorption coefficient approach is used, the assumptions implicit in that approach are verified;

(4) Uncertainty is adequately represented in parameter development for conceptual models, process-level models, and alternative conceptual models, considered in developing the abstraction of radionuclide transport in the unsaturated zone. This may be done either through sensitivity analyses or use of conservative limits;

Acceptance Criterion 4, Model Uncertainty Is Characterized and Propagated through the Model Abstraction:

(1) Alternative modeling approaches of features, events, and processes are considered and are consistent with available data and current scientific understanding, and the results and limitations are appropriately considered in the abstraction;

(2) Conceptual model uncertainties are adequately defined and documented, and effects on conclusions regarding performance are properly assessed;

(3) Consideration of conceptual model uncertainty is consistent with available site characterization data, laboratory experiments, field measurements, natural analog information and process-level modeling studies; and the treatment of conceptual model uncertainty does not result in an under-representation of the risk estimate; and

(4) Appropriate alternative modeling approaches are consistent with available data and current scientific knowledge, and appropriately consider their results and limitations, using tests and analyses that are sensitive to the processes modeled. For example, for radionuclide transport through fractures, the U.S. Department of Energy adequately considers alternative modeling approaches, to develop its understanding of fracture distributions and ranges of fracture flow and transport properties in the unsaturated zone.

No Key Technical Issues were identified with respect to the work presented in this report.

Additional criteria identified in *Technical Work Plan for: Unsaturated Zone Transport Model Report Integration* (Bechtel SAIC Company, LLC (BSC) 2004 [DIRS 171282], Sections 3.3, 3.4, and 3.5) are the "Level of Accuracy, Precision, and Representativeness of Results", "Completion Criteria" and "Other Requirements". The Level of Accuracy, Precision, and Representativeness of Results state:

"*All reports addressed in this TWP will state the level of accuracy, precision, and representativeness for the results of the model, and how these were determined. Uncertainties associated with these models are a function of the specific application, and should be determined by the use of model-specific validation test cases.*"

The level of accuracy and precision is addressed in Section 6.4.3. The level of representativeness is addressed in Sections 6.4 and 7.2.2. Uncertainties are treated in Sections 6.4.5, 6.6, and 7.2.3.

The Completion Criteria state:

"This work will be done consistent with the activities performed as part of Technical Work Plan: Regulatory Integration Evaluation of Analysis and Model Reports Supporting the TSPA-LA (BSC 2004 [DIRS 169377]) and will fulfill a portion of the Phase 2 work identified in that plan. It will also satisfy the requirements of AP-16.1Q, Condition Reporting and Resolution, to enable closure of the condition reports, if any, generated as a result of the Corrective Action Program noted in Section 1.2."

This is addressed as a part of the Regulatory Integration Evaluation (BSC 2004 [DIRS 169377]) and the Other Requirements state:

"The boundary conditions for this work will be established in related process model documents and applicable Information Exchange Drawings."

These Information Exchange Drawings are described in Section 4.1

4.3 CODES, STANDARDS, AND REGULATIONS

No specific formally established standards have been identified as applying to this modeling activity.

INTENTIONALLY LEFT BLANK

5. ASSUMPTIONS

The following assumptions are used in the absence of direct confirming data or evidence to perform the model activity. Other model assumptions are described in Section 6 of this model report.

1. Diffusion in the rock matrix may be used as limiting upper values for diffusion in fractures.

   Diffusion coefficients in fracture water have not been directly determined. Generally speaking, diffusion in unsaturated geologic materials has been found to be sensitive to water content ["Diffusion Coefficients in Gravel Under Unsaturated Conditions" (Conca and Wright 1990 [DIRS 101582], p. 1,055; *Dynamics of Fluids in Porous Media* (Bear 1972 [DIRS 156269], Sections 4.8.2 and 4.8.3)]. Experimental evidence concerning diffusion in unsaturated granular materials is presented in Conca and Wright (1990 [DIRS 101582]). These experiments were performed on nonporous granular materials in which diffusion occurred through water films along the granular surfaces. The water content of these materials were on the order of 0.5 to 5 percent and diffusion coefficients ranged from about 10^{-13} m^2/s to 10^{-11} m^2/s (Conca and Wright 1990 [DIRS 101582], Figures 10–13). The analogous water content of a fracture continuum is the fracture water saturation, which is also roughly in this range (see Appendix G). The range for matrix diffusion coefficients is about an order of magnitude larger (see Figure 6-23). This information suggests that the use of diffusion coefficients in the rock matrix as surrogates for diffusion coefficients in the fractures is conservative. Fractures in the welded tuff repository host rock are different than the nonporous granular materials investigated by Conca and Wright (1990 [DIRS 101582]) due to differences in geometry and the connection to a porous rock matrix. Therefore, limiting values for diffusion coefficients in the fractures are taken to be the effective diffusion coefficients in the neighboring rock matrix. This assumption is used in Sections 6.3.2.2 and 6.4.5 and does not require further confirmation because the assumption represents a reasonable upper bound.

2. Standard deviation of fracture frequency may be derived from the correlation with the mean value.

   Values for fracture frequency and the standard deviation for fracture frequency have been determined for several hydrogeologic model units in the unsaturated zone. These data show a strong correlation (see Figure 6-21). For two of the hydrogeologic model units addressed in this report (the tsw35 and tsw36), estimates of the mean fracture frequency are available, but not for the standard deviations. The correlation is used to estimate standard deviations for fracture frequency for these units. This assumption, used in Section 6.4.5, is considered adequate and does not require further confirmation.

3. A correlation between permeability, porosity, and effective diffusion coefficient developed for water-saturated rock matrix is extended to unsaturated conditions by using the effective permeability and water content in place of the permeability and porosity.

This extension to unsaturated conditions is appropriate because for unsaturated flow, the character of the gas phase is not significant other than the space that it occupies. The gas phase could be replaced by solid (rock mineral) which would result in exact equivalence between the unsaturated water content and porosity and effective unsaturated permeability and permeability. This assumption, used in Section 6.4.5, is considered adequate does not require further confirmation because, as discussed for Assumption 1, the treatment of diffusion represents a reasonable upper bound.

6. MODEL DISCUSSION

This section begins with a summary of hydrogeologic conditions relevant to drift scale radionuclide transport as well as the drift shadow model and the fracture-matrix partitioning model in Section 6.1. Section 6.2 considers the features, processes, and events that the model report covers, followed by a description of the development of the shadow zone model in Section 6.3 and of the fracture-matrix partitioning model in Section 6.4. Section 6.5 presents an assessment of the effects of the air gap in the fracture. Section 6.6 compares the fracture-matrix partitioning model and the drift shadow model.

6.1 INTRODUCTION

Hydrogeology at Yucca Mountain

Yucca Mountain consists of alternating layers of welded and nonwelded volcanic tuffs. The repository horizon lies in the unsaturated zone (UZ), approximately 300 m below the ground surface and 300 m above the water table. This horizon consists of welded tuffs composed of a dense porous rock matrix, which is highly fractured. Fracture permeability in the welded tuffs is on the order of darcies ($\sim 10^{-12}$ m^2), and the rock matrix permeability is on the order of microdarcies ($\sim 10^{-18}$ m^2) [*Calibrated Properties Model* (BSC 2004 [DIRS 169857], Table 6-8)]. Given these rock characteristics and the estimated range of water percolation rates of 1 to 11 mm/year [*Simulation of Net Infiltration for Modern and Potential Future Climates* (BSC 2004 [DIRS 170007], Table 6-10)], most of the water flux in the repository host rock is expected to flow in the fractures with a smaller component flowing through the rock matrix. Although most of the flow is in the fractures, more than 99 percent of the water volume resides in the rock matrix due to the larger porosity and water saturation in the matrix compared to the fractures. The key scientific notebooks (with relevant pages) used in this study are presented in Table 6-1.

Table 6-1. Scientific Notebooks Used in this Model Report

LBNL Scientific Notebook ID	M&O Scientific Notebook ID	Relevant Pages	Citation
YMP-LBNL-SZ-JEH-1	SN-LBNL-SCI-205-V1	115–181; 193–194	Houseworth 2003 [DIRS 163233]
YMP-LBNL-SZ-JEH-2	SN-LBNL-SCI-239-V1	211–231	Wang 2003 [DIRS 163234]
YMP-LBNL-DSRT-JEH-1	SN-LBNL-SCI-236-V1	5–145	Wang 2003 [DIRS 163234]

Drift Shadow Alternative Model

The Drift Shadow Alternative Model is developed in Section 6.3. The phenomenon of flow diversion around a cavity was investigated for a homogeneous porous medium by Philip et al. ["Unsaturated Seepage and Subterranean Holes: Conspectus, and Exclusion Problem for Circular Cylindrical Cavities" (Philip et al. 1989 [DIRS 105743])]. This diversion of flow was shown to result in flow velocities in a zone beneath the drift that are reduced relative to the undisturbed flow velocities away from the drift. In particular, the flow velocity at the base of the drift is exactly zero. The zone beneath the drift was also found to have lower water saturation

than the undisturbed zone. This region of reduced flow velocity and water saturation beneath the drift is known as the drift shadow (Philip et al. 1989 [DIRS 105743]).

For a quasi-linear representation of the hydrogeologic properties, Philip et al. (1989 [DIRS 105743]) found that the extent of the drift shadow is a function of the characteristic sorptive length scale and the drift radius. The quasi-linear model is a special case in which the logarithm of the relative permeability is linearly proportional to the capillary pressure, where the constant of proportionality is equal to 2, divided by the sorptive length scale. The shape of the drift shadow is governed by the ratio of the drift radius to the sorptive length scale. This ratio is a measure of the relative importance of gravitational forces compared with the capillary forces that define flow patterns around the drift. Philip et al. (1989 [DIRS 105743], p. 24) showed that the drift shadow becomes more elongated (relative to coordinates scaled by the drift radius) as the dimensionless ratio increases (i.e., the gravitational gradient becomes more dominant). Diagrams showing contours of equal flow velocity are given in Philip et al. (1989 [DIRS 105743], Figure 3). Bordering the shadow, near the edge of the drift, a zone of enhanced flow occurs where the flow diverted from the top of the drift is focused.

Capillary effects are much stronger in the matrix than in the fractures of a fractured rock. Based on the results of Philip et al. (1989 [DIRS 105743]), the fracture continuum is expected to behave as a gravity-dominated system and the rock matrix as a capillary-dominated system. Therefore, the reduction in flow below the drift is expected to be much more significant for the fracture continuum than for the matrix continuum. Furthermore, the very low water content of the fracture continuum below the drift, caused by very low saturation and porosity (compared to the matrix continuum), means that the vast majority of the water immediately below the drift will be in the rock matrix.

In this report, the drift shadow model results suggest the use of the fracture-matrix partitioning model described below. This model is used as an alternative model for qualitative comparison with the Fracture-Matrix Partitioning Model described below. Comparisons between expected results for transport based on the fracture-matrix partitioning model method and the drift shadow model are used for model validation in Section 7.

Fracture-Matrix Partitioning (Primary) Model

Results of the drift shadow model rely on the use of the dual-continuum approach for drift-scale flow and transport in a fractured rock beneath a waste emplacement drift. A fracture-matrix partitioning model, developed in Section 6.4, considers the case in which fracture flow occurs in a region close to the base of the waste emplacement drift, relaxing the reliance on the dual-continuum process description of flow around a waste emplacement drift. The fracture-matrix partitioning model sets unperturbed fracture flow directly below the base of waste emplacement drifts. This approximation in neglecting the drift shadow effect on flow is based on the idea that the drift shadow may not be as spatially extensive as presented in Section 6.3, due to heterogeneity and anisotropy in fracture characteristics, as well as discrete fracture effects. Under these conditions, the partitioning of radionuclides from the waste emplacement drift to the rock fractures and matrix is an important process, given the more active hydrologic environment beneath waste emplacement drifts in this model. The fracture-matrix partitioning model establishes the fraction of radionuclides released to the rock fractures and

matrix. The output of this model can be used as an alternative model for comparison with the EBS Radionuclide Transport Model [*EBS Radionuclide Transport Abstraction* (BSC 2004 [DIRS 169868])]. The transport model and the associated flow model used in total system performance assessment (TSPA) are mountain-scale models that do not represent the drifts and, therefore, do not include any effects of the drift shadow on flow or radionuclide transport beneath waste emplacement drifts.

6.2 FEATURES, EVENTS, AND PROCESSES

The following table of features, events, and processes (FEPs) was taken from the License Application (LA) FEP List (DTN: MO0407SEPFEPLA.000 [DIRS 170760]). The LA FEP List is a revision to the previous project FEP list [*The Development of Information Catalogued in REV00 of the YMP FEP Database* (Freeze et al. 2001 [DIRS 154365])] used to develop the list of FEPs in the *Technical Work Plan for: Unsaturated Zone Transport Model Report Integration* (BSC 2004 [DIRS 171282], Table 2.1.5-1). The selected FEPs are those taken from the LA FEP List that are relevant to the subject matter of this report. The cross-reference for each FEP to the relevant sections of this report is given below (Table 6-2). Screening arguments for both included and excluded FEPs are summarized in *Features, Events, and Processes in UZ Flow and Transport* (BSC 2004 [DIRS 170012]).

Consistent with the use of this model report to only provide alternative conceptual models for comparison to the model implemented in TSPA (as described in Section 1), none of the FEPs shown in Table 6-2 is included in TSPA through the output of this report. Rather, the disposition of these FEPs is traceable through the output of two other model reports (BSC 2004 [DIRS 169861] and BSC 2004 [DIRS 169131]). One FEP, 2.2.07.21.0A, is included in TSPA-LA through the outputs of (BSC 2004 [DIRS 169868]). That EBS radionuclide transport report may also take inputs developed in this document, and thereby inherently includes the FEPs associated with those inputs.

Table 6-2. Features, Events, and Processes Addressed in This Report

LA FEP Number	FEP Name	Cross Reference Section
1.2.02.01.0A	Fractures	6.3.2.3 and 6.4.5
1.3.01.00.0A	Climate change	6.4.6
1.4.01.01.0A	Climate modification increases recharge	6.4.6
2.1.08.01.0A	Water influx at the repository	6.3.2.2 and 6.4.5
2.1.08.02.0A	Enhanced influx at the repository	6.4.5
2.2.03.01.0A	Stratigraphy	6.4.5
2.2.03.02.0A	Rock properties of host rock and other units	6.3.2.3 and 6.4.5
2.2.07.02.0A	Unsaturated groundwater flow in the geosphere	6.3.3 and 6.4.1
2.2.07.04.0A	Focusing of unsaturated flow (fingers, weeps)	6.4.5
2.2.07.08.0A	Fracture flow in the UZ	6.3.3 and 6.4.1
2.2.07.15.0B	Advection and dispersion in the UZ	6.3.3.2 and 6.4.1
2.2.07.20.0A	Flow diversion around repository drifts	6.3.3.1 and 6.4.1

Table 6-2. Features, Events, and Processes Addressed in This Report (Continued)

LA FEP Number	FEP Name	Cross Reference Section
2.2.07.21.0A	Drift shadow forms below repository	6.3.3.1 and 6.4.1
2.2.08.05.0A	Diffusion in the UZ	6.3.2.3 and 6.4.5
2.2.08.08.0B	Matrix diffusion in the UZ	6.3.2.3 and 6.4.5
2.2.08.09.0B	Sorption in the UZ	6.3.2.3

6.3 DRIFT SHADOW ALTERNATIVE MODEL

6.3.1 Conceptual Model and Numerical Implementation of the Drift Shadow Model

This conceptual model used for the drift shadow model accounts for the effects of capillary, gravity, and viscous forces through the Darcy formulation for unsaturated flow. Transport processes are represented using mass conservation principles accounting for advection, diffusion, and sorption processes. The dual-permeability conceptual model is used to represent flow and transport in fractured rock. The dual-permeability model allows for flow and transport in a fracture continuum and a matrix continuum with advective and diffusive exchange between these continua. The conceptual model for fracture-matrix exchange also incorporates the active fracture model ["An Active Fracture Model for Unsaturated Flow and Transport in Fractured Rocks" (Liu et al. 1998 [DIRS 105729])], in which the fraction of flowing fractures is postulated to be a function of fracture saturation. This type of behavior is a result of flow instabilities caused by gravitational instability in combination with spatially heterogeneous properties, which leads to water flow in only a portion of the connected fracture system. One consequence of the active fracture model is a reduction in fracture-matrix interaction, needed to calibrate the dual-permeability flow model to observed matrix water saturations and potentials at Yucca Mountain ["Calibrating Hydrogeologic Parameters for the 3-D Site-Scale Unsaturated Zone Model of Yucca Mountain, Nevada (Bandurraga and Bodvarsson 1999 [DIRS 103949])]. Thus, the drift-shadow conceptual model uses a standard continuum representation of flow and transport in a fractured rock.

The conceptual flow and transport models are implemented numerically using an integral finite-difference method. Flow calculations are carried out to steady-flow conditions using the iTOUGH2 V4.0 (LBNL 1999 [DIRS 139918]) EOS9 module [*TOUGH2 User's Guide, Version 2.0* (Pruess et al. 1999 [DIRS 160778])], which simulates unsaturated flow according to Richards' equation ["Capillary Conduction of Liquids Through Porous Mediums" (Richards 1931 [DIRS 104252])]. The flow model calibration has been performed using the TOUGH family of software (BSC 2001 [DIRS 161316]), thus the compatibility of the parameters between the parameter development and their implementation in this report lead to the selection of the iTOUGH2 V4.0 [DIRS 139918] software over other possible software and computational methods. Transport calculations are then performed for steady-state flow conditions using the EOS9nT module of TOUGH2 (TOUGH2 V1.11MEOS9NTV1.0 [DIRS 113943] in Table 3-1) [*EOS9nT: A TOUGH2 Module for the Simulation of Water Flow and Solute/Colloid Transport in the Subsurface* (Moridis et al. 1999 [DIRS 123093])]. The transport module first solves Richards equation to establish the steady-state flow field. The solute concentrations are sufficiently small

such that they have no dynamic effects on the flow (e.g., the density or viscosity). This allows transport equations to be decoupled from flow equations. Transport equations are solved using a Laplace transform method (Moridis et al. 1999 [DIRS 123093], Section 3.2) applicable to steady-state flow conditions. Compatibility between the flow calculations with iTOUGH2 V4.0 (LBNL 1999 [DIRS 139918]) and the transport calculations with TOUGH2 V.11MEOS9NTV1.0 (LBNL 1999 [DIRS 113943]) lead to the selection of the TOUGH2 V4.0 software over other possible software and computational methods. Other direct finite-difference approaches for treating the time dependence of the transport problem were not used because the Laplace transform method provides a semi-analytical treatment of the time derivatives that eliminates the need for time discretization or any restrictions on time-step size.

An important factor in the drift shadow problem, as discussed in Section 6.1, is the diversion of percolation flux around the drift such that water does not enter the drift. A considerable amount of theoretical and experimental work has been conducted to evaluate seepage for the waste emplacement drifts at Yucca Mountain ["Evolutions of the Unsaturated Zone Testing at Yucca Mountain" (Wang and Bodvarsson 2003 [DIRS 163215]); "Inverse and Predictive Modeling of Seepage into Underground Openings" (Finsterle et al. 2003 [DIRS 163214]); "Seepage into Drifts with Mechanical Degradation" (Li and Tsang 2003 [DIRS 163714]); *Abstraction of Drift Seepage* (BSC 2004 [DIRS 169131])]. This work indicates that the percolation flux encountering a drift will be completely diverted if the percolation flux is less than a value known as the seepage threshold. The seepage threshold depends on the capillary properties of the fracture system, the size and shape of the drift, and the heterogeneity in fracture properties.

The drift shadow model is used in this report as an alternative model to the fracture-matrix partitioning model discussed in Section 6.4. Results of the drift shadow model are used for qualitative comparison with the fracture-matrix partitioning model as presented in Section 7. The model calculations were carried out using property sets (discussed in Section 6.3.2.3) available at the time the original calculations were performed (Houseworth 2003 [DIRS 163233]). Additional documentation of the work presented in Section 6.3 is provided in Scientific Notebook by Houseworth (2003 [DIRS 163233], pp. 115–181,; 193–194).

6.3.2 Numerical Grid, Boundary Conditions, and Parameter Development

6.3.2.1 Numerical Grid

The calculations presented here are for a two-dimensional, homogeneous, dual-permeability model of an emplacement drift. Figure 6.3-1 shows the grid used in the calculations developed using the software CutDrift V1.0 [DIRS 152816]. The area around the 5 m diameter drift uses a refined grid of 0.2 m × 0.2 m. Farther from the drift, the grid coarsens to approximately 2 m × 2 m. Simulations for a single-continuum flow field around an open drift using the same spatial discretization were found to be in agreement with an analytical solution (Houseworth et al., 2003 [DIRS 164394], Section 3.1). This comparison indicates that the grid has sufficient spatial resolution. The drift is represented by two grid blocks that provide horizontal and vertical connections to the bordering rock grids after removing the grid blocks originally generated in the drift region. The depth to the bottom of the drift shadow model was chosen roughly on the character of the flow fields. At 45 meters below the drift, the flow field is found to have nearly returned to the unperturbed state (see Figures 6.2 through 6.4).

The 5 m drift diameter used in this calculation differs from the 5.5 m drift diameter in the current repository design. This smaller diameter may be used because the effects of a smaller drift diameter, given no drift seepage, will result in a conservative estimate of the effects of a drift on transport beneath the drift. This is because the magnitude of the drift shadow effect is a function of the size of the drift; as the drift becomes smaller, the effects of the drift on the flow beneath the drift also become smaller.

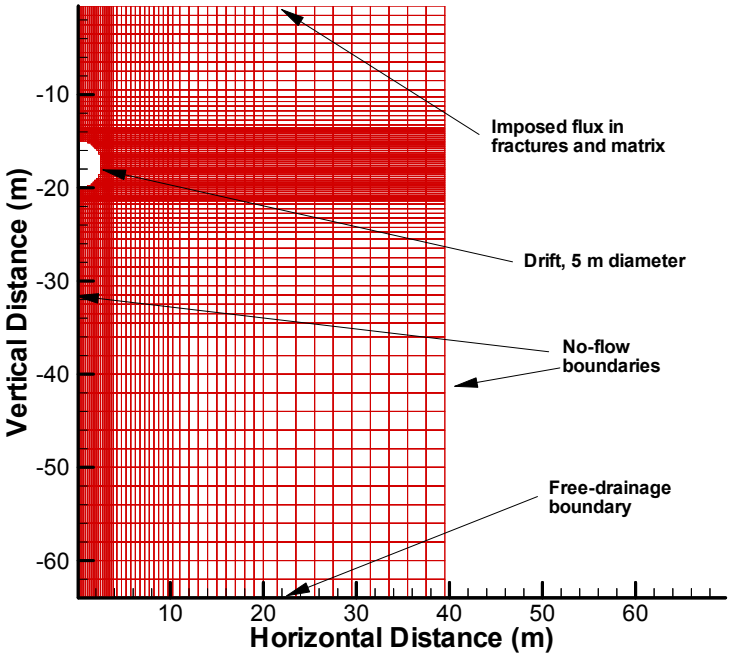

Output DTN: LB0307DSRADTRN.001.

Figure 6-1. Grid and Boundary Conditions

6.3.2.2 Boundary Conditions

As shown in Figure 6-1, the model uses a no-flow symmetry condition along the vertical centerline of the drift. Similarly, the far lateral boundary is a no-flow boundary due to the symmetry condition reflecting the periodic, 81 m drift spacing. Note that the grid lines in Figure 6-1 illustrate the position of the grid centers, not the grid boundaries; thus the far lateral boundary is 40.5 m from the centerline. The bottom boundary condition is free gravity drainage (no capillary pressure gradient). The center of the drift is 17.5 m below the top of the model domain, and the drift has a radius of 2.5 m. Hydrological properties are assigned to the drift such that the capillary pressure is zero for all values of water saturation.

Flow is introduced at the top boundary at a prescribed flow rate. For the dual-continuum model calculations, flow rates are prescribed separately for the fracture and matrix continua. This is necessary to develop a flow field compatible with results from the mountain-scale unsaturated zone flow model. The flow rates in Table 6-3 were chosen to cover a range of total flows while keeping matrix saturations within the range of observed values, approximately 0.80 to 0.95 [*Calibrated Properties Model* (BSC 2001 [DIRS 161316]), Section 6.1.4]. For higher total

percolation rates expected for future climates, BSC (2001 [DIRS 158726], Tables 6-23 and 6-24) shows that the percentage of the total percolation moving in the matrix is lower, however the absolute matrix flux increases as expected under wetter climate conditions. Therefore, the percentage of total flux in the matrix is adjusted to allow for more flow in the matrix than found at the lower percolation rates, short of saturating the matrix. Table 6-3 gives the values of flow rates investigated here. Note the cited fracture flow rate and matrix flow rate in Table 6-3 and elsewhere in this report refer to the flow rate maintained at the upper boundary of the model. Because of fracture-matrix interaction and flow diversion, the local flow rates at other locations in the model will vary.

Table 6-3. Flow Rates Investigated

Total Flow Rate (mm/yr)	Fracture Flow Rate (mm/yr)	Matrix Flow Rate (mm/yr)
10	9.85	0.15
10	9.15	0.85
100	99.55	0.45
100	98.4	1.6
300	299.0	1.0

Output DTN: LB0307DSRADTRN.001.

6.3.2.3 Parameters

Parameters used here for the drift-shadow model are from previous work for the Site Recommendation. Parameters for the License Application have changed; however, the general character of the rock remains the same, i.e., the fractures and matrix in the repository host rock are distinct continua with large differences in permeability, porosity, and capillary pressure characteristics. Differences in parameters between Site Recommendation and License Application do not impact the qualitative behavior of flow and transport in the drift shadow. This can be seen through the comparison of transport behavior as computed for Site Recommendation in BSC (2001 [DIRS 158726], Figures 6-54 through 6-56) and BSC (2004 [DIRS 169861], Figure 6.7-1). In particular, transport of radionuclides released in the drift shadow will be orders of magnitude longer than transport of radionuclides released to unperturbed fracture flow for either parameter set. Given that the drift shadow model presented here is only used for qualitative comparison with the fracture-matrix partitioning model discussed in Section 6.4, the older parameter set is adequate for the intended use of this alternative model.

Capillary pressure and relative permeability functions of saturation for the fracture and matrix continua are based on the van Genuchten formulation ["A Closed-Form Equation for Predicting the Hydraulic Conductivity of Unsaturated Soils" (van Genuchten 1980 [DIRS 100610])]. The property set for the tsw35 hydrogeologic unit (BSC 2001 [DIRS 161316]), which corresponds to the lower lithophysal unit of the Topopah Spring tuff, is used in the flow calculations. This property set is used because about 80 percent of the waste emplacement areas in the repository reside in this unit (see Table 4-9 and Appendix H). The hydrological data are summarized in Tables 6-4 and 6-5 for the Topopah Spring Tuff Lower Lithophysal unit, one of the repository host rock units for waste emplacement drifts. Matrix and mountain-scale fracture properties are given in DTN: LB997141233129.001 [DIRS 104055].

The calibrated property set for dual-permeability flow and transport calculations is based on permeability values obtained by calibrating a mountain-scale model against saturation, water potential, and pneumatic pressure data, using a large-scale model of Yucca Mountain [(Bandurraga and Bodvarsson 1999 [DIRS 103949]; "Characterization and Prediction of Subsurface Pneumatic Response at Yucca Mountain, Nevada" (Ahlers et al. 1999 [DIRS 109715])]. Permeability measured at the drift scale has been found to be roughly one order of magnitude smaller than that inferred from measurements at the mountain scale (BSC 2001 [DIRS 161316], Section 6.2). This difference results from the difference in sampling volume between mountain-scale and drift-scale measurements. Mountain-scale measurements capture the sparse, but highly permeable, fracture pathways not present in the typical smaller sampling volume. Because of the smaller length scales addressed in this model (tens of meters rather than hundreds of meters), the drift-scale fracture permeability is more appropriate. Drift-scale fracture permeability, shown in Table 6-6, was derived in the Calibrated Properties Model (BSC 2001 [DIRS 161316]; DTN: LB990861233129.001 [DIRS 110226]). All other properties at the drift scale were kept the same as the site-scale properties, as recommended in *Calibrated Properties Model* (BSC 2001 [DIRS 161316], Section 6.2). However, for fracture-matrix interaction to be approximately the same for the mountain-scale and drift-scale properties, the drift-scale active fracture parameter, γ, must be increased from 0.41 to 0.81 (see Figure 6.3-4). This is a result of the change in fracture permeability between these property sets. An evaluation of the mountain-scale versus drift-scale properties with respect to the active fracture parameter is discussed further in Section 6.3.3.1.

Table 6-4. Hydrological Properties for the tsw35—Matrix Properties (Drift-Scale and Mountain-Scale)

Permeability	Porosity	van Genuchten α	van Genuchten m	Residual saturation	Satiated saturation	Rock grain density
k_m (m^2)	ϕ_m (-)	α_m (1/Pa)	m_m (-)	S_{lrm} (-)	S_{lsm} (-)	ρ_g (kg/m^3)
3.04E-17	0.131	6.44E-6	0.236	0.12	1.00	2540

DTN: LB997141233129.001 [DIRS 104055], BSC 2001 [DIRS 161316].

Table 6-5. Hydrological Properties for the tsw35—Fracture Properties (Mountain-Scale Permeability)

Mountain-scale permeability	Porosity	van Genuchten α	van Genuchten m	Residual saturation	Satiated saturation	Active fracture parameter	Frequency	Fracture to matrix connection area
k_f (m^2)	ϕ_f (-)	α_f (1/Pa)	m_f (-)	S_{lrf} (-)	S_{lsf} (-)	γ (-)	f (1/m)	A (m^2/m^3)
4.51E-11	1.5E-2	7.39E-4	0.611	0.01	1.00	0.41	3.16	9.68

DTN: LB997141233129.001 [DIRS 104055], BSC 2001 [DIRS 161316], BSC 2001 [DIRS 159725].

Table 6-6. Hydrological Properties for the tsw35—Drift-Scale Fracture Permeability

Drift-Scale Permeability
k_f (m^2)
1.29E-12

DTN: LB990861233129.001
[DIRS 110226], BSC 2001
[DIRS 161316].

Transport calculations require the specification of matrix diffusion and sorption parameters. For TSPA, sorption and diffusion parameters have been characterized using a statistical approach to account for the variability found in measured values [*Unsaturated Zone and Saturated Zone Transport Properties (U0100)* (BSC 2001 [DIRS 160828])]. The parameters used in the calculations reported here have been chosen to be the expected (mean) values used in the site recommendation base case [*Total System Performance Assessment for the Site Recommendation* (CRWMS M&O 2000 [DIRS 153246], Section 3.7.3)]. The drift-shadow transport calculations presented here are for technetium, neptunium, and plutonium. These radionuclides were chosen because of their significance in dose calculations for TSPA (CRWMS M&O 2000 [DIRS 153246], Figure 4.1-19a). Under the oxidizing conditions expected in the UZ, the aqueous form of technetium is the negatively charged pertechnetate ion (TcO_4^-), which is nonsorbing. Under the relevant geochemical conditions, aqueous neptunium has been found to be weakly sorbing to the volcanic rock, and aqueous plutonium has been found to be strongly sorbing (BSC 2001 [DIRS 160828], Section 6.4.4.1.4). Therefore, the aqueous radionuclides investigated here span the range of expected sorption behavior. Matrix sorption coefficients are given in DTN: LA0003AM831341.001 [DIRS 148751]. Implementation of sorption coefficients in a transport model also requires specification of the rock bulk density. Rock bulk density in the tsw35 is given in DTN: LB997141233129.001 [DIRS 104055]. Note that sorption is only accounted for in the matrix because values for sorption in the fractures have not been measured and are difficult to estimate.

Values for the effective diffusion coefficients in the matrix are taken from DTN: LA0003JC831362.001 [DIRS 149557]. The effective diffusion coefficient for technetium in tuff matrix is found to be smaller than for neptunium or plutonium. This is postulated to be a result of the large size and negative charge of the pertechnetate ion, leading to exclusion from a portion of the matrix pore space and a lower tortuosity. Parameters used for transport are given in Table 6-7.

Table 6-7. Transport Properties for the tsw35

	Matrix Diffusion Coefficient (m^2/s)	Matrix Sorption Coefficient (m^3/kg)
Technetium	3.2×10^{-11}	0
Neptunium	1.6×10^{-10}	3.0×10^{-4}
Plutonium	1.6×10^{-10}	3.75×10^{-2}

DTNs: LA0003AM831341.001 [DIRS 148751] and LA0003JC831362.001 [DIRS 149557].

For diffusion in the fractures, a representative average diffusion coefficient in water, 1.6×10^{-9} m^2/s, is adjusted by the tortuosity, where the fracture tortuosity is approximated by the

matrix tortuosity (see Section 4.1.5 and 6.4.5). The free-water diffusion coefficient is based on the average of the values given in Table 4-8. No sorption is accounted for in the fractures owing to the limited information and likely limited effects on transport.

Hydrodynamic dispersion is not expected to play a significant role in the transport of radionuclides in the fractures, because of the predominant role of differential advection resulting from fracture-matrix interaction as the main dispersive mechanism. The dispersive effects of fracture-matrix interaction are explicitly modeled, so they do not need to be represented in the form of a dispersion coefficient. Low velocities and short correlation lengths in the matrix make hydrodynamic dispersion negligible compared to molecular diffusion, which is included. With this in mind, hydrodynamic dispersion is not included in the model.

The transport of aqueous radionuclides is calculated without including the effects of radioactive decay. For technetium, neptunium, and certain isotopes of plutonium, the half-lives are long relative to the transport times in the drift-shadow model.

6.3.3 Results of Analysis

6.3.3.1 Flow Field Results and Parameter Sets

Unsaturated flow calculations were performed for a dual-continuum model using the mountain-scale and drift-scale property sets shown in Tables 6-4 to 6-6 and the flow rates shown in Table 6-3. The van Genuchten relative permeability relationship is used for these TOUGH2 calculations. The repository design locates about 80 percent of the emplacement drifts in the tsw35 hydrogeologic unit (see Appendix H). Results of flow calculations using the mountain-scale property set are shown in Figure 6-2.

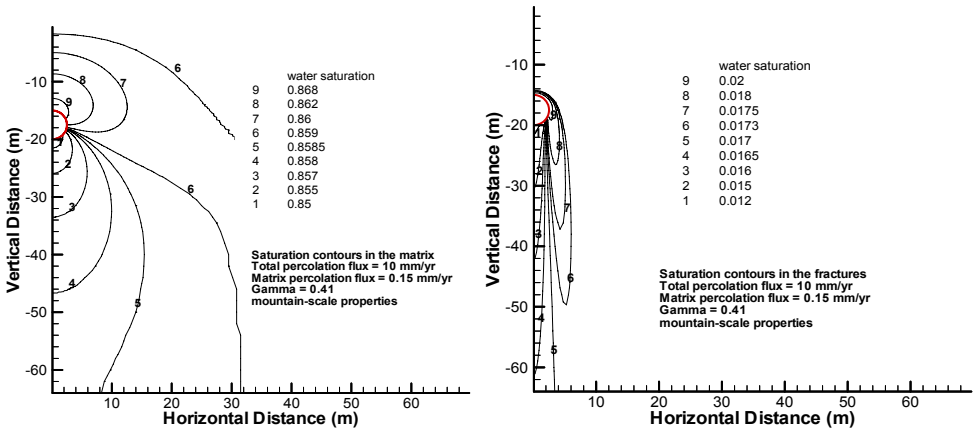

Figure 6-2. Fracture and Matrix Vertical Flux and Saturation Contours Using Mountain-Scale Property Set: (a) Matrix Saturation; (b) Fracture Saturation; (c) Matrix Flux (note 0.15 mm/yr = 4.75×10^{-9} kg/m^2-s); (d) Fracture Flux (note 9.85 mm/yr = 3.12×10^{-7} kg/m^2-s)

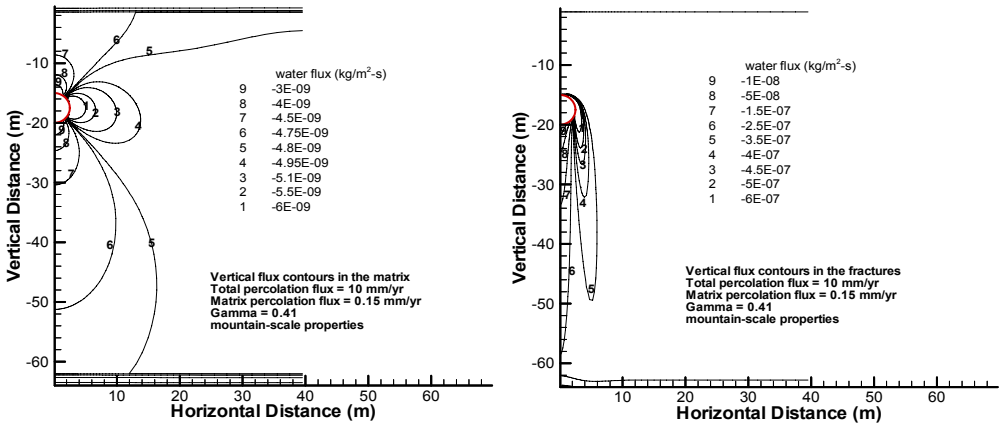

Output DTN: LB0307DSRADTRN.002.

Figure 6-2. Fracture and Matrix Vertical Flux and Saturation Contours Using Mountain-Scale Property Set: (a) Matrix Saturation; (b) Fracture Saturation; (c) Matrix Flux (note 0.15 mm/yr = 4.75×10^{-9} kg/m^2-s); (d) Fracture Flux (note 9.85 mm/yr = 3.12×10^{-7} kg/m^2-s) (Continued)

The drift shadow is seen to be long and narrow for gravity-dominated fracture flow (Figures 6-2b and 6-2d), resulting in a decrease in fracture flow for several drift diameters below the drift. For example, the flow rate within about three drift diameters, on the drift centerline below the emplacement drift, is less than 50 percent of the undisturbed flow rate. The matrix, on the other hand, has a much shorter drift shadow (Figures 6-2a and 6-2c), with the flow rate in the matrix less than 50 percent of the undisturbed flow rate within approximately 0.2 drift diameters below the bottom of the drift (Figure 6-2c).

The original drift-scale property set is the same as the modified drift-scale property set with the exception of the active fracture parameter, γ. In the original drift-scale property set, γ is assigned a value of 0.41, which is the same as for the mountain-scale property set. The vertical flow and water saturation contours for the original drift-scale property set are shown in Figure 6-3. However, as shown by comparing Figures 6-2 and 6-3, the resulting flow and saturation contours are substantially altered for the drift-scale property set. In particular, global vertical gradients of matrix water saturation and flow appearing in Figures 6-3a and 6-3c contrasts with the corresponding plots in Figures 6-2a and 6-2c. The water saturation contours in Figure 6-3 indicate a much greater degree of fracture-matrix interaction than that found for the mountain-scale property set. This can be seen by the increase of matrix water saturation with depth. Given that the matrix properties are unchanged, the only mechanism that would explain this pattern is an increase in water flux from the fractures to the matrix. The flow model calibration against measured values of matrix water potential and saturation was conducted for the mountain-scale property set. Therefore, the original drift-scale property does not appear to be consistent with the field data.

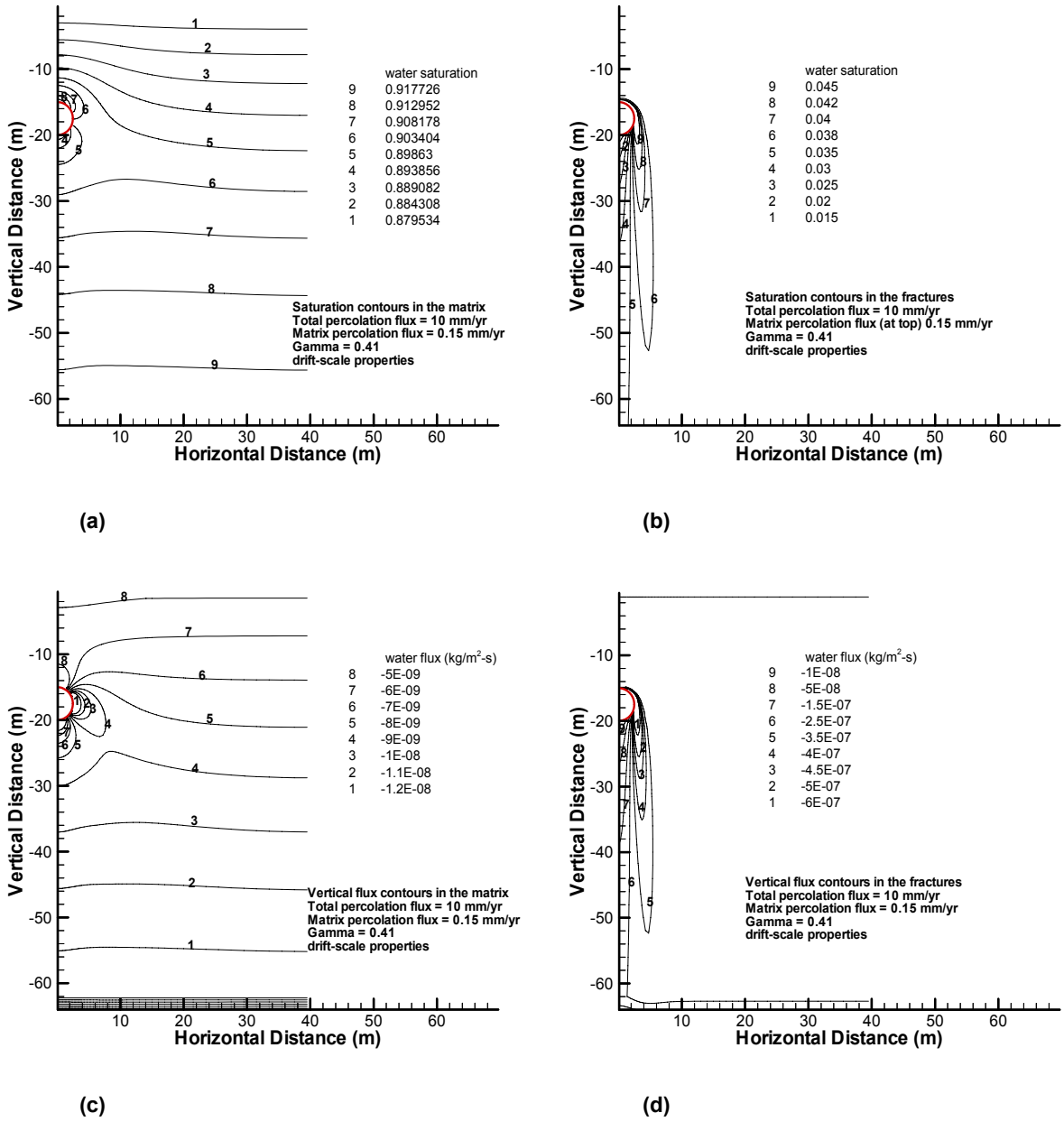

Output DTN: LB0307DSRADTRN.002.

Figure 6-3. Fracture and Matrix Vertical Flux and Saturation Contours using Drift-Scale Property Set and γ = 0.41 (a) Matrix Saturation; (b) Fracture Saturation; (c) Matrix Flux; (d); Fracture Flux

The differences in fracture-matrix interaction found for mountain-scale and drift-scale parameters may be understood from the van Genuchten relationships as modified for the active fracture model. As proposed in Liu et al. (1998 [DIRS 105729], Equation 1), the fraction of active fractures, f_a, is defined by

$$f_a = S_e^{\gamma} \qquad \text{(Eq. 6-1)}$$

where γ is an empirical parameter of the active fracture model. S_e is the effective fracture saturation defined by

$$S_e = \frac{S_f - S_r}{1 - S_r} \quad \text{(Eq. 6-2)}$$

where S_f is the fracture water saturation and S_r is the residual fracture water saturation. The active fracture parameter, γ, is constrained to be less than or equal to one such that the saturation of the active fractures is less than or equal to one. Liu et al. (1998 [DIRS 105729], Equations 5 and 9) derive the following relationships for fracture capillary pressure, P_c , and relative permeability, k_r , using the van Genuchten formulation (van Genuchten 1980 [DIRS 100610]) in combination with the active fracture concept:

$$P_c(S_e) = \frac{1}{\alpha}\left[S_e^{(\gamma-1)/m} - 1\right]^{1-m} \quad \text{(Eq. 6-3)}$$

$$k_r(S_e) = S_e^{(1+\gamma)/2}\left[1 - \left\{1 - S_e^{(1-\gamma)/m}\right\}^m\right]^2 \quad \text{(Eq. 6-4)}$$

Figures 6-2 and 6-3 show that fracture water saturation is expected to be low, in the range of 0.01 to 0.05. The effective water saturation range is even lower in magnitude. Therefore, it is appropriate to consider an expansion of the capillary pressure and relative permeability functions for low water saturation. The first-order expansions of the capillary pressure and relative permeability functions for low water saturation (such that $S^{(1-\gamma)/m}$ is small) are

$$P_c(S_e) \approx \frac{1}{\alpha} S_e^{\left(\frac{1-m}{m}\right)(\gamma-1)} \quad \text{(Eq. 6-5)}$$

$$k_r(S_e) \approx m^2 S_e^{\frac{4(1-\gamma)+m(1+\gamma)}{2m}} \quad \text{(Eq. 6-6)}$$

Flux in the fractures, q_f, can be approximated as free gravity drainage, i.e., the flux in the fractures equals the effective hydraulic conductivity. The effective hydraulic conductivity of the fractures is equal to the product of the saturated hydraulic conductivity, K_s, times the relative permeability. Using this approximation, the fracture saturation is given by

$$S_e \approx \left(\frac{q_f}{K_s m^2}\right)^{\frac{2m}{4(1-\gamma)+m(1+\gamma)}} \quad \text{(Eq. 6-7)}$$

Substituting this into Equation 6-5 gives

$$P_c \approx \frac{1}{\alpha}\left(\frac{K_s m^2}{q_f}\right)^{\frac{2(1-\gamma)(1-m)}{4(1-\gamma)+m(1+\gamma)}} \quad \text{(Eq. 6-8)}$$

Note that the exponent of K_s is always positive. This relationship shows that for a fixed q_f, as K_s decreases, P_c also decreases. This leads to a larger pressure difference between the fractures and matrix and, therefore, greater fracture-to-matrix imbibition flow as K_s decreases. This is consistent with the changes in fracture-matrix interaction observed in Figures 6-2 and 6-3 using the mountain-scale and drift-scale fracture permeabilities.

The noted increase in fracture-matrix interaction suggests that the fracture-matrix interaction parameter, γ, needs to be modified for use with the lower drift-scale fracture permeability. Measurements to establish γ at the drift scale are not available. However, one of the key calibration metrics used to establish the value of γ for the mountain-scale flow model is matrix saturation (BSC 2001 [DIRS 161316], Section 6). Figure 6-4 shows the matrix saturation contours using the drift-scale property set over a range of values for γ. Increasing the value of γ reduces fracture-matrix interaction. The matrix water saturation contours for the drift-scale properties with γ set to 0.81 (Figure 6-4d) appear to be consistent with saturation contours for the mountain-scale property set (Figure 6-4a). Therefore, the modified drift-scale parameter set is believed to be more consistent with field observations. Note that the current calibrated properties values (BSC 2004 [DIRS 169857], Section 6, Tables 6-8 through 6-10) were developed using the lower drift-scale fracture permeabilities, and the values of γ have increased from the previous values for the repository host rock units (BSC 2001 [DIRS 161316], Section 6, Tables 13-15). This is true even though matrix permeabilities are reduced in the current property set, which if everything else was held constant, would lead to a lower value of γ.

Calibration of the UZ Flow Model (Bandurraga and Bodvarsson 1999 [DIRS 103949], Section 4) and comparisons of geochemical composition of perched water (water from the fracture continuum) and matrix pore water [*Analysis of Geochemical Data for the Unsaturated Zone* (BSC 2003 [DIRS 168343], Section 7.5)] suggest that the fracture and matrix continua are only weakly connected. The UZ Flow Model requires reduced fracture-matrix interaction areas for calibration against field measurements of water saturation and potential (Liu et al. 1998 [DIRS 105729], Section 1). Perched water and matrix pore waters are found to be significantly different in composition (BSC 2003 [DIRS 168343], Section 7.5), indicating a lack of geochemical equilibrium between the fracture and matrix continua. Although the hydrological and geochemical evidence indicates that the fracture and matrix continua are only weakly coupled, quantitative estimates of parameters reflecting this aspect of the fractured rock system are uncertain. Furthermore, this aspect of the system has a large impact on radionuclide transport in the drift shadow and beyond.

Flow calculations for percolation rates of 10 mm/year and 100 mm/year have been performed and are used in the transport calculations discussed below. Flow behavior for higher total percolation rates also have been investigated. Complete diversion of seepage is found for total percolation rates up to 300 mm/year. Between the 300 and 350 mm/year total percolation rate, gravitational forces overcome the seepage threshold and water enters the drift.

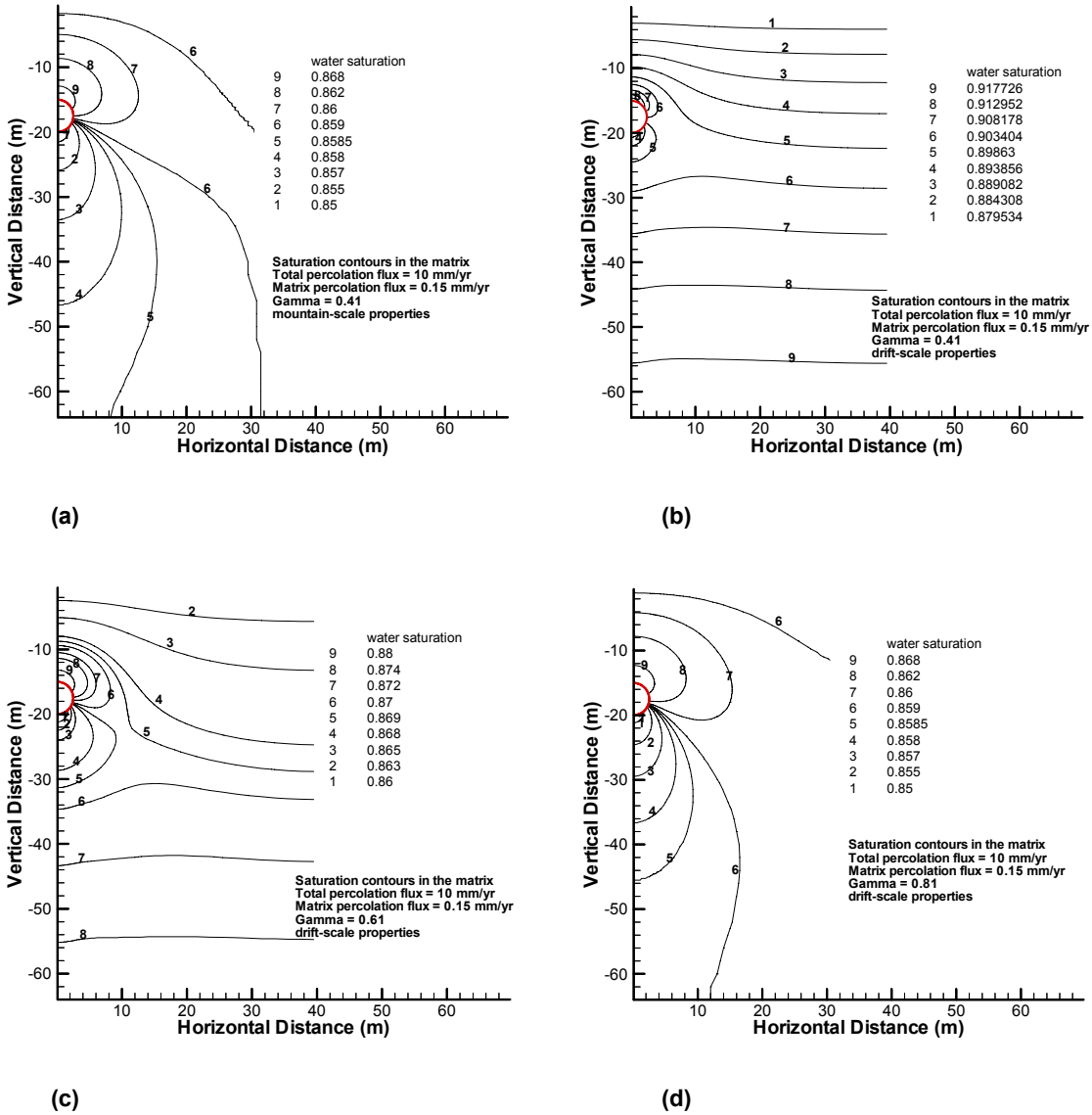

Output DTN: LB0307DSRADTRN.002.

Figure 6-4. Matrix Saturation Contours Using Different Property Sets: (a) Mountain-Scale; (b) Drift-Scale, γ = 0.41; (c) Drift-Scale, γ = 0.61; (d); Drift-Scale, γ = 0.81

6.3.3.2 Transport Results

Transport calculations were run for a dual-permeability flow and transport system using the EOS9nT module of TOUGH2 (Moridis et al. 1999 [DIRS 123093]). In all cases, 1 kg of radionuclide is available for release from the waste emplacement drift. Connections are made from two cells inside the drift, where the radionuclides originate, to the fractures and rock matrix cells adjacent to the bottom of the drift and within 1.1 meter of the drift centerline (Houseworth 2003 [DIRS 163233], p. 118). Radionuclides enter the fracture and matrix cells from the drift cells at rates determined by diffusive transport processes, because water does not flow through the drift cells.

Breakthrough curves for transport to the bottom of the model (45 m below the bottom of the emplacement drift, as seen in Figure 6-1) are shown for technetium, neptunium, and plutonium in Figures 6-5a through 6-5d. These figures compare the transport results for total percolation rates of 10 mm/year and 100 mm/year for 2 matrix percolation cases each (see Table 6-3).

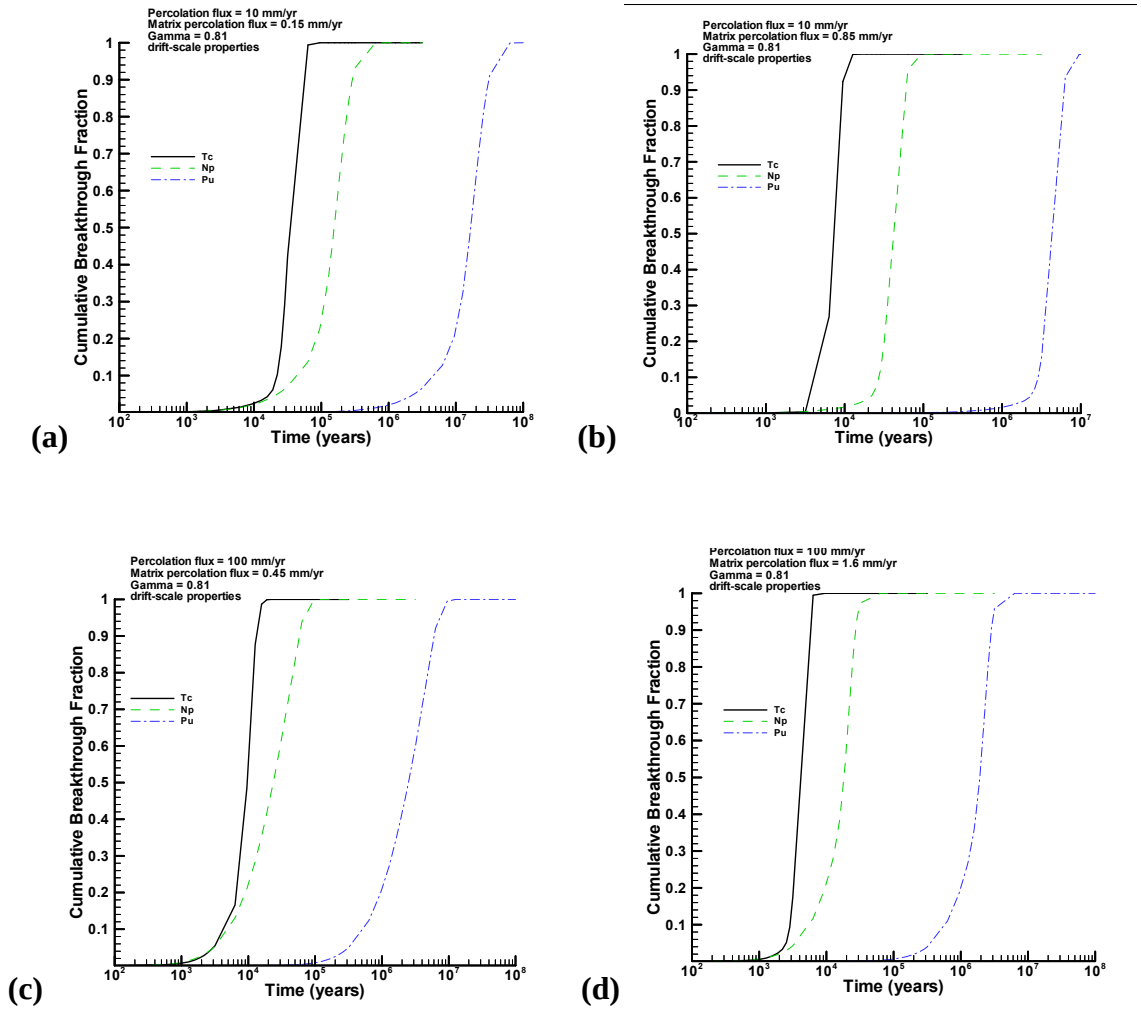

Output DTN: LB0307DSRADTRN.002.

Figure 6-5. Breakthrough Curves for Drift Shadow Transport: (a) Total Percolation Flux = 10 mm/year, Matrix Percolation Flux = 0.15 mm/year; (b) Total Percolation Flux = 10 mm/year, Matrix Percolation Flux = 0.85 mm/year; (c) Total Percolation Flux = 100 mm/year, Matrix Percolation Flux = 0.45 mm/year; (d) Total Percolation Flux = 100 mm/year, Matrix Percolation Flux = 1.6 mm/year

A comparison of the 50 percent breakthrough with approximate matrix advection-transport times can be made (Table 6-8). Approximate advection-transport times are computed from the flux introduced to the matrix divided by the approximate water content and retardation factor. Advective transport times are approximate, because flow rates vary as a result of the drift shadow effect and in response to fracture-matrix exchange. Nevertheless, flow patterns discussed

earlier indicate that the variations in flux and water saturation in the matrix are minor. Therefore, the approximate advective transport time is considered reasonable. The retardation factor is given by the relationship [derived from *Groundwater* (Freeze and Cherry 1979 [DIRS 101173], p. 404]

$$R = 1 + \frac{\rho_m (1-\phi) K_d}{\phi S_w} \quad \text{(Eq. 6-9)}$$

where ρ_m is the grain density (2,540 kg/m^3), ϕ is the porosity (0.131), K_d is the sorption coefficient (see Table 6-7), and S_w is the water saturation (see Table 6-8).

Table 6-8. Advective Transport Times and Computed Transport Times

Radionuclide	Total Percolation Flux (mm/yr)	Matrix Percolation Flux (mm/yr)	Water Saturation	Retardation Factor	Advective Travel Time in Matrix (years)	50% Breakthrough Time (years) (Output-DTN: LB0307DSRADTRN.002)
Technetium	10	0.15	0.86	1	3.4E+04	3.6E+04
Neptunium	10	0.15	0.86	6.9	2.3E+05	1.6E+05
Plutonium	10	0.15	0.86	740	2.5E+07	1.7E+07
Technetium	10	0.85	0.96	1	6.7E+03	7.5E+03
Neptunium	10	0.85	0.96	6.3	4.2E+04	4.4E+04
Plutonium	10	0.85	0.96	660	4.4E+06	4.6E+06
Technetium	100	0.45	0.94	1	1.2E+04	9.6E+03
Neptunium	100	0.45	0.94	6.4	7.9E+04	2.4E+04
Plutonium	100	0.45	0.94	670	8.3E+06	2.5E+06
Technetium	100	1.60	0.98	1	3.6E+03	4.4E+03
Neptunium	100	1.60	0.98	6.2	2.2E+04	1.8E+04
Plutonium	100	1.60	0.98	650	2.3E+06	1.9E+06

Output DTN: LB0307DSRADTRN.002.

In general, the advective travel time in the matrix is close to the value of the 50 percent breakthrough time for all percolation fluxes, suggesting that transport in the drift shadow is dominated by matrix advection. Because of the diversion of flow around the drift, radionuclides move from the drift to the rock by diffusion. Diffusive releases preferentially enter the matrix rather than the fractures because the water content (porosity times water saturation) in the matrix is roughly 1,000 times larger than in the fractures immediately beneath the drift. In some cases, the 50 percent breakthrough time is longer than the advective travel time. This happens for some of the technetium breakthrough curves (such as the case for 10 mm/year total flux with 0.85 mm/year flux in the matrix) because the computed advective travel times in Table 6-8 ignore the hydrodynamic effects of the drift shadow. For neptunium and plutonium, some of the 50 percent breakthrough times are shorter than the advective travel times because of diffusive exchange between the matrix and the fractures. This occurs for the sorbing radionuclides, which have longer advective travel times and have more time for diffusive release from the matrix to the fractures. In the fractures, travel times are relatively short.

6.3.3.3 Transport Sensitivity Analysis

Figure 6-6 compares breakthrough curves for technetium under different total percolation flux and matrix flux cases. The breakthrough curve sensitivity to total percolation flux is found to be low, with much greater sensitivity to the rate of percolation flux in the matrix. This result further substantiates the hypothesis that transport in the drift shadow is predominantly in the matrix.

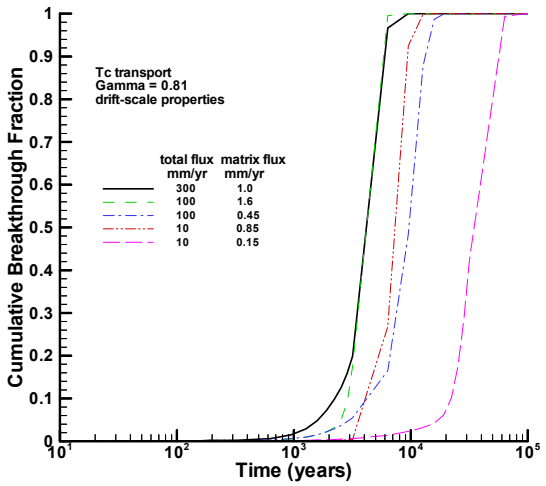

Output DTN: LB0307DSRADTRN.002.

Figure 6-6. Technetium Transport as a Function of Total Percolation Flux and Matrix Percolation Flux

Figures 6-7a and 6-7b compare Tc transport in the drift shadow to transport in the unperturbed flow field for 10 mm/year and 100 mm/year total percolation fluxes. The releases in the unperturbed flow field were made in cells near the right-hand boundary of the model, at the same vertical coordinate as the bottom of the drift. Two types of releases were investigated; releases that are initiated in the fractures and releases that are initiated in the matrix. The drift-shadow breakthrough curve is shown for comparison. These results clearly demonstrate that releases to fractures transport at much greater velocities. These results also indicate that the drift-shadow effect is approximately equivalent to initiation of transport in the matrix. The dynamics of the drift shadow flow field have only a second-order effect on the breakthrough curves.

Figure 6-8 shows a sensitivity calculation for the effects of the active fracture parameter, γ, on breakthrough curves for Tc. This figure clearly shows that fracture-matrix interaction is a key factor in the rate of transport in the drift shadow. As γ is reduced, the amount of fracture-matrix interaction increases, resulting in greater matrix-to-fracture diffusive exchange. Increased interaction results in more contaminant movement from the matrix to fractures in the shadow and as a result more transport in the fractures and, therefore, more rapid transport through the drift shadow

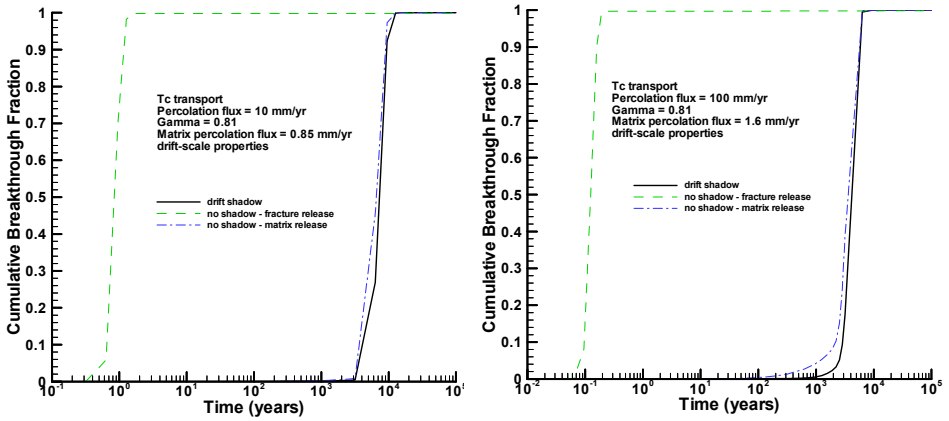

(a) **(b)**

Output-DTN: LB0307DSRADTRN.002.

Figure 6-7. Sensitivity Calculations Comparing Drift Shadow Transport with Transport in Unperturbed Flow Field: (a) Total Percolation Flux = 10 mm/year, Matrix Percolation Flux = 0.85 mm/year; (b) Total Percolation Flux = 100 mm/year, Matrix Percolation Flux = 1.6 mm/year

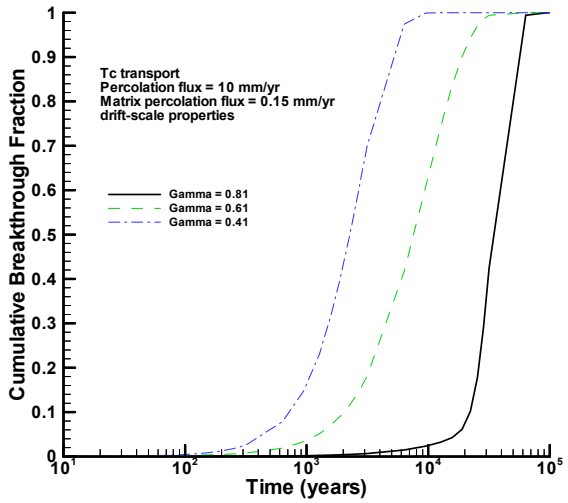

Output DTN: LB0307DSRADTRN.002.

Figure 6-8. Sensitivity Calculation for Technetium Transport Using Different Values of γ

6.4 FRACTURE-MATRIX PARTITIONING MODEL

Results of sensitivity studies presented in Section 6.3 suggest that the main effect of the drift shadow is that, with no seepage, radionuclides are transported by diffusion into the fractures and matrix of the surrounding rock; because most of the water is in the matrix, most of the radionuclides are released to the matrix. The most important factor controlling the breakthrough

curves is the partitioning of the release between the fracture and matrix continua. The fracture-matrix partitioning model presented here focuses on the partitioning of releases from drifts between the rock fractures and matrix. The fracture-matrix partitioning model sets unperturbed fracture flow directly below the base of waste emplacement drifts. This approximation in neglecting the drift shadow effect on flow is based on the idea that the drift shadow may not be as spatially extensive as presented in Section 6.3, due to heterogeneity and anisotropy in fracture characteristics, as well as discrete fracture effects. As in Section 6.3, the fracture-matrix partitioning model is limited to drifts without seepage or other sources of water that may result in advective-dominated transport in the drift invert, i.e., transport through the drift invert to the rock is dominated by diffusion. For the initial release of radionuclides, the transient concentration front passing from the invert into the rock will initially be dominated by diffusion. However, as the concentration approaches a steady condition, transport in the rock will be dominated by advection. This is due to the reduction in the radionuclide concentration gradient at the drift wall over time for a steady radionuclide source concentration. The radionuclide concentration gradient at the drift wall relaxes for greater offset between the drift wall and the flowing fracture. The water content of the matrix is always dominant over the water content of the fractures, so diffusive exchange between the invert and the rock will predominantly enter the matrix. However, for the steady transport condition following the initial transient period, the final distribution of releases becomes a function of the water content and flux in the fractures and matrix. Because the unperturbed flux (no effects of the drift on the flow field) in the repository host rock is predominantly in the fractures, the distribution of releases from the invert between the fractures and matrix is controlled by the relative influence of the flux and the water content of the fractures and matrix.

Note that calculations reported in *Advection Versus Diffusion in the Invert* (BSC 2003 [DIRS 170881], Sections 6.6–6.8, Attachment X) indicate that even without drift seepage, water will enter the drift laterally from the rock into the crushed tuff invert as a result of capillary forces. The invert is a dual continuum in which the intragranular porosity (micropores) of the crushed tuff grains are the original porosity of the rock matrix and the intergranular porosity (macropores) between the crushed tuff grains has much larger pore spaces analogous to the rock fractures. The predicted flow pattern shows water entering laterally from the rock into the invert along the sides and then flowing out of the invert at the bottom of the drift. This flow is restricted to the micropores of the crushed tuff and the rock matrix (BSC 2003 [DIRS 170881], Section 6.11). The crushed tuff micropores are assigned the same capillary and permeability characteristics as the rock matrix, so from the perspective of flow, the rock matrix and micropores of the crushed tuff invert constitute a uniform and continuous flow domain. This is a reasonable approximation for diffusive transport through the intragranular porosity because the grains will be in capillary contact providing continuous diffusion pathways through the invert. Flow exchange from the crushed tuff micropores with the rock fractures and macropores of the crushed tuff is excluded by capillary pressure differences. A similar flow pattern between the rock fractures and crushed tuff macropores is not predicted due to the weaker capillarity of the fractures and the capillary barrier presented by the crushed tuff macropores relative to the rock fractures. The predicted micropore-matrix flow will lead to greater partitioning of radionuclide flux from the invert into the rock matrix than would be predicted by the fracture-matrix partitioning model, which is based on pure diffusive transport through the invert. This is because the advective transport process through the intragranular porosity delivers radionuclides to the rock matrix exclusively, as opposed to diffusion, which leads to

radionuclides entering both the rock fractures and rock matrix. Therefore, the neglect of this flow is conservative for the prediction of radionuclide partitioning from the drift into the rock fractures and matrix, and subsequent effects on radionuclide transport through the unsaturated zone.

The results of the fracture-matrix partitioning model are to be used as an alternative model for comparison with the EBS Radionuclide Transport Model [*EBS Radionuclide Transport Abstraction* (BSC 2004 [DIRS 169868])].

6.4.1 Conceptual and Mathematical Model Development

Figure 6-9 shows a diagram of the fracture-matrix partitioning model given this conceptual background. Beneath the waste package, the invert ranges in depth from 675 mm to 806 mm, with an average depth of 741 mm. The total invert depth variation is approximately 17 percent of the average depth beneath the waste package. Sensitivity to invert thickness is included in the model, but the second-order effects of the curvature of the drift-rock interface are not included. Rather than include the entire invert-rock interface, the model is restricted to a domain from the centerline of a fracture to a boundary at the midpoint between fractures (Figure 6-10). The boundary along the fracture centerline and the boundary along the midpoint between fractures are approximate symmetry boundaries. The top and bottom boundaries correspond to the top and bottom of the invert.

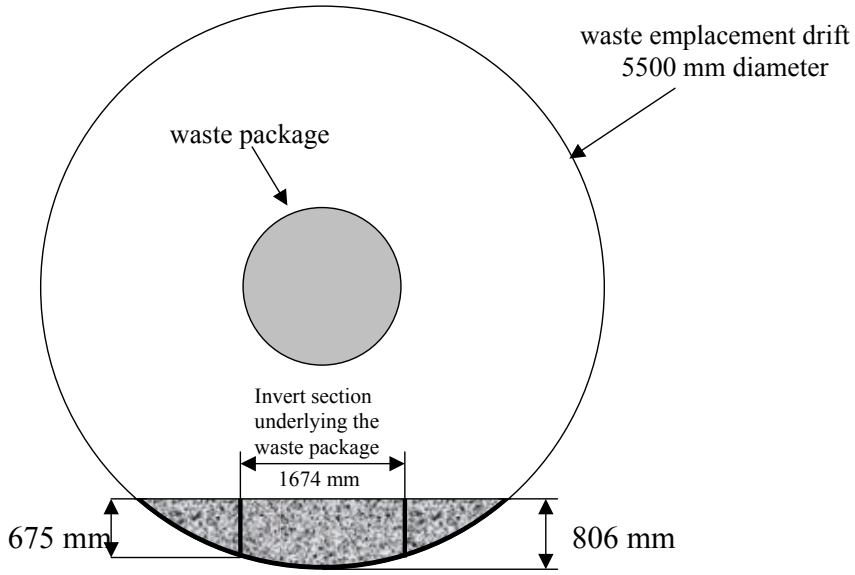

Sources: BSC 2003 [DIRS 164101].

Figure 6-9. Schematic of Waste Emplacement Drift Configuration

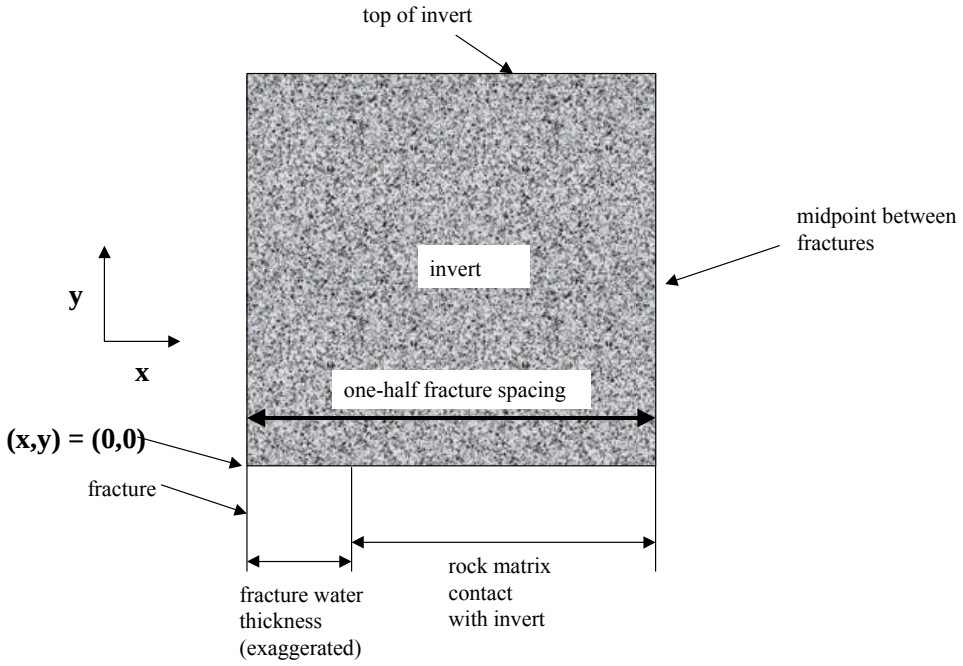

Figure 6-10. Schematic Diagram of Modeling Domain

The governing equation for steady diffusion in a homogeneous invert is [derived from *The Mathematics of Diffusion* (Crank 1975 [DIRS 122990], Equation 1.3, Section 1.3)]

$$\nabla^2 C(x, y) = 0 \qquad \text{(Eq. 6-10)}$$

where C is the mass concentration of radionuclide and x and y are spatial coordinates.

The boundary condition at the top of the invert has a fixed radionuclide concentration,

$$C(x, y_m) = C_m \qquad \text{(Eq. 6-11)}$$

where y_m is the y coordinate for the top of the invert and C_m is the radionuclide concentration at the top of the invert. No-flux boundary conditions are imposed on the lateral boundaries as a result of symmetry along these boundaries:

$$\frac{\partial C}{\partial x}(0, y) = 0 \qquad \text{(Eq. 6-12)}$$

$$\frac{\partial C}{\partial x}(h_f, y) = 0 \qquad \text{(Eq. 6-13)}$$

where h_f is the x coordinate for the midpoint between fractures.

The boundary condition at the bottom of the invert is that the diffusive flux of radionuclides from the invert is equal to the radionuclide flux into the rock. This radionuclide flux into the rock is

split into two portions; flux into the rock matrix and flux into the fracture of the domain considered. To determine this flux, one must establish the vertical position of fracture flow relative to the waste emplacement drift. The high permeability and low capillary pressure of the fractures in the repository host rock are conditions conducive to gravity-driven flow. For fracture flow to move around the drift and contact the invert at a point underneath a waste package, the trajectory needs to be approximately 3 to 1 horizontal to vertical motion. Furthermore, the vertical projection for the portion of the invert beneath the waste package available for contact with horizontal flow is only about 13 cm (see Figure 6-9). Thus, flow in vertical fractures is not expected to have a sufficient lateral flow component to result in fracture flow immediately beneath a waste emplacement drift. However, under certain circumstances related to the local fracture connectivity, subhorizontal fractures may be capable of redirecting flow in a fracture network in a near-horizontal direction. Under these circumstances, the extent of the drift shadow could be substantially reduced compared with the model results presented in Sections 6.3.3.1 and 6.3.3.2.

The limitation on where fracture flow may occur beneath a waste emplacement drift is associated with the probability of the vertical position of a subhorizontal fracture beneath a waste emplacement drift in association with a vertical fracture. Because of fracture spacing and the random relationship between fracture connections and the drift, the distance of a subhorizontal fracture connection to a vertical fracture beneath the waste emplacement drift, Δy_f, lies between 0 and the fracture spacing (see Figure 6-11). This distance (Δy_f) has a uniform distribution, so the expected value for the vertical distance to the closest potential fracture flow beneath a waste emplacement drift is one-half the fracture spacing.

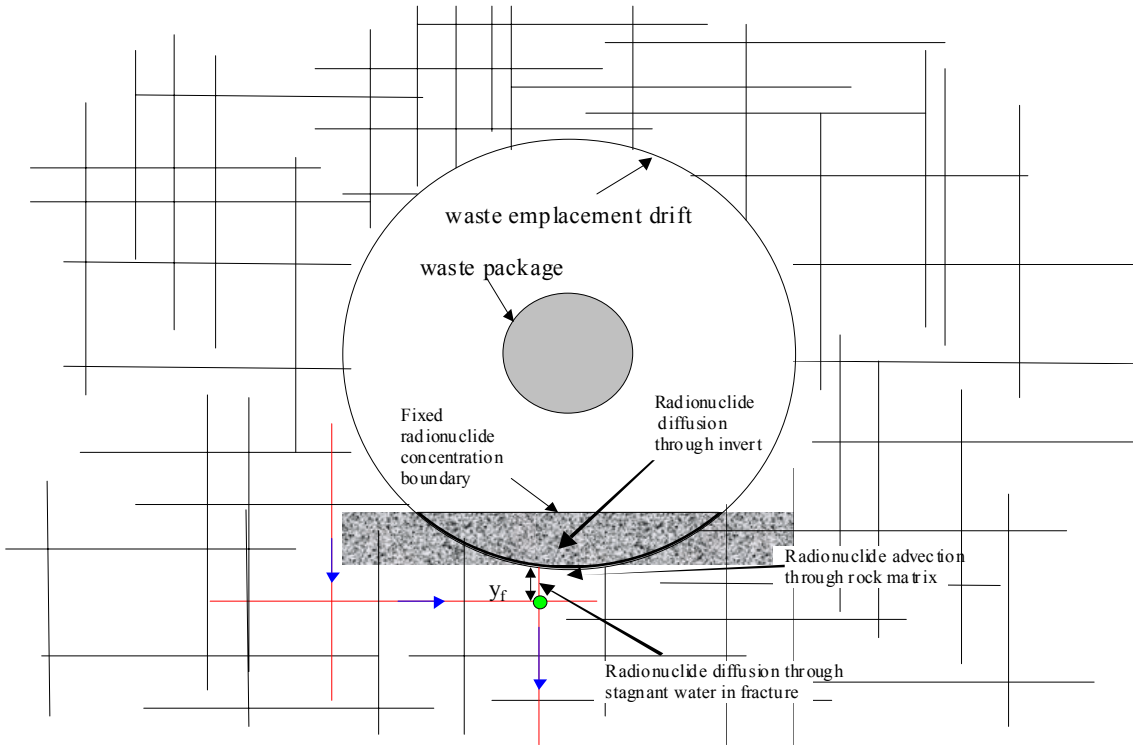

Figure 6-11. Schematic of Fracture Network, Waste Emplacement Drift, and Transport Processes

The radionuclide mass flux along any streamline through this connection (green circle in Figure 6-11), under steady flow and constant concentration conditions, will be equal to the fracture water flux times the concentration. Given that the water in the fracture between the drift and the connection is not flowing, the flux into the connection is diffusive and the water saturation of the fracture will be at its residual value. The steady-state flux balance along a fracture streamline is given by

$$-D_{ef}\left(\frac{C(x,0)-C_{fn}(x)}{\Delta y_f}\right)=q_{wf}C_{fn}(x) \quad \text{for} \quad 0<x<b \qquad \text{(Eq. 6-14)}$$

where D_{ef} is the diffusion coefficient for steady diffusive flux in the fracture, C_{fn} is the radionuclide mass concentration at the connection point in the fracture network, and b is the half-water thickness in the fracture. Note that this water film thickness represents the residual saturation of the fracture, therefore, the fracture is unsaturated. Because the fracture is identified discretely rather than as a continuum, the local water flux in the discrete fracture, q_{wf}, is equal to the continuum fracture flux (e.g., from a dual-permeability flow model) divided by the fracture water content, and thus is a velocity at points across the water film. Note that q_{wf} is negative. Solving Equation 6-14 for C_{fn} gives

$$C_{fn}(x)=\frac{C(x,0)}{1+\frac{(-q_{wf})\Delta y_f}{D_{ef}}} \quad \text{for} \quad 0<x<b \qquad \text{(Eq. 6-15)}$$

Therefore, the radionuclide mass flux, $q_{rad}(x)$, into the fracture at the drift wall may be expressed as

$$q_{rad}(x)=q_{wf}C_{fn}(x)=\frac{q_{wf}C(x,0)}{1-\frac{q_{wf}\Delta y_f}{D_{ef}}} \quad \text{for} \quad 0<x<b \qquad \text{(Eq. 6-16)}$$

Note that the effects of fracture-matrix exchange are neglected. However, neglecting this mechanism leads to greater radionuclide partitioning into the fracture at the drift wall. This is because the lower radionuclide concentrations in the fracture as compared to the matrix will lead to diffusive fracture-matrix transfers from the matrix to the fractures in the region immediately below the drift. Therefore, radionuclide flux into the fracture from the drift will be reduced because it will be in competition with radionuclide entry into the fracture from the rock matrix.

Owing to the continuity of the matrix, the radionuclide flux into the matrix is equal to the matrix water flux, q_m, times the radionuclide concentration at the drift boundary,

$$q_{rad}(x)=q_m C(x,0) \quad \text{for} \quad b<x<h_f \qquad \text{(Eq. 6-17)}$$

Therefore, the balance between diffusive radionuclide flux in the invert and the advective radionuclide flux into the rock may be written in the form

$$-D_{el}\frac{\partial C}{\partial y}(x,0) = q(x)C(x,0) \qquad \text{(Eq. 6-18)}$$

where D_{el} is the effective diffusive mass-transfer coefficient for steady diffusive radionuclide flux in the invert. The generalized water flux function, $q(x)$, is given by

$$q(x) = \frac{q_{wf}}{1-\dfrac{q_{wf}\Delta y_f}{D_{ef}}} = q_{fe} \quad \text{for} \quad 0 < x < b \qquad \text{(Eq. 6-19)}$$

$$q(x) = q_m \quad \text{for} \quad b < x < h_f \qquad \text{(Eq. 6-20)}$$

A schematic water flux profile is shown in Figure 6-12. In the fracture water ($x = 0$ to $x = b$), the equivalent "flux", q_{fe} , is given by Equation 6- 19. The water flux in the matrix ($x = b$ to $x = h_f$) is given by Equation 6- 20. The generalized water flux function in the fracture domain ($0 < x < b$) has the water flux that would result in the same radionuclide mass transport by advection as occurs through the fracture by diffusion.

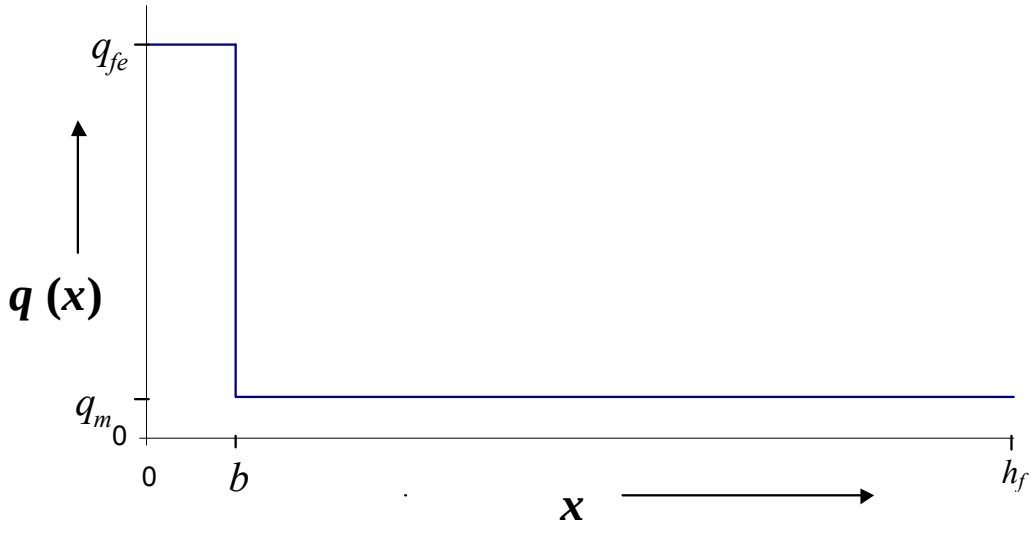

Figure 6-12. Schematic Generalized Water Flux Profile at the Drift Wall

Note that the fracture-matrix partitioning model does not include any representation of the air that is present in an unsaturated fracture at the invert-rock interface. Aqueous radionuclides cannot enter the rock through the gas phase, therefore, the presence of air in the fracture represents a barrier to radionuclide transfer to the rock. The justification for not including this feature of the unsaturated fracture in the model is given in Section 6.5.

6.4.2 Dimensionless Representation

The model described by Equations 6-10 to 6-13 and 6-18 to 6-20 can be put into a dimensionless form, which reduces the number of independent parameters that need to be considered. The dimensionless concentration, C_d, is defined by

$$C_d = \frac{C}{C_m} - 1 \qquad \text{(Eq. 6-21)}$$

The range of C_d varies between 0 and -1. The reason for the normalization by subtracting 1 is to simplify the boundary condition at the top of the invert. The dimensionless distance coordinates, x_d and y_d, are given by

$$x_d = \frac{x}{h_f} \qquad \text{(Eq. 6-22)}$$

and

$$y_d = y_{dm} - \frac{y}{h_f} \qquad \text{(Eq. 6-23)}$$

where x_d varies between 0 and 1 and y_d between 0 and $y_{dm} = \frac{y_m}{h_f}$.

Writing Equations 6-10 through 6-13 and 6-18 in terms of the dimensionless variables gives

$$\nabla_d^2 C_d(x_d, y_d) = 0 \qquad \text{(Eq. 6-24)}$$

$$C_d(x_d, 0) = 0 \qquad \text{(Eq. 6-25)}$$

$$\frac{\partial C_d}{\partial x_d}(0, y_d) = 0 \qquad \text{(Eq. 6-26)}$$

$$\frac{\partial C_d}{\partial x_d}(1, y_d) = 0 \qquad \text{(Eq. 6-27)}$$

$$\frac{\partial C_d}{\partial y_d}(x_d, y_{dm}) = q_d(x_d)\left(C_d(x_d, y_{dm}) + 1\right) \qquad \text{(Eq. 6-28)}$$

where the dimensionless Laplacian operator is defined by $\nabla_d^2 \equiv \frac{\partial^2}{\partial x_d^2} + \frac{\partial^2}{\partial y_d^2}$ and the dimensionless water flux, $q_d(x_d)$, on the right-hand side of Equation 6-28 is defined as follows:

$$q_d = Pe_{fe} = \frac{q_{fe} h_f}{D_{eI}} \quad \text{for} \quad 0 < x_d < b_d \tag{Eq. 6-29}$$

$$q_d = Pe_m = \frac{q_m h_f}{D_{eI}} \quad \text{for} \quad b_d < x_d \le 1 \tag{Eq. 6-30}$$

$$q_d = \frac{1}{2}\left(Pe_{fe} + Pe_m\right) \quad \text{for} \quad x_d = b_d \tag{Eq. 6-31}$$

where

$$b_d = \frac{b}{h_f} \tag{Eq. 6-32}$$

The average value at the boundary, $x_d = b_d$, is used to have a definition for the dimensionless water flux at all points in the domain. Based on the dimensionless form in Equations 6-24 through 6-32, the following dimensionless groups may be identified:

$Pe_m \equiv$ matrix – invert mass transfer Peclet number

$Pe_{fe} \equiv$ fracture – invert mass transfer Peclet number

$\theta_f = b_d \equiv$ fracture water content

$y_{dm} \equiv$ dimensionless invert depth.

6.4.3 Solution Method

The solution of Equation 6-24 subject to the boundary conditions defined in Equations 6-25 to 6-28 may be obtained using an expansion in cosines and hyperbolic tangent functions. The general solution that satisfies Equation 6-24 and boundary conditions, Equations 6-25 to 6-27 is

$$C_d\left(x_d, y_d\right) = B_0 y_d + \sum_{j=1}^{\infty} B_j \cos\left(j\pi x_d\right)\sinh\left(j\pi y_d\right) \tag{Eq. 6-33}$$

which may be verified by direct substitution. Substituting Equation 6-33 into Equation 6-28 gives

$$A_0\left(1 - q_d\left(x_d\right) y_{dm}\right) + \sum_{j=1}^{\infty} A_j \cos\left(j\pi x_d\right)\left[j\pi - q_d\left(x_d\right)\tanh\left(j\pi y_{dm}\right)\right] = q_d\left(x_d\right) \tag{Eq. 6-34}$$

or

$$\sum_{j=0}^{\infty} M_{ij} A_j = q_{di} \qquad \text{(Eq. 6-35)}$$

where

$$M_{i0} = \left(1 - q_d\left(x_{di}\right) y_{dm}\right) \qquad \text{(Eq. 6-36)}$$

$$M_{ij} = \cos\left(j\pi x_{di}\right)\left[j\pi - q_d\left(x_{di}\right)\tanh\left(j\pi y_{dm}\right)\right] \quad \text{for} \quad i > 0 \qquad \text{(Eq. 6-37)}$$

$$q_{di} = q_d\left(x_{di}\right) \qquad \text{(Eq. 6-38)}$$

$$A_j = B_j \cosh\left(j\pi y_{dm}\right) \qquad \text{(Eq. 6-39)}$$

The transformation from B_j to A_j is introduced to eliminate numerical difficulties in the evaluation of $\cosh\left(j\pi y_{dm}\right)$ and $\sinh\left(j\pi y_{dm}\right)$ for large j. The concentration at the invert-rock interface may be written as

$$C_d\left(x_d, y_{dm}\right) = A_0 y_{dm} + \sum_{j=1}^{\infty} A_j \cos\left(j\pi x_d\right)\tanh\left(j\pi y_{dm}\right) \qquad \text{(Eq. 6-40)}$$

The usual Fourier method for determining the coefficients, A_j, cannot be used because of the term in Equation 6-34 that involves the product of the cosine and the dimensionless water flux. However, a Fourier solution does exist, because if the steady concentration at the boundary $y_d = y_{dm}$ were known, then the coefficients could be determined through standard methods using the orthogonality properties of the cosine series. An alternative method to determine the coefficients may be developed by noting that a finite range for j is expected to be sufficient in practice based on the similarity of this solution method with Fourier series and the known convergence characteristics of the Fourier series [*A First Course in Partial Differential Equations* (Weinberger 1965 [DIRS 163216], Section 18)]. For a finite sum from j = 0 to j = j_{max}, Equation 6-34 may be considered as a set of j_{max}+1 linear equations, corresponding to the set of points $x_{d0} \ldots x_{dj_{\max}}$, in j_{max}+1 unknowns, $A_0 \ldots A_{j_{\max}}$, as shown in Equation 6-35. This solution method will be referred to as the discrete transform method. See Appendix L for a demonstration of the equivalence of the discrete transform method with the standard Fourier series method. Alternative solution methods include direct numerical approaches, such as the finite difference method. These methods were not selected because the solution to the problem is amenable using the semi-analytic approach presented here.

The cumulative dimensionless radionuclide flux in the fracture, F_{df}, and in the matrix, F_{dm}, may be calculated by integrating the diffusive flux on the left hand side of Equation 6-28 over x_d. Equation 6-33 is used for $C_d(x_d, y_d)$ to compute the derivative evaluated at y_{dm}. The result is

$$F_{dfD} = b_d A_0 + \sum_{j=1}^{j_{\max}} A_j \sin(j\pi b_d) \qquad \text{(Eq. 6-41)}$$

$$F_{dmD} = (1 - b_d) A_0 - \sum_{j=1}^{j_{\max}} A_j \sin(j \pi b_d) \qquad \text{(Eq. 6-42)}$$

The cumulative dimensionless radionuclide flux in the fracture, F_{df}, and in the matrix, F_{dm}, may also be calculated by integrating the advective flux on the right-hand side of Equation 6-28 over x_d. Equation 6-40 is used for $C_d(x_d, y_{dm})$ and the flux in Equations 6-29 and 6-30 for the fracture and matrix, respectively.

$$F_{dfA} = Pe_{fe} \left(b_d \left(1 + A_0 y_{dm}\right) + \sum_{j=1}^{j_{max}} \frac{A_j}{j\pi} tanh\left(j \pi y_{dm}\right) sin\left(j \pi b_d\right) \right) \qquad \text{(Eq. 6-43)}$$

$$F_{dmA} = Pe_m \left(\left(1 - b_d\right)\left(1 + A_0 y_{dm}\right) - \sum_{j=1}^{j_{max}} \frac{A_j}{j\pi} tanh\left(j \pi y_{dm}\right) sin\left(j \pi b_d\right) \right) \qquad \text{(Eq. 6-44)}$$

The solution method presented below will involve calculating each of these advective and diffusive fluxes for the matrix and the fracture domains. The accuracy of the solution, meaning number of terms included in the expansion, is determined by comparing the results for the diffusive flux on the left hand side of Equation 6-28 and the advective flux on the right hand side of Equation 6-28.

6.4.4 Solution Behavior

A typical case is investigated here to provide insight into the solution behavior. This case, called nominal case 1, is parameterized as shown in Table 6-9.

Table 6-9. Parameters for Nominal Case

Parameter	Value
fracture water content	0.0001
fracture Peclet number	-1
matrix Peclet number	-0.004
dimensionless invert depth	4

Output-DTN: LB0307FMRADTRN.001.

The dimensionless invert depth of 4 means that the invert is 4 times deeper than the fracture half-spacing (see definition of the dimensionless invert depth following Equation 6-23). The computational details leading to the results for the cases summarized here are given in a

scientific notebook by Wang (2003 [DIRS 163234], SN-LBNL-SCI-236-V1, pp. 5–118). An example of the nominal-case calculations is presented in Appendix J.

The concentration profile at the drift wall is shown for a nominal case 1 in Figure 6-13. The concentration drop at the left boundary results from the higher radionuclide mass flux entering the fracture. Lateral diffusive mass flux in the invert leads to additional radionuclide mass transfer into the fracture. The flux profile is shown in Figure 6-14, which shows the large flux near $x_d = 0$ in the fracture zone. Note that the scale on this figure is selected to show how the flux profile behaves moving from the fracture to the matrix; the maximum value in the fracture zone is approximately 0.98. The matrix flux near the fracture is depressed on account of the reduced radionuclide concentration in the invert.

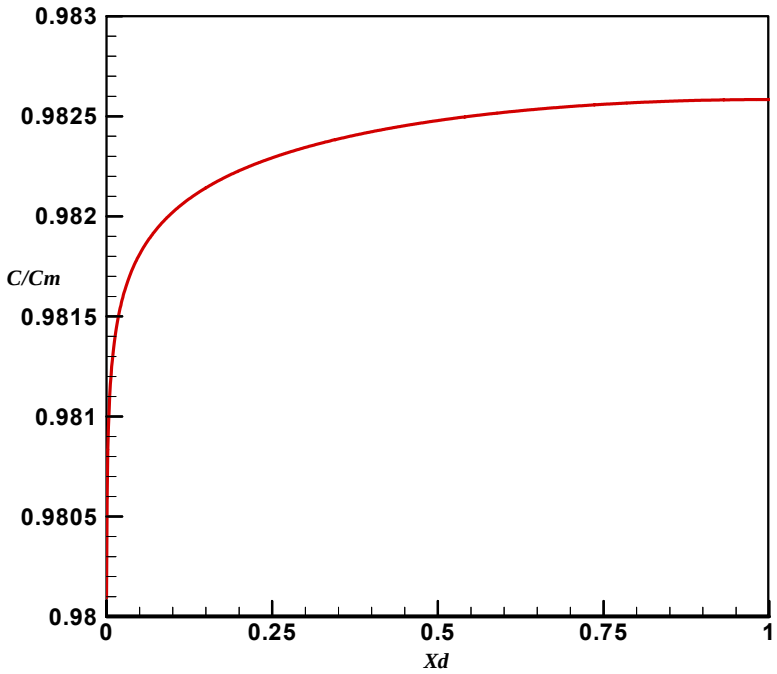

Output DTN: LB0307FMRADTRN.001.

Figure 6-13. Plot of C/Cm at the Solution Locations for the Fourier Coefficients—Nominal Case 1

Dimensionless radionuclide flux ratios are computed for both the flux in the invert at the drift wall and for the flux in the rock at the drift wall. The flux ratio on the invert side of the boundary is given by

$$P_{rI} = \frac{F_{dfD}}{F_{dfD} + F_{dmD}}$$

and the flux ratio in the rock at the drift wall is given by

$$P_r = \frac{F_{dfA}}{F_{dfA} + F_{dmA}},$$

as computed from Equations 6-41 through 6-44. These two dimensionless flux ratios are the partitioning ratio between the fracture and the matrix in the rock beneath the invert. The diffusive and advective flux ratios are 0.024 and 0.022, respectively. The discrepancy between these flux terms provides an estimator for the accuracy of the discrete transform solution. For an infinite number of terms, the two flux ratios would be equal.

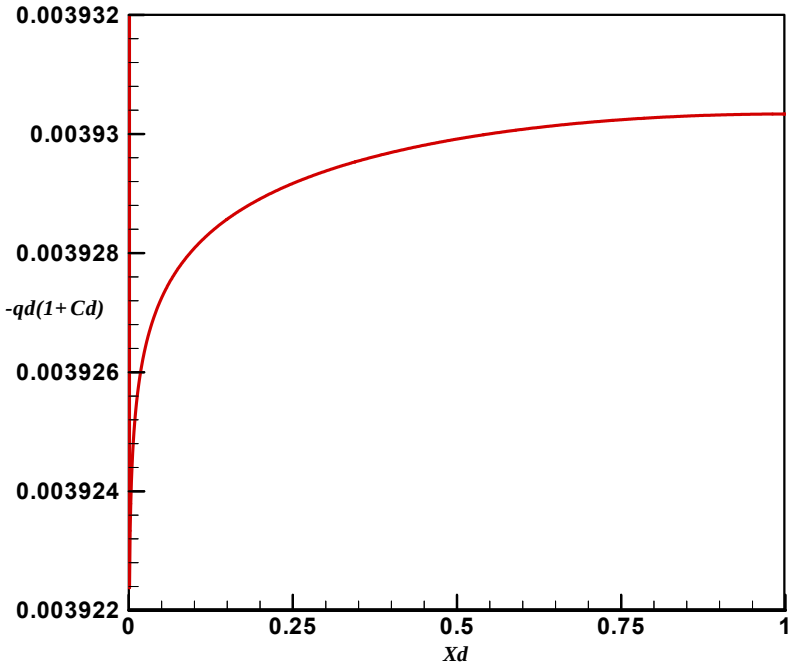

Output DTN: LB0307FMRADTRN.001.

Figure 6-14. Plot of Negative of Local Dimensionless Flux at the Solution Points for the Discrete Transform Coefficients—Nominal Case 1

The solution of Equation 6-35 may be evaluated through a comparison of the left-hand side and right-hand side at intermediate points to the solution points used for computing the discrete transform coefficients. The intermediate points lie along the drift wall boundary between the solution points , x_{di}, given in Equations 6-36 and 6-38. Figure 6-15 provides this comparison at different scales, to give a perspective on the entire solution as well as the fit near the fracture where rapid changes in the function occur. The series approximation to the curve is seen to have greater error and oscillations about the target function near the fracture, with a rapid reduction in differences moving away from the fracture.

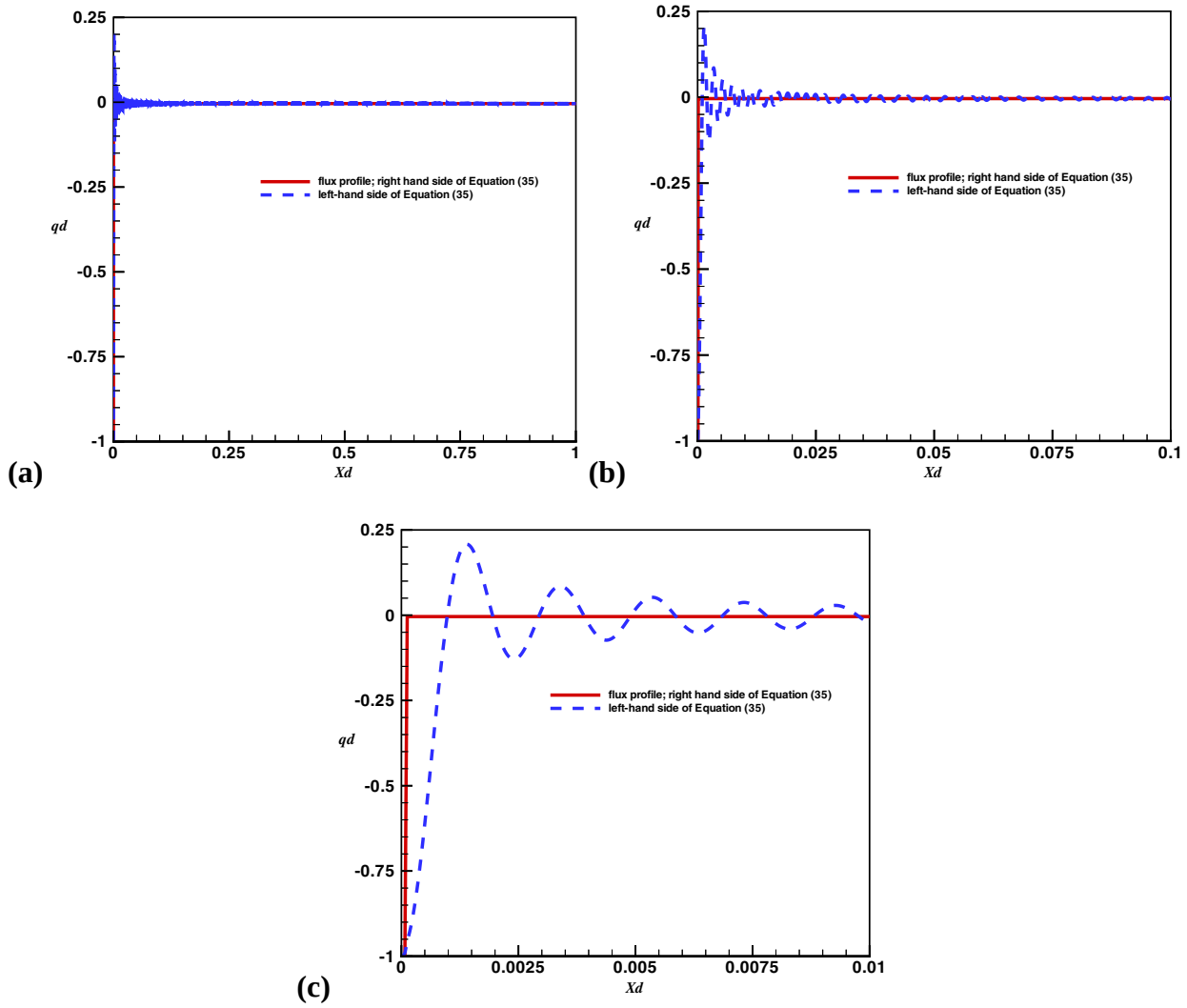

Output DTN: LB0307FMRADTRN.001.

Figure 6-15. Comparison Plot at Intermediate Points to Solution for Discrete Transform Coefficients, q_d, right-hand side of Equation 6-(35) (Solid Red Line) left-hand side of Equation 6-(35) (Dotted Blue Line) for 1,024 Terms (a) Entire Domain, (b) Region Near Fracture, and (c) Fracture Close-Up – Nominal Case 1

The solution accuracy may also be evaluated through comparisons of the invert and rock radionuclide flux terms at the drift wall. For the solution points (x_d) in the equation for the discrete transform coefficients, the flux in the invert and in the rock at the drift wall are identical. However, deviations between these flux terms at intermediate locations provide an indication of solution accuracy. In Figure 6-16, the comparison of these two fluxes is made at intermediate values of x_d. This comparison points out that the calculations for diffusive flux in the invert are subject to oscillations of greater magnitude than the calculation for advective flux in the rock. This suggests that the advective flux ratio will provide a more accurate estimate than the diffusive flux ratio, even though both rely on the discrete Fourier transform solution. This occurs because the first-order terms for the advective radionuclide flux in Equations 6-43 and 6-44 are a fairly good approximation to the full solutions.

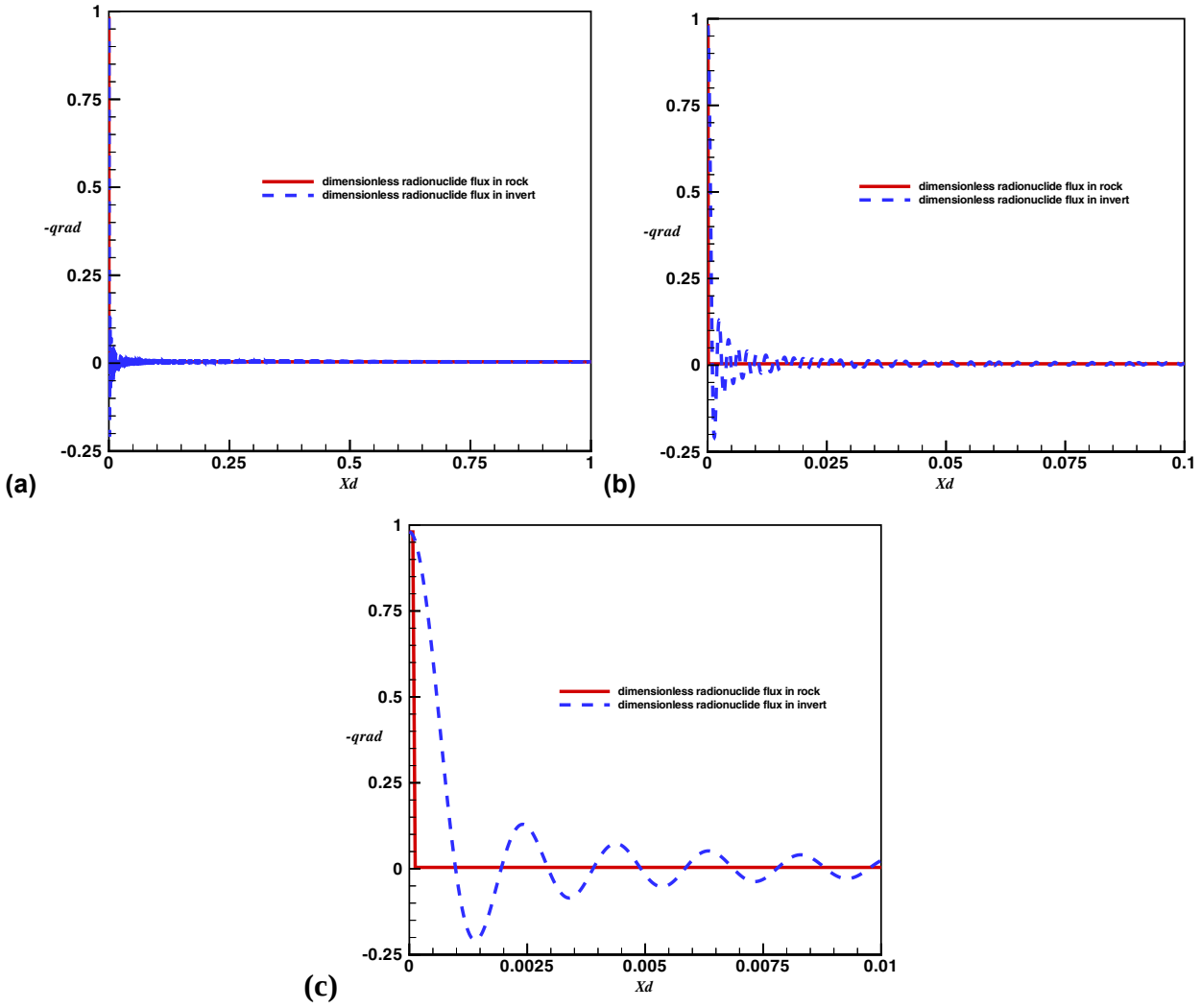

Output DTN: LB0307FMRADTRN.001.

Figure 6-16. Comparison Plot of Flux in the Invert (Dotted Blue Line) and Rock (Solid Red Line) at the Drift Wall for 1,024 Terms: (a) Entire Domain, (b) Region Near Fracture, and (c) Fracture Close-Up – Nominal Case 1

The behavior of the solution with successively larger numbers of coefficients is shown in Figures 6-17 and 6-18. The solutions are seen to generally improve with larger numbers of coefficients. Table 6-10 gives the change in the dimensionless radionuclide flux ratio over a range of 1,024 to 4,096 Fourier coefficients. The value of the flux ratio as computed from the advective flux in the rock is found to change by less than 2 percent as compared to 4 percent for the diffusive flux ratio. The variability of the results (to be shown below) is on the order of a factor of 10, so the accuracy of the solution with 1,024 points is sufficient. Because of the greater stability of the flux ratio as computed from the advective flux in the rock, this ratio will be used to determine the flux ratios.

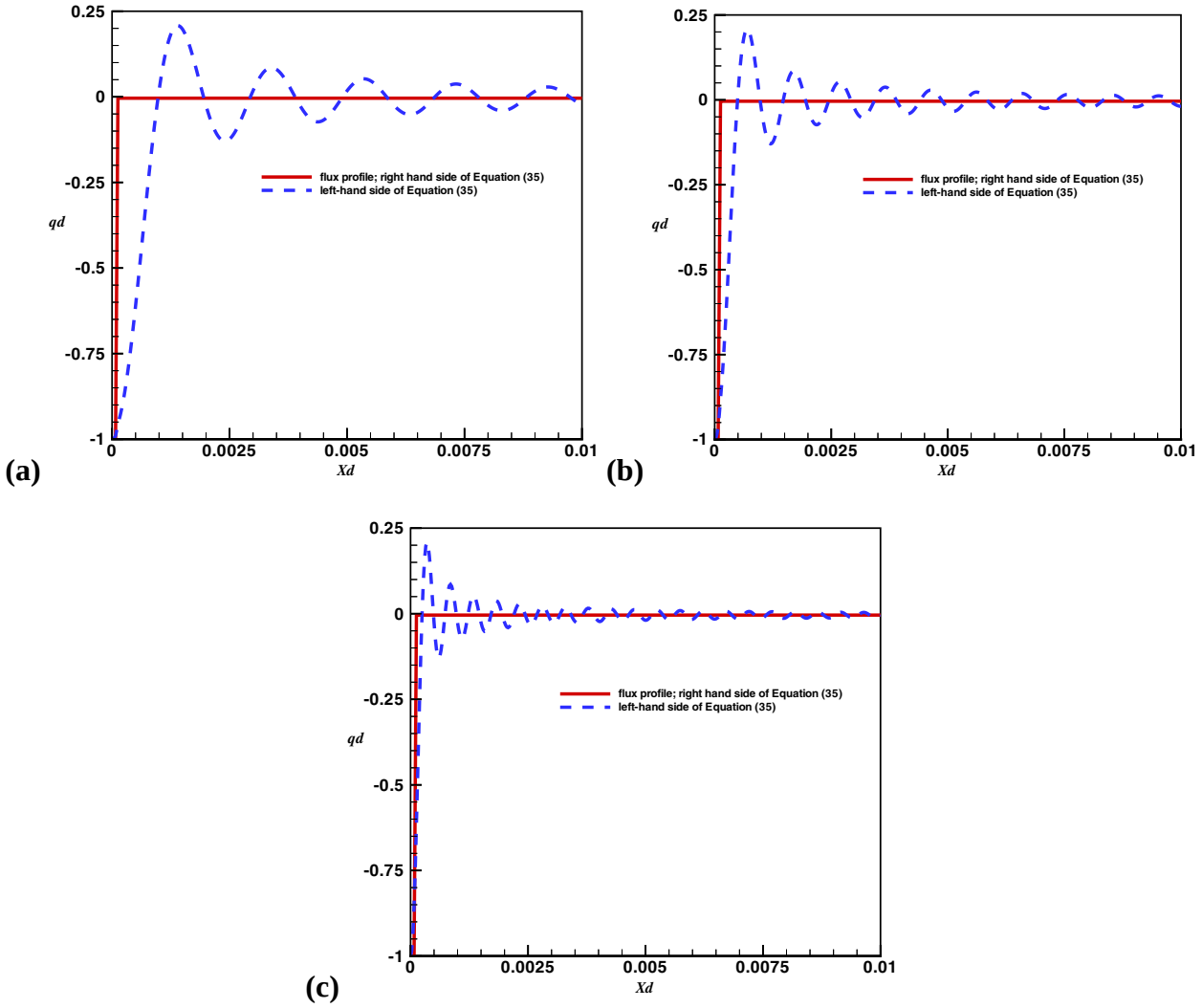

Output DTN: LB0307FMRADTRN.001.

Figure 6-17. Comparison Plot at Intermediate Points to Solution for Discrete Transform Coefficients, showing q_d, right-hand side of Equation 6-(35) (Solid Red Line) left-hand side of Equation 6-(35) (Dotted Blue Line): (a) 1,024 Points, (b) 2,048 Points, and (c) 4,096 Points – Nominal Case 1

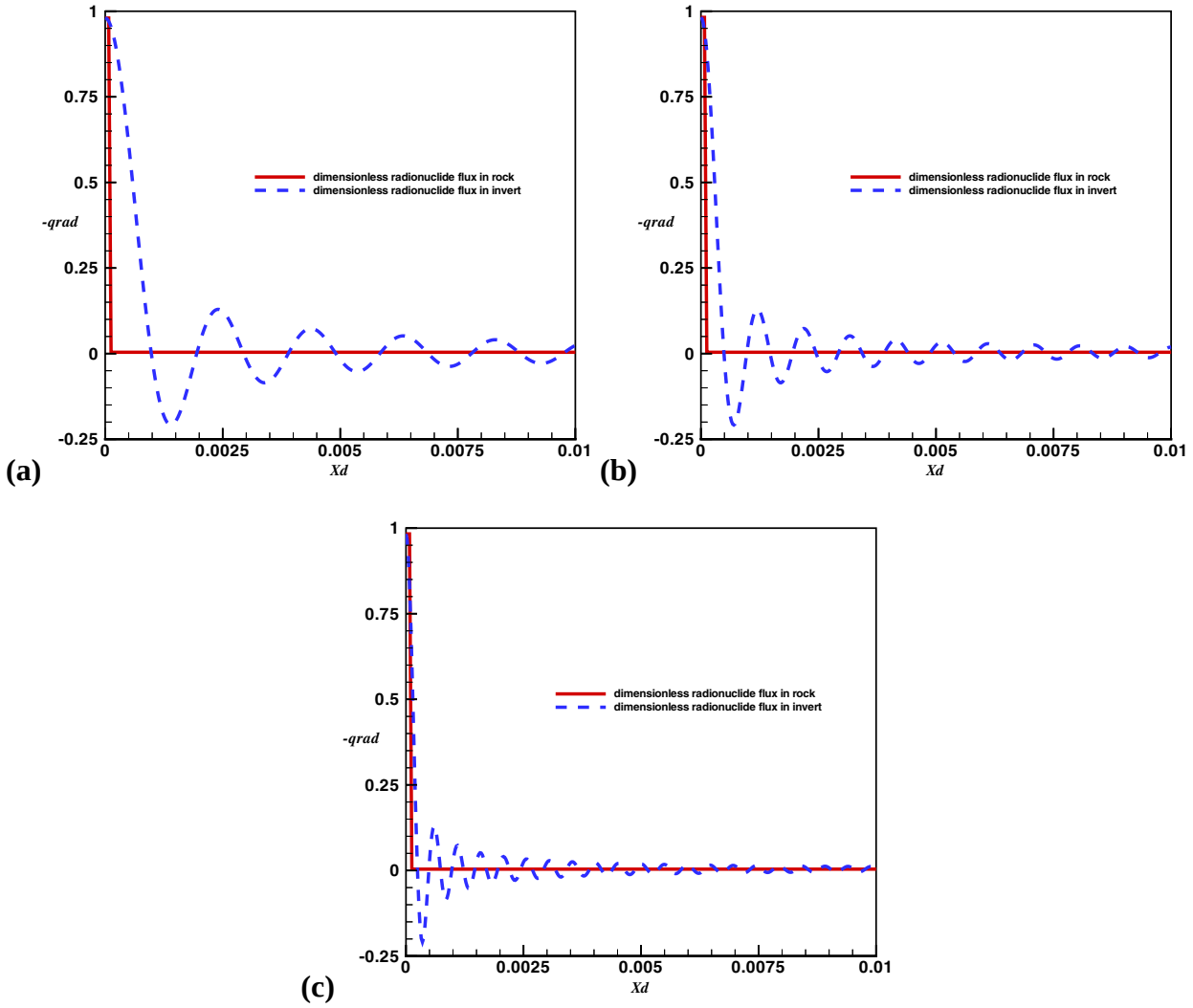

Output DTN: LB0307FMRADTRN.001.

Figure 6-18. Comparison Plot of Flux in the Invert (Solid Red Line) and Rock (Dotted Blue Line) at the Drift Wall: (a) 1,024 Points, (b) 2,048 Points, and (c) 4,096 Points – Nominal Case 1

Similar behavior is found for nominal case 2 with fracture water content of 0.0005 and all other parameters unchanged. Figures 6-19 and 6-20 show similar convergence characteristics for Nominal Case 2 as compared with Nominal Case 1. Again, the advective flux ratio is seen to be more stable in Table 6-11 over the selected number of coefficients.

Table 6-10. Advective and Diffusive Flux Ratios for Nominal Case 1

Nominal Case 1 Results		
Number of Fourier Coefficients	**Advective Flux Ratio in Rock**	**Diffusive Flux Ratio in Invert**
1024	0.02434	0.02211
2048	0.02436	0.02301
4096	0.02438	0.02213

Output DTN: LB0307FMRADTRN.001.

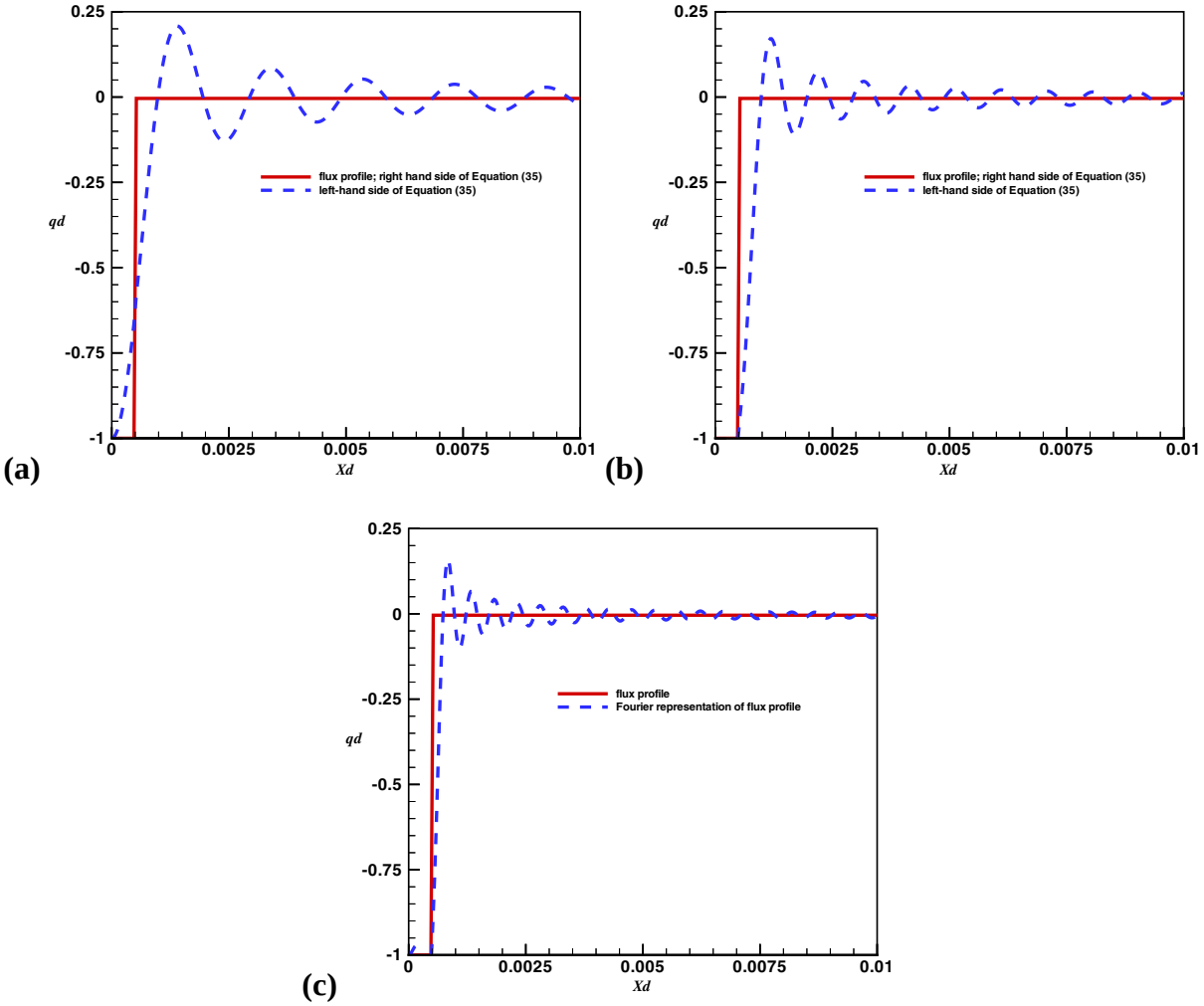

Output DTN: LB0307FMRADTRN.001.

Figure 6-19. Comparison Plot at Intermediate Points to Solution for Discrete Transform Coefficients, showing q_d, right-hand side of Equation 6-(35) (Solid Red Line) left-hand side of Equation 6-(35) (Dotted Blue Line): (a) 1,024 Points, (b) 2,048 Points, and (c) 4,096 Points – Nominal Case 2

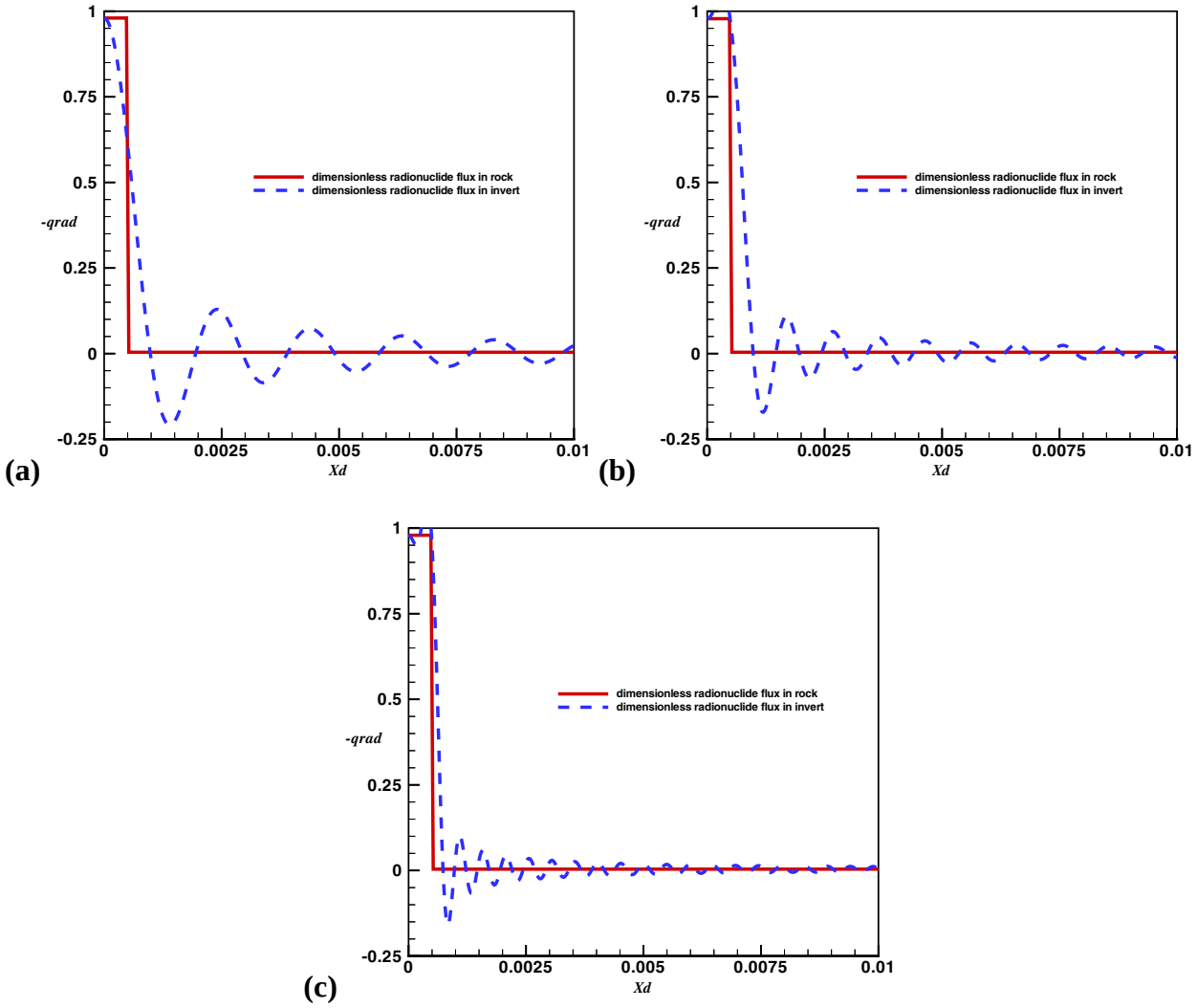

Output DTN: LB0307FMRADTRN.001.

Figure 6-20. Comparison Plot of Flux in the Invert (Solid Red Line) and Rock (Dotted Blue Line) at the Drift Wall: (a) 1,024 Points, (b) 2,048 Points, and (c) 4,096 Points – Nominal Case 2

Table 6-11. Advective and Diffusive Flux Ratios for Nominal Case 2

Nominal Case 2 Results		
Number of Fourier Coefficients	Advective Flux Ratio in Rock	Diffusive Flux Ratio in Invert
1024	0.1109	0.0965
2048	0.1108	0.1096
4096	0.1109	0.1108

Output DTN: LB0307FMRADTRN.001.

6.4.5 Model Parameterization and Sampling

Domain Investigated

The model parameters are selected to represent the range of conditions expected across the waste emplacement locations. These locations encompass for model units within the Topopah Spring Tuff; tsw33 (Topopah Spring Tuff Upper Lithophysal), tsw34 (Topopah Spring Tuff Middle Nonlithophysal), tsw35 (Topopah Spring Tuff Lower Lithophysal), and the tsw36 (Topopah Spring Tuff Lower Nonlithophysal). The numerical grid for the mountain-scale site-scale model represents the waste emplacement locations through 433 gridblocks (excluding fault cells) that span the four model units (BSC 2004 [DIRS 169861], Figure 6.1-1). The percentage of waste emplacement within each of the model units is given in Appendix H, with more than 80 percent within the tsw35.

Fracture Frequency

The dimensionless invert depth is computed from the invert depth divided by the half of the fracture spacing, $h_f d$. Fracture half-spacing may be computed from

$$h_f = \frac{1}{2} f^{-1} \qquad \text{(Eq. 6-45)}$$

where f is the fracture frequency. The fracture frequency mean and standard deviation for the repository host rock units (BSC 2004 [DIRS 170038]; DTN: LB0205REVUZPRP.001 [DIRS 159525]) are used to derive a sampled set of fracture spacings (see Section 4.1). A correlation of the data from all the model units having both the mean and the standard deviation in fracture frequency is shown in Figure 6-21. This figure shows a strong correlation between the average fracture frequency and the standard deviation in fracture frequency. The standard deviation in fracture frequency for the tsw35 and tsw36 are computed from the correlation in Figure 6-21. Fracture frequency is modeled as a lognormal distribution to account for the semi-infinite range of the fracture frequency. Details of the sampling method are given in Appendix A.

Water Flux and Saturation

Fracture and matrix flux and water saturation values are taken from the output of the UZ Flow Model for the repository host rock (see Section 4.1). The flow model provides 433 fracture and matrix flux pairs in the repository host rock, as discussed in Appendix B. The flow model output also provides the matrix relative permeability, which is used below for computing matrix diffusion.

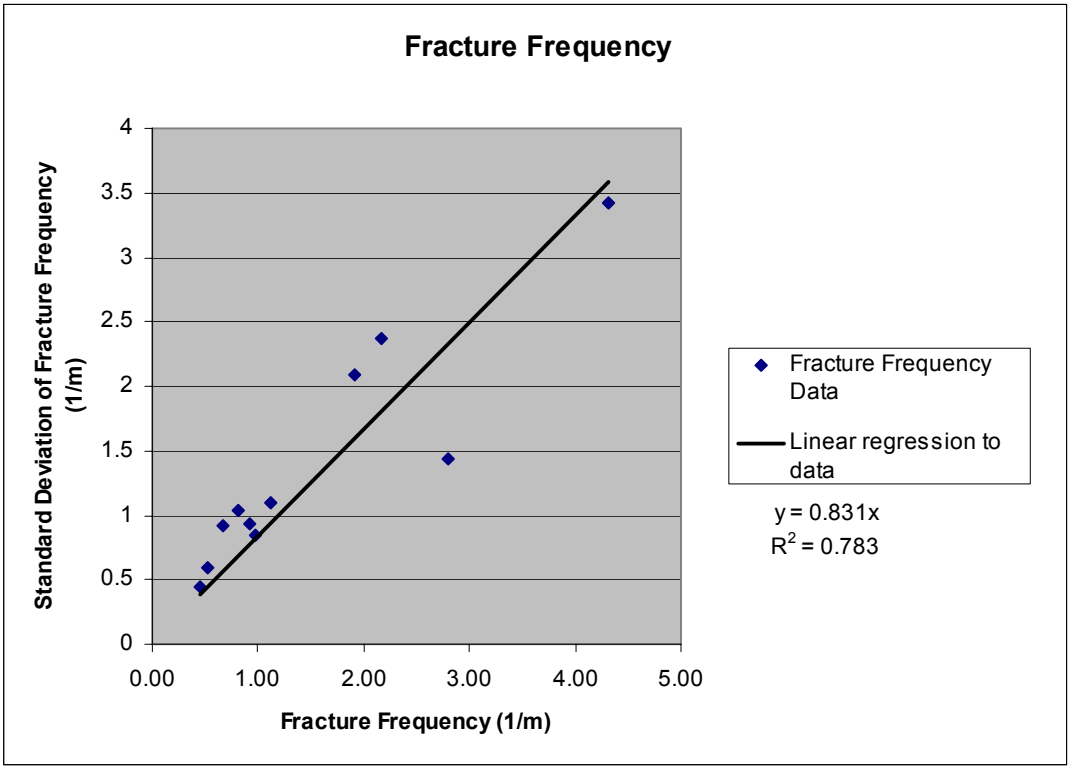

Output-DTN: LB0307FMRADTRN.001.

NOTE: Linear regression forced through origin.

Figure 6-21. Fracture Frequency Correlation

Flow Focusing

In addition to the average flow rates predicted by the mountain-scale model, flow focusing at the drift scale is including through a flow-focusing factor. This factor (see Section 4.1) is sampled and used in combination with the sampled fracture water flux from the mountain-scale model (BSC 2004 [DIRS 167652], Figure 6-26; DTN: LB0406U0075FCS.002 [DIRS 170712]).

$$P = -0.3137F^4 + 5.4998F^3 - 35.66F^2 + 102.3F - 11.434 \qquad \text{(Eq. 6-46)}$$

where F is the flow focusing factor and P is the cumulative probability for the value of F. Details of the sampling method are given in Appendix C. Fracture saturations are adjusted for flow focusing through the van Genuchten relationship (van Genuchten, 1980 [DIRS 100610], Equation 8) and the approximation of unit gradient flow in the fractures:

$$q_f = \frac{k_f g}{\nu} S_{fn}^{\frac{1}{2}} \left[1 - \left(1 - S_{fn}^{\frac{1}{m}} \right)^m \right]^2 \qquad \text{(Eq. 6-47)}$$

where g is the acceleration of gravity, ν is the kinematic viscosity of water, S_{fn} is the normalized fracture saturation $\frac{S_f - S_{fr}}{1 - S_{fr}}$, S_f is the physical fracture saturation, S_{fr} is the residual fracture saturation (S_{fr} is a significant fraction of the typical ambient S_f), m is the van Genuchten pore size distribution factor, and q_f is the fracture water flux. Adjusting q_f by the flow focusing factor, F, gives

$$Fq_f = \frac{k_f g}{\nu} S_{fna}^{\frac{1}{2}} \left[1 - \left(1 - S_{fna}^{\frac{1}{m}} \right)^m \right]^2 \qquad \text{(Eq. 6-48)}$$

where S_{fna} is the adjusted normalized fracture saturation. Taking the ratio of Equations 48 to 47 gives

$$F = \frac{S_{fna}^{\frac{1}{2}} \left[1 - \left(1 - S_{fna}^{\frac{1}{m}} \right)^m \right]^2}{S_{fn}^{\frac{1}{2}} \left[1 - \left(1 - S_{fn}^{\frac{1}{m}} \right)^m \right]^2} \qquad \text{(Eq. 6-49)}$$

Using the fact that fracture saturations are low, the numerator may be expanded for small S_{fna} (such that $S_{fma}^{\frac{1}{m}}$ is small) and solved for S_{fna}, as detailed in Appendix G:

$$S_{fna} = \left[\left(\frac{F}{m^2} \right) S_{fn}^{\frac{1}{2}} \left\{ 1 - \left(1 - S_{fn}^{\frac{1}{m}} \right)^m \right\}^2 \right]^{\frac{2m}{4+m}} \qquad \text{(Eq. 6-50)}$$

Fracture and Matrix Porosity

Fracture porosity is needed to define the fracture water velocity and to define the fracture water content in contact with the drift invert. A standard deviation in fracture porosity is available only for the tsw34 model unit. The standard deviation for the other host rock units are computed from the ratio of the standard deviation to the mean in the tsw34, multiplied by the average porosity for each host rock unit. The fracture porosity is described by a beta distribution to reflect the physical limits of 0 and 1 for this parameter. Details of the sampling method are given in Appendix D. A similar sampling is performed for matrix porosity as described in Appendix D.

Fracture Residual Saturation

The fracture saturation at the drift wall is given the same value as that in the flowing fracture beneath the drift. Although physical saturations are reported from the flow model, flow calibrations are based on permeability and capillary pressure relationships that are a function of normalized saturation. Therefore, the uncertainty in the normalized fracture saturation is accounted for via the lower, mean, and upper infiltration cases, but this does not account for uncertainty in the residual saturation. The value for residual water saturation in fractures is available in the calibrated hydrological property sets (DTN: LB03023DSSCP9I.001 [DIRS 163044]), which for all infiltration cases is 0.01. Currently, there are no data from Yucca Mountain that could be used to assess the uncertainty in residual fracture saturation. In general, experiments may be expected to overestimate residual wetting-phase saturations because it is difficult to assess the end of a drainage process. The wetting phase tends to maintain continuity during the drainage process ["Hydraulic Continuity of Residual Wetting Phase in Porous Media" (Dullien et al. 1986 [DIRS 163221], p. 201)], which leads to drainage experiments that only asymptotically approach residual saturation at an ever-decreasing rate. Therefore, the time scales for laboratory experiments become a factor in the determination of the residual saturation. Dullien et al. (1986 [DIRS 163221], p. 203) investigated residual wetting-phase saturation in sandstones and found that with increasing capillary pressure, the wetting-phase saturation continued to drop, and no "irreducible" saturation could be determined. The uncertainty in residual saturation in fractures is modeled using a log-uniform distribution with a range of 0.001 to 0.1. This distribution has a median of 0.01 and spans the range of residual saturation values measured for higher permeability capillary media ["Residual Equilibrium Saturation of Porous Media" (Dombrowski and Brownell 1954 [DIRS 163222], Figure 7, p. 1,213)]. Sampling for fracture water saturation, including the uncertainty in residual saturation is described in Appendix G. The magnitude of the residual water saturation is found to be a significant fraction of the typical total fracture water saturation.

Diffusion Coefficient for the Invert

The invert diffusion coefficient was developed based on an empirical correlation with the water content (BSC 2001 [DIRS 156700], pp. 23–25, Equation (37)):

$$\log\left(\frac{D_{eI}}{D_0}\right) = 1.849 \log \theta_I \qquad \text{(Eq. 6-51)}$$

where D_0 is the diffusion coefficient in water factor and θ_I is the invert water content. The coefficient in this correlation, 1.849 was more recently updated to a value of 1.863 (BSC 2003 Section 6.2 [DIRS 170881]). For a typical invert water content of 0.046, the change in exponent results in a difference in D_{eI} of about 4 percent. However, the total uncertainty range for D_{eI} spans a factor of 43 due to uncertainties in invert water content and the free-water diffusion coefficient (see Appendix E). Therefore, the effect of the difference in the exponent is negligible. The invert water content is found to be essentially equal to the intergranular solid content (1 minus the intergranular porosity) times the matrix porosity of the invert material grains, or $\left(1-\phi_{Ig}\right)\phi_m$ (BSC 2003 [DIRS 170881], Section 6.4). The tuff matrix material for the invert will be taken from the tsw36 repository host rock horizon (BSC 2003 [DIRS 170881],

Sections 5.8 and 6.4). Therefore, the matrix porosity in the invert is sampled based on the variability in matrix porosity in the Tptpln lithostratigraphic unit, which is equivalent to the TM2 and TM1 hydrogeologic units (*Analysis of Hydrologic Properties Data*, BSC 2004 [DIRS 170038], Table 6-1). A suitable range of values for the intergranular porosity is estimated to be 0.4 to 0.48 (Hilf 1975 [DIRS 169699], p. 257; BSC 2003 [DIRS 170881], Section 4.1.4). The range of porosities is derived from values of the maximum void ratios for poorly graded sand (SP) as given in Hilf (1975 [DIRS 169699], p. 257). The maximum void ratio for poorly graded sand is used to represent the possible range void ratios for uncompacted tuff grains. Porosity is computed from the void ratio e as $e/(1+e)$. Intergranular porosity is sampled as a uniform random distribution over the range identified in Section 4.1.1. The uncertainty in D_0 is based on the range of values for strong electrolyte diffusion coefficients in aqueous solution (Weast and Astle 1979 [DIRS 102865]) given in Section 4.1.1. This is a sufficiently wide range of free-water diffusion coefficients for radionuclides, based on reported values of 2.2×10^{-9} m^2/s for tritiated water ["Diffusion of Helium in Water-Saturated, Compacted Sodium Montmorillonite (Sato et al. 2001 [DIRS 164047])], 1.9×10^{-9} m^2/s for pertechnetate (TcO_4^-) ["Ionic Diffusion Coefficients of Cs+, Pb^2+, Sm^3+, Ni^2+, SeO_4^{2-} and TcO_4^- in Free Water Determined from Conductivity Measurements (Sato et al. 1996 [DIRS 163213])], and 1.1×10^{-9} m^2/s for bicarbonate [*Electrochemical Systems* (Newman 1973 [DIRS 148719])]. These are sampled as a lognormal distribution to account for the semi-infinite range of this parameter. Details concerning the sampling methods used for the diffusive mass transfer coefficient are given in Appendix E.

Diffusion Coefficients in Fractured Rock

Diffusion coefficients in fracture water have not been directly determined. Generally speaking, diffusion in unsaturated geologic materials has been found to be sensitive to water content (Conca and Wright 1990 [DIRS 101582], p. 1,055; Bear 1972 [DIRS 156269], Sections 4.8.2 and 4.8.3). Experimental evidence concerning diffusion in unsaturated granular materials is presented in Conca and Wright (1990 [DIRS 101582]). These experiments were performed on nonporous granular materials in which diffusion occurred through water films along the granular surfaces. The water content of these materials ranged from 0.5 to 5 percent and diffusion coefficients ranged from about 10^{-13} m^2/s to 10^{-11} m^2/s (Conca and Wright 1990 [DIRS 101582], Figures 10–13). The analogous water content of a fracture continuum is the fracture water saturation, which is also roughly in this range (see Appendix G). The range for matrix diffusion coefficients is about an order of magnitude larger (see Figure 6-23). This information suggests that the use of diffusion coefficients in the rock matrix as surrogates for diffusion coefficients in the fractures is conservative. Fractures in the welded tuff repository host rock are different than the nonporous granular materials investigated by Conca and Wright (1990 [DIRS 101582]) due to differences in geometry and the connection to a porous rock matrix. As discussed in Section 4.1.5, limiting values for diffusion coefficients in the fractures are taken to be the effective diffusion coefficients in the neighboring rock matrix. Distributions for matrix diffusion coefficients for cations and anions are given in Appendix I. Additional corroborative information on diffusion coefficients in rock matrix is given in Reimus et al. (2002 [DIRS 163008]), where a correlation for diffusion in the rock matrix was developed based on laboratory and field data. The correlation establishes a quantitative relationship between the porosity and permeability of a saturated rock matrix to the effective diffusion coefficient. This correlation may be extended for unsaturated conditions by using the water content as an

equivalent parameter for porosity under saturated conditions and the unsaturated effective permeability for the saturated permeability. This extension to unsaturated conditions is appropriate because for unsaturated flow, the character of the gas phase is not significant other than the space that it occupies. The gas phase could be replaced by solid (rock mineral) which would result in exact equivalence between the unsaturated water content and porosity and effective unsaturated permeability and permeability. The correlation is then (BSC 2004 [DIRS 170042], Equation 6-19; Reimus et al. 2002 [DIRS 163008], Equation 2.5)

$$\log(D_m) = -3.49 + 1.38\theta_m + 0.165\log(k_w) \quad \text{(Eq. 6-52)}$$

where D_m is the effective diffusion coefficient in cm^2/s, θ_m is the matrix water content, and k_w is the effective permeability to water in m^2. Data confirm that this correlation provides a reasonable estimate for matrix diffusion in Yucca Mountain volcanic rocks (DTN: SN0306T0502103.006 [DIRS 163944]; BSC 2004 [DIRS 170042], Section 6.5.2.6) The data from Reimus et al. (2002 [DIRS 163008]) suggests that the range of diffusion coefficients for tritium, bicarbonate, and pertechnetate individually are roughly similar to the range of mean values for each. This suggests that a single broad distribution scaled by the range of values between cations and anions from DTN: LA0003JC831362.001 [DIRS 149557] would provide a better representation of the uncertainty in matrix diffusion. To capture this in a single distribution, consider the following transformation:

$$X = \log\left(\frac{D_0}{D_m}\right) \quad \text{(Eq. 6-53)}$$

where D_0 is the limiting upper value for D_m. This value is given in DTN: LA0003JC831362.001 [DIRS 149557] as 10^{-9} m^2/s. The average for X is

$$\mu_X = \log(D_0) - \overline{\log(D_m)} \quad \text{(Eq. 6-54)}$$

If we stipulate that the variable X ranges from 0 to infinity, then D_m is constrained to be less than 10^{-9} m^2/s.

Given the semi-infinite range for X, it can be sampled as a lognormal distribution. This introduces the second logarithmic transformation, Y,

$$Y = \ln(X) \quad \text{(Eq. 6-55)}$$

The mean for Y is taken to be

$$\mu_Y = \ln(\mu_X) \quad \text{(Eq. 6-56)}$$

such that the mean is unchanged by the transformation to a lognormal distribution. The distribution of diffusion coefficients based on Equations 53 and 55 and a normal distribution for Y is called the "primary distribution". Distribution parameters for Y may be obtained by setting $\overline{\log(D_m)}$ to be the log of the geometric mean of the mean values in DTN: LA0003JC831362.001

[DIRS 149557] and then adjusting the standard deviation for *Y* such that it covers the range of values represented by cations and anions in DTN: LA0003JC831362.001 [DIRS 149557]. The standard deviation of 0.3 for *Y* results in a spread for the distribution that is representative of the spread of values in DTN: LA0003JC831362.001 [DIRS 149557], as shown in Figure 6-22.

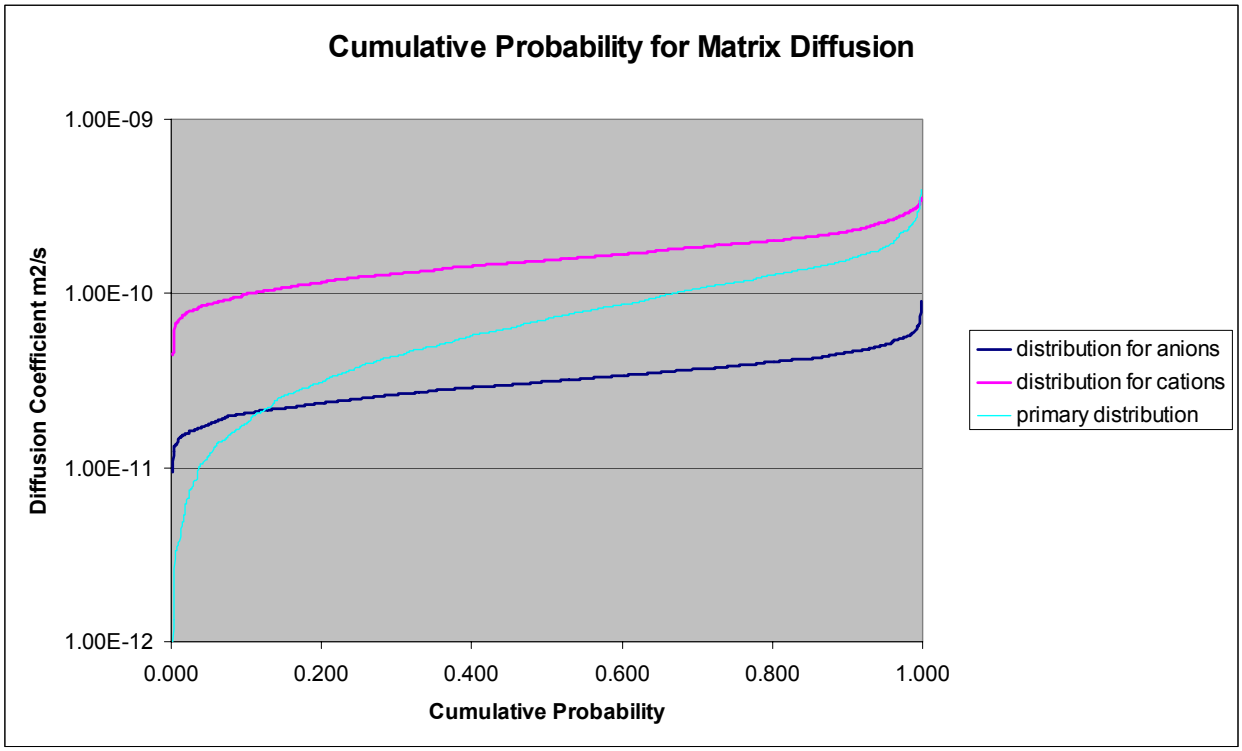

DTN: LA0003JC831362.001 [DIRS 149557].

Output DTN: LB0307FMRADTRN.001.

Figure 6-22. Cumulative Probability for Matrix Diffusion

See Appendix I for a discussion of the methods used to generate the distributions for cations, anions, and the Reimus correlation. The range of values for the UZ may be examined using 5th and 95th percentile values for water content and effective matrix permeability. Doing this, the a "low" distribution may be computed based on Equation 6-52 by assigning the mean using the 5th percentile water content and effective matrix permeability and a "high" distribution may be based on the 95th percentile of values of these quantities. The results are shown in Figure 6-23.

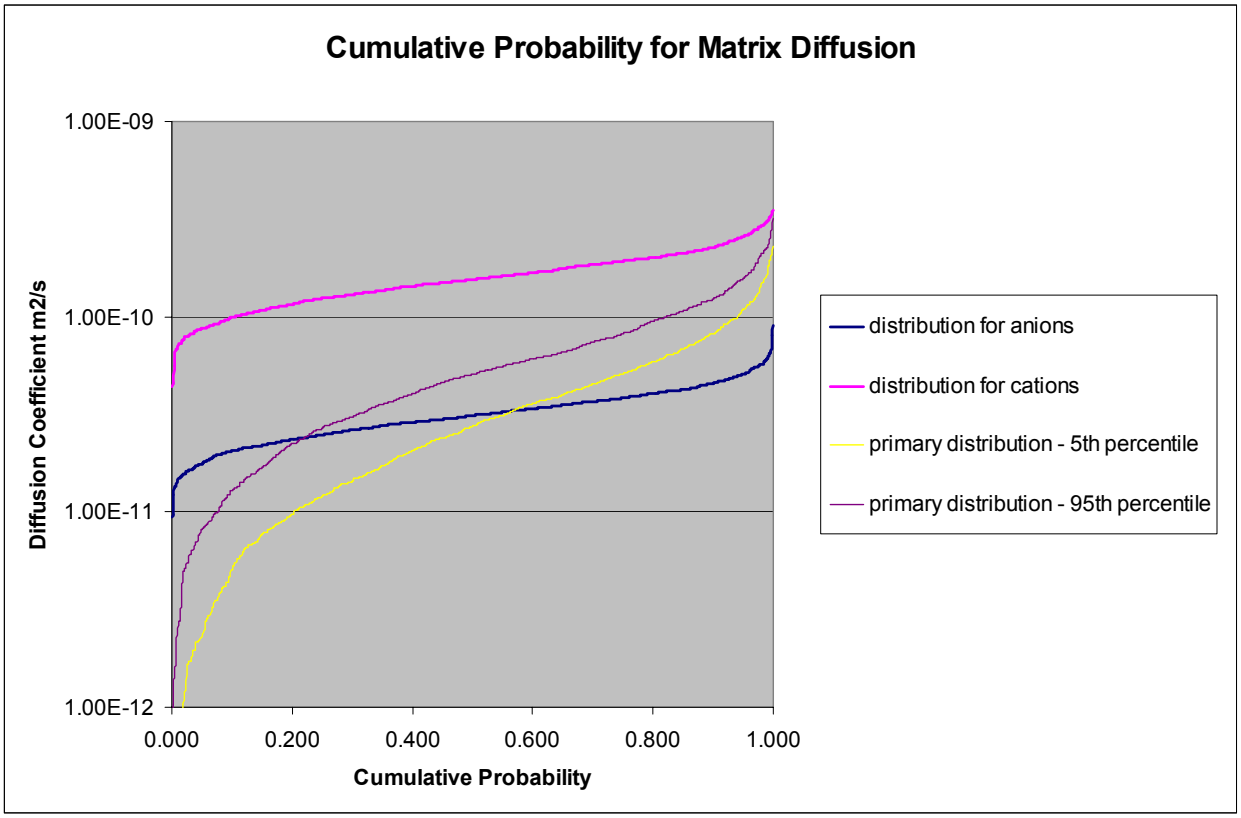

DTN: LA0003JC831362.001 [DIRS 149557].

Output DTN: LB0307FMRADTRN.001.

Figure 6-23. Comparison of Cation/Anion Distributions with Primary Distributions at 5th and 95th Percentile for Effective Permeability, Mean Glacial Transition Climate

See Appendix I for a discussion of the methods used to generate the low and high distributions for the Reimus correlation. The data used to develop the distributions in DTN: LA0003JC831362.001 [DIRS 149557] were from diffusion measurements under saturated conditions. As a consequence, the generally lower values represented by the Reimus distributions are expected. The comparison with measured diffusion coefficients for tritium, technetium, and bicarbonate (Table 6-12) is given in Figure 6-24. Again, the correlations for the UZ are lower than the measured values, which were all performed under saturated conditions.

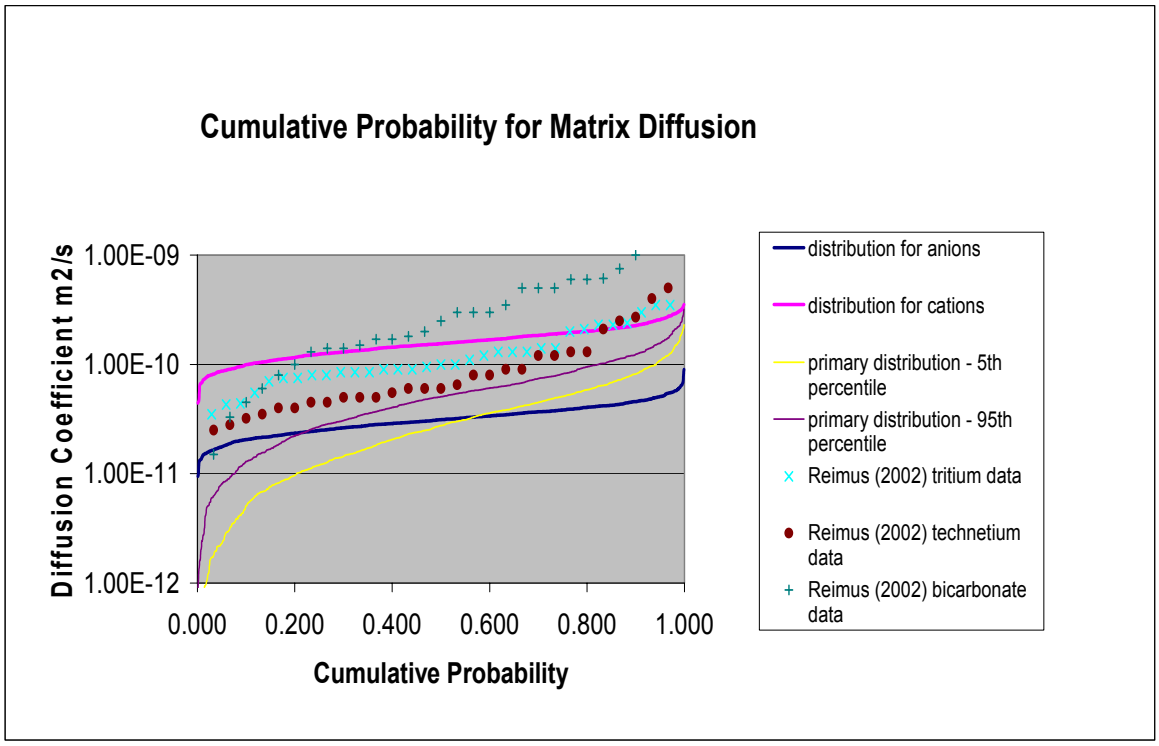

Source: Reimus et al. 2002 [DIRS 163008], Table 2-4.

DTN: LA0003JC831362.001 [DIRS 149557].

Output DTN: LB0307FMRADTRN.001.

Figure 6-24. Comparison of the Distributions with Diffusion Data

Table 6-12. Diffusion Data from Reimus et al. (2002 [DIRS 163008], Table 2-4)

Sample Description	^{3}H Diffusion coefficient, cm^2/s	^{99}Tc Diffusion coefficient, cm^2/s	^{14}C Diffusion coefficient, cm^2/s
UE20c 2856D	1.1E-06	8.0E-07	6.0E-07
UE20c 2856E	8.5E-07	6.0E-07	4.5E-07
UE20c 2856F	9.0E-07	5.0E-07	3.3E-07
UE20c 2856F	2.3E-06	2.5E-06	1.7E-06
UE20c 2856F	1.3E-06	1.2E-06	8.0E-07
UE20c 2858A	1.2E-06	9.0E-07	3.0E-06
UE20c 2858A	1.0E-06	4.0E-07	1.7E-06
UE20c 2809A	7.5E-07	n.a.	n.a.
UE20c 2809B*	1.4E-06	n.a.	n.a.
UE20c 2751A	1.4E-06	6.0E-07	5.0E-06

Table 6-12. Diffusion Data from Reimus et al. (2002 [DIRS 163008], Table 2-4) (Continued)

Sample Description	^{3}H Diffusion coefficient, cm^2/s	^{99}Tc Diffusion coefficient, cm^2/s	^{14}C Diffusion coefficient, cm^2/s
UE20c 2751B*	1.3E-06	5.0E-07	5.0E-06
UE20c 2908A	3.0E-06	2.7E-06	1.3E-06
UE20c 2908D*	2.4E-06	2.1E-06	2.5E-06
UE20f 2842	5.5E-07	5.0E-07	1.5E-07
UE18t 1003A	1.3E-06	n.a.	n.a.
UE18t 1003B*	7.0E-07	n.a.	n.a.
UE18t 1387.5A	8.5E-07	4.5E-07	3.0E-06
UE18t 1387.5A	8.5E-07	6.5E-07	1.8E-06
UE18t 1387.5B	8.0E-07	6.0E-07	6.1E-06
UE18t 1387.5B	9.5E-07	9.0E-07	3.0E-06
UE18t 1390	9.0E-07	5.5E-07	7.5E-06
UE18t 1390	7.5E-07	4.0E-07	1.1E-05
UE18r 2228A	4.4E-07	3.5E-07	6.0E-06
UE18r 2228A	4.3E-07	3.2E-07	6.0E-06
UE18r 2228B	3.5E-07	1.3E-06	2.0E-05
PM1 4823A	3.5E-06	1.2E-06	1.5E-06
PM1 4823B*	3.5E-06	1.3E-06	5.0E-06
PM2 4177A	2.1E-06	8.0E-07	1.4E-06
PM2 4177A	8.0E-07	2.5E-07	1.4E-06
PM2 4177B	2.3E-06	5.0E-06	3.5E-06
PM2 4177B	9.0E-07	4.5E-07	1.0E-06
PM2 4177C*	2.0E-06	4.0E-06	1.0E-05
PM2 4177C*	1.0E-06	2.8E-07	2.0E-06

NOTE: *Denotes diffusion cell with a mineralized fracture surface.
n.a. = data not available.

See Appendix I for a discussion of the methods used to compare these distributions with the measurements.

Water content is derived from the sampled water saturation (Appendix B) times the sampled matrix porosity (Appendix D) for the model unit. The effective permeability is computed from the relative permeability and matrix permeability

$$k_w = k_m k_{rw} \quad \text{(Eq. 6-57)}$$

where k_m is the saturated permeability of the matrix and k_{rw} is the relative permeability from the flow model output. The matrix permeability is not sampled because the flow and saturation information is consistent only with the mean values. Details concerning the sampling methods used for the matrix diffusion coefficient are given in Appendix F.

The parameters derived are combined to provide values of the dimensionless parameters identified in Section 6.4.2 across the flow model grid locations within the repository host rock. Computation of these parameters across the grid locations is described in Appendix G.

A summary of the parameters used for the fracture-matrix partitioning model, initially presented in Section 4 of this report, is given in Table 6-13.

Table 6-13. Inputs for the Fracture-Matrix Partitioning Model

Input Name	Input Description	Input Source	Value or Distribution	Type of Uncertainty
f	fracture frequency	LB0205REVUZPRP.001 [DIRS 159525]	log-normal	epistemic
S_{fr}	fracture residual saturation	LB0208UZDSCPLI.002 [DIRS 161788], LB0208UZDSCPMI.002 [DIRS 161243], LB0302UZDSCPUI.002 [DIRS 161787]	log-uniform	epistemic
S_f	fracture saturation	LB03023DSSCP9I.001 [DIRS 163044]	empirical	epistemic
F	flow focusing factor	DTN LB0406U0075FCS.002 [DIRS 170712]; BSC 2004 [DIRS 167652], Section 6.8	empirical	epistemic
m	fracture van Genuchten pore size distribution parameter	LB0208UZDSCPLI.002 [DIRS 161788], LB0208UZDSCPMI.002 [DIRS 161243], LB0302UZDSCPUI.002 [DIRS 161787]	single value	n.a.
q_{wf}	water flux in fracture	LB03023DSSCP9I.001 [DIRS 163044]	empirical	epistemic
ϕ_f	fracture porosity	LB0205REVUZPRP.001 [DIRS 159525]	beta	epistemic
ϕ_m	matrix porosity	LB0207REVUZPRP.002 [DIRS 159672]	beta	epistemic
S_m	matrix saturation	LB03023DSSCP9I.001 [DIRS 163044]	empirical	epistemic
k_m	matrix saturated permeability	LB03023DSSCP9I.001 [DIRS 163044]	empirical	epistemic
k_{rm}	matrix relative permeability	LB03023DSSCP9I.001 [DIRS 163044]	empirical	epistemic
D_m	diffusion in rock matrix	SN0306T0502103.006 [DIRS 163944]; BSC 2004 [DIRS 170042], Equation 6-19.	ln- log- normal	epistemic
q_m	water flux in matrix	LB03023DSSCP9I.001 [DIRS 163044]	empirical	epistemic
ϕ_{lg}	invert intergranular porosity	Hilf 1975 [DIRS 169699], p. 257; BSC 2003 [DIRS 170881], Sections 4.1.4 and 6.3	uniform	epistemic
D_0	free-water diffusion coefficient	Weast and Astle 1979 [DIRS 102865], p. F-62	log-normal	epistemic
D_{el}	Invert diffusion correlation	BSC 2001 [DIRS 156700], pp. 23–25	n.a.	n.a.
y_m	invert depth	BSC 2003 [DIRS 164101]	uniform	epistemic
n.a.	waste emplacement areas in each host rock unit	BSC 2004 [DIRS 168370]	single value	n.a.

NOTE: n.a. = not applicable.

6.4.6 Model Results

Calculations are performed for the lower, mean, and upper scenarios of the glacial transition climate. This climate is the largest fraction of the compliance period and is the portion of the compliance period when radionuclide transport is more probable. Furthermore, mean infiltration rates for the glacial transition scenarios range from 2.4 to 32 mm/year [*UZ Flow Models and Submodels* (BSC 2004 [DIRS 169861]), Table 6.1-2]. This range nearly encompasses the entire mean infiltration range infiltration scenarios from monsoon and present-day climates, which range from 1.3 to 19 mm/year (BSC 2004 [DIRS 169861], Table 6.1-2). Therefore, using results derived for the glacial transition climate for the lower, mean, and upper infiltration scenarios, respectively, under modern and monsoon climate, are not expected to result in an underestimate of radionuclide transport.

As discussed in Section 6.4.5, parameter uncertainty is included in the model development through sampling of the 433 different repository locations that have been assigned parameters. The sampling is performed to provide a representation of the frequency distribution of the fraction of the total radionuclide flux from a drift that enters the fractures. A set of 24 samples was randomly selected for each climate scenario. This total number of samples allows for taking one sample each from the tsw33 and tsw36 host rock horizons in a representative proportion to the tsw34 (3 samples) and the tsw35 (19 samples), based on the repository layout. Estimation theory indicates that for 95 percent confidence limits, 24 samples provide an estimate of the mean that is within

$$\pm \frac{1.96}{\sqrt{24-1}} S = \pm 0.41 S \qquad \text{(Eq. 6-58)}$$

[*Introduction to Mathematical Statistics* (Hogg and Craig 1978 [DIRS 163236], pp. 212–215)], where S is the sample standard deviation. The details of the sampling methods used for each infiltration case are given in Appendix H.

Computed results for each climate scenario are shown in Figures 6-25a-c using the dimensionless flux ratios as discussed in Section 6.4.4. Calculation details are given in Wang (2003 [DIRS 163234], SN-LBNL-SCI-236-V1, pp. 101–145), but the method used is the same as discussed in Section 6.4.4 and Appendix J. Results for the lower and mean infiltration scenarios are more similar and, in general, have a larger proportion released to the fractures than the higher infiltration case. This difference primarily results from the influence of the higher matrix water flux on the transport from the drift into the rock matrix under the higher infiltration scenario. The variation in fracture flux and water saturation among the different infiltration scenarios is found to have a second-order effect on fracture-matrix partitioning.

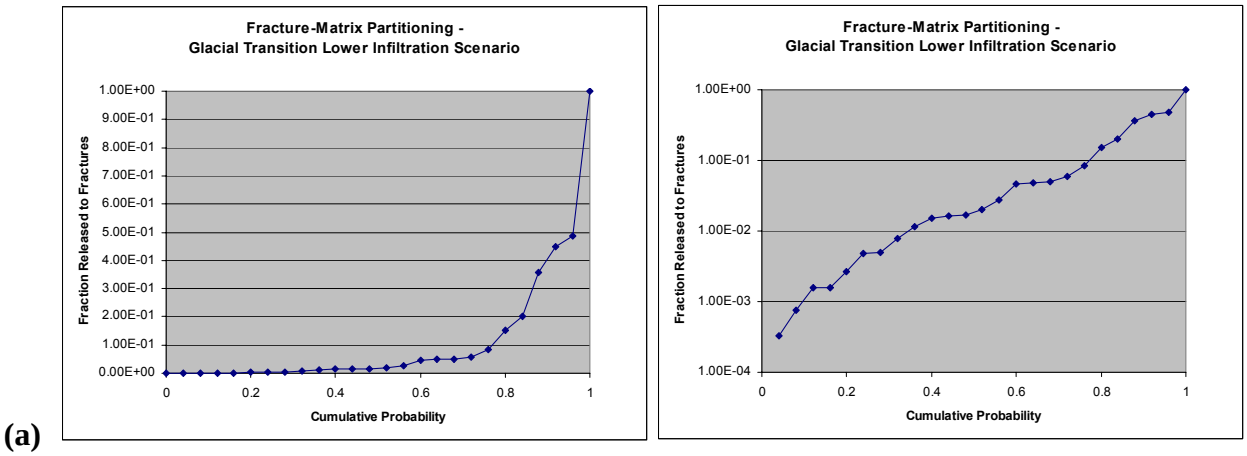

(a)

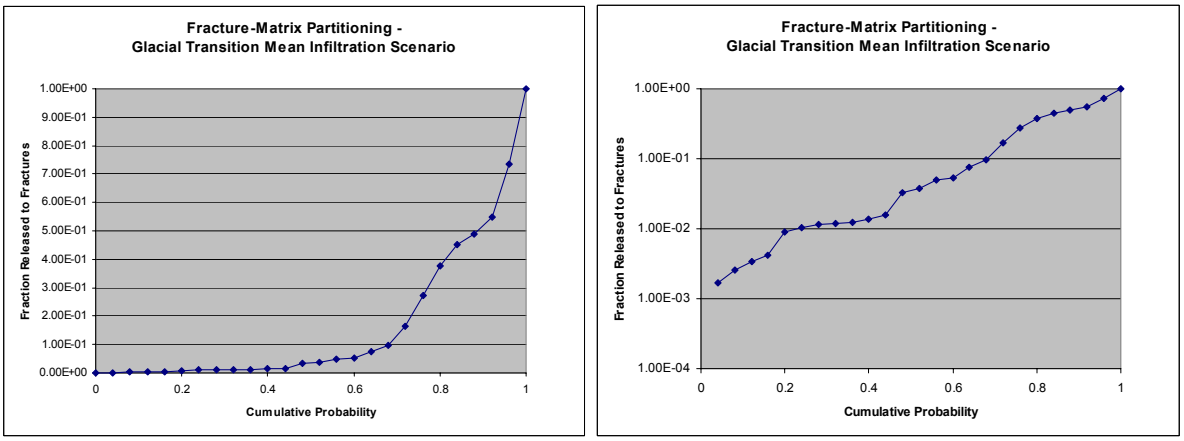

(b)

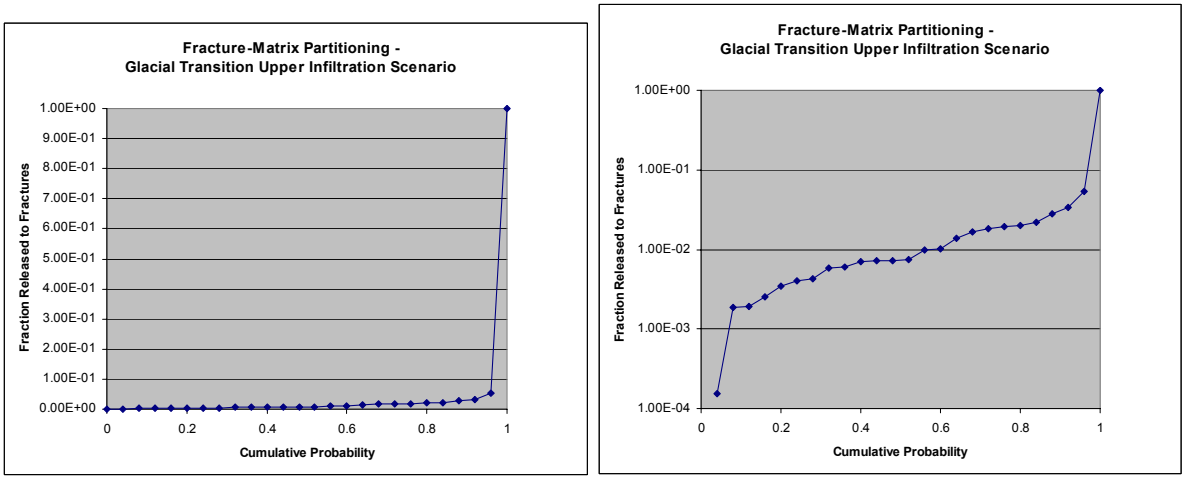

(c)

Output DTN: LB0307FMRADTRN.001.

Figure 6-25. Fracture-Matrix Partitioning Distributions for the (a) Lower, (b) Mean, and (c) Upper Glacial-Transition Infiltration Scenarios – Linear Scale on Left-Hand Side; Logarithmic Scale on Right-Hand Side

Distributions are based on the values for fracture-matrix partitioning and then ordered, to establish an empirical cumulative probability distribution. The distribution for the upper scenario has smaller releases to the fractures because of the larger advective water flux in the matrix. The average matrix water flux for the upper infiltration scenario is 0.08 mm/year compared with average matrix fluxes for the mean and lower scenarios of 0.035 and 0.027 mm/year, respectively. Furthermore, the median matrix fluxes for the upper, mean, and lower infiltration scenarios are 6.6, 1.6, and 1.6 mm/year, respectively. The similarity of the matrix flux for the lower and mean scenarios is the main reason for the similarity in the flux partitioning between the fractures and matrix. The other factors, such as the fracture Peclet number and fracture water content, tend to be random variables defined by the invert and fracture diffusion coefficients, offset of fracture flow from the drift, and residual fracture saturation not strongly affected by the infiltration scenario. Figures 6-25a–c show that the lower and mean scenarios result in distributions similar to the upper scenario. A comparison of the lower and mean scenarios is given in Figure 6-26.

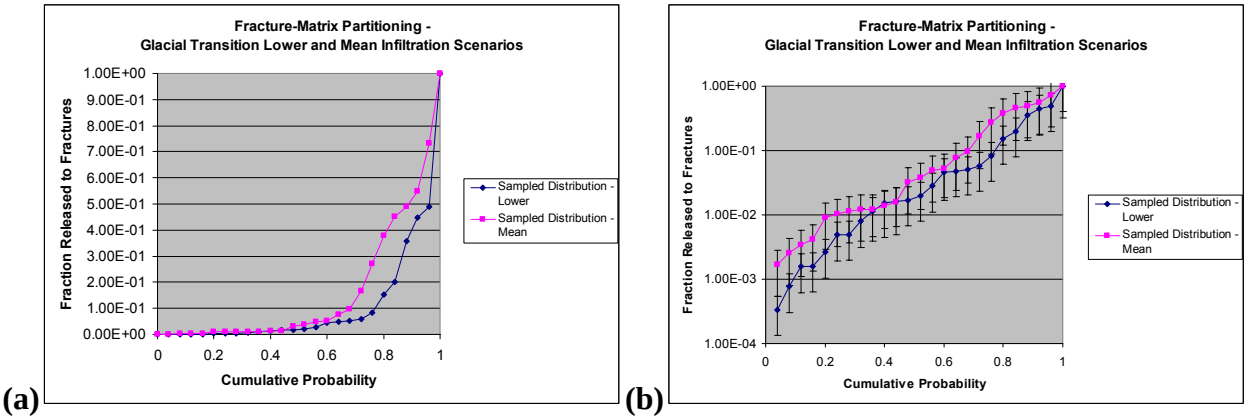

Output DTN: LB0307FMRADTRN.001.

Figure 6-26. Comparison of Lower and Mean Scenarios – (a) Linear Scale on Left-Hand Side; (b) Logarithmic Scale on Right-Hand Side

The comparisons in Figure 6-26a show on a linear scale that the distributions are fairly similar. The logarithmic plot shows the comparison with error bars set by the relative error in the mean. The overlap of the confidence limits for the lower and mean cases suggests combining these distributions into a single distribution. This distribution is shown in Figure 6-27.

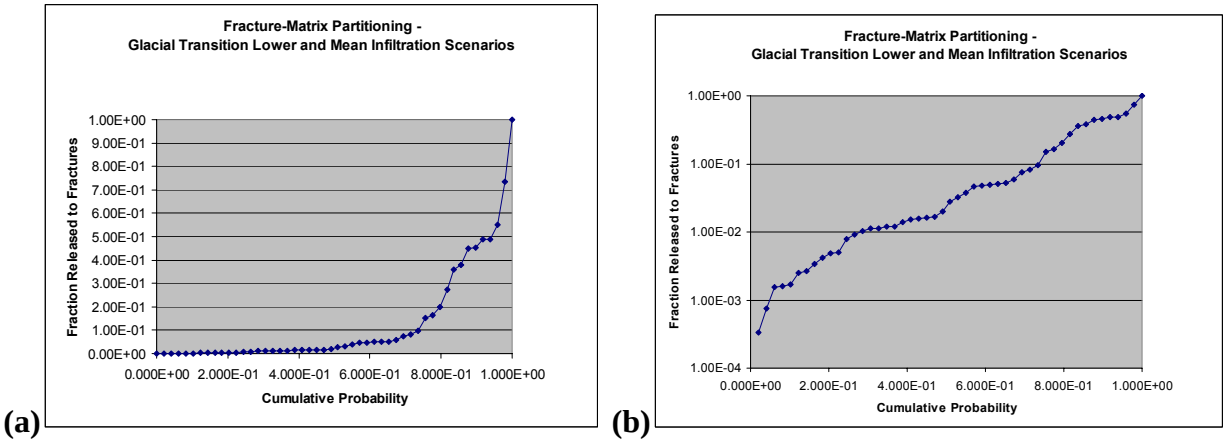

Output DTN: LB0307FMRADTRN.001.

Figure 6-27. Composite Distribution from the Lower and Mean Scenarios – (a) Linear Scale on Left-Hand Side; (b) Logarithmic Scale on Right-Hand Side

The uncertainty in the sampled distributions is shown in Figure 6-28. This uncertainty is based on the 95th percentile confidence interval estimates as presented in Equation 6-58.

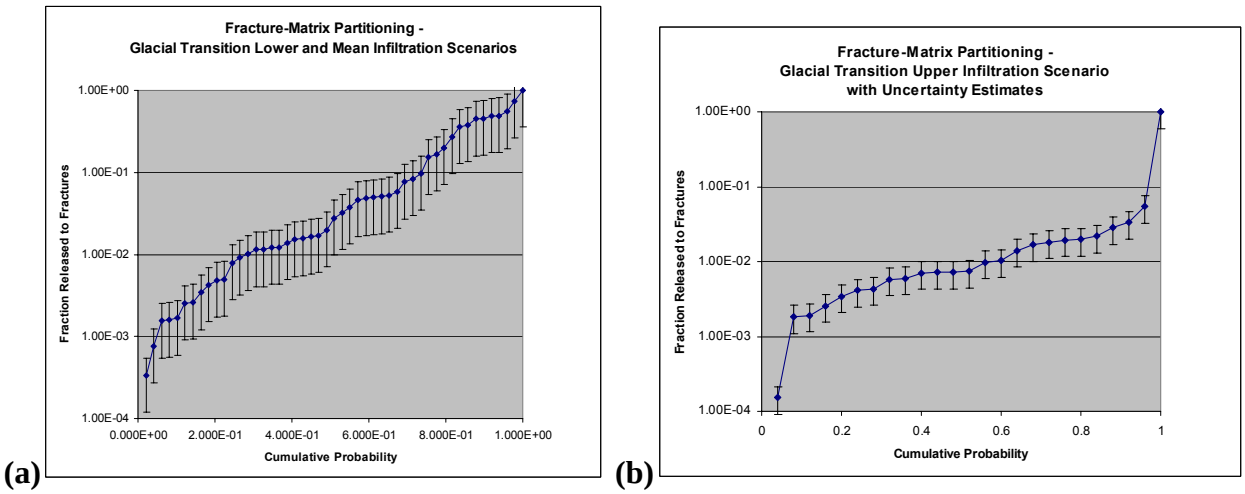

Output DTN: LB0307FMRADTRN.001.

Figure 6-28. Fracture-Matrix Partitioning Distributions with 95th Percentile Confidence Intervals: (a) Composite Distribution for the Lower and Mean Infiltration Scenarios and (b) Distribution for the Upper Infiltration Scenario

The combined distribution of percentage released to fractures for lower and mean infiltration scenarios under the glacial transition climate was derived for infiltration rates of 2.5 and 17.8 mm/year (*Simulation of Net Infiltration for Modern and Potential Future Climates,* BSC 2004 [DIRS 170007], Table 6-19). Present-day and monsoon climates range from 1.3 to 19.8 mm/year (BSC 2004 [DIRS 170007], Tables 6-10 and 6-14). Therefore, the combined distribution given in Figure 6-28a is applicable over all climates and infiltration scenarios except for the glacial transition upper infiltration case. For the glacial transition upper infiltration scenario, the distribution shown in Figure 6-28b is applicable.

Table 6-14. Cumulative Distributions for Fracture-Matrix Partitioning Factor: (a) Composite Distribution for the Glacial Transition Lower and Mean Infiltration Scenarios; (b) Distribution for the Glacial Transition Upper Infiltration Scenario

(a) Lower and Mean Infiltration Scenario		(b) Upper Infiltration Scenario	
Cumulative Probability	**Sampled Distribution**	**Cumulative Probability**	**Sampled Distribution**
0.000E+00	0.00	0	0.00
2.041E-02	3.33E-04	0.040	1.53E-04
4.082E-02	7.60E-04	0.080	1.84E-03
6.122E-02	1.55E-03	0.120	1.91E-03
8.163E-02	1.58E-03	0.160	2.56E-03
1.020E-01	1.67E-03	0.200	3.45E-03
1.224E-01	2.53E-03	0.240	4.08E-03
1.429E-01	2.63E-03	0.280	4.32E-03
1.633E-01	3.41E-03	0.320	5.79E-03
1.837E-01	4.22E-03	0.360	5.98E-03
2.041E-01	4.86E-03	0.400	7.08E-03
2.245E-01	4.97E-03	0.440	7.14E-03
2.449E-01	7.86E-03	0.480	7.21E-03
2.653E-01	9.08E-03	0.520	7.37E-03
2.857E-01	1.02E-02	0.560	9.81E-03
3.061E-01	1.139E-02	0.600	1.02E-02
3.265E-01	1.141E-02	0.640	1.40E-02
3.469E-01	1.209E-02	0.680	1.68E-02
3.673E-01	1.214E-02	0.720	1.82E-02
3.878E-01	1.39E-02	0.760	1.95E-02
4.082E-01	1.52E-02	0.800	1.98E-02
4.286E-01	1.55E-02	0.840	2.18E-02
4.490E-01	1.63E-02	0.880	2.83E-02
4.694E-01	1.69E-02	0.920	3.34E-02
4.898E-01	1.99E-02	0.960	5.44E-02
5.102E-01	2.79E-02	1	1.00E+00
5.306E-01	3.24E-02		
5.510E-01	3.77E-02		
5.714E-01	4.63E-02		
5.918E-01	4.82E-02		
6.122E-01	4.94E-02		
6.327E-01	5.04E-02		
6.531E-01	5.26E-02		
6.735E-01	5.85E-02		
6.939E-01	7.61E-02		
7.143E-01	8.34E-02		
7.347E-01	9.68E-02		
7.551E-01	1.52E-01		
7.755E-01	1.66E-01		
7.959E-01	2.00E-01		
8.163E-01	2.72E-01		
8.367E-01	3.58E-01		
8.571E-01	3.77E-01		
8.776E-01	4.49E-01		
8.980E-01	4.53E-01		
9.184E-01	4.88E-01		
9.388E-01	4.90E-01		
9.592E-01	5.50E-01		
9.796E-01	7.34E-01		
1.000E+00	1.00E+00		

Output DTN: LB0307FMRADTRN.001.

NOTE: A fourth significant figure is given for the sampled distribution values where three significant figures result in a repeated value.

Table 6-15. Statistics for the Fracture-Matrix Partitioning Factor Distributions: (a) Lower and Mean Infiltration Scenarios for Glacial Transition Climate; (b) Upper Infiltration Scenario for Glacial Transition Climate

	(a) Lower and Mean Infiltration Scenario	(b) Upper Infiltration Scenario
Average of Fracture—Matrix Partitioning Factors	1.16E-01	1.27E-02
Standard Deviation of Fracture-Matrix Partitioning Factors	1.82E-01	1.25E-02
95th Percentile Confidence Interval (Equation 6-58)	7.45E-02	5.11E-03
95th Percentile Confidence Interval—Percentage of Average	64.5%	40.2%

Output DTN: LB0307FMRADTRN.001.

The sensitivity of the results to the invert diffusive mass transfer coefficient have been investigated to address the potential effects of different invert materials on the fracture-matrix partitioning. The modeling results for the partitioning coefficient (the fraction of the radionuclide releases that enter the fractures) are plotted against the diffusive mass transfer coefficient for the invert in Figure 6-29. The sensitivity results show that the fraction released to fractures has only a very weak correlation with the invert diffusive mass transfer coefficient. Invert properties affect the partitioning results only through the invert diffusive mass transfer coefficient. Furthermore, the invert diffusive mass transfer coefficient is only affected by the invert porosities (Section 6.4.5). Therefore, the main results that are derived using properties of the invert intragranular porosity from the tsw36 are also applicable if the invert consists of materials from the other host rock units having different intragranular porosities, i.e. the tsw33, tsw34, and tsw35.

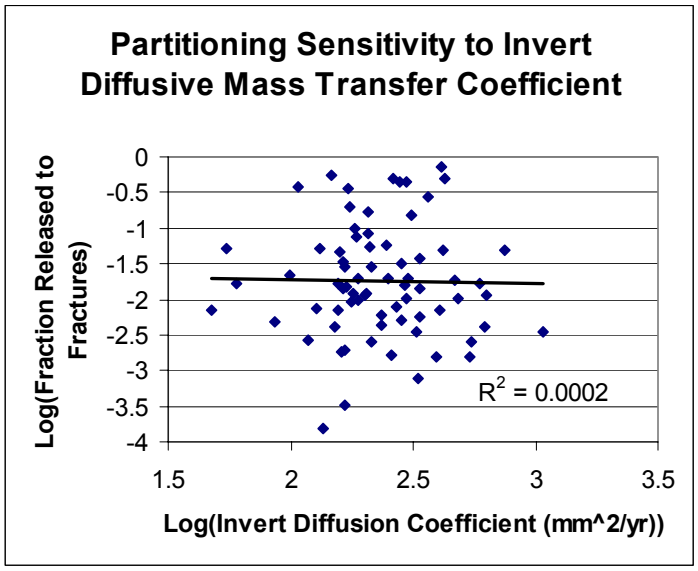

Output DTN: LB0307FMRADTRN.001.

Figure 6-29. Fracture-Matrix Partitioning Sensitivity to Invert Diffusive Mass Transfer Coefficient

6.5 EFFECTS OF AIR IN FRACTURE

The results found for the model as discussed in Section 6.4 may be compared with the first-order model predictions from Equations 43 and 44. The fracture-matrix partitioning ratio, P_r, to first order is:

$$P_r = \frac{Pe_{fe} b_d}{Pe_m (1 - b_d) + Pe_{fe} b_d} \quad \text{(Eq. 6-59)}$$

A comparison of the predictions for the fracture-matrix partitioning model based on Equation 6-59 with the results in Section 6.4 is given below. Inputs for this calculation are presented in Appendix H.

Table 6-16. Comparison of First-Order Model to Full Model

	Average Fracture-Matrix Partitioning Ratio	
	Full model	**First-order model**
Lower case	8.61E-02	8.92E-02
Mean case	1.45E-01	1.51E-01
Upper case	1.27E-02	1.33E-02

The results indicate that the first-order model explains most of the partitioning behavior. The first-order model is independent of the Fourier coefficients, as shown in Equation 6-59. Therefore, the solution is not sensitive to the details of the boundary conditions and location of the water film along the invert-rock boundary.

If the air gap in the fracture is included, the first-order solution becomes:

$$P_{ra} = \frac{Pe_{fe} b_d}{Pe_m (1 - \phi_f) + Pe_{fe} b_d} \quad \text{(Eq. 6-60)}$$

where P_{ra} is the partitioning ratio including the air gap and ϕ_f is the fracture porosity. Equation 6-60 may be written in terms of P_r giving,

$$P_{ra} = \frac{P_r}{1 - (1 - P_r)\left(\frac{\phi_f - b_d}{1 - b_d}\right)} \quad \text{(Eq. 6-61)}$$

The ratio of P_{ra} to P_r is unity for $P_r = 1$ and is largest for $P_r = 0$. The maximum ratio is

$$\frac{P_{ra}}{P_r} = \frac{1 - b_d}{1 - \phi_f} \quad \text{(Eq. 6-62)}$$

However, ϕ_f and b_d are both much less than 1 so Equation 6-60 may be approximated as,

$$\frac{P_{ra}}{P_r} = 1 + \phi_f - b_d \quad \text{(Eq. 6-63)}$$

Therefore, the maximum relative error is,

$$\frac{P_{ra} - P_r}{P_r} = \phi_f - b_d \quad \text{(Eq. 6-64)}$$

which is less than the fracture porosity. This result supports the model approximation that the solution is not sensitive to the placement of the no-flux boundary either immediately adjacent to the water film (as in the model presented in Section 6.4) or displaced from this water film by an air gap in the fracture.

6.6 COMPARISON OF FRACTURE-MATRIX PARTITIONING MODEL AND DRIFT SHADOW MODEL

Sections 6.3 and 6.4 present two models concerning the behavior of flow and transport in the region beneath waste emplacement drifts. In Section 6.3, the drift shadow model uses the dual-continuum method to show that a substantial perturbation to the flow field exists beneath waste emplacement drifts. A large zone of reduced flow is found for the fracture continuum, with a much smaller perturbation to the flow for the matrix continuum. The transport through the drift shadow is found to be much slower than transport initiated in unperturbed fracture flow. Sensitivity studies indicate that this behavior is largely due to initiation of transport in the matrix and the subsequent slow migration of radionuclides through the matrix to the fractures.

The fracture-matrix partitioning model presented in Section 6.4 is based on the premise that fracture flow around a drift does not behave like a homogeneous continuum, but that heterogeneity, anisotropy, and discrete fracture effects may result in water movement in the fractures much closer to the waste emplacement drift than found in Section 6.3. With the approximation of fracture flow close to the base of the waste emplacement drift, partitioning of releases from the drifts is not necessarily dominated by the relatively large matrix water content as compared with the fracture water content. The dynamics of the flow field in this model result in a competition between the fracture and matrix continua for radionuclide releases, and that leads to greater partitioning of the releases to the fractures. The greater releases of radionuclides to fractures and the more active flow system in the fracture-matrix partitioning model leads to more rapid transport of radionuclides in the UZ. Therefore, the fracture-matrix partitioning model was chosen to be used for validation of the EBS radionuclide transport abstraction model [*EBS Radionuclide Transport Abstraction* (BSC 2004 [DIRS 169868])] so that radionuclide transport in the unsaturated zone is not underestimated.

7. VALIDATION

The drift-scale radionuclide transport model is intended to be used as an alternative model for comparison with the engineered barrier system (EBS) radionuclide transport model (*EBS Radionuclide Transport Abstraction*, BSC 2004 [DIRS 169868]). For that purpose, two alternative models have been developed for drift-scale radionuclide transport. One of the alternative models is a dual-continuum flow and transport model called the drift shadow model. The effects of variations in the flow field and fracture-matrix interaction in the vicinity of a waste emplacement drift are investigated through sensitivity studies using the drift shadow model (Houseworth et al. 2003 [DIRS 164394]). In this model, the flow is significantly perturbed (reduced) beneath the waste emplacement drifts. However, comparisons of transport in this perturbed flow field with transport in an unperturbed flow field show similar results if the transport is initiated in the rock matrix. This has led to a second alternative model, called the fracture-matrix partitioning model, that focuses on the partitioning of radionuclide transport between the fractures and matrix upon exiting the waste emplacement drift. The fracture-matrix partitioning model computes the partitioning of diffusive radionuclide transport from the invert (for drifts without seepage) into the rock water in the fractures and matrix.

This section describes the validation of the fracture-matrix partitioning model. Note that the term model as presented in this section refers to both the mathematical model and its underlying conceptual model. This model is intended to support validation of the TSPA component model "Radionuclide Transport from Waste Package to Drift Wall through Invert" through comparisons of the fracture-matrix partitioning results for drifts without seepage. AP-2.27Q, *Planning for Science Activities* (Attachment 3, Table 1) requires Level I validation for models supporting that TSPA component. The criteria for confidence building during model development are given in *Technical Work Plan for: Unsaturated Zone Transport Model Report Integration* (BSC 2004 [DIRS 171282], Section 2.2.4), consistent with AP-SIII.10Q, *Models*, Paragraph 5.3.2b). The general criteria for post-model development validation are given in AP-SIII.10Q, *Models*, Paragraph 5.3.2c). As specified in Attachment 3 of AP-2.27Q, the Level I post-development model validation must implement a single, appropriate method from this list.

The results of the fracture-matrix partitioning model as shown in Figure 6-28 are intended to be used as an alternative model for comparison with the EBS radionuclide transport model. This use is limited to conditions applicable to the fracture-matrix partitioning model, which means drifts without seepage or other sources of advective transport (excluding the capillary driven flow between the rock matrix and the intragranular porosity of the invert, as discussed in Section 6.4). The range of intended use is for drifts without seepage or other sources of significant advective transport inside the drift (such as condensate flow). The range of use also encompasses the range of possible flow conditions in the rock and parameter ranges as discussed in Section 6.4.5. The level of confidence required is limited as a result of the expectation that a large fraction of the drifts will either have advective radionuclide transport through the invert from water seeping into the drifts and/or from condensation [(BSC 2004 [DIRS 169131], Tables 6.8-1 and 6.8-2; *In-Drift Natural Convection and Condensation* (BSC 2004 [DIRS 164327], Section 6.3.7)] and because this is an alternative model that does not provide direct input to TSPA. As a result, the diffusive transport mechanism investigated in the fracture-matrix partitioning model is not expected to have a significant impact on performance;

hence the required level of confidence in the model validation is relatively low, commensurate with a Level I validation.

Section 7.1 discusses confidence building during model development which establishes the reasons for confidence in the fracture-matrix partitioning model. Section 7.2 provides a detailed discussion of post-development validation activities, including the underlying rationale for comparison with the drift shadow model, a summary discussion of the rationale for introducing the fracture-matrix partitioning model to account for uncertainties in the drift shadow model; and demonstration of the conservative results obtained from the fracture-matrix partitioning model in comparison with the drift shadow model. This conservatism is tied to the effects of the partitioning on UZ transport, and the justification of a conservative model is based on the following points:

1. The drift shadow model is approximately equivalent to 100% matrix release, as shown in Figure 6-7.

2. Transport for fracture release is orders of magnitude faster than for matrix release, shown in Figure 6-7 for the drift shadow model and in Figure 7-2 for the site-scale UZ transport model. Note that the results for the drift shadow model domain are not quantitatively the same as for the site-scale model domain. This is a result of the drift shadow model being limited to fractured rock within the tsw35 rock unit and does not account for the effects of the full path length to the water table, other rock units, and other hydrogeologic features, as represented in the site-scale unsaturated zone transport model results.

3. The fracture matrix partitioning model results in a non-negligible fraction of releases to the fractures for non-seeping drifts, as shown by the partitioning factor to fractures in Figure 6-28. Furthermore, this figure indicates that the model propagates a wide range of uncertainty from the input parameters into the output partitioning factor.

7.1 CONFIDENCE BUILDING DURING MODEL DEVELOPMENT TO ESTABLISH SCIENTIFIC BASIS AND ACCURACY FOR INTENDED USE

For Level I validation, Section 2.2.4 of BSC (2004 [DIRS 171282]) specifies the following steps for Confidence Building During Model Development: The development of the model should be documented in accordance with the requirements of Section 5.3.2b) of AP-SIII.10Q. The development of the fracture-matrix partitioning model has been conducted according to all of the applicable requirements, as follows:

1. Selection of input parameters and/or input data, and a discussion of how the selection process builds confidence in the model. [AP-SIII.10Q 5.3.2(b) (1)]

   The types and quality of data selected as input builds confidence in the model. The inputs to the fracture-matrix partitioning model are presented in Section 4.1. The inputs describing hydrologic properties have been taken from site-specific measurements, e.g. fracture frequency and fracture porosity as discussed in Section 4.1.1, laboratory measurements on analogous materials, e.g. matrix diffusion as discussed in Section 4.1.5, or from models based on accepted scientific principles

and calibrated to site-specific data, e.g. water flux and water saturation in the rock as discussed in Section 4.1.2. Other sources of information including scientific data from handbooks, e.g. free-water diffusion coefficients as discussed in Section 4.1.6, and design information is taken from IEDs, e.g. the repository layout relative to the host rock units as discussed in Section 4.1.7. Thus, this criterion is appropriately addressed.

2. Description of calibration activities, and/or initial boundary condition runs, convergences, and a discussion of how the activity or activities build confidence in the model. Inclusion of a discussion of impacts of any non-convergence runs [(AP-SIII.10Q 5.3.2(b)(2)].

   The construction of the fracture-matrix partitioning model is discussed in detail in Section 6.4, with specific information on boundary conditions given in Section 6.4.1. Given that the model is steady-state, initial conditions are not applicable. Model calibration was not performed because the model was compared to an alternative conceptual model (i.e., the drift shadow model) in lieu of test data. Model run convergence for the fracture-matrix partitioning model is described in Section 6.4.4. The convergence variations were found to be on the order of a few percent (Section 6.4.4), significantly less than 50 percent specified in the criterion and significantly less than the uncertainty in model output, which is found to be on the order of a factor of 10 to 100 (Section 6.4.6). Therefore, the criterion for calibration and run convergence is met.

3. Discussion of the impacts of uncertainties to the model results. [(AP-SIII.10Q 5.3.2(b)(3)].

   Addressing Future States/Uncertainty - The effects of future climates and uncertainties are addressed in ways which build confidence in the models. Changes in future climate are expected to result in changes in flow and water saturation in the unsaturated zone, as discussed in Section 6.4.6. However, the range of uncertainty in climate conditions for the glacial-transition climate state was found to be comparable to that for the range of conditions under all climate states. The glacial-transition climate state is also expected to occur for most of the compliance period (from 2000 to 10,000 years). Furthermore, the effects of changes in hydrologic conditions were found to be relatively small except for the wettest conditions anticipated under the glacial-transition climate state. Therefore, the fracture-matrix partitioning model could be based on the range of conditions under the glacial-transition climate state only.

   Parameter uncertainty in the fracture-matrix partitioning model is defined for parameters that affect the model output as discussed in Section 6.4.5. The uncertainty is based on direct, site-specific measurements, e.g. matrix porosity, inferences from analogous measurements, e.g. diffusion under saturated conditions in analogous rock samples, and uncertainty in model output, e.g. models of unsaturated flow using site-specific measurements and uncertainties. Uncertainty is either sampled directly, e.g. fracture frequency, or is treated as discrete states as in the UZ flow model output.

Because model uncertainty in the fracture-matrix partitioning model is incorporated by using a conservative approximation to flow processes in a fracture network beneath a waste emplacement drift, as discussed above under Addressing the Use of Assumptions/ Simplifications, the treatment of uncertainty builds confidence.

Addressing the Propagation of Uncertainty - Uncertainties are propagated in a way which builds confidence. The uncertainty in parameters are sampled directly using a Monte Carlo methodology to derive the uncertainty in the output from the fracture-matrix partitioning model as presented in Section 6.4.6. Furthermore, the uncertainty resulting from the finite sample size used for the Monte Carlo analysis is also addressed. The uncertainty in model output is shown in Figure 6-28 and also is presented in Table 6-14. The range of uncertainty in the partitioning factor may be represented by the ratio of the mean plus one standard deviation divided by the mean minus one standard deviation. For the lower-mean climate states this range of uncertainty is on the order of 100; for the upper climate state this range of uncertainty is on the order of 10. These results show that uncertainty in the inputs translates into a broad range of uncertainty in the output of the fracture-matrix partitioning model. Therefore, the criterion for discussing the impacts of uncertainty is addressed.

7.2 POST-DEVELOPMENT MODEL VALIDATION TO SUPPORT THE SCIENTIFIC BASIS OF THE MODEL

Post-development model validation activities followed the model validation plan described in Section planned in the *Technical Work Plan for: Unsaturated Zone Transport Model Report Integration* (BSC 2004 [DIRS 171282], Section 2.2.4). The method chosen for model validation is corroboration with alternative models. In particular, BSC (2004 [DIRS 171282], Section 2.2.4) states for corroboration with alternative models:

"Results of the fracture-matrix partitioning model, in which flow is undisturbed immediately below the drift, will be evaluated. A comparison of this case with the dual-continuum model provides information on the sensitivity of the radionuclide partitioning to matrix and fractures upon leaving the waste emplacement drift, as a function of the flow field characteristics. The alternative model that results in greater radionuclide releases to the fractures will be used as an alternative model for validation of the EBS Radionuclide Transport Model. A discussion of the model uncertainties will also be provided."

This model validation is based on a conservative model approach as discussed in Section 5.3.1b)2) in AP-SIII.10Q.

7.2.1 Rationale for Selecting the Drift Shadow Model as the Alternative Conceptual Model

The drift-shadow model is used as the alternative conceptual model to validate the fracture-matrix partitioning model. The drift shadow model is a standard process-based representation of flow and transport processes in fractured rock that represent a reasonable, credible, technical approach using scientific principles. The specific drift shadow model presented in Section 6.3 provides a detailed process-level description of the phenomena of

unsaturated flow and transport in a fractured rock near a waste emplacement drift ["Flow and Transport in the Drift Shadow in a Dual-Continuum Model" (Houseworth et al. 2003 [DIRS 164394])]. This model accounts for the presence of fractures and a porous rock matrix using a standard process-based description of unsaturated flow in a dual continuum that predicts the hydrodynamic effects of a waste emplacement drift on unsaturated flow patterns. The model parameters are based on the drift-scale calibrated properties parameter set, with an adjustment to the active fracture parameter as discussed in Section 6.3.3.1 to account for the effects of the lower fracture permeability on fracture-matrix interaction as compared with the mountain-scale fracture permeabilities. Similarly, transport is modeled using a standard process-based description for an unsaturated dual-continuum using parameters applicable to advection, diffusion, sorption, and fracture-matrix interaction. The model uses the same conceptual basis as described in *Conceptual and Numerical Models for UZ Flow and Transport* (BSC 2004 [DIRS 170035]). The fundamental process representations for flow and transport used by the drift shadow model are the same as those used for other drift-scale models as discussed in *Seepage Model for PA Including Drift Collapse* (BSC 2004 [DIRS 167652]); *Seepage Calibration Model and Seepage Testing Data* (BSC 2004 [DIRS 170034]); *Drift-Scale THC Seepage Model* (BSC 2004 [DIRS 169856]); *Drift-Scale Coupled Processes (DST and TH Seepage) Models* (BSC 2004 [DIRS 170338]); and *Drift Scale THM Model* (BSC 2004 [DIRS 169864]), as well as mountain-scale models as discussed in *UZ Flow Models and Submodels* (BSC 2004 [DIRS 169861]); *Radionuclide Transport Models Under Ambient Conditions* (BSC 2004 [DIRS 164500]); and *Mountain-Scale Coupled Processes (TH/THC/THM)* (BSC 2004 [DIRS 169866]). Therefore, there is substantial precedent for using the drift shadow model for describing flow and transport in a fractured rock.

The drift shadow flow model predictions for flow patterns in a single continuum have been found to quantitatively agree with an analytical model for unsaturated flow around a drift (Houseworth et al. 2003 [DIRS 164394], Figure 2), as shown in Figure 7-1. Figure 7-1a presents flow patterns for the case where capillary forces are relatively strong compared with gravity forces, as in the rock matrix at Yucca Mountain. Figure 7-1b presents flow patterns for the case where capillary forces are relatively weak compared with gravity forces, as in the fractures at Yucca Mountain. Although the drift shadow model presented in Section 6 uses a dual-continuum to represent a fractured rock, the flow patterns for the matrix continuum and fracture continuum in the dual-continuum model in Figures 6-2 through 6-4 are similar to those shown in Figure 7-1. The dual-continuum behavior in the rock matrix and fractures is similar to the single-continuum solutions because fracture-matrix interaction has only a small effect on the flow patterns. Therefore, the scientific basis of the drift shadow model is found to be adequate.

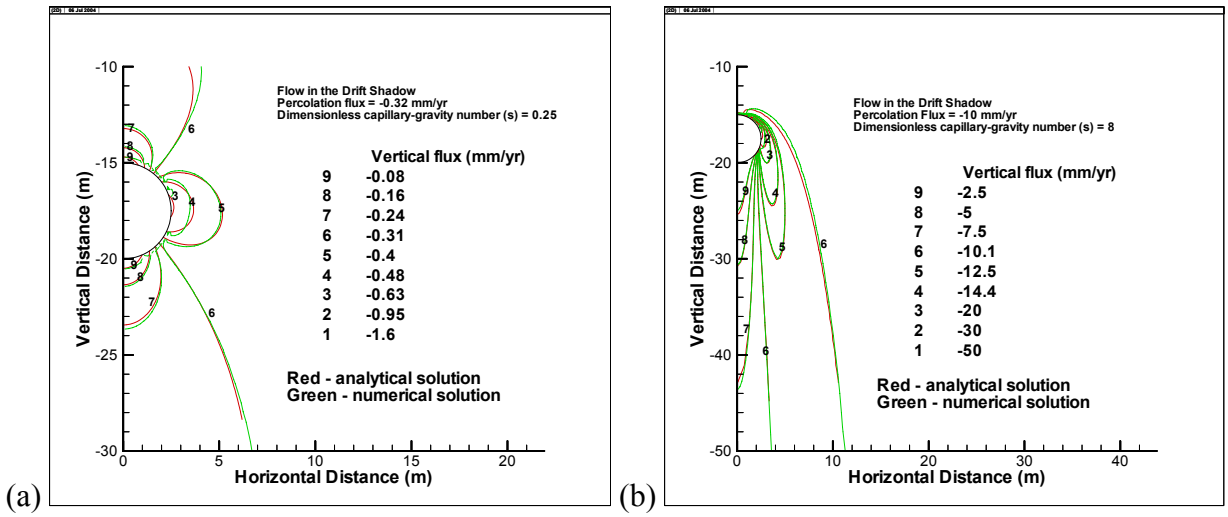

Source: Houseworth et al. 2003 [DIRS 164394], Figure 2.

Figure 7-1. Comparison of the Numerical Model for a Single-Continuum With the Analytical Model of Philip et al. (1989 [DIRS 105743]) a) Flow Contours Representative of Rock Matrix b) Flow Contours Representative of Rock Fractures

7.2.2 Rationale for Introducing the Fracture-Matrix Partitioning Model

The primary reason for not directly using the drift shadow model in the TSPA is that there is presently a lack of relevant observational data and that it is difficult to obtain such data from in situ tests. Existing data for natural analogs presented in BSC (2004 [DIRS 169218]) are not relevant or useful for the drift-scale radionuclide transport problem. In addition, not all features of fractured rock have been explored in the drift shadow model. For example, heterogeneity of the fracture network and potential effects of discrete fractures may lead to a reduction in the extent of the drift shadow. Given these limitations and the potentially large beneficial effect of drift-scale processes on reducing radionuclide transport rates through the UZ, a more flexible modeling approach is appropriate. To that end, the fracture-matrix partitioning model has been developed to limit the reliance on process descriptions of flow and transport in the fractures near a waste emplacement drift. This necessarily results in approximations from the standpoint of the theoretical framework used for the drift shadow model. The fracture-matrix partitioning model uses the following approximations that lead to greater flow and transport in fractures beneath a waste emplacement drift:

1. Fracture flow occurs beneath a waste emplacement drift within a distance less than the fracture spacing. Given fracture spacings that are, on average, less than one meter, the zone of reduced flow is greatly reduced in comparison with the shadow zone predicted by the drift shadow model.

2. The initial transient period, which is initially dominated by diffusive transfer into the rock, is not treated. This initial radionuclide partitioning ratio will be equal to the water content ratio of the fractures and matrix, and will only asymptotically approach the predicted fracture-matrix partitioning ratio.

3. The effects of dryout during the boiling and rewetting periods are ignored, during which fracture water saturations are disproportionately reduced in comparison with the matrix. This will lead to preferential entry of radionuclides to the matrix during this thermally perturbed period.

4. All fractures are flowing in the fracture-matrix partitioning model as opposed to the active fracture model, where only a subset of the fractures is flowing. This leads to greater contact between the invert and flowing fractures and, therefore, greater releases from the invert to the rock fractures.

7.2.3 Validation Results

The results of the fracture matrix partitioning model clearly lead to more rapid radionuclide transport through the UZ as compared with the drift shadow model. The probability distribution for the partitioning ratio between the fractures and matrix for the drift interface model allows a non-zero fraction of the releases initially into the fractures, which will lead to relatively rapid transport through the UZ for that release fraction. Differences in transport times from the repository to the water table for fracture versus matrix release are shown in Figure 7-2 for present-day mean climate using the site-scale transport process model. This figure shows that releases to fractures will lead to significantly more rapid transport than releases to matrix. By comparison, the drift shadow model predicts transport times, shown in Figure 6-5 (a) and (b), similar to or longer than those shown in Figure 7-2 for matrix release.

In summary, the fracture-matrix partitioning model is valid based on the following results:

1. The transport results shown in Figure 6-7 demonstrate that releases to the matrix in an undisturbed flow field behave similarly to transport through the drift shadow. The figure also shows that releases to fractures in an undisturbed flow field travel through the model domain in about one year compared with several thousand years for releases to the matrix or the drift shadow. Transport times are also found to be substantially longer for matrix release as compared with fracture release in the mountain-scale UZ transport results shown in Figure 7-2. Note that the results for the drift shadow model domain are not quantitatively the same as for the site-scale model domain. This is a result of the drift shadow model being limited to fractured rock within a single repository host-rock unit and does not account for the effects of the full path length to the water table, other rock units, and other hydrogeologic features, as represented in the site-scale unsaturated zone transport model results.

2. The drift shadow model results in Figures 6-5 and 6-6 shows that transport times through the model domain are thousands to tens of thousands of years for essentially all radionuclides under a wide range of fracture and matrix flow conditions.

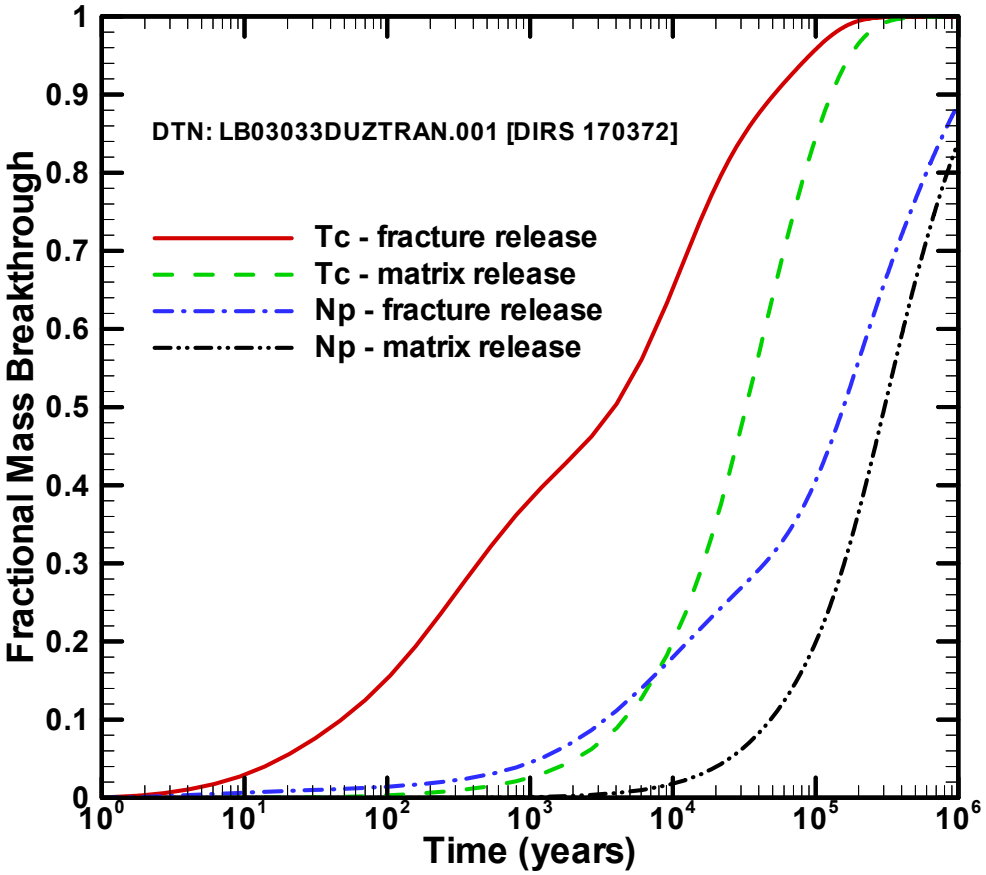

Source: Modified from Figure 6.7-3 BSC 2004 [DIRS 169861]).

NOTE: Radionuclide decay not included in transport calculation.

Figure 7-2. Breakthrough Curves for Fracture and Matrix Release.

3. As can be seen in Table 6-14, the fracture-matrix partitioning model gives a distribution of releases to fractures ranging from roughly 0.1 percent to 50 percent for the 5th to 95th percentile values, with a mean of 11.6 percent for all climate scenarios except for the glacial-transition upper climate scenario. The distribution of releases for the glacial-transition upper climate scenario is roughly 0.02 percent to 5 percent for the 5th to 95th percentile values, with an average of 1.27 percent. These releases to undisturbed fracture flow will result in transport through the near-drift region (drift-shadow model domain) that are orders of magnitude faster than releases to the matrix or in the drift shadow model.

For all of these reasons, based on points 1, 2, and 3, the fracture-matrix partitioning model will result in a fast component of transport not found in the drift shadow model and leads to a conservative representation of drift-scale transport as compared to the drift shadow model. This satisfies the post-development model validation requirements presented in the technical work plan (BSC 2004 [DIRS 171282], Section 2.2.4) that the alternative model results in greater

radionuclide releases to the fractures will be used as an alternative model for validation of the EBS radionuclide transport model.

7.3 VALIDATION SUMMARY

The fracture-matrix partitioning model has been validated by applying acceptance criteria as described above. Activities requirements for confidence building during model development have been satisfied (Section 7.1). Also, the post-development validation requirement defined in the BSC (2004 [DIRS 171282], Section 2.2.4) has been fulfilled, including corroboration of model results with the alternative conceptual model (Section 7.2). The model development and post-development validation activities described establish the scientific bases for the fracture-matrix partitioning model. No future activities need to be accomplished for model validation. Based on this, the fracture-matrix partitioning model is considered to be adequate and sufficiently accurate for the intended purpose and validate the level of confidence required by the model's relative importance to the potential performance of the repository system.

INTENTIONALLY LEFT BLANK

8. CONCLUSIONS

The diversion of all percolating water around a waste emplacement drift results in an environment of greatly diminished flow inside the drift. In such an environment, the primary transport mechanism for radionuclides to migrate from the drift to the surrounding rock is by diffusion. Because of the relatively large water content of the matrix in comparison with the fractures, diffusive releases from waste emplacement drifts are highly partitioned to the matrix. Transport time for radionuclides initiated in the matrix has been found to be orders of magnitude longer than for radionuclides initiated in undisturbed fracture flow. The average (or 50 percent) breakthrough times in the submodel presented in Section 6.3.3.2 are dominated by matrix advection. Simulation results show that for these cases, most of the radionuclide mass still remains in the matrix at breakthrough. Therefore, the effects of the drift shadow on transport extend beyond the existing model boundary. For radionuclide releases from drifts without seepage, the results presented in this section indicate that transport times to the water table will be thousands to tens of thousands of years for nonsorbing radionuclides (such as technetium). For sorbing radionuclides, the transport times are considerably longer, according to the degree of sorption. For a weakly sorbing radionuclide such as neptunium, transport times are tens of thousands to hundreds of thousands of years. For a strongly sorbing radionuclide such as plutonium, transport times range from millions to tens of millions of years.

Sensitivity calculations show that the main effect of the drift shadow on transport is that radionuclide transport is initiated in the matrix. Subsequent effects of the drift shadow on the dynamics of the fracture or matrix flow fields have much less influence on transport. The long transport pathways in the matrix primarily result from initiation of transport in the matrix combined with the relatively "disconnected" nature of the fracture and matrix continua. Varying degrees of fracture-matrix interaction in the dual-permeability model are shown to have a significant influence on transport in the drift shadow.

The lack of observational evidence for the drift shadow has led to the development of the fracture-matrix partitioning model. In this model, the sensitivity results from the drift shadow model are used to focus the discussion of drift-scale transport on the behavior of radionuclide releases from drifts without seepage. In particular, the most important factor is the initiation of transport in the fractures or the matrix. The fracture-matrix partitioning model allows for undisturbed fracture flow to occur some distance beneath the drift, flow that is scaled by the fracture spacing to account for uncertainty in the drift shadow effect. Additional uncertainty is captured through sampling distributions for the following factors:

1. Fracture and matrix water flux and saturation and matrix effective permeability over a wide range of average flow rates representing uncertainty in the UZ flow fields

2. Flow-focusing effects to account for uncertainty in variations in flow at the drift scale, which is smaller than the spatial resolution of the mountain-scale flow model

3. Invert thickness, porosity characteristics, and molecular diffusion rates that influence diffusive characteristics of the invert

4. Matrix diffusion rates, including the influence of partial matrix saturation

5. Fracture and matrix porosity and fracture residual saturation.

The fracture-matrix partitioning model assesses the fraction of releases from drifts without seepage to the fractures and matrix in the underlying rock. This assessment is based on a steady state transport model where radionuclides diffuse through the crushed tuff invert in the drift to the fractures and matrix in the underlying rock. Due to the discrete nature of fractures and blockage of fracture flow by the drift, fracture flow is offset from the base of the drift by a fraction of the fracture spacing. Conversely, the continuous nature of the rock matrix leads to advective water flux in the rock immediately below the drift. Thus, diffusive releases from the invert are transported away from the drift by advection in the rock matrix and by diffusion through the fractures to the point where fracture flow begins. The developed partitioning distributions are shown in Figure 6-28. These distributions are a result of uncertainties in the inputs (see Table 6-14). Similarity in the partitioning distribution for the lower and mean infiltration scenarios leads to the composite distribution for the fracture-matrix partitioning in 6-28a. The upper infiltration scenario leads to a distinct distribution as shown in 6-28b. Uncertainties in the distributions resulting from sampling uncertainties are indicated by the error bars in Figure 6-28.

Output from this report for the drift shadow model is captured in Output-DTNs: LB0307DSRADTRN.001 and LB0307DSRADTRN.002 and in Output-DTN: LB0307FMRADTRN.001 for the fracture-matrix partitioning model.

Following release from the drifts to the rock, the radionuclide transport process in TSPA is simulated using the particle-tracking model, which does not account for the effects of the drift on the flow field [*Particle Tracking Model and Abstraction of Transport Processes* (BSC 2004 [DIRS 170041])]. Thus, radionuclides are transported from the drifts in the undisturbed, UZ flow field. Use of these results for the partitioning of fracture-matrix releases is restricted to drifts with radionuclide releases dominated by diffusion, which in general are drifts without seepage.

Confirmatory information comparing the drift shadow model flow predictions with an analytical model are given in Section 7.1. Confirmatory information from the mountain-scale UZ transport model concerning the effects of initiating transport in the rock fractures or rock matrix is given in Section 7.3.

8.1 BARRIER DESCRIPTION

The findings in this model report support the conclusion that for drifts without seepage, radionuclide releases from the drift to the rock will be preferentially partitioned to the rock matrix. Furthermore, initiation of transport in the rock matrix has a significant effect on the subsequent transport through the unsaturated zone. The difference in transport times through the drift-scale model domain for radionuclide transport initiated in rock matrix versus the fractures for undisturbed flow conditions is thousands to tens of thousands of years. The preferential release of radionuclides from drifts without seepage to the rock matrix results in substantial delays in radionuclide transport, leading to the conclusion that the presence of the drift, with or

without a drift shadow, plays an important role in the delay of radionuclide transport. The magnitude of this effect on performance of the repository is a function of fraction of drifts that do not seep.

8.2 HOW THE ACCEPTANCE CRITERIA ARE ADDRESSED

2.2.1.3.7.3 Radionuclide Transport in the Unsaturated Zone

Acceptance Criterion 1, System Description and Model Integration Are Adequate.

(2) The description of the aspects of hydrology, geology, geochemistry, design features, physical phenomena, and couplings, that may affect radionuclide transport in the unsaturated zone, is adequate. For example, the description includes changes in transport properties in the unsaturated zone, from water-rock interaction. Conditions and assumptions in the total system performance assessment abstraction of radionuclide transport in the unsaturated zone are readily identified, and consistent with the body of data presented in the description;

Descriptions of the aspects of processes and features that affect radionuclide transport in the unsaturated zone are provided in the following sections as indicated: hydrology (Sections 6.1, 6.3.1, 6.4, 6.4.1), geology (Sections 6.3.2.3, 6.4.5), geochemistry (Section 6.3.2.3), design features (6.3.2.1, 6.4.1, 6.4.5), physical phenomena (6.1, 6.3.1, 6.4.1), and couplings (Sections 1, 7.2). The adequacy of these descriptions is demonstrated by their consistency with the available data. The methodology accounts for these factors at a level consistent with the available data and uncertainty, such that the potential for radionuclide transport in the unsaturated zone (UZ) is not underestimated. This includes the introduction of the fracture-matrix partitioning model, as discussed in Section 7.2, to address limitations in the available data and the potential effects of different flow patterns on radionuclide partitioning between the fractures and rock matrix upon existing the drift. Distributions for flow and transport parameters have been developed to account for the level of uncertainty in the available data, as discussed in Section 6.4.5.

(6) Guidance in NUREG-1297 and NUREG-1298 (Altman et al. 1988 [DIRS 103597] and [DIRS 103750]), or other acceptable approaches, is followed for peer review and data qualification.

This report was developed using processes and procedures consistent with the QARD, which commits to the requirements in NUREG-1297 and NUREG-1298. This report was developed in accordance with AP-SIII.10Q, *Models*, which implements those commitments for model reports.

Acceptance Criterion 2, Data are Sufficient for Model Justification.

(1) Geological, hydrological, and geochemical values, used in the license application, are adequately justified (e.g., flow-path length, sorption coefficients, retardation factors, colloid concentrations, etc.). Adequate descriptions of how the data were used, interpreted, and appropriately synthesized into the parameters are provided;

Data are sufficient to support the geological, hydrological, and geochemical values because they are based on supporting reports that define the model units, associated hydrological properties, and resulting flow field predictions. Specifically, the use of qualified fracture property data to determine fracture frequency and fracture porosity is discussed in Section 4.1.1, data on flow in the unsaturated zone are discussed in Section 4.1.2, a flow focusing factor for flow in fractures and other fracture hydrologic characteristics are discussed in Section 4.1.3, data for matrix porosity and permeability are discussed in Section 4.1.4, data used to develop a correlation between the matrix diffusion coefficient and the porosity and permeability of the rock matrix under saturated conditions are discussed in Section 4.1.5, data used for diffusion in the crushed tuff invert are discussed in Section 4.1.6, and design data used in the evaluation of transport from the invert to the rock is discussed in Section 4.1.7, Descriptions, of how the data are used, interpreted, and synthesized into parameters are given in Sections 4.1, 6.3.2.3 and 6.4.5. The results are adjusted to account for effects of scale between the mountain-scale flow model and the drift-scale phenomena considered in this report (Sections 6.3.3.1 and 6.4.5).

Acceptance Criterion 3, Data Uncertainty Is Characterized and Propagated through the Model Abstraction.

(1) Models use parameter values, assumed ranges, probability distributions, and bounding assumptions that are technically defensible, reasonably account for uncertainties and variabilities, and do not result in an under-representation of the risk estimate;

The parameters used are based on and consistent with available data from Yucca Mountain as presented in Sections 6.3.2.3 and 6.4.5. Section 6.3.5 contains discussions of how capillary pressure and relative permeability functions of saturation for the fracture and matrix continua are based on the van Genuchten relation; how the property set for dual-permeability flow and transport calculations was calibrated; how matrix diffusion and sorption parameters were characterized statistically to span the range of sorption behavior; how the free-water diffusion coefficient was derived from data; how the dispersive effects fracture-matrix interaction are explicitly modeled; and why parameters from the Site Recommendation are still valid for the drift-shadow model. Section 6.4.5 contains discussions of how data or relations were used to calculate the model parameters which represent the range of conditions expected across the waste emplacement location, i.e. fracture frequency, water flux and saturation, flow focusing, fracture residual saturation, diffusion coefficient for the invert, and diffusion coefficient in fractured rock. Uncertainties and variabilities in parameters are evaluated, reasonably accounted for, and adequately represented as discussed in Section 6.4.5 and Appendices A through I.

(2) For those radionuclides where the total system performance assessment abstraction indicates that transport in fractures and matrix in the unsaturated zone is important to waste isolation: (i) estimated flow and transport parameters are appropriate and valid, based on techniques that may include laboratory experiments, field measurements, natural analog research, and process-level modeling studies, conducted under conditions relevant to the unsaturated zone at Yucca Mountain; and (ii) models are demonstrated to adequately reproduce field transport test results. For example, if a sorption coefficient approach is used, the assumptions implicit in that approach are verified;

Two models are considered for transport in fractures and matrix: (1) the fracture-matrix partitioning model introduced in Section 6.1 and described in Section 6.4; and (2) the dual-permeability conceptual model described in Section 6.3. For both models, the estimated flow and transport parameters are appropriate and valid because they are based on and consistent with available data from Yucca Mountain, including field measurements for hydrological properties of fractures and laboratory measurements of the hydrological and transport properties of the rock matrix (Sections 6.3.2.3 and 6.4.5). Process-level modeling studies were conducted to calibrate some of the hydrological parameters as discussed in Section 4.1.

> (4) Uncertainty is adequately represented in parameter development for conceptual models, process-level models, and alternative conceptual models, considered in developing the abstraction of radionuclide transport in the unsaturated zone. This may be done either through sensitivity analyses or use of conservative limits;

Uncertainty is adequately represented in the model parameters used because they are based on and consistent with the scenarios and range of available data from Yucca Mountain. An extensive assessment of parameter uncertainties and variabilities was conducted and implemented in the model calculations to ensure that these factors are adequately represented in the model (see Sections 6.4.5, 6.4.6, and Appendices A through I).

> **Acceptance Criterion 4, Model Uncertainty Is Characterized and Propagated through the Model Abstraction.**
>
> (1) Alternative modeling approaches of features, events, and processes are considered and are consistent with available data and current scientific understanding, and the results and limitations are appropriately considered in the abstraction;

The alternative models of fracture-matrix partitioning and dual permeability are considered and are consistent with available data and current scientific understanding of observed features and processes. The results and limitations are appropriately considered in the abstraction, as described in Sections 6.3.1 and 6.4. This includes treatment of the effects of fractures both as a continuum and as discrete features and alternative representations of flow processes in fractures.

> (2) Conceptual model uncertainties are adequately defined and documented, and effects on conclusions regarding performance are properly assessed;

Conceptual model uncertainties are identified, principally in terms of the effects of fracture flow in the vicinity of the waste emplacement drift in Sections 6.3.1 and 6.4. The effects of these uncertainties on conclusions regarding performance are conservatively addressed in Sections 7 and 8.

> (3) Consideration of conceptual model uncertainty is consistent with available site characterization data, laboratory experiments, field measurements, natural analog information and process-level modeling studies; and the treatment of conceptual model uncertainty does not result in an under-representation of the risk estimate; and

Conceptual model uncertainty is addressed by considering the alternative models of fracture-matrix partitioning and dual permeability, which include standard flow and transport models for unsaturated rock that are consistent with available data and current scientific knowledge and conservative modeling methods intended to bound conceptual model uncertainties (Section 7 and 8). The fracture matrix alternative model is the more conservative of the two because it incorporates approximations which predict increased flow and transport in fractures beneath a waste emplacement drift, as discussed in Section 7.3. The more conservative representation between the alternative models is selected for use in downstream products such that the identified model uncertainty does not result in an underestimate of radionuclide transport (Sections 7 and 8).

> (4) Appropriate alternative modeling approaches are consistent with available data and current scientific knowledge, and appropriately consider their results and limitations, using tests and analyses that are sensitive to the processes modeled. For example, for radionuclide transport through fractures, the U.S. Department of Energy adequately considers alternative modeling approaches, to develop its understanding of fracture distributions and ranges of fracture flow and transport properties in the unsaturated zone.

Alternative modeling approaches are appropriate because they include standard flow and transport models for unsaturated rock that are consistent with available data and current scientific knowledge. These alternative models result in an understanding of fracture distributions, ranges of fracture flow, and transport properties in the unsaturated zone as discussed in Section 8. As discussed in Section 7.1, the drift shadow model accounts for the presence of fractures and a porous rock matrix by using a standard process-based description of unsaturated flow in a dual continuum, and model parameters are based on the drift-scale calibrated properties parameter set. As discussed in Section 7.2, the fracture-matrix partitioning model was developed to limit reliance on process descriptions of flow and transport in the fractures near a waste emplacement drift and incorporates approximations which conservatively predict increased flow and transport in fractures beneath a waste emplacement drift, as discussed in Section 7.3.

9. INPUTS AND REFERENCES

9.1 DOCUMENTS CITED

Abramowitz, M. and Stegun, I.A., eds. 1972. *Handbook of Mathematical Functions with Formulas, Graphs, and Mathematical Tables.* National Bureau of Standards, Applied Mathematics Series. 55, 1046. Washington, D.C.: U.S. Department of Commerce. TIC: 229060. 103280

Ahlers, C.F.; Finsterle, S.; and Bodvarsson, G.S. 1999. "Characterization and Prediction of Subsurface Pneumatic Response at Yucca Mountain, Nevada." *Journal of Contaminant Hydrology, 38,* (1-3), 47-68. New York, New York: Elsevier. TIC: 244160. 109715

Altman, W.D.; Donnelly, J.P.; and Kennedy, J.E. 1988. *Peer Review for High-Level Nuclear Waste Repositories: Generic Technical Position.* NUREG-1297. Washington, D.C.: U.S. Nuclear Regulatory Commission. TIC: 200651. 103597

Altman, W.D.; Donnelly, J.P.; and Kennedy, J.E. 1988. *Qualification of Existing Data for High-Level Nuclear Waste Repositories: Generic Technical Position.* NUREG-1298. Washington, D.C.: U.S. Nuclear Regulatory Commission. TIC: 200652. 103750

Bandurraga, T.M. and Bodvarsson, G.S. 1999. "Calibrating Hydrogeologic Parameters for the 3-D Site-Scale Unsaturated Zone Model of Yucca Mountain, Nevada." *Journal of Contaminant Hydrology, 38,* (1-3), 25-46. New York, New York: Elsevier. TIC: 244160. 103949

Bear, J. 1972. *Dynamics of Fluids in Porous Media.* Environmental Science Series. Biswas, A.K., ed. New York, New York: Elsevier. TIC: 217356. 156269

BSC (Bechtel SAIC Company) 2001. *Analysis of Hydrologic Properties Data.* ANL-NBS-HS-000002 REV 00 ICN 01. Las Vegas, Nevada: Bechtel SAIC Company. ACC: MOL.20020429.0296. 159725

BSC (Bechtel SAIC Company) 2001. *Calibrated Properties Model.* MDL-NBS-HS-000003 REV 00 ICN 01. Las Vegas, Nevada: Bechtel SAIC Company. ACC: MOL.20020311.0012. 161316

BSC (Bechtel SAIC Company) 2001. *Invert Diffusion Properties Model.* ANL-EBS-MD-000031 REV 01 ICN 01. Las Vegas, Nevada: Bechtel SAIC Company. ACC: MOL.20010801.0315. 156700

BSC (Bechtel SAIC Company) 2001. *Unsaturated Zone and Saturated Zone Transport Properties (U0100).* ANL-NBS-HS-000019 REV 00 ICN 02. Las Vegas, Nevada: Bechtel SAIC Company. ACC: MOL.20020311.0017. 160828

BSC (Bechtel SAIC Company) 2001. *UZ Flow Models and Submodels.* MDL-NBS-HS-000006 REV 00 ICN 01. Las Vegas, Nevada: Bechtel SAIC Company. ACC: MOL.20020417.0382. 158726

BSC (Bechtel SAIC Company) 2003. *Advection Versus Diffusion in the Invert.* ANL-EBS-MD-000063 REV 00. Las Vegas, Nevada: Bechtel SAIC Company. ACC: DOC.20040217.0004. 170881

BSC (Bechtel SAIC Company) 2003. *Analysis of Geochemical Data for the Unsaturated Zone.* ANL-NBS-HS-000017 REV 00 ICN 02, with errata. Las Vegas, Nevada: Bechtel SAIC Company. ACC: MOL.20020314.0051; DOC.20031015.0006. 168343

BSC (Bechtel SAIC Company) 2003. *Repository Design Project, Repository/PA IED Emplacement Drift Committed Materials (2).* 800-IED-WIS0-00302-000-00A. Las Vegas, Nevada: Bechtel SAIC Company. ACC: ENG.20030627.0004. 164101

BSC (Bechtel SAIC Company) 2004. *Abstraction of Drift Seepage.* MDL-NBS-HS-000019, Rev. 01. Las Vegas, Nevada: Bechtel SAIC Company. 169131

BSC (Bechtel SAIC Company) 2004. *Analysis of Hydrologic Properties Data.* ANL-NBS-HS-000042, Rev. 00. Las Vegas, Nevada: Bechtel SAIC Company. 170038

BSC (Bechtel SAIC Company) 2004. *Calibrated Properties Model.* MDL-NBS-HS-000003, Rev. 02. Las Vegas, Nevada: Bechtel SAIC Company. 169857

BSC (Bechtel SAIC Company) 2004. *Conceptual Model and Numerical Approaches for UZ Flow and Transport.* MDL-NBS-HS-000005 REV 01. Las Vegas, Nevada: Bechtel SAIC Company. 170035

BSC (Bechtel SAIC Company) 2004. *D&E / PA/C IED Emplacement Drift Configuration and Environment.* 800-IED-MGR0-00201-000-00B. Las Vegas, Nevada: Bechtel SAIC Company. ACC: ENG.20040326.0001. 168489

BSC (Bechtel SAIC Company) 2004. *D&E / PA/C IED Interlocking Drip Shield and Emplacement Pallet.* 800-IED-WIS0-00401-000-00D. Las Vegas, Nevada: Bechtel SAIC Company. ACC: ENG.20040503.0018. 169220

BSC (Bechtel SAIC Company) 2004. *D&E / PA/C IED Subsurface Facilities.* 800-IED-WIS0-00103-000-00A. Las Vegas, Nevada: Bechtel SAIC Company. ACC: ENG.20040309.0028. 168370

BSC (Bechtel SAIC Company) 2004. *Drift Scale THM Model.* MDL-NBS-HS-000017, Rev. 01. Las Vegas, Nevada: Bechtel SAIC Company. 169864

BSC (Bechtel SAIC Company) 2004. *Drift-Scale Coupled Processes (DST and TH Seepage) Models.* MDL-NBS-HS-000015, Rev. 01. Las Vegas, Nevada: Bechtel SAIC Company. 170338

BSC (Bechtel SAIC Company) 2004. *Drift-Scale THC Seepage Model.* MDL-NBS-HS-000001, Rev. 03. Las Vegas, Nevada: Bechtel SAIC Company. 169856

BSC (Bechtel SAIC Company) 2004. *EBS Radionuclide Transport Abstraction.* ANL-WIS-PA-000001, Rev. 01. Las Vegas, Nevada: Bechtel SAIC Company. 169868

BSC (Bechtel SAIC Company) 2004. *Features, Events, and Processes in UZ Flow and Transport.* ANL-NBS-MD-000001, Rev. 03. Las Vegas, Nevada: Bechtel SAIC Company. 170012

BSC (Bechtel SAIC Company) 2004. *In-Drift Natural Convection and Condensation.* MDL-EBS-MD-000001, Rev. 00. Las Vegas, Nevada: Bechtel SAIC Company. 164327

BSC (Bechtel SAIC Company) 2004. *Mountain-Scale Coupled Processes (TH/THC/THM).* MDL-NBS-HS-000007, Rev. 02. Las Vegas, Nevada: Bechtel SAIC Company. 169866

BSC (Bechtel SAIC Company) 2004. *Multiscale Thermohydrologic Model.* ANL-EBS-MD-000049, Rev. 02. Las Vegas, Nevada: Bechtel SAIC Company. 169565

BSC (Bechtel SAIC Company) 2004. *Natural Analogue Synthesis Report.* TDR-NBS-GS-000027 REV 01. Las Vegas, Nevada: Bechtel SAIC Company. ACC: DOC.20040524.0008. 169218

BSC (Bechtel SAIC Company) 2004. *Particle Tracking Model and Abstraction of Transport Process.* MDL-NBS-HS-000020, Rev. 01. Las Vegas, Nevada: Bechtel SAIC Company. 170041

BSC (Bechtel SAIC Company) 2004. *Postclosure Modeling and Analyses Design Parameters.* TDR-MGR-MD-000037 REV 00. Las Vegas, Nevada: Bechtel SAIC Company. 169885

BSC (Bechtel SAIC Company) 2004. *Q-List.* 000-30R-MGR0-00500-000-000 REV 00. Las Vegas, Nevada: Bechtel SAIC Company. ACC: ENG.20040721.0007. 168361

BSC (Bechtel SAIC Company) 2004. *Radionuclide Transport Models Under Ambient Conditions.* MDL-NBS-HS-000008, Rev. 02. Las Vegas, Nevada: Bechtel SAIC Company. 164500

BSC (Bechtel SAIC Company) 2004. *Saturated Zone Flow and Transport Model Abstraction.* MDL-NBS-HS-000021, Rev. 02. Las Vegas, Nevada: Bechtel SAIC Company. 170042

BSC (Bechtel SAIC Company) 2004. *Seepage Calibration Model and Seepage Testing Data.* MDL-NBS-HS-000004, Rev. 03. Las Vegas, Nevada: Bechtel SAIC Company. 170034

BSC (Bechtel SAIC Company) 2004. *Seepage Model for PA Including Drift Collapse.* MDL-NBS-HS-000002, Rev. 03. Las Vegas, Nevada: Bechtel SAIC Company. 167652

BSC (Bechtel SAIC Company) 2004. *Simulation of Net Infiltration for Present-Day and Potential Future Climates.* MDL-NBS-HS-000023, Rev. 00. Las Vegas, Nevada: Bechtel SAIC Company. 170007

BSC (Bechtel SAIC Company) 2004. *Technical Work Plan for: Regulatory Integration Evaluation of Analysis and Model Reports Supporting the TSPA-LA.* TWP-MGR-PA-000014 REV 00. Las Vegas, Nevada: Bechtel SAIC Company. ACC: DOC.20040408.0004. 169377

BSC (Bechtel SAIC Company) 2004. *Technical Work Plan for: Unsaturated Zone Transport Model Report Integration.* TWP-MGR-HS-000002 REV 00 ICN 01. Las Vegas, Nevada: Bechtel SAIC Company. ACC: DOC.20040816.0001. 171282

BSC (Bechtel SAIC Company) 2004. *UZ Flow Models and Submodels.* MDL-NBS-HS-000006, Rev. 02. Las Vegas, Nevada: Bechtel SAIC Company. 169861

Canori, G.F. and Leitner, M.M. 2003. *Project Requirements Document.* TER-MGR-MD-000001 REV 02. Las Vegas, Nevada: Bechtel SAIC Company. ACC: DOC.20031222.0006. 166275

Conca, J.L. and Wright, J. 1990. "Diffusion Coefficients in Gravel Under Unsaturated Conditions." *Water Resources Research, 26,* (5), 1055-1066. Washington, D.C.: American Geophysical Union. TIC: 237421. 101582

Crank, J. 1975. *The Mathematics of Diffusion.* 2nd Edition. 1983 Reprint. Oxford, England: Clarendon Press. TIC: 9662. 122990

CRWMS M&O 2000. *Invert Configuration and Drip Shield Interface.* TDR-EDS-ST-000001 REV 00. Las Vegas, Nevada: CRWMS M&O. ACC: MOL.20000505.0232. 136255

CRWMS M&O 2000. *Total System Performance Assessment for the Site Recommendation.* TDR-WIS-PA-000001 REV 00 ICN 01. Las Vegas, Nevada: CRWMS M&O. ACC: MOL.20001220.0045. 153246

Dombrowski, H.S. and Brownell, L.E. 1954. "Residual Equilibrium Saturation of Porous Media." *Industrial & Engineering Chemistry, 46,* (6), 1207-1219. Easton, Pennsylvania: American Chemical Society. TIC: 254309. 163222

Dullien, F.A.L.; Lai, F.S.Y.; and MacDonald, I.F. 1986. "Hydraulic Continuity of Residual Wetting Phase in Porous Media." *Journal of Colloid and Interface Science, 109,* (1), 201-218. New York, New York: Academic Press. TIC: 254308. 163221

Finsterle, S.; Ahlers, C.F.; Trautz, R.C.; and Cook, P.J. 2003. "Inverse and Predictive Modeling of Seepage into Underground Openings." *Journal of Contaminant Hydrology, 62-63,* 89-109. New York, New York: Elsevier. TIC: 254205. 163214

Freeze, G.A.; Brodsky, N.S.; and Swift, P.N. 2001. *The Development of Information Catalogued in REV00 of the YMP FEP Database.* TDR-WIS-MD-000003 REV 00 ICN 01. Las Vegas, Nevada: Bechtel SAIC Company. ACC: MOL.20010301.0237. 154365

Freeze, R.A. and Cherry, J.A. 1979. *Groundwater.* Englewood Cliffs, New Jersey: Prentice-Hall. TIC: 217571. 101173

Hilf, J.W. 1975. "Compacted Fill." Chapter 7 of *Foundation Engineering Handbook.* Winterkorn, H.F. and Fang, H.-Y., eds. New York, New York: Van Nostrand Reinhold. TIC: 248400. 169699

Hogg, R.V. and Craig, A.T. 1978. *Introduction to Mathematical Statistics.* 4th Edition. New York, New York: Macmillan. TIC: 254311. 163236

Houseworth, J. 2003. UZ PMR for SR - Shadow Zone. Scientific Notebook SN-LBNL-SCI-205-V1. ACC: MOL.20030319.0086. 163233

Houseworth, J.E.; Finsterle, S.; and Bodvarsson, G.S. 2003. "Flow and Transport in the Drift Shadow in a Dual-Continuum Model." *Journal of Contaminant Hydrology, 62-63,* 133-156. New York, New York: Elsevier. TIC: 254205. 164394

Li, G. and Tsang, C-F. 2003. "Seepage into Drifts with Mechanical Degradation." *Journal of Contaminant Hydrology, 62-63,* 157-172. New York, New York: Elsevier. TIC: 254205. 163714

Liu, H.H.; Doughty, C.; and Bodvarsson, G.S. 1998. "An Active Fracture Model for Unsaturated Flow and Transport in Fractured Rocks." *Water Resources Research, 34,* (10), 2633-2646. Washington, D.C.: American Geophysical Union. TIC: 243012. 105729

Moridis, G.J.; Wu, Y-S.; and Pruess, K. 1999. *EOS9nT: A TOUGH2 Module for the Simulation of Water Flow and Solute/Colloid Transport in the Subsurface.* LBNL-42351. Berkeley, California: Lawrence Berkeley National Laboratory. TIC: 246520. 123093

Newman, J. 1973. *Electrochemical Systems.* Englewood Cliffs, New Jersey: Prentice-Hall. TIC: 210201. 148719

NRC (U.S. Nuclear Regulatory Commission) 2003. *Yucca Mountain Review Plan, Final Report.* NUREG-1804, Rev. 2. Washington, D.C.: U.S. Nuclear Regulatory Commission, Office of Nuclear Material Safety and Safeguards. TIC: 254568. 163274

Philip, J.R.; Knight, J.H.; and Waechter, R.T. 1989. "Unsaturated Seepage and Subterranean Holes: Conspectus, and Exclusion Problem for Circular Cylindrical Cavities." *Water Resources Research, 25,* (1), 16-28. Washington, D.C.: American Geophysical Union. TIC: 239117. 105743

Pruess, K.; Oldenburg, C.; and Moridis, G. 1999. *TOUGH2 User's Guide, Version 2.0.* LBNL-43134. Berkeley, California: Lawrence Berkeley National Laboratory. TIC: 253038. 160778

Reimus, P.W.; Ware, S.D.; Benedict, F.C.; Warren, R.G.; Humphrey, A.; Adams, A.; Wilson, B.; and Gonzales, D. 2002. *Diffusive and Advective Transport of ^{3}H, ^{14}C, and ^{99}Tc in Saturated, Fractured Volcanic Rocks from Pahute Mesa, Nevada.* LA-13891-MS. Los Alamos, New Mexico: Los Alamos National Laboratory. TIC: 253905. 163008

Richards, L.A. 1931. "Capillary Conduction of Liquids Through Porous Mediums." *Physics, 1,* 318-333. [New York, New York: American Physical Society]. TIC: 225383. 104252

Sato, H.; Yui, M.; and Yoshikawa, H. 1996. "Ionic Diffusion Coefficients of Cs+, Pb^{2}}+, Sm^{3}+, Ni^{2}+, SeO^{2-4} and TcO^{-4} in Free Water Determined from Conductivity Measurements." *Journal of Nuclear Science and Technology, 33,* (12), 950-955. Tokyo, Japan: Atomic Energy Society of Japan. TIC: 254307. 163213

Sato, S.; Otsuka, T.; Kuroda, Y.; Higashihara, T.; and Ohashi, H. 2001. "Diffusion of Helium in Water-Saturated, Compacted Sodium Montmorillonite." *Journal of Nuclear Science and Technology, 38,* (7), 577-580. [Tokyo, Japan: Atomic Energy Society of Japan]. TIC: 254463. 164047

van Genuchten, M.T. 1980. "A Closed-Form Equation for Predicting the Hydraulic Conductivity of Unsaturated Soils." *Soil Science Society of America Journal, 44,* (5), 892-898. Madison, Wisconsin: Soil Science Society of America. TIC: 217327. 100610

Wang, J.S. 2003. "Scientific Notebooks Referenced in Model Report U0230 Drift-Scale Radionuclide Transport MDL-NBS-HS-000016 REV 00." Interoffice correspondence from J.S. Wang (BSC) to File, August 18, 2003, with attachments. ACC: MOL.20030818.0293. 163234

Wang, J.S.Y. and Bodvarsson, G.S. 2003. "Evolution of the Unsaturated Zone Testing at Yucca Mountain." *Journal of Contaminant Hydrology, 62-63,* 337-360. New York, New York: Elsevier. TIC: 254205. 163215

Weast, R.C. and Astle, M.J., eds. 1979. *CRC Handbook of Chemistry and Physics.* 60th Edition. 2nd Printing 1980. Boca Raton, Florida: CRC Press. TIC: 245312. 102865

Weinberger, H.F. 1965. *A First Course in Partial Differential Equations.* New York, New York: John Wiley & Sons. TIC: 254310. 163216

9.2 CODES, STANDARDS, REGULATIONS, AND PROCEDURES

10 CFR 63. Energy: Disposal of High-Level Radioactive Wastes in a Geologic Repository at Yucca Mountain, Nevada. Readily available. 156605

AP-2.22Q, Rev. 1. *Classification Analyses and Maintenance of the Q-List*. Washington, D.C.: U.S. Department of Energy, Office of Civilian Radioactive Waste Management. ACC: DOC.20030807.0002.

AP-2.27Q, Rev. 1, ICN 4. *Planning for Science Activities*. Washington, D.C.: U.S. Department of Energy, Office of Civilian Radioactive Waste Management. ACC: DOC.20040610.0006.

AP-SI.1Q, Rev. 5, ICN 1. *Software Management.* Washington, D.C.: U.S. Department of Energy, Office of Civilian Radioactive Waste Management. ACC: DOC.20030708.0001.

AP-SIII.10Q, Rev. 2, ICN 7. *Models.* Washington, D.C.: U.S. Department of Energy, Office of Civilian Radioactive Waste Management. ACC: DOC.20040920.0002.

9.3 SOURCE DATA, LISTED BY DATA TRACKING NUMBER

LA0003AM831341.001. Probability Distributions for Sorption Coefficients (Kd's). Submittal date: 03/29/2000. 148751

LA0003JC831362.001. Preliminary Matrix Diffusion Coefficients for Yucca Mountain Tuffs. Submittal date: 4/10/2000. 149557

LB0205REVUZPRP.001. Fracture Properties for UZ Model Layers Developed from Field Data. Submittal date: 05/14/2002. 159525

LB0207REVUZPRP.002. Matrix Properties for UZ Model Layers Developed from Field and Laboratory Data. Submittal date: 07/15/2002. 159672

LB0208UZDSCPLI.002. Drift-Scale Calibrated Property Sets: Lower Infiltration Data Summary. Submittal date: 08/26/2002. 161788

LB0208UZDSCPMI.002. Drift-Scale Calibrated Property Sets: Mean Infiltration Data Summary. Submittal date: 08/26/2002. 161243

LB0210THRMLPRP.001. Thermal Properties of UZ Model Layers: Data Summary. Submittal date: 10/25/2002. 160799

LB03023DSSCP9I.001. 3-D Site Scale UZ Flow Field Simulations for 9 Infiltration Scenarios. Submittal date: 02/28/2003. 163044

LB0302UZDSCPUI.002. Drift-Scale Calibrated Property Sets: Upper Infiltration Data Summary. Submittal date: 02/05/2003. 161787

LB03033DUZTRAN.001. TC and NP Distributions/Transport in UZ Flow-Fields. Submittal date: 03/28/2003. 170372

LB0406U0075FCS.002. Flow Focusing in Heterogeneous Fractured Rock: Summaries. Submittal date: 06/30/2004. 170712

LB990861233129.001. Drift Scale Calibrated 1-D Property Set, FY99. Submittal date: 08/06/1999. 110226

LB997141233129.001. Calibrated Basecase Infiltration 1-D Parameter Set for the UZ Flow and Transport Model, FY99. Submittal date: 07/21/1999. 104055

MO0407SEPFEPLA.000. LA FEP List. Submittal date: 07/20/2004. 170760

SN0306T0502103.006. Data Spreadsheets to Support Parameter Uncertainty Development. Submittal date: 06/05/2003. 163944

9.4 OUTPUT DATA, LISTED BY DATA TRACKING NUMBER

LB0307DSRADTRN.001. Drift Shadow Model: Simulations. Submittal date: 07/24/2003.

LB0307DSRADTRN.002. Drift Shadow Model: Data Summaries. Submittal date: 07/24/2003.

LB0307FMRADTRN.001. Fracture-Matrix Partitioning Model: Spreadsheet Calculations. Submittal date: 07/31/2003.

9.5 SOFTWARE CODES

LBNL (Lawrence Berkeley National Laboratory) 1999. *Software Code: EXT.* V1.0. Sun. 10047-1.0-00. 134141

LBNL (Lawrence Berkeley National Laboratory) 1999. *Software Code: iTOUGH2.* V4.0. SUN, DEC. 10003-4.0-00. 139918

LBNL (Lawrence Berkeley National Laboratory) 1999. *Software Code: TOUGH2.* V1.11 MEOS9nTV1.0. MAC, SUN, DEC/Alpha, PC. 10065-1.11MEOS9NTV1.0-00. 113943

LBNL (Lawrence Berkeley National Laboratory) 2000. *Software Routine: AddBound.* V1.0. SUN w/Unix OS. 10357-1.0-00. 152823

LBNL (Lawrence Berkeley National Laboratory) 2000. *Software Routine: CutDrift.* V1.0. SUN w/Unix OS. 10375-1.0-00. 152816

APPENDIX A

SAMPLING FOR FRACTURE FREQUENCY (OR FRACTURE SPACING)

SAMPLING FOR FRACTURE FREQUENCY (OR FRACTURE SPACING)

This appendix provides additional information pertaining to Section 6.4.5 of the main text. Fracture frequency sampling uses the mean and standard deviations as given in Table A-1. The standard deviations for the tsw35 and tsw36 units are computed using the correlation shown in Figure 6-21. The mean and standard deviation for the natural logarithm of *f* is related to the mean and standard deviation for *f* through the following relationships (Hogg and Craig 1978 [DIRS 163236], pp. 180 and 432) (see Appendix K for detailed derivation):

$$\mu_{\ln(f)} = \ln\left(\mu_f\right) - \frac{1}{2}\ln\left(1 + \frac{\sigma_f^2}{\mu_f^2}\right) \quad \text{(Eq. A-1)}$$

$$\sigma_{\ln(f)} = \sqrt{\ln\left(1 + \frac{\sigma_f^2}{\mu_f^2}\right)} \quad \text{(Eq. A-2)}$$

Table A-1. Fracture Frequency and Standard Deviation

	Frequency (m^{-1})	Std Dev Frequency (m^{-1})	Equation A-1	Equation A-2
UZ Model Layer	μ_f	σ_f	$\mu_{\ln(f)}$	$\sigma_{\ln(f)}$
tsw33	0.81	1.03	-0.692	0.981
tsw34	4.32	3.42	1.22	0.698
tsw35	3.16	2.63	0.887	0.725
tsw3[67]	4.02	3.34	1.13	0.725

DTN: LB0205REVUZPRP.001 [DIRS 159525].
Output DTN: LB0307FMRADTRN.001.

The sampling for the lognormal distribution uses the rational approximation of the inverse cumulative probability distribution for a Gaussian random variable as given in Equation 26.2.23 of *Handbook of Mathematical Functions with Formulas, Graphs, and Mathematical Tables* (Abramowitz and Stegun 1972 [DIRS 103280]). See Scientific Notebook by Wang (2003 [DIRS 163234], SN-LBNL-SCI-236-V1, pp. 40–42) for a discussion of the generation of Gaussian random numbers. Table A-2 presents a portion of the output from the formulation as performed in an Excel spreadsheet for the tsw35 model unit. See Wang (2003 [DIRS 163234], SN-LBNL-SCI-236-V1, p. 46) and Output-DTN: LB0307FMRADTRN.001 for the complete output.

The sequence of calculations is as follows:

Column A: Uniform random numbers generated by the Excel spreadsheet function RAND() and saved. These are the cumulative probabilities, *p*.

Column B: The normalized Gaussian random number corresponding to the cumulative probability in Column A.

Column C: The corresponding random natural logarithm of fracture frequency is derived from the normalized Gaussian random variable through the normalization definition:

$$f = x_p \sigma_{\ln(f)} + \mu_{\ln(f)} \quad \text{(Eq. A-3)}$$

where $\mu_{\ln(f)}$ and $\sigma_{\ln(f)}$ are defined in Equations A-1 and A-2.

In Excel, this is

Crn=Brn*Irn+Hrn

Column D: This column calculates the fracture frequency through the identity

$$f = \exp(\ln(f)) \quad \text{(Eq. A-4)}$$

In Excel, this is

Drn=exp(Crn)

Column E: The fracture half-spacing, in millimeters, is computed from the fracture frequency based on the relationship

$$h_f = \frac{1000}{2f} \quad \text{(Eq. A-5)}$$

In Excel, this is

Ern=1000/(2*Drn)

Column F: Uniform random numbers generated by the Excel spreadsheet function RAND() and saved.

Column G: The distance beneath the drift where fracture flow occurs, in millimeters, is defined by a uniform random distribution between 0 and the fracture spacing. Therefore, this is just the uniform random number between 0 and 1 in Column O, multiplied by the corresponding fracture spacing. In Excel, this is

Grn=2*Ern*Frn

Column H: Contains the value of $\mu_{\ln(f)}$ as computed from Equation A-1

Column I: Contains the value of $\sigma_{\ln(f)}$ as computed from Equation A-2.

Table A-2. Fracture Frequency and Spacing in the tsw35

	A	B	C	D	E	F	G	H	I
1	Fixed Uniform Random Number (P)	xP - norm. Gaussian random number	x – Gaussian random number	Fracture frequency (m-1)	Fracture Half-Spacing (mm)	Fixed Uniform Random Number (P)	Distance for fracture flow beneath drift (mm)	mean ln(f) tsw35	Standard deviation ln(f) tsw35
2	5.8511E-01	2.1459E-01	1.04E+00	2.84E+00	1.76E+02	4.5126E-01	1.59E+02	8.87E-01	7.25E-01
3	5.4439E-01	1.1124E-01	9.68E-01	2.63E+00	1.90E+02	9.1458E-01	3.48E+02		
4	6.4091E-01	3.6045E-01	1.15E+00	3.15E+00	1.59E+02	3.3211E-01	1.05E+02		
5	5.9792E-01	2.4755E-01	1.07E+00	2.91E+00	1.72E+02	8.5178E-01	2.93E+02		
6	3.5424E-01	-3.7345E-01	6.16E-01	1.85E+00	2.70E+02	5.2193E-01	2.82E+02		
7	2.0906E-01	-8.0950E-01	3.00E-01	1.35E+00	3.70E+02	6.2457E-02	4.63E+01		
8	3.6657E-01	-3.4052E-01	6.40E-01	1.90E+00	2.64E+02	6.0227E-01	3.18E+02		
9	2.4803E-01	-6.8040E-01	3.94E-01	1.48E+00	3.37E+02	9.8595E-02	6.65E+01		
10	1.3127E-01	-1.1205E+00	7.47E-02	1.08E+00	4.64E+02	5.1294E-01	4.76E+02		
11	3.9488E-01	-2.6619E-01	6.94E-01	2.00E+00	2.50E+02	7.5245E-01	3.76E+02		
12	3.5507E-01	-3.7123E-01	6.18E-01	1.85E+00	2.70E+02	5.5208E-02	2.98E+01		
13	3.2690E-01	-4.4805E-01	5.62E-01	1.75E+00	2.85E+02	4.1146E-01	2.35E+02		
14	7.3161E-01	6.1735E-01	1.33E+00	3.80E+00	1.32E+02	1.6819E-01	4.43E+01		
15	3.7473E-01	-3.1891E-01	6.56E-01	1.93E+00	2.60E+02	1.0001E-03	5.19E-01		
16	4.3275E-01	-1.6904E-01	7.64E-01	2.15E+00	2.33E+02	3.3327E-02	1.55E+01		
17	2.2638E-01	-7.5058E-01	3.43E-01	1.41E+00	3.55E+02	5.1599E-01	3.66E+02		
18	4.8791E-01	-3.0228E-02	8.65E-01	2.38E+00	2.11E+02	7.7558E-01	3.27E+02		
19	9.6566E-01	1.8210E+00	2.21E+00	9.09E+00	5.50E+01	1.4702E-01	1.62E+01		
20	9.9064E-01	2.3515E+00	2.59E+00	1.34E+01	3.74E+01	7.1911E-02	5.38E+00		
21	7.6046E-01	7.0750E-01	1.40E+00	4.05E+00	1.23E+02	4.8032E-01	1.18E+02		
22	6.5544E-01	3.9961E-01	1.18E+00	3.24E+00	1.54E+02	4.3202E-01	1.33E+02		
23	2.8080E-01	-5.8009E-01	4.66E-01	1.59E+00	3.14E+02	6.6853E-02	4.19E+01		
24	9.7585E-01	1.9751E+00	2.32E+00	1.02E+01	4.92E+01	7.7782E-01	7.65E+01		
25	9.9035E-01	2.3403E+00	2.58E+00	1.32E+01	3.77E+01	1.9658E-01	1.48E+01		
26	4.8014E-01	-4.9667E-02	8.51E-01	2.34E+00	2.13E+02	8.7179E-01	3.72E+02		
27	6.7670E-01	4.5806E-01	1.22E+00	3.38E+00	1.48E+02	1.0364E-01	3.06E+01		
28	6.7628E-02	-1.4940E+00	-1.96E-01	8.22E-01	6.08E+02	5.7641E-02	7.01E+01		
29	3.8513E-01	-2.9160E-01	6.76E-01	1.97E+00	2.54E+02	3.0107E-01	1.53E+02		
30	6.0259E-01	2.5965E-01	1.08E+00	2.93E+00	1.71E+02	9.8363E-01	3.36E+02		

Output DTN: LB0307FMRADTRN.001.

INTENTIONALLY LEFT BLANK

APPENDIX B

FRACTURE AND MATRIX FLUXES AND WATER SATURATIONS

FRACTURE AND MATRIX FLUXES AND WATER SATURATIONS

This appendix provides additional information pertaining to Section 6.4.5 of the main text. Fracture and matrix water saturations and fluxes and matrix relative permeabilities are available from the UZ Flow Model results. As discussed in Section 4.1.2, the lower, mean, and upper infiltration scenarios for the glacial transition climate are evaluated. Table B-1 gives an example of the fluxes, saturations, and matrix relative permeabilities for mean infiltration scenario for model grid cells within the waste emplacement horizon, excluding fault zones. The values are arranged by rock unit (tsw33, tsw34, tsw35, and tsw36). The flux for a given cell is a vector with three components; therefore, the component with the maximum fracture flux (and corresponding matrix flux) was selected for each cell. See Scientific Notebook by Wang (2003 [DIRS 163234], SN-LBNL-SCI-236-V1, pp. 47–52) for a discussion of how these values were extracted from the 3-D flow fields. Table B-1 gives a portion of the values extracted for the tsw33 and tsw34 model units. See Wang (2003 [DIRS 163234], SN-LBNL-SCI-236-V1, pp. 50–53) and Output-DTN: LB0307FMRADTRN.001 for the complete output.

The matrix saturations and matrix relative permeabilities as presented here may be used as input for the TSPA to support the EBS Radionuclide Transport Model [*EBS Radionuclide Transport Abstraction* BSC 2004 [DIRS 169868])]. This is contained in the *Flow and Saturation Data from UZ Flow Model.xls* spreadsheet in the output DTN: LB0307FMRADTRN.001.

Table B-1. Fracture and Matrix Fluxes, Saturations, and Matrix Relative Permeability—Glacial Transition Mean

	A	B	C	D	E	F	G	H
1	Rock Unit	Fracture Cell Name	Fracture Flux (mm/yr)	Fracture Saturation	Matrix Cell Name	Matrix Flux (mm/yr)	Matrix Saturation	Matrix Relative Permeability
2	tsw33	F012Bl76	5.3967E+00	1.3240E-02	M012Bl76	2.4032E-01	9.3761E-01	1.1223E-01
3	tsw33	F012Bl78	5.7350E+00	1.3264E-02	M012Bl78	1.4520E-01	9.0879E-01	7.1708E-02
4	tsw33	F012Cl72	4.8155E+00	1.3061E-02	M012Cl72	1.3236E+00	9.9786E-01	5.4681E-01
5	tsw33	F012Cl74	6.6185E+00	1.3454E-02	M012Cl74	5.1798E-01	9.7267E-01	2.1822E-01
6	tsw33	F012Cm70	9.7583E+00	1.3937E-02	M012Cm70	5.0937E-01	9.7432E-01	2.2678E-01
7	tsw33	F012Dg58	1.0083E+01	1.4374E-02	M012Dg58	2.2577E-01	9.3205E-01	1.0250E-01
8	tsw33	F012Dl68	1.3328E+01	1.4453E-02	M012Dl68	5.3696E-01	9.7656E-01	2.3933E-01
9	tsw33	F012Dl70	6.9879E+00	1.3254E-02	M012Dl70	5.5948E-01	9.7693E-01	2.4154E-01
10	tsw33	F012Dl71	3.5104E+00	1.2386E-02	M012Dl71	1.2656E+00	9.9586E-01	4.7057E-01
11	tsw33	F012Dl75	4.4996E+00	1.2746E-02	M012Dl75	2.6302E-01	9.4760E-01	1.3303E-01
12	tsw33	F012Dl77	4.2020E+00	1.2657E-02	M012Dl77	2.1155E-01	9.3789E-01	1.1275E-01
13	tsw33	F012Dl79	5.5142E+00	1.3038E-02	M012Dl79	4.4544E-01	9.6898E-01	2.0103E-01
14	tsw33	F012Ef89	1.8602E+01	1.4758E-02	M012Ef89	1.4086E-01	9.5004E-01	1.3891E-01
15	tsw33	F012Eg 2	1.5102E+01	1.5319E-02	M012Eg 2	1.1983E-01	9.2449E-01	9.0951E-02
16	tsw33	F012Eg14	4.0953E+00	1.2794E-02	M012Eg14	5.8384E-02	9.0131E-01	6.4266E-02
17	tsw33	F012Eg25	4.2045E+00	1.2854E-02	M012Eg25	5.3101E-02	8.5649E-01	3.4394E-02
18	tsw33	F012Eg36	6.6068E+00	1.3531E-02	M012Eg36	1.1091E-01	9.1961E-01	8.4365E-02
19	tsw33	F012Eg47	7.4195E+00	1.3779E-02	M012Eg47	1.6404E-01	9.1500E-01	7.8658E-02
20	tsw33	F012Eh 1	2.5267E+01	1.6781E-02	M012Eh 1	1.8512E-01	9.3937E-01	1.1556E-01
21	tsw33	F012El73	4.1465E+00	1.2600E-02	M012El73	4.8153E-01	9.7170E-01	2.1347E-01
22	tsw33	F012Fg26	4.5607E+00	1.2340E-02	M012Fg26	1.0880E-01	9.4168E-01	1.2012E-01

Table B-1. Fracture and Matrix Fluxes, Saturations, and Matrix Relative Permeability—Glacial Transition Mean (Continued)

	A	B	C	D	E	F	G	H
	Rock Unit	**Fracture Cell Name**	**Fracture Flux (mm/yr)**	**Fracture Saturation**	**Matrix Cell Name**	**Matrix Flux (mm/yr)**	**Matrix Saturation**	**Matrix Relative Permeability**
23	tsw33	F012Fg59	3.4216E+01	1.6465E-02	M012Fg59	3.2473E-01	9.6741E-01	1.9434E-01
24	tsw33	F012Fg70	3.3638E+01	1.6356E-02	M012Fg70	2.1330E-01	9.5857E-01	1.6265E-01
25	tsw33	F012Fg80	2.0564E+01	1.6174E-02	M012Fg80	1.4723E-01	9.3185E-01	1.0217E-01
26	tsw33	F012Fg90	1.9384E+01	1.6000E-02	M012Fg90	1.3500E-01	9.2880E-01	9.7324E-02
27	tsw34	F0013g 3	3.5168E+00	1.4929E-02	M0013g 3	1.2727E-02	9.5988E-01	2.0111E-01
28	tsw34	F0013g48	2.6890E+01	2.2664E-02	M0013g48	1.5652E-02	9.7120E-01	2.5171E-01
29	tsw34	F0013g91	1.4310E+01	1.9454E-02	M0013g91	1.4594E-02	9.6798E-01	2.3541E-01
30	tsw34	F0013h 2	9.6354E+00	1.9077E-02	M0013h 2	6.9779E-02	9.6752E-01	2.3319E-01

Output DTN: LB0307FMRADTRN.001.

APPENDIX C

SAMPLING FOR FLOW FOCUSING FACTOR

SAMPLING FOR FLOW FOCUSING FACTOR

This appendix provides additional information pertaining to Section 6.4.5 of the main text. The cumulative probability distribution for the flow-focusing factor is given by BSC (2004 [DIRS 167652], Figure 6-26; DTN: LB0406U0075FCS.002 [DIRS 170712]):

$$P = -0.3137F^4 + 5.4998F^3 - 35.66F^2 + 102.3F - 11.434 \qquad \text{(Eq. C-1)}$$

where F is the flow-focusing factor and P is the cumulative probability in as a percentage. The correlation is limited to a range of F between approximately 0.12 to 5. The equation is evaluated and interpolated to evenly spaced values of P, 1, 2, 3, …, 100. Then, the factor is sampled using a uniform random number scaled between 1 and 100 and truncated to an integer. This factor does not depend on any particular properties of the host rock. Table C-1 presents a portion of the output from the formulation as performed in an Excel spreadsheet. See Wang (2003 [DIRS 163234], SN-LBNL-SCI-236-V1, p. 54) and DTN: LB0307FMRADTRN.001 for the complete output.

The flow-focusing factor as presented here may be used as input for the TSPA to support the EBS Radionuclide Transport Model [*EBS Radionuclide Transport Abstraction* BSC 2004 [DIRS 169868])]. This is contained in the *Flow Focusing Factor.xls* spreadsheet in the output DTN: LB0307FMRADTRN.001.

The sequence of calculations are described here:

Column A: This column contains a series of values for the normalized flux generated between 0.12 and 5.02.

Column B: The cumulative probability is computed from the relationship given in Equation C-1. In Excel, this is calculated as

Brn=-11.434 +102.3*Arn-35.66*Arn^2+5.4998*Arn^3-0.3137*Arn^4

Column C: A series of evenly spaced values of the cumulative probability.

Column D: The normalized flux is interpolated to the evenly spaced values in Column C. This is done using the following Excel formula:

Drn=Arn+(Crn-Brn)*((A(rn+1)-Arn)/(B(rn+1)-Brn))

Column E: A uniform random number between 1 and 100 is used to randomly select a normalized flux. The Excel formula is

Ern=1+99*RAND(),

which is copied and saved in Column E.

Column F: Round off the random number to an integer. The Excel formula is

Frn=ROUND(Ern,0)

Column G: Use the random integer to find the corresponding normalized flux. The Excel formula is

Grn=INDEX(D$3:D$103,Frn)

Table C-1. Flow-Focusing Factor

	A	B	C	D	E	F	G
1	Normalized Flux	Cumulative Probability (%)	Cumulative Probability (%)	Interpolated Normalized Flux	Fixed Uniform Random Number	Uniform Random Integer	Flow Focusing Factor
2	1.16E-01	8.81E-07	0.00E+00	1.16E-01	7.8382E+01	78	1.47E+00
3	1.20E-01	3.38E-01	1.00E+00	1.27E-01	9.1213E+01	91	2.10E+00
4	1.30E-01	1.27E+00	2.00E+00	1.38E-01	5.2710E+01	53	8.51E-01
5	1.40E-01	2.20E+00	3.00E+00	1.49E-01	6.2073E+01	62	1.04E+00
6	1.50E-01	3.13E+00	4.00E+00	1.60E-01	3.7861E+01	38	5.96E-01
7	1.60E-01	4.04E+00	5.00E+00	1.71E-01	2.6944E+01	27	4.38E-01
8	1.80E-01	5.86E+00	6.00E+00	1.82E-01	2.0972E+01	21	3.60E-01
9	1.90E-01	6.75E+00	7.00E+00	1.93E-01	5.6278E+01	56	9.09E-01
10	2.00E-01	7.64E+00	8.00E+00	2.04E-01	8.8144E+01	88	1.91E+00
11	2.10E-01	8.53E+00	9.00E+00	2.15E-01	8.6708E+01	87	1.85E+00
12	2.20E-01	9.40E+00	1.00E+01	2.27E-01	8.6516E+00	9	2.15E-01
13	2.30E-01	1.03E+01	1.10E+01	2.38E-01	8.9982E+01	90	2.03E+00
14	2.40E-01	1.11E+01	1.20E+01	2.50E-01	6.3578E+01	64	1.08E+00
15	2.60E-01	1.28E+01	1.30E+01	2.62E-01	5.0222E+01	50	7.95E-01
16	2.70E-01	1.37E+01	1.40E+01	2.74E-01	5.7781E+01	58	9.49E-01
17	2.80E-01	1.45E+01	1.50E+01	2.86E-01	3.7505E+01	38	5.96E-01
18	2.90E-01	1.54E+01	1.60E+01	2.98E-01	4.0043E+01	40	6.27E-01
19	3.00E-01	1.62E+01	1.70E+01	3.10E-01	1.1477E+01	11	2.38E-01
20	3.10E-01	1.70E+01	1.80E+01	3.22E-01	3.7317E+00	4	1.60E-01
21	3.30E-01	1.86E+01	1.90E+01	3.35E-01	4.9257E+00	5	1.71E-01
22	3.40E-01	1.94E+01	2.00E+01	3.47E-01	6.5344E+01	65	1.10E+00
23	3.50E-01	2.02E+01	2.10E+01	3.60E-01	2.9530E+01	30	4.79E-01
24	3.60E-01	2.10E+01	2.20E+01	3.72E-01	4.2111E+01	42	6.59E-01
25	3.80E-01	2.26E+01	2.30E+01	3.85E-01	4.7234E+01	47	7.42E-01
26	3.90E-01	2.34E+01	2.40E+01	3.98E-01	7.4482E+01	74	1.34E+00
27	4.00E-01	2.41E+01	2.50E+01	4.12E-01	7.9962E+01	80	1.55E+00
28	4.20E-01	2.56E+01	2.60E+01	4.25E-01	4.3791E+01	44	6.92E-01
29	4.30E-01	2.64E+01	2.70E+01	4.38E-01	1.5301E+01	15	2.86E-01
30	4.40E-01	2.71E+01	2.80E+01	4.52E-01	8.8079E+01	88	1.91E+00

Output-DTN: LB0307FMRADTRN.001.

APPENDIX D

SAMPLING FOR FRACTURE AND MATRIX POROSITY

SAMPLING FOR FRACTURE AND MATRIX POROSITY

This appendix provides additional information pertaining to Section 6.4.5 of the main text. Fracture and matrix average porosity values and standard deviations are given in Section 4.1.1. No standard deviations are available for fracture porosity in the tsw33, tsw35, and tsw36. Therefore, values were computed such that the ratio of the standard deviation to the mean in these units is the same as the ratio for the tsw34. The average and standard deviations for fracture and matrix porosities are given in Table D-1.

Table D-1. Fracture and Matrix Porosity Data

UZ Model Layer	Average fracture porosity[a] (-)	Fracture porosity Std deviation[a] (-)	Average Matrix Porosity[b]	Standard Deviation for Matrix Porosity[b]
tsw33	5.8E-3	1.71E-03[c]	0.155	0.030
tsw34	8.5E-3	2.50E-03	0.111	0.020
tsw35	9.6E-3	2.82E-03[c]	0.131	0.031
tsw3[67]	1.3E-2	3.82E-03[c]	0.103	0.025

[a] DTN: LB0205REVUZPRP.001 [DIRS 159525].
[b] DTN: LB0207REVUZPRP.002 [DIRS 159672].
[c] Derived values – see text above.

Porosities are modeled using the beta distribution, with the mean values and standard deviations as indicated in Table D-1 and for all cases, a maximum of 1 and a minimum of 0.

The sampling for the beta distribution uses the approximation for the inverse as given in Equation 26.5.22 of Abramowitz and Stegun (1972 [DIRS 103280]). This method requires the generation of a Gaussian random number. Gaussian random numbers are computed using the rational approximation for the inverse cumulative probability distribution for a Gaussian random variable, as given in Equation 26.2.23 of Abramowitz and Stegun (1972 [DIRS 103280]). See Scientific Notebook by Wang (2003 [DIRS 163234], SN-LBNL-SCI-236-V1, pp. 40–42) for a discussion of the generation of Gaussian random numbers. Table D-2 presents a portion of the output from the formulation as performed in an Excel spreadsheet for the fracture and matrix porosities of the tsw35 model unit. See Wang (2003 [DIRS 163234], SN-LBNL-SCI-236-V1, p. 59) and DTN: LB0307FMRADTRN.001 for the complete output.

The sequence of calculations are as follows:

Column A: Uniform random numbers generated by the Excel spreadsheet function RAND() and saved. These are the cumulative probabilities, p.

Column B: The normalized Gaussian random number corresponding to the cumulative probability in Column A.

Column C: The parameter λ in the beta inverse function is given by Abramowitz and Stegun (1972 [DIRS 103280], Equation 26.5.22):

$$\lambda = \frac{y_p^2 - 3}{6} \qquad \text{(Eq. D-1)}$$

where y_p is defined in Column B. In Excel, this is

Crn=(Brn^2-3)/6

Column D: The parameter w in the beta inverse function is given by Abramowitz and Stegun (1972 [DIRS 103280], Equation 26.5.22):

$$w = \frac{y_p(h+\lambda)^{\frac{1}{2}}}{h} - \left(\frac{1}{2b-1} - \frac{1}{2a-1}\right)\left(\lambda + \frac{5}{6} - \frac{2}{3h}\right) \quad \text{(Eq. D-2)}$$

In Excel, this is

Drn= (Brn*(($J$2+Crn)^0.5)/$J$2)-((2*$I$2-1)^(-1)-(2*$H$2-1)^(-1))*(Crn+(5/6)-2/(3*$J$2))

Column E: The beta random number, x_p, is given by Abramowitz and Stegun (1972 [DIRS 103280], Equation 26.5.22):

$$x_p \approx \frac{a}{a + be^{2w}} \quad \text{(Eq. D-3)}$$

In Excel, this is

Ern=$H$2/($H$2+$I$2*EXP(2*Drn))

Column F: Contains the value of the mean porosity, μ_ϕ, from Table D-1

Column G: Contains the value of the porosity standard deviation, σ_ϕ, from Table D-1

Column H: The beta distribution parameter a is derived from Abramowitz and Stegun (1972 [DIRS 103280], Equation 26.1.33) (see Appendix K for a detailed derivation of Equations (D-4) and (D-5)):

$$a = \mu_\phi\left[\frac{\mu_\phi(1-\mu_\phi)}{\sigma_\phi^2} - 1\right] \quad \text{(Eq. D-4)}$$

In Excel, this is

H2=F2*((F2*(1-F2)/G2^2)-1)

Column I: The beta distribution parameter b is given by Abramowitz and Stegun (1972 [DIRS 103280], Equation 26.1.33):

$$b = (1-\mu_\phi)\left[\frac{\mu_\phi(1-\mu_\phi)}{\sigma_\phi^2} - 1\right] \quad \text{(Eq. D-5)}$$

In Excel, this is

$$I2=(1-F2)*((F2*(1-F2)/G2^2)-1)$$

Column J: The parameter *h* in the beta inverse function is given by Abramowitz and Stegun (1972 [DIRS 103280], Equation 26.5.22):

$$h = 2\left(\frac{1}{2a-1}+\frac{1}{2b-1}\right)^{-1} \quad \text{(Eq. D-6)}$$

In Excel, this is

$$J2=2*((2*H2-1)^(-1)+(2*I2-1)^(-1))^(-1)$$

Table D-2. Fracture Porosity in the tsw35

	A	B	C	D	E	F	G	H	I	J
1	Fixed Uniform Random Number (P)	yP - normalized Gaussian random number	Beta inverse param. -λ	Beta inverse param. - w	xP - Beta random number (Fracture Porosity)	mean fracture porosity - tsw35	standard deviation fracture porosity - tsw35	Beta dist. Param. - a	Beta dist. Param. - b	Beta inverse param. - h
2	6.1798E-01	2.9975E-01	-4.8503E-01	6.02E-02	8.52E-03	9.60E-03	2.82E-03	1.15E+01	1.18E+03	4.35E+01
3	4.6680E-01	-8.3116E-02	-4.9885E-01	1.88E-03	9.56E-03					
4	6.3399E-01	3.4200E-01	-4.8051E-01	6.68E-02	8.41E-03					
5	6.5133E-01	3.8846E-01	-4.7485E-01	7.41E-02	8.29E-03					
6	8.7752E-01	1.1628E+00	-2.7465E-01	2.00E-01	6.45E-03					
7	3.6128E-01	-3.5460E-01	-4.7904E-01	-3.82E-02	1.04E-02					
8	3.3315E-01	-4.3080E-01	-4.6907E-01	-4.92E-02	1.06E-02					
9	5.7646E-02	-1.5752E+00	-8.6467E-02	-2.06E-01	1.44E-02					
10	3.4838E-01	-3.8926E-01	-4.7475E-01	-4.32E-02	1.05E-02					
11	6.3949E-01	3.5665E-01	-4.7880E-01	6.91E-02	8.37E-03					
12	6.3466E-01	3.4378E-01	-4.8030E-01	6.71E-02	8.40E-03					
13	2.1067E-01	-8.0391E-01	-3.9229E-01	-1.02E-01	1.18E-02					
14	1.8567E-01	-8.9384E-01	-3.6684E-01	-1.15E-01	1.20E-02					
15	6.9110E-01	4.9856E-01	-4.5857E-01	9.15E-02	8.01E-03					
16	5.2111E-01	5.2811E-02	-4.9954E-01	2.23E-02	9.18E-03					
17	7.6460E-02	-1.4296E+00	-1.5940E-01	-1.87E-01	1.39E-02					
18	1.2759E-01	-1.1380E+00	-2.8418E-01	-1.48E-01	1.29E-02					
19	2.2382E-01	-7.5911E-01	-4.0396E-01	-9.59E-02	1.16E-02					
20	3.9235E-01	-2.7278E-01	-4.8760E-01	-2.62E-02	1.01E-02					
21	4.7861E-01	-5.3507E-02	-4.9952E-01	6.31E-03	9.48E-03					
22	2.9629E-01	-5.3472E-01	-4.5235E-01	-6.42E-02	1.09E-02					

Table D-2. Fracture Porosity in the tsw35 (Continued)

	A	B	C	D	E	F	G	H	I	J
	Fixed Uniform Random Number (P)	yP - normalized Gaussian random number	Beta inverse param. -λ	Beta inverse param. - w	xP - Beta random number (Fracture Porosity)	mean fracture porosity - tsw35	standard deviation fracture porosity - tsw35	Beta dist. Param. - a	Beta dist. Param. - b	Beta inverse param. - h
23	2.9692E-02	-1.8858E+00	9.2682E-02	-2.45E-01	1.56E-02					
24	8.1567E-01	8.9887E-01	-3.6534E-01	1.56E-01	7.04E-03					
25	9.1682E-01	1.3842E+00	-1.8064E-01	2.38E-01	5.98E-03					
26	3.2410E-01	-4.5583E-01	-4.6537E-01	-5.28E-02	1.07E-02					
27	2.3452E-01	-7.2378E-01	-4.1269E-01	-9.09E-02	1.15E-02					
28	4.4601E-01	-1.3546E-01	-4.9694E-01	-5.93E-03	9.71E-03					
29	4.5832E-01	-1.0442E-01	-4.9818E-01	-1.30E-03	9.62E-03					
30	3.6776E-01	-3.3734E-01	-4.8103E-01	-3.57E-02	1.03E-02					

Output DTN: LB0307FMRADTRN.001.

Table D-3. Matrix Porosity in the tsw35

	A	B	C	D	E	F	G	H	I	J
1	Fixed Uniform Random Number (P)	yP - normalized Gaussian random number	Beta inverse param. -λ	Beta inverse param. - w	xP - Beta random number (Matrix Porosity)	mean matrix porosity - tsw35	standard deviation matrix porosity - tsw35	Beta dist. Param. - a	Beta dist. Param. - b	Beta inverse param. - h
2	8.2838E-01	9.4770E-01	-3.5031E-01	1.45E-01	1.01E-01	1.31E-01	3.10E-02	1.54E+01	1.02E+02	5.19E+01
3	1.4598E-01	-1.0538E+00	-3.1491E-01	-1.31E-01	1.64E-01					
4	9.2170E-01	1.4169E+00	-1.6542E-01	2.15E-01	8.93E-02					
5	2.3816E-01	-7.1196E-01	-4.1552E-01	-8.68E-02	1.52E-01					
6	1.9194E-01	-8.7064E-01	-3.7367E-01	-1.08E-01	1.57E-01					
7	2.3945E-01	-7.0779E-01	-4.1651E-01	-8.62E-02	1.52E-01					
8	8.6837E-01	1.1188E+00	-2.9138E-01	1.70E-01	9.69E-02					
9	5.1569E-01	3.9223E-02	-4.9974E-01	1.46E-02	1.28E-01					
10	7.6814E-01	7.3249E-01	-4.1058E-01	1.13E-01	1.07E-01					
11	1.3291E-01	-1.1128E+00	-2.9361E-01	-1.39E-01	1.66E-01					
12	5.2042E-01	5.1084E-02	-4.9957E-01	1.63E-02	1.27E-01					
13	3.0449E-01	-5.1112E-01	-4.5646E-01	-6.02E-02	1.45E-01					
14	6.2932E-01	3.2962E-01	-4.8189E-01	5.52E-02	1.19E-01					
15	7.8249E-01	7.8041E-01	-3.9849E-01	1.20E-01	1.06E-01					
16	2.1576E-02	-2.0227E+00	1.8187E-01	-2.52E-01	2.00E-01					
17	1.0799E-01	-1.2374E+00	-2.4479E-01	-1.55E-01	1.70E-01					
18	7.6286E-01	7.1526E-01	-4.1473E-01	1.10E-01	1.08E-01					

Table D-3. Matrix Porosity in the tsw35 (Continued)

	A	B	C	D	E	F	G	H	I	J
	Fixed Uniform Random Number (P)	yP - normalized Gaussian random number	Beta inverse param. -λ	Beta inverse param. - w	xP - Beta random number (Matrix Porosity)	mean matrix porosity - tsw35	standard deviation matrix porosity - tsw35	Beta dist. Param. - a	Beta dist. Param. - b	Beta inverse param. - h
19	2.3410E-01	-7.2515E-01	-4.1236E-01	-8.85E-02	1.53E-01					
20	3.1982E-01	-4.6778E-01	-4.6353E-01	-5.44E-02	1.44E-01					
21	1.5005E-01	-1.0362E+00	-3.2104E-01	-1.29E-01	1.63E-01					
22	8.6802E-01	1.1172E+00	-2.9199E-01	1.70E-01	9.69E-02					
23	6.3793E-02	-1.5240E+00	-1.1290E-01	-1.91E-01	1.81E-01					
24	7.1773E-01	5.7574E-01	-4.4475E-01	9.03E-02	1.12E-01					
25	2.6452E-02	-1.9361E+00	1.2476E-01	-2.42E-01	1.96E-01					
26	1.2687E-03	-3.0192E+00	1.0192E+00	-3.70E-01	2.40E-01					
27	6.7080E-01	4.4170E-01	-4.6748E-01	7.11E-02	1.16E-01					
28	1.7696E-01	-9.2694E-01	-3.5680E-01	-1.15E-01	1.59E-01					
29	8.9801E-02	-1.3422E+00	-1.9975E-01	-1.68E-01	1.74E-01					
30	1.4850E-01	-1.0429E+00	-3.1873E-01	-1.30E-01	1.64E-01					

Output DTN: LB0307FMRADTRN.001.

INTENTIONALLY LEFT BLANK

APPENDIX E

SAMPLING FOR INVERT DIFFUSIVE MASS TRANSFER COEFFICIENTS

SAMPLING FOR INVERT DIFFUSIVE MASS TRANSFER COEFFICIENTS

This appendix provides additional information pertaining to Section 6.4.5 of the main text. The invert diffusive mass-transfer coefficient is based upon the correlation presented in *Invert Diffusion Properties Model* (BSC 2001 [DIRS 156700], pp. 23–25, Equation (37)):

$$\log\left(\frac{D_{eI}}{D_0}\right) = 1.849 \log \theta_I \qquad \text{(Eq. E-1)}$$

where D_{eI} is the invert diffusive mass-transfer coefficient, D_0 is the coefficient of diffusion in water, and θ_I is the invert water content. As discussed in Section 6.4.5, the invert water content is related to the invert grain microporosity, times the fraction of the bulk volume occupied by the grains, i.e.:

$$\theta_I = (1 - \phi_{Ig})\phi_m \qquad \text{(Eq. E-2)}$$

where ϕ_{Ig} is the intergranular porosity of the invert and ϕ_m is the microporosity of the grains. The invert material is planned to be taken from the tsw36 unit, and the sampling for the porosity of this material is discussed in Appendix D. The intergranular porosity has an expected value of 0.45 (BSC 2003 [DIRS 170881], Section 6.3) and a range from 0.4 to 0.48. A distribution representative of these characteristics can be produced by noting that a uniform random sample between 0.4 and 0.45 will on average produce a value of 0.425. Similarly, a uniform random sample between 0.45 and 0.48 will on average produce a value of 0.465. If samples are drawn from these two distributions in some proportion, x , for the range of 0.4 to 0.45 and (1-x) for the range of 0.45 to 0.48, then an overall average of 0.45 will be achieved if x = 0.375.

Table E-1 presents a portion of the output from the formulation as performed in an Excel spreadsheet for the fracture and matrix porosities of the tsw35 model unit. See Wang (2003 [DIRS 163234], SN-LBNL-SCI-236-V1, p. 64) and DTN: LB0307FMRADTRN.001 for the complete output. The sequence of calculations are as follows:

Column A: Uniform random numbers generated by the Excel spreadsheet function RAND() and saved.

Column B: Scale the random number in Column B to between 0.4 and 0.45

Brn=0.4+Arn*0.05

Column C: Uniform random numbers generated by the Excel spreadsheet function RAND() and saved.

Column D: Scale the random number in Column E to between 0.45 and 0.48

Drn=0.45+Crn*0.03

Column E: Calculate the weighted average of columns B and D to give the invert intergranular porosity.

Ern=0.375*Brn+0.625*Drn

The statistical properties for the diffusion coefficient in water, D_0, are derived from the data from Weast and Astle 1979 [DIRS 102865], presented in Section 4.1.1. The diffusion coefficient is sampled as a lognormal distribution, with the mean and standard deviation of log(D_0) being 4.69 and 0.150, respectively, where D_0 is in mm/year.

See Scientific Notebook by Wang (2003 [DIRS 163234], SN-LBNL-SCI-236-V1, pp. 40–42) for a discussion of the generation of Gaussian random numbers. Table E-2 presents a portion of the output from the formulation as performed in an Excel spreadsheet for the diffusion coefficient. See Wang (2003 [DIRS 163234], SN-LBNL-SCI-236-V1, p. 67) and DTN: LB0307FMRADTRN.001 for the complete output

The sequence of calculations are as follows:

Column A: Uniform random numbers generated by the Excel spreadsheet function RAND() and saved. These are the cumulative probabilities, p.

Column B: The normalized Gaussian random number corresponding to the cumulative probability in Column A.

Column C: The corresponding random base-10 logarithm of fracture frequency is derived from the normalized Gaussian random variable through the normalization definition:

$$f = x_p \sigma_{\log(D_0)} + \mu_{\log(D_0)} \quad \text{(Eq. E-3)}$$

where $\mu_{\log(D_0)}$ and $\sigma_{\log(D_0)}$ are the mean and variance of $\log(D_0)$.

In Excel, this is

Crn=Brn*$F$2+$E$2

Column D: This column calculates the diffusion coefficient through the identity

$$D_0 = 10^{\log(D_0)} \quad \text{(Eq. E-4)}$$

In Excel, this is

Drn=10^(Crn)

Table E-1. Intergranular Porosity

	A	B	C	D	E
1	Fixed Uniform Random Number (P)	Random Porosity between 0.4 and 0.45	Fixed Uniform Random Number (P)	Random Porosity between 0.45 and 0.48	Intergranular porosity
2	4.1774E-01	4.2089E-01	4.7017E-01	4.6411E-01	4.48E-01
3	8.1015E-01	4.4051E-01	3.8268E-01	4.6148E-01	4.54E-01
4	7.0390E-01	4.3519E-01	2.6241E-01	4.5787E-01	4.49E-01
5	1.9219E-01	4.0961E-01	1.5264E-01	4.5458E-01	4.38E-01
6	6.8994E-01	4.3450E-01	7.1428E-01	4.7143E-01	4.58E-01
7	1.5716E-01	4.0786E-01	8.3342E-02	4.5250E-01	4.36E-01
8	6.6607E-01	4.3330E-01	4.5951E-01	4.6379E-01	4.52E-01
9	6.5736E-01	4.3287E-01	5.7148E-02	4.5171E-01	4.45E-01
10	1.0713E-01	4.0536E-01	2.5464E-01	4.5764E-01	4.38E-01
11	2.9326E-01	4.1466E-01	1.8206E-01	4.5546E-01	4.40E-01
12	2.8986E-01	4.1449E-01	4.8610E-01	4.6458E-01	4.46E-01
13	8.9896E-01	4.4495E-01	8.8812E-01	4.7664E-01	4.65E-01
14	9.2404E-01	4.4620E-01	2.3375E-01	4.5701E-01	4.53E-01
15	2.1126E-01	4.1056E-01	4.6330E-01	4.6390E-01	4.44E-01
16	9.7667E-01	4.4883E-01	1.5419E-01	4.5463E-01	4.52E-01
17	8.7149E-02	4.0436E-01	3.6447E-02	4.5109E-01	4.34E-01
18	1.0232E-01	4.0512E-01	9.8288E-01	4.7949E-01	4.52E-01
19	9.1436E-02	4.0457E-01	2.3091E-01	4.5693E-01	4.37E-01
20	2.0876E-01	4.1044E-01	1.6027E-01	4.5481E-01	4.38E-01
21	4.6890E-01	4.2344E-01	9.6731E-01	4.7902E-01	4.58E-01
22	2.4024E-01	4.1201E-01	4.6734E-01	4.6402E-01	4.45E-01
23	7.3021E-01	4.3651E-01	9.8400E-01	4.7952E-01	4.63E-01
24	5.9356E-01	4.2968E-01	8.7017E-02	4.5261E-01	4.44E-01
25	5.8208E-01	4.2910E-01	8.1004E-01	4.7430E-01	4.57E-01
26	8.3132E-01	4.4157E-01	6.2164E-01	4.6865E-01	4.58E-01
27	6.5032E-01	4.3252E-01	3.1289E-01	4.5939E-01	4.49E-01
28	3.9302E-02	4.0197E-01	1.1715E-01	4.5351E-01	4.34E-01
29	1.9354E-01	4.0968E-01	7.8522E-01	4.7356E-01	4.50E-01
30	7.4822E-03	4.0037E-01	8.6992E-01	4.7610E-01	4.48E-01

Output DTN: LB0307FMRADTRN.001.

Table E-2. Free-Water Diffusion Coefficients

	A	B	C	D	E	F
1	Fixed Uniform Random Number (P)	x_P - norm. Gaussian random number	x - Gaussian random number	Free-water Diffusion Coefficient (mm^2/yr)	mean $\log(D_0)$ (mm^2/yr)	standard deviation $\log(D_0)$
2	8.6421E-01	1.0995E+00	4.85E+00	7.16E+04	4.69E+00	1.50E-01
3	2.3687E-01	-7.1615E-01	4.58E+00	3.82E+04		
4	4.7360E-01	-6.6043E-02	4.68E+00	4.79E+04		
5	4.7725E-01	-5.6898E-02	4.68E+00	4.80E+04		
6	3.1923E-01	-4.6944E-01	4.62E+00	4.16E+04		
7	3.2902E-01	-4.4220E-01	4.62E+00	4.20E+04		
8	4.9136E-01	-2.1600E-02	4.69E+00	4.86E+04		
9	8.4999E-01	1.0364E+00	4.85E+00	7.01E+04		
10	9.5489E-01	1.6946E+00	4.94E+00	8.79E+04		
11	2.0629E-01	-8.1919E-01	4.57E+00	3.69E+04		
12	1.4971E-01	-1.0377E+00	4.53E+00	3.42E+04		
13	5.3725E-01	9.3274E-02	4.70E+00	5.06E+04		
14	5.0698E-01	1.7446E-02	4.69E+00	4.93E+04		
15	2.5667E-01	-6.5333E-01	4.59E+00	3.91E+04		
16	9.7563E-01	1.9712E+00	4.99E+00	9.68E+04		
17	8.2452E-01	9.3265E-01	4.83E+00	6.76E+04		
18	8.5117E-01	1.0414E+00	4.85E+00	7.02E+04		
19	5.1257E-01	3.1418E-02	4.69E+00	4.95E+04		
20	1.2745E-01	-1.1386E+00	4.52E+00	3.31E+04		
21	5.9803E-01	2.4783E-01	4.73E+00	5.34E+04		
22	4.2537E-01	-1.8780E-01	4.66E+00	4.59E+04		
23	8.0602E-01	8.6319E-01	4.82E+00	6.60E+04		
24	1.7123E-01	-9.4925E-01	4.55E+00	3.53E+04		
25	8.3000E-01	9.5408E-01	4.83E+00	6.81E+04		
26	6.0404E-01	2.6339E-01	4.73E+00	5.36E+04		
27	4.4891E-01	-1.2814E-01	4.67E+00	4.69E+04		
28	9.1953E-01	1.4022E+00	4.90E+00	7.95E+04		
29	9.5815E-01	1.7300E+00	4.95E+00	8.90E+04		
30	1.7662E-01	-9.2825E-01	4.55E+00	3.55E+04		

Output-DTN: LB0307FMRADTRN.001.

The invert diffusion coefficient is computed using the intergranular porosity and matrix porosity from tsw36 (Appendix D), Equations E-1 and E-2, and the free-water diffusion coefficient. Table E-2 presents a portion of the output from the formulation as performed in an Excel spreadsheet for the invert diffusive mass transfer coefficient. See Wang (2003 [DIRS 163234], SN-LBNL-SCI-236-V1, p. 69) and DTN: LB0307FMRADTRN.001 for the complete output. The ratio of the maximum to minimum of the sampled diffusion coefficients spans a factor of approximately 43.

The sequence of calculations are described here:

Column A: Intergranular Porosity

Column B: Matrix Porosity (tsw36)

Column C: Invert water content computed from Equation E-2. In Excel, this is

Crn=(1-Arn)*Brn

Column D: Free-water diffusion coefficient

Column E: Invert diffusive mass transfer coefficient computed from Equation E-1. In Excel, this is

Ern=Drn*Crn^1.849

Table E-3. Invert Diffusive Mass Transfer Coefficients

	A	B	C	D	E
1	Intergranular Porosity	Matrix Porosity - tsw36	Invert Water Content	Free-Water Diffusion Coefficient (mm/r)	Invert Diffusive Mass Transfer Coefficient (mm^2/yr)
2	4.48E-01	1.51E-01	8.34E-02	7.16E+04	7.25E+02
3	4.54E-01	9.24E-02	5.05E-02	3.82E+04	1.53E+02
4	4.49E-01	8.54E-02	4.70E-02	4.79E+04	1.68E+02
5	4.38E-01	9.61E-02	5.40E-02	4.80E+04	2.18E+02
6	4.58E-01	8.26E-02	4.48E-02	4.16E+04	1.34E+02
7	4.36E-01	1.35E-01	7.60E-02	4.20E+04	3.58E+02
8	4.52E-01	1.09E-01	5.99E-02	4.86E+04	2.67E+02
9	4.45E-01	8.37E-02	4.65E-02	7.01E+04	2.41E+02
10	4.38E-01	1.23E-01	6.89E-02	8.79E+04	6.24E+02
11	4.40E-01	1.31E-01	7.31E-02	3.69E+04	2.93E+02
12	4.46E-01	6.76E-02	3.75E-02	3.42E+04	7.89E+01
13	4.65E-01	1.15E-01	6.18E-02	5.06E+04	2.94E+02
14	4.53E-01	1.05E-01	5.76E-02	4.93E+04	2.51E+02
15	4.44E-01	1.75E-01	9.71E-02	3.91E+04	5.24E+02
16	4.52E-01	7.95E-02	4.35E-02	9.68E+04	2.94E+02
17	4.34E-01	5.44E-02	3.08E-02	6.76E+04	1.09E+02
18	4.52E-01	1.33E-01	7.27E-02	7.02E+04	5.51E+02
19	4.37E-01	1.12E-01	6.30E-02	4.95E+04	2.99E+02
20	4.38E-01	1.32E-01	7.39E-02	3.31E+04	2.68E+02
21	4.58E-01	1.33E-01	7.18E-02	5.34E+04	4.10E+02
22	4.45E-01	9.39E-02	5.22E-02	4.59E+04	1.95E+02

Table E-3. Invert Diffusive Mass Transfer Coefficients (Continued)

	A	B	C	D	E
	Intergranular Porosity	**Matrix Porosity - tsw36**	**Invert Water Content**	**Free-Water Diffusion Coefficient (mm/r)**	**Invert Diffusive Mass Transfer Coefficient (mm2/yr)**
23	4.63E-01	1.38E-01	7.42E-02	6.60E+04	5.38E+02
24	4.44E-01	1.09E-01	6.08E-02	3.53E+04	1.99E+02
25	4.57E-01	3.70E-02	2.01E-02	6.81E+04	4.94E+01
26	4.58E-01	1.23E-01	6.67E-02	5.36E+04	3.59E+02
27	4.49E-01	4.55E-02	2.51E-02	4.69E+04	5.14E+01
28	4.34E-01	1.02E-01	5.79E-02	7.95E+04	4.09E+02
29	4.50E-01	5.68E-02	3.13E-02	8.90E+04	1.47E+02
30	4.48E-01	1.25E-01	6.90E-02	3.55E+04	2.53E+02

Output DTN: LB0307FMRADTRN.001.

APPENDIX F

SAMPLING FOR MATRIX DIFFUSION COEFFICIENTS

SAMPLING FOR MATRIX DIFFUSION COEFFICIENTS

This appendix provides additional information pertaining to Section 6.4.5 of the main text. Matrix diffusion coefficients are derived based on the correlation discussed in Section 6.4.5 (Equation 6-52):

$$\log(D_m) = -3.49 + 1.38\theta_m + 0.165\log(k_w) \quad \text{(Eq. F-1)}$$

where D_m is in cm^2/s and k_w is in m^2. The water-content values of the matrix are derived from the matrix porosities given in Appendix D, times the matrix water saturations given in Appendix B. The effective permeability to water is derived using the equation given in Section 6.4.5 (Equation 6-57):

$$k_w = k_m k_{rw} \quad \text{(Eq. F-2)}$$

where the matrix permeabilities are given in Table 4-6. A portion of the output from the above relationship for matrix diffusion coefficient for each of the model grid locations are shown in Table F-1. See Wang (2003 [DIRS 163234], SN-LBNL-SCI-236-V1, p. 84) and DTN: LB0307FMRADTRN.001 for the complete output.

The sequence of calculations is given here:

Column A: Cell name from Appendix B.

Column B: Matrix water saturation from Appendix B.

Column C: Matrix porosity from Appendix D.

Column D: Matrix water content equals matrix water saturation, times matrix porosity. In Excel, this is

Drn=Brn*Crn

Column E: Matrix relative permeability from Appendix B

Column F: The effective permeability is computed using Equation F-2. In Excel, this is

Frm=$N$2*Ern

Column G: The logarithm of the mean matrix diffusion coefficient is computed using Equation F-1. In Excel, this is

Grn=-3.49+1.38*Drn+0.165*LOG(Frn)

Column H: The matrix diffusion coefficient is computed from the identity

$$D_m = 10^{\log(D_m)} \quad \text{(Eq. F-3)}$$

and converted from cm^2/s to $mm^2/year$. In Excel, this is

Hrn=(10^Grn)*100*3600*24*365.25

Column I: Uniform random numbers generated by the Excel spreadsheet function RAND() and saved. These are the cumulative probabilities, *p*.

Column J: The normalized Gaussian random number corresponding to the cumulative probability in Column H.

Column K: The distributed random variable, *Y*, in Equation 6-55 is defined by

$$Y = \ln\left(\log\left(\frac{D_0}{D_m}\right)\right) \quad \text{(Eq. F-4)}$$

where D_m is given in Column G and $D_0 = 10^{-9}$ $m^2/s = 31557.6$ $mm^2/year$. In Excel, this is

Krn=ln(log(31558/Hrn))

Column L: The corresponding random value of *Y* is derived from the normalized Gaussian random variable through the normalization definition:

$$Y = x_p \sigma_Y + \overline{Y} \quad \text{(Eq. F-5)}$$

where $\overline{Y}$ and σ_Y are the mean and variance for *Y*. As discussed in Section 6.4.5, σ_Y =0.3.

In Excel, this is

Lrn=Jrn*Orn+Krn

Column M: Inverting Equation F-4, the random value of *Y* is transformed back to a diffusion coefficient through the relationship

$$D_m = D_0 10^{-\exp(Y)}$$

In Excel, this is

Mrn=31558*10^(-exp(Lrn))

Column N: Matrix permeability from Table 4-6

Column O: Standard deviation for *Y*

Table F-1. Matrix Diffusion Coefficients in the tsw35, Mean Infiltration Scenario

	A	B	C	D	E	F	G	H	I	J	K	L	M	N	O
1	Cell Name	Matrix Water Saturation	Matrix Porosity	Matrix Water Content	Relative Perme-ability	Effective Perme-ability m^2	log(D_m) cm^2/s	D_m mm^2/yr	Fixed Uniform Random Number (P)	Norma-lized Gaussian Random Number	Mean of Y	Sampled Y	Sampled D_m mm^2/yr	Perme-ability m^2	Std Dev Y
2	F0014f19	8.5119E-01	1.01E-01	8.64E-02	1.1513E-02	5.16E-20	-6.55E+00	8.83E+02	2.8703E-02	-1.9006E+00	4.40E-01	-1.30E-01	4.18E+03	4.48E-	3.00E-
3	F0014f31	8.3762E-01	1.64E-01	1.37E-01	9.1980E-03	4.12E-20	-6.50E+00	1.00E+03	1.0475E-01	-1.2551E+00	4.05E-01	2.83E-02	2.95E+03		
4	F0014f67	8.3178E-01	8.93E-02	7.43E-02	8.3545E-03	3.74E-20	-6.59E+00	8.06E+02	9.7688E-01	1.9937E+00	4.66E-01	1.06E+00	4.00E+01		
5	F0014f80	8.3701E-01	1.52E-01	1.27E-01	9.1054E-03	4.08E-20	-6.51E+00	9.67E+02	1.9728E-01	-8.5123E-01	4.15E-01	1.59E-01	2.12E+03		
6	F0014g17	8.3776E-01	1.57E-01	1.32E-01	9.2192E-03	4.13E-20	-6.51E+00	9.84E+02	6.8327E-01	4.7643E-01	4.10E-01	5.53E-01	5.77E+02		
7	F0014g83	8.3757E-01	1.52E-01	1.27E-01	9.1904E-03	4.12E-20	-6.51E+00	9.69E+02	5.6143E-01	1.5428E-01	4.14E-01	4.60E-01	8.21E+02		
8	F0014h13	8.3672E-01	9.69E-02	8.11E-02	9.0624E-03	4.06E-20	-6.58E+00	8.34E+02	4.4206E-02	-1.7042E+00	4.56E-01	-5.53E-02	3.57E+03		
9	F0014h21	8.3566E-01	1.28E-01	1.07E-01	8.9063E-03	3.99E-20	-6.54E+00	9.03E+02	3.6072E-01	-3.5609E-01	4.34E-01	3.27E-01	1.29E+03		
10	F0014h67	8.4732E-01	1.07E-01	9.10E-02	1.0797E-02	4.84E-20	-6.55E+00	8.86E+02	8.3538E-01	9.7559E-01	4.39E-01	7.32E-01	2.63E+02		
11	F0014h77	8.4210E-01	1.66E-01	1.40E-01	9.9040E-03	4.44E-20	-6.49E+00	1.02E+03	4.6970E-01	-7.5832E-02	3.99E-01	3.76E-01	1.10E+03		
12	F0014h82	8.3832E-01	1.27E-01	1.07E-01	9.3047E-03	4.17E-20	-6.54E+00	9.09E+02	1.4114E-01	-1.0752E+00	4.32E-01	1.09E-01	2.42E+03		
13	F0014i13	8.3837E-01	1.45E-01	1.22E-01	9.3129E-03	4.17E-20	-6.52E+00	9.54E+02	3.7451E-01	-3.1949E-01	4.18E-01	3.23E-01	1.31E+03		
14	F0014i18	8.3830E-01	1.19E-01	9.97E-02	9.3013E-03	4.17E-20	-6.55E+00	8.89E+02	2.6836E-01	-6.1745E-01	4.38E-01	2.53E-01	1.63E+03		
15	F0014i48	8.3729E-01	1.06E-01	8.88E-02	9.1484E-03	4.10E-20	-6.57E+00	8.56E+02	7.5006E-01	6.7438E-01	4.49E-01	6.51E-01	3.81E+02		
16	F0014l54	8.3708E-01	2.00E-01	1.67E-01	9.1172E-03	4.08E-20	-6.46E+00	1.10E+03	5.5094E-01	1.2776E-01	3.77E-01	4.16E-01	9.63E+02		
17	F0014l56	8.3869E-01	1.70E-01	1.43E-01	9.3628E-03	4.19E-20	-6.49E+00	1.02E+03	4.1410E-02	-1.7349E+00	3.99E-01	-1.22E-01	4.11E+03		
18	F0014l57	8.3979E-01	1.08E-01	9.06E-02	9.5337E-03	4.27E-20	-6.56E+00	8.67E+02	8.9647E-01	1.2619E+00	4.45E-01	8.24E-01	1.66E+02		
19	F0014m62	8.4322E-01	1.53E-01	1.29E-01	1.0090E-02	4.52E-20	-6.50E+00	9.88E+02	4.7281E-01	-6.8031E-02	4.08E-01	3.88E-01	1.06E+03		
20	F0014m63	8.3760E-01	1.44E-01	1.21E-01	9.1946E-03	4.12E-20	-6.52E+00	9.48E+02	6.9257E-01	5.0273E-01	4.20E-01	5.71E-01	5.36E+02		
21	F0014m64	8.4056E-01	1.63E-01	1.37E-01	9.6557E-03	4.33E-20	-6.50E+00	1.01E+03	8.9833E-01	1.2723E+00	4.03E-01	7.84E-01	2.03E+02		
22	F0014m65	8.4299E-01	9.69E-02	8.17E-02	1.0051E-02	4.50E-20	-6.57E+00	8.51E+02	7.1121E-01	5.5653E-01	4.51E-01	6.18E-01	4.41E+02		
23	F0014n24	8.6049E-01	1.81E-01	1.56E-01	1.3442E-02	6.02E-20	-6.45E+00	1.13E+03	9.5768E-01	1.7248E+00	3.69E-01	8.87E-01	1.18E+02		
24	F0014n26	8.5652E-01	1.12E-01	9.57E-02	1.2580E-02	5.64E-20	-6.53E+00	9.23E+02	6.3064E-01	3.3310E-01	4.28E-01	5.28E-01	6.37E+02		
25	F0014o29	8.4453E-01	1.96E-01	1.66E-01	1.0310E-02	4.62E-20	-6.45E+00	1.12E+03	7.0273E-01	5.3187E-01	3.72E-01	5.32E-01	6.26E+02		
26	F0014o31	8.5044E-01	2.40E-01	2.04E-01	1.1370E-02	5.09E-20	-6.39E+00	1.28E+03	7.1114E-01	5.5635E-01	3.30E-01	4.97E-01	7.16E+02		
27	F014Af20	8.3851E-01	1.16E-01	9.70E-02	9.3349E-03	4.18E-20	-6.55E+00	8.82E+02	3.6621E-01	-3.4147E-01	4.41E-01	3.38E-01	1.25E+03		
28	F014Af43	8.3937E-01	1.59E-01	1.34E-01	9.4685E-03	4.24E-20	-6.50E+00	9.94E+02	7.4439E-01	6.5661E-01	4.07E-01	6.04E-01	4.68E+02		
29	F014Af56	8.3128E-01	1.74E-01	1.45E-01	8.2857E-03	3.71E-20	-6.50E+00	1.01E+03	8.2489E-01	9.3409E-01	4.03E-01	6.83E-01	3.30E+02		
30	F014Af68	8.3726E-01	1.64E-01	1.37E-01	9.1432E-03	4.10E-20	-6.50E+00	9.98E+02	4.9809E-01	-4.7678E-03	4.05E-01	4.04E-01	1.00E+03		

Output-DTN: LB0307FMRADTRN.001.

INTENTIONALLY LEFT BLANK

APPENDIX G

SAMPLING FOR FRACTURE AND MATRIX PECLET NUMBERS, FRACTURE WATER CONTENT, AND DIMENSIONLESS INVERT DEPTH

SAMPLING FOR FRACTURE AND MATRIX PECLET NUMBERS, FRACTURE WATER CONTENT, AND DIMENSIONLESS INVERT DEPTH

This appendix provides additional information pertaining to Section 6.4.5 of the main text. Fracture Peclet numbers are computed using Equations 19 and 29 from the main text. These are:

$$q_{fe} = \frac{q_{wf}}{1 + \frac{\left(-q_{wf}\right)\Delta y_f}{D_{ef}}} \qquad \text{(Eq. G-1)}$$

and

$$Pe_{fe} = \frac{q_{fe} h_f}{D_{eI}} \qquad \text{(Eq. G-2)}$$

Fracture flow is adjusted using the flow-focusing factor in Appendix C

$$q_{wfa} = q_{wf} F \qquad \text{(Eq. G-3)}$$

and the fracture saturation is adjusted as shown in Equation 6-50 in the main text.

$$S_{fna} = \left[\left(\frac{F}{m^2} \right) S_{fn}^{\frac{1}{2}} \left\{ 1 - \left(1 - S_{fn}^{\frac{1}{m}} \right)^m \right\}^2 \right]^{\frac{2m}{4+m}} \qquad \text{(Eq. G-4)}$$

where S_{fn} is the normalized fracture saturation

$$S_{fn} = \frac{S_f - S_{fr}}{1 - S_{fr}} \qquad \text{(Eq. G-5)}$$

and the adjusted physical saturation, S_{fa}, is given by

$$S_{fa} = S_{fr} + \left(1 - S_{fr}\right) S_{fna} \qquad \text{(Eq. G-6)}$$

The fixed parameters used are given in Table 4-4.

The fracture residual saturation is sampled as discussed in Section 6.4.5. A portion of the output for the sampling of fracture residual saturation is shown in Table G-1. See Wang (2003 [DIRS 163234], SN-LBNL-SCI-236-V1, p. 62) and DTN: LB0307FMRADTRN.001 for the complete output.

The fracture percolation flux and fracture saturation as presented here may be used as input for the TSPA to support the EBS Radionuclide Transport Model [*EBS Radionuclide Transport*

Abstraction BSC 2004 [DIRS 169868])]. This is contained in the *Fracture Flux and Water Content with Flow Focusing r1.xls* spreadsheet in the output DTN: LB0307FMRADTRN.001.

The fracture residual saturation as presented here may be used as input for the TSPA to support the EBS Radionuclide Transport Model [*EBS Radionuclide Transport Abstraction* BSC 2004 [DIRS 169868])]. This is contained in the *Fracture Residual Saturation.xls* spreadsheet in the output DTN: LB0307FMRADTRN.001.

The matrix percolation flux as presented here may be used as input for the TSPA to support the EBS Radionuclide Transport Model [*EBS Radionuclide Transport Abstraction* BSC 2004 [DIRS 169868])]. This is contained in the *Matrix Peclet Number.xls* spreadsheet in the output DTN: LB0307FMRADTRN.001.

The sequence of calculations is as follows:

Column A: Uniform random numbers generated by the Excel spreadsheet function RAND() and saved.

Column B: The uniform random number in Column A, which ranges between 0 and 1, is converted to a uniform random number between -3 and -1. In Excel, this is

Brn=-3+2*Arn

Column C: The sampled S_{fr} is computed from the relationship

$$S_{fr} = 10^{RN}$$

where RN is the random number between -3 and -1 in Column B. In Excel, this is

Crn=10^Brn

Table G-1. Sampled Fracture Residual Saturations

	A	B	C
1	Fixed Uniform Random Number	Uniform Random Number between -3 and -1	Sampled S_{fr}
2	9.5775E-01	-1.0845E+00	8.2318E-02
3	9.4855E-01	-1.1029E+00	7.8906E-02
4	8.4093E-01	-1.3181E+00	4.8068E-02
5	8.1139E-01	-1.3772E+00	4.1954E-02
6	2.4515E-01	-2.5097E+00	3.0924E-03
7	6.0656E-01	-1.7869E+00	1.6335E-02
8	1.6459E-01	-2.6708E+00	2.1339E-03
9	8.3698E-01	-1.3260E+00	4.7201E-02
10	1.7917E-01	-2.6417E+00	2.2821E-03
11	7.5053E-01	-1.4989E+00	3.1700E-02
12	3.5867E-01	-2.2827E+00	5.2161E-03
13	9.4585E-01	-1.1083E+00	7.7927E-02
14	7.8309E-01	-1.4338E+00	3.6828E-02
15	4.9868E-01	-2.0026E+00	9.9396E-03

Table G-1. Sampled Fracture Residual Saturations (Continued)

	A	B	C
	Fixed Uniform Random Number	Uniform Random Number between -3 and -1	Sampled S_{fr}
16	8.3823E-01	-1.3235E+00	4.7475E-02
17	5.1569E-01	-1.9686E+00	1.0749E-02
18	5.2289E-01	-1.9542E+00	1.1112E-02
19	9.0574E-01	-1.1885E+00	6.4787E-02
20	4.4778E-01	-2.1044E+00	7.8627E-03
21	6.5841E-01	-1.6832E+00	2.0740E-02
22	6.1984E-01	-1.7603E+00	1.7365E-02
23	5.8284E-02	-2.8834E+00	1.3079E-03
24	9.6211E-01	-1.0758E+00	8.3987E-02
25	9.6423E-01	-1.0715E+00	8.4814E-02
26	2.8823E-01	-2.4235E+00	3.7711E-03
27	6.7397E-01	-1.6521E+00	2.2281E-02
28	2.0593E-01	-2.5881E+00	2.5815E-03
29	4.4110E-01	-2.1178E+00	7.6241E-03
30	4.4855E-01	-2.1029E+00	7.8905E-03

Output-DTN: LB0307FMRADTRN.001.

A portion of the output for the fracture flux and water content sampling for the mean infiltration scenario are shown in Table G-2. See Wang (2003 [DIRS 163234], SN-LBNL-SCI-236-V1, p. 88) and DTN: LB0307FMRADTRN.001 for the complete output.

The sequence of calculations is given here:

Column A: Rock unit.

Column B: Cell name.

Column C: Fracture flux (negative of) from Appendix B.

Column D: Flow focusing factor from Appendix C.

Column E: Fracture saturation from Appendix B.

Column F: Fracture normalized saturation using Equation G-5. In Excel this is

Frn=(Ern-$M$2)/(1-$M$2)

Column G: Adjusted normalized fracture saturation using Equation G-4. In Excel, this is

Grn= ((Drn/($N$2^2))*Frn^0.5*(1-(1-Frn^(1/$N$2))^$N$2)^2)^(2*$N$2/(4+$N$2))

Column H: Sampled fracture residual saturation (see above).

Column I: Adjusted physical fracture saturation using Equation G-6. In Excel, this is

$$Irn= Hrn+Grn*(1-Hrn)$$

Column J: Fracture porosity from Appendix D.

Column K: Adjusted fracture water velocity, which is equal to the fracture flux, times the flow-focusing factor, divided by the fracture porosity and the adjusted physical fracture saturation. In Excel, this is

$$Krn= Drn*Crn/(Irn*Jrn)$$

Column L: Fracture water content. In Excel, this is

$$Lrn=Irn*Jrn$$

Column M: Fracture residual saturation from Table 4-4.

Column N: Fracture van Genuchten pore size distribution factor, *m*, from Table 4-4.

Table G-2. Fracture Flux and Water Content for Mean Infiltration Scenario

	A	B	C	D	E	F	G	H	I	J	K	L	M	N
1	Rock Unit	Cell Name	q_f (mm/yr)	F	S_f	S_{fn}	S_{fna}	Sampled S_{fr}	S_{fa}	φ_f	q_{wf} (mm/yr)	Fracture Water Content	S_{fr}	*m*
2	tsw33	F012Bl76	-5.3967E+00	1.47E+00	1.32E-02	3.27E-03	3.64E-03	8.2318E-02	8.57E-02	5.98E-03	-1.55E+04	5.12E-04	0.01	0.633
3	tsw33	F012Bl78	-5.7350E+00	2.10E+00	1.33E-02	3.30E-03	4.04E-03	7.8906E-02	8.26E-02	4.70E-03	-3.11E+04	3.89E-04		
4	tsw33	F012Cl72	-4.8155E+00	8.51E-01	1.31E-02	3.09E-03	2.96E-03	4.8068E-02	5.09E-02	7.40E-03	-1.09E+04	3.77E-04		
5	tsw33	F012Cl74	-6.6185E+00	1.04E+00	1.35E-02	3.49E-03	3.52E-03	4.1954E-02	4.53E-02	4.21E-03	-3.59E+04	1.91E-04		
6	tsw33	F012Cm70	-9.7583E+00	5.96E-01	1.39E-02	3.98E-03	3.45E-03	3.0924E-03	6.53E-03	3.62E-03	-2.46E+05	2.36E-05		
7	tsw33	F012Dg58	-1.0083E+01	4.38E-01	1.44E-02	4.42E-03	3.53E-03	1.6335E-02	1.98E-02	5.48E-03	-4.07E+04	1.09E-04		
8	tsw33	F012Dl68	-1.3328E+01	3.60E-01	1.45E-02	4.50E-03	3.40E-03	2.1339E-03	5.53E-03	8.18E-03	-1.06E+05	4.52E-05		
9	tsw33	F012Dl70	-6.9879E+00	9.09E-01	1.33E-02	3.29E-03	3.20E-03	4.7201E-02	5.03E-02	2.82E-03	-4.49E+04	1.41E-04		
10	tsw33	F012Dl71	-3.5104E+00	1.91E+00	1.24E-02	2.41E-03	2.88E-03	2.2821E-03	5.15E-03	6.95E-03	-1.87E+05	3.58E-05		
11	tsw33	F012Dl75	-4.4996E+00	1.85E+00	1.27E-02	2.77E-03	3.28E-03	3.1700E-02	3.49E-02	5.49E-03	-4.36E+04	1.91E-04		
12	tsw33	F012Dl77	-4.2020E+00	2.15E-01	1.27E-02	2.68E-03	1.76E-03	5.2161E-03	6.97E-03	4.11E-03	-3.16E+04	2.86E-05		
13	tsw33	F012Dl79	-5.5142E+00	2.03E+00	1.30E-02	3.07E-03	3.73E-03	7.7927E-02	8.14E-02	4.79E-03	-2.88E+04	3.90E-04		
14	tsw33	F012Ef89	-1.8602E+01	1.08E+00	1.48E-02	4.81E-03	4.91E-03	3.6828E-02	4.16E-02	5.88E-03	-8.23E+04	2.44E-04		
15	tsw33	F012Eg 2	-1.5102E+01	7.95E-01	1.53E-02	5.37E-03	5.05E-03	9.9396E-03	1.49E-02	6.52E-03	-1.23E+05	9.75E-05		
16	tsw33	F012Eg14	-4.0953E+00	9.49E-01	1.28E-02	2.82E-03	2.78E-03	4.7475E-02	5.01E-02	4.80E-03	-1.62E+04	2.41E-04		
17	tsw33	F012Eg25	-4.2045E+00	5.96E-01	1.29E-02	2.88E-03	2.50E-03	1.0749E-02	1.32E-02	4.03E-03	-4.71E+04	5.32E-05		
18	tsw33	F012Eg36	-6.6068E+00	6.27E-01	1.35E-02	3.57E-03	3.14E-03	1.1112E-02	1.42E-02	4.52E-03	-6.44E+04	6.43E-05		
19	tsw33	F012Eg47	-7.4195E+00	2.38E-01	1.38E-02	3.82E-03	2.58E-03	6.4787E-02	6.72E-02	4.84E-03	-5.44E+03	3.25E-04		
20	tsw33	F012Eh 1	-2.5267E+01	1.60E-01	1.68E-02	6.85E-03	4.15E-03	7.8627E-03	1.20E-02	6.55E-03	-5.14E+04	7.84E-05		
21	tsw33	F012El73	-4.1465E+00	1.71E-01	1.26E-02	2.63E-03	1.62E-03	2.0740E-02	2.23E-02	8.15E-03	-3.89E+03	1.82E-04		
22	tsw33	F012Fg26	-4.5607E+00	1.10E+00	1.23E-02	2.36E-03	2.43E-03	1.7365E-02	1.98E-02	3.55E-03	-7.18E+04	7.02E-05		
23	tsw33	F012Fg59	-3.4216E+01	4.79E-01	1.65E-02	6.53E-03	5.34E-03	1.3079E-03	6.64E-03	7.72E-03	-3.20E+05	5.13E-05		
24	tsw33	F012Fg70	-3.3638E+01	6.59E-01	1.64E-02	6.42E-03	5.73E-03	8.3987E-02	8.92E-02	4.17E-03	-5.95E+04	3.73E-04		
25	tsw33	F012Fg80	-2.0564E+01	7.42E-01	1.62E-02	6.24E-03	5.75E-03	8.4814E-02	9.01E-02	6.26E-03	-2.71E+04	5.64E-04		
26	tsw33	F012Fg90	-1.9384E+01	1.34E+00	1.60E-02	6.06E-03	6.57E-03	3.7711E-03	1.03E-02	3.97E-03	-6.36E+05	4.10E-05		
27	tsw34	F0013g 3	-3.5168E+00	1.55E+00	1.49E-02	4.98E-03	5.61E-03	2.2281E-02	2.78E-02	1.13E-02	-1.73E+04	3.15E-04		
28	tsw34	F0013g48	-2.6890E+01	6.92E-01	2.27E-02	1.28E-02	1.16E-02	2.5815E-03	1.41E-02	1.16E-02	-1.13E+05	1.64E-04		
29	tsw34	F0013g91	-1.4310E+01	2.86E-01	1.95E-02	9.55E-03	6.78E-03	7.6241E-03	1.44E-02	8.94E-03	-3.18E+04	1.28E-04		
30	tsw34	F0013h 2	-9.6354E+00	1.91E+00	1.91E-02	9.17E-03	1.09E-02	7.8905E-03	1.87E-02	4.37E-03	-2.25E+05	8.19E-05		

Output-DTN: LB0307FMRADTRN.001.

A portion of the output for the fracture Peclet number is shown in Table G-3 for the mean infiltration scenario. See Wang (2003 [DIRS 163234], SN-LBNL-SCI-236-V1, p. 89) and DTN: LB0307FMRADTRN.001 for the complete output.

The sequence of calculations is given here:

Column A: Rock unit.

Column B: Cell name.

Column C: The adjusted fracture flux (q_{wf}) as shown in Table G-2.

Column D: Fracture half-spacing from Appendix A.

Column E: Distance to fracture flow below drift from Appendix A.

Column F: Effective diffusion coefficient in the fracture from Appendix F.

Column G: Effective fracture velocity using Equation F-1. In Excel, this is

Grn= Crn/(1+(-Crn*Ern/Frn))

Column H: Diffusive mass transfer coefficient for the invert from Appendix E.

Column I: Fracture Peclet number computed using Equation F-2. In Excel, this is

Irn= Grn*Drn/Hrn

Table G-3. Fracture Peclet Number for the Mean Infiltration Scenario

	A	B	C	D	E	F	G	H	I
1	Rock Unit	Cell Name	q_{wf} (mm/yr)	h_f (mm)	Δy_f (mm)	D_{ef} (mm^2/yr)	q_{fe} (mm/yr)	D_{el} (mm^2/yr)	Pe_{fe}
2	tsw33	F012Bl76	-1.55E+04	1.26E+03	5.70E+02	3.31E+02	-5.81E-01	7.25E+02	-1.01E+00
3	tsw33	F012Bl78	-3.11E+04	4.14E+03	4.88E+03	2.27E+03	-4.65E-01	1.53E+02	-1.26E+01
4	tsw33	F012Cl72	-1.09E+04	4.60E+02	5.36E+02	6.23E+02	-1.16E+00	1.68E+02	-3.18E+00
5	tsw33	F012Cl74	-3.59E+04	1.35E+03	1.59E+03	2.53E+03	-1.59E+00	2.18E+02	-9.90E+00
6	tsw33	F012Cm70	-2.46E+05	1.84E+03	1.83E+03	4.63E+03	-2.53E+00	1.34E+02	-3.49E+01
7	tsw33	F012Dg58	-4.07E+04	8.46E+02	1.27E+03	7.77E+02	-6.13E-01	3.58E+02	-1.45E+00
8	tsw33	F012Dl68	-1.06E+05	4.10E+02	5.88E+02	1.12E+03	-1.91E+00	2.67E+02	-2.93E+00
9	tsw33	F012Dl70	-4.49E+04	8.27E+02	1.18E+02	5.82E+01	-4.95E-01	2.41E+02	-1.70E+00
10	tsw33	F012Dl71	-1.87E+05	5.00E+02	1.88E+01	3.80E+03	-2.02E+02	6.24E+02	-1.62E+02
11	tsw33	F012Dl75	-4.36E+04	2.84E+03	5.37E+03	2.54E+03	-4.73E-01	2.93E+02	-4.60E+00
12	tsw33	F012Dl77	-3.16E+04	4.09E+02	6.79E+02	2.80E+03	-4.12E+00	7.89E+01	-2.14E+01
13	tsw33	F012Dl79	-2.88E+04	2.55E+03	3.22E+03	1.54E+03	-4.78E-01	2.94E+02	-4.16E+00
14	tsw33	F012Ef89	-8.23E+04	3.36E+02	5.01E+02	2.82E+03	-5.62E+00	2.51E+02	-7.51E+00

Table G-3. Fracture Peclet Number for the Mean Infiltration Scenario (Continued)

	A	B	C	D	E	F	G	H	I
	Rock Unit	Cell Name	q_{wf} (mm/yr)	h_f (mm)	Δy_f (mm)	D_{ef} (mm^2/yr)	q_{fe} (mm/yr)	D_{el} (mm^2/yr)	Pe_{fe}
15	tsw33	F012Eg 2	-1.23E+05	1.10E+03	5.94E+02	6.67E+02	-1.12E+00	5.24E+02	-2.36E+00
16	tsw33	F012Eg14	-1.62E+04	4.82E+02	5.22E+01	1.09E+03	-2.08E+01	2.94E+02	-3.40E+01
17	tsw33	F012Eg25	-4.71E+04	7.49E+02	7.20E+02	3.05E+02	-4.24E-01	1.09E+02	-2.93E+00
18	tsw33	F012Eg36	-6.44E+04	6.35E+02	4.83E+02	7.93E+02	-1.64E+00	5.51E+02	-1.89E+00
19	tsw33	F012Eg47	-5.44E+03	1.60E+03	7.33E+02	8.73E+02	-1.19E+00	2.99E+02	-6.39E+00
20	tsw33	F012Eh 1	-5.14E+04	1.49E+03	1.36E+03	1.58E+03	-1.16E+00	2.68E+02	-6.48E+00
21	tsw33	F012El73	-3.89E+03	6.33E+02	7.25E+02	3.81E+03	-5.25E+00	4.10E+02	-8.11E+00
22	tsw33	F012Fg26	-7.18E+04	1.79E+03	2.45E+03	1.29E+03	-5.25E-01	1.95E+02	-4.82E+00
23	tsw33	F012Fg59	-3.20E+05	1.21E+03	3.60E+02	2.41E+03	-6.68E+00	5.38E+02	-1.51E+01
24	tsw33	F012Fg70	-5.95E+04	1.94E+03	1.23E+03	3.09E+03	-2.51E+00	1.99E+02	-2.45E+01
25	tsw33	F012Fg80	-2.71E+04	2.17E+02	2.59E+01	1.36E+03	-5.22E+01	4.94E+01	-2.30E+02
26	tsw33	F012Fg90	-6.36E+05	1.23E+03	2.41E+03	3.28E+03	-1.36E+00	3.59E+02	-4.66E+00
27	tsw34	F0013g 3	-1.73E+04	1.48E+02	2.91E+02	3.13E+01	-1.07E-01	5.14E+01	-3.10E-01
28	tsw34	F0013g48	-1.13E+05	1.66E+02	1.45E+01	8.82E+01	-6.08E+00	4.09E+02	-2.47E+00
29	tsw34	F0013g91	-3.18E+04	1.66E+02	8.55E+01	1.90E+03	-2.22E+01	1.47E+02	-2.50E+01
30	tsw34	F0013h 2	-2.25E+05	1.85E+02	1.12E+02	6.04E+02	-5.38E+00	2.53E+02	-3.93E+00

Output-DTN: LB0307FMRADTRN.001.

The matrix Peclet number is computed using Equation 6-30 from the main text, which is

$$Pe_m = \frac{q_m h_f}{D_{el}} \qquad \text{(Eq. G-7)}$$

An example of the sampling for the matrix Peclet number is shown in Table G-4. See Wang (2003 [DIRS 163234], SN-LBNL-SCI-236-V1, p. 91) for the file directory information containing the complete results.

The sequence of calculations is as follows:

Column A: Rock unit.

Column B: Cell name.

Column C: Matrix flux from Appendix B.

Column D: Fracture half-spacing from Appendix A.

Column E: Diffusive mass-transfer coefficient for the invert from Appendix V.

Column F: Matrix Peclet number computed using Equation G-7. In Excel, this is

Frn= Crn*Drn/Ern

Table G-4. Matrix Peclet Numbers for Mean Infiltration Scenario

	A	B	C	D	E	F
1	Rock Unit	Cell Name	q_m (mm/yr)	h_f (mm)	D_{el} (mm^2/yr)	Pe_m
2	tsw33	M012Bl76	-2.4032E-01	1.26E+03	7.25E+02	-4.18E-01
3	tsw33	M012Bl78	-1.4520E-01	4.14E+03	1.53E+02	-3.93E+00
4	tsw33	M012Cl72	-1.3236E+00	4.60E+02	1.68E+02	-3.63E+00
5	tsw33	M012Cl74	-5.1798E-01	1.35E+03	2.18E+02	-3.22E+00
6	tsw33	M012Cm70	-5.0937E-01	1.84E+03	1.34E+02	-7.02E+00
7	tsw33	M012Dg58	-2.2577E-01	8.46E+02	3.58E+02	-5.34E-01
8	tsw33	M012Dl68	-5.3696E-01	4.10E+02	2.67E+02	-8.25E-01
9	tsw33	M012Dl70	-5.5948E-01	8.27E+02	2.41E+02	-1.92E+00
10	tsw33	M012Dl71	-1.2656E+00	5.00E+02	6.24E+02	-1.01E+00
11	tsw33	M012Dl75	-2.6302E-01	2.84E+03	2.93E+02	-2.55E+00
12	tsw33	M012Dl77	-2.1155E-01	4.09E+02	7.89E+01	-1.10E+00
13	tsw33	M012Dl79	-4.4544E-01	2.55E+03	2.94E+02	-3.87E+00
14	tsw33	M012Ef89	-1.4086E-01	3.36E+02	2.51E+02	-1.88E-01
15	tsw33	M012Eg 2	-1.1983E-01	1.10E+03	5.24E+02	-2.51E-01
16	tsw33	M012Eg14	-5.8384E-02	4.82E+02	2.94E+02	-9.55E-02
17	tsw33	M012Eg25	-5.3101E-02	7.49E+02	1.09E+02	-3.67E-01
18	tsw33	M012Eg36	-1.1091E-01	6.35E+02	5.51E+02	-1.28E-01
19	tsw33	M012Eg47	-1.6404E-01	1.60E+03	2.99E+02	-8.81E-01
20	tsw33	M012Eh 1	-1.8512E-01	1.49E+03	2.68E+02	-1.03E+00
21	tsw33	M012El73	-4.8153E-01	6.33E+02	4.10E+02	-7.44E-01
22	tsw33	M012Fg26	-1.0880E-01	1.79E+03	1.95E+02	-9.99E-01
23	tsw33	M012Fg59	-3.2473E-01	1.21E+03	5.38E+02	-7.32E-01
24	tsw33	M012Fg70	-2.1330E-01	1.94E+03	1.99E+02	-2.08E+00
25	tsw33	M012Fg80	-1.4723E-01	2.17E+02	4.94E+01	-6.47E-01
26	tsw33	M012Fg90	-1.3500E-01	1.23E+03	3.59E+02	-4.61E-01
27	tsw34	M0013g 3	-1.2727E-02	1.48E+02	5.14E+01	-3.67E-02
28	tsw34	M0013g48	-1.5652E-02	1.66E+02	4.09E+02	-6.35E-03
29	tsw34	M0013g91	-1.4594E-02	1.66E+02	1.47E+02	-1.65E-02
30	tsw34	M0013h 2	-6.9779E-02	1.85E+02	2.53E+02	-5.10E-02

Output-DTN: LB0307FMRADTRN.001.

The dimensionless invert depth is computed from the invert depth, divided by the fracture half-spacing. The variation in the invert depth is sampled as a uniform random number between 675 mm and 806 mm (see Figure 6-9). A portion of the output for the dimensionless invert depth is shown in Table G-5. See Wang (2003 [DIRS 163234], SN-LBNL-SCI-236-V1, p. 94) and DTN: LB0307FMRADTRN.001 for the complete output.

The sequence of calculations is as follows:

Column A: Rock unit.

Column B: Cell name.

Column C: Uniform random numbers generated by the Excel spreadsheet function RAND() and saved.

Column D: Generate random invert depth between 675 and 806 mm. In Excel, this is

$$Drn= 675+(806-675)*Crn$$

Column E: Fracture half-spacing from Appendix A.

Column F: Dimensionless invert depth is computed from the ratio of the invert depth to the fracture half-spacing. In Excel, this is

$$Frn= Drn/Ern$$

Table G-5. Dimensionless Invert Depth (Independent of Infiltration Scenario)

	A	B	C	D	E	F
1	Rock Unit	Cell Name	Fixed Uniform Random Number	Invert Depth (mm)	h_f (mm)	Dimensionless Invert Depth
2	tsw33	F012Bl76	5.3041E-01	7.44E+02	1.26E+03	5.91E-01
3	tsw33	F012Bl78	1.7330E-01	6.98E+02	4.14E+03	1.68E-01
4	tsw33	F012Cl72	2.3364E-01	7.06E+02	4.60E+02	1.53E+00
5	tsw33	F012Cl74	7.5332E-01	7.74E+02	1.35E+03	5.72E-01
6	tsw33	F012Cm70	5.8412E-01	7.52E+02	1.84E+03	4.08E-01
7	tsw33	F012Dg58	8.0829E-01	7.81E+02	8.46E+02	9.23E-01
8	tsw33	F012Dl68	4.2416E-01	7.31E+02	4.10E+02	1.78E+00
9	tsw33	F012Dl70	8.3845E-01	7.85E+02	8.27E+02	9.50E-01
10	tsw33	F012Dl71	6.5790E-01	7.61E+02	5.00E+02	1.52E+00
11	tsw33	F012Dl75	4.3296E-01	7.32E+02	2.84E+03	2.57E-01
12	tsw33	F012Dl77	2.7310E-01	7.11E+02	4.09E+02	1.74E+00
13	tsw33	F012Dl79	3.7391E-01	7.24E+02	2.55E+03	2.83E-01
14	tsw33	F012Ef89	3.6039E-01	7.22E+02	3.36E+02	2.15E+00
15	tsw33	F012Eg 2	6.4304E-01	7.59E+02	1.10E+03	6.91E-01
16	tsw33	F012Eg14	5.1883E-01	7.43E+02	4.82E+02	1.54E+00
17	tsw33	F012Eg25	6.3216E-01	7.58E+02	7.49E+02	1.01E+00
18	tsw33	F012Eg36	6.1548E-01	7.56E+02	6.35E+02	1.19E+00
19	tsw33	F012Eg47	8.8158E-01	7.90E+02	1.60E+03	4.93E-01

Table G-5. Dimensionless Invert Depth (Independent of Infiltration Scenario (Continued)

	A	B	C	D	E	F
	Rock Unit	Cell Name	Fixed Uniform Random Number	Invert Depth (mm)	h_f (mm)	Dimensionless Invert Depth
20	tsw33	F012Eh 1	1.8140E-01	6.99E+02	1.49E+03	4.68E-01
21	tsw33	F012El73	7.6937E-01	7.76E+02	6.33E+02	1.23E+00
22	tsw33	F012Fg26	2.3021E-01	7.05E+02	1.79E+03	3.94E-01
23	tsw33	F012Fg59	1.1181E-01	6.90E+02	1.21E+03	5.69E-01
24	tsw33	F012Fg70	3.0337E-01	7.15E+02	1.94E+03	3.68E-01
25	tsw33	F012Fg80	6.3025E-01	7.58E+02	2.17E+02	3.49E+00
26	tsw33	F012Fg90	9.3048E-01	7.97E+02	1.23E+03	6.50E-01
27	tsw34	F0013g 3	4.4532E-01	7.33E+02	1.48E+02	4.94E+00
28	tsw34	F0013g48	6.5840E-01	7.61E+02	1.66E+02	4.58E+00
29	tsw34	F0013g91	3.3859E-01	7.19E+02	1.66E+02	4.34E+00
30	tsw34	F0013h 2	5.0435E-01	7.41E+02	1.85E+02	4.01E+00

Output-DTN: LB0307FMRADTRN.001.

APPENDIX H

SAMPLING FOR THE PARAMETER SETS USED IN THE CALCULATION OF FRACTURE-MATRIX RADIONUCLIDE FLUX DISTRIBUTIONS FROM WASTE EMPLACEMENT DRIFTS

SAMPLING FOR THE PARAMETER SETS USED IN THE CALCULATION OF FRACTURE-MATRIX RADIONUCLIDE FLUX DISTRIBUTIONS FROM WASTE EMPLACEMENT DRIFTS

This appendix provides additional information pertaining to Sections 6.4.6 and 6.5 of the main text. Each case investigated for the calculation of the radionuclide fracture-matrix flux fraction, for radionuclide transport from the waste emplacement drift invert into the rock, requires four dimensionless parameters. These were the parameters given at the end of Section 6.4.2; they are repeated here:

$Pe_m \equiv$ matrix – invert mass transfer Peclet number

$Pe_{fe} \equiv$ fracture – invert mass transfer Peclet number

$\theta_f \equiv$ fracture water content

$y_{dm} \equiv$ dimensionless invert depth

The design information in Table 4-9 (BSC 2004 [DIRS 168370], 800-IED-WIS0-00103-000-00A) may be used to compute the percentage of total waste-emplacement drift area in each of the four rock units (tsw33, tsw34, tsw35, and tsw36). Note that in the IED geologic lithostratigraphic units are used. The correspondence between these units the UZ flow model units are as follows: the tptpul is the tsw33, the tptpmn in the tsw34, the tptpll is the tsw35, and the tptpln is the tsw36. The total percentage of waste emplacement in each of the four rock units is shown in Table H-1:

Table H-1. Percentage of Waste Emplacement in Each Rock Unit

	Drift Area (m^2)	%tsw33	%tsw34	%tsw35	%tsw36	Drift Area tsw33 (m^2)	Drift Area tsw34 (m^2)	Drift Area tsw35 (m^2)	Drift Area tsw36 (m^2)	Total Drift Area (m^2)
Panel 1	298850	0	40	60	0	0	119172	179678	0	
Panel 2	1477867	0	5	91	4	0	80213	1341147	56507	
Panel 3	1862136	12	22	66	0	224398	416618	1221120	0	
Panel 4	1344299	0	0	95	5	0	0	1271323	72976	
						224398	616003	4013268	129483	4983152
			Overall Fractions =			4.5%	12.4%	80.5%	2.6%	

Source: Table 4-9.

The percentages are rounded to the nearest percent, except for tsw33, which is truncated to 4 percent such that the total is 100 percent. For a total of 24 samples, this leads to the following expected number of samples in each rock unit as given in Table H-2:

Table H-2. Number of Samples in Each Rock Unit

Rock unit	Number of samples in each rock unit
Tsw33	1
Tsw34	3
Tsw35	19
Tsw36	1

Random sampling for each of these dimensionless parameters at every model grid across a laterally continuous section through the repository horizon is presented in Appendix G. These parameters are assembled and sampled to provide the cases computed for fracture-matrix release fractions. The sampling selects 24 random parameter sets from each infiltration scenario. To ensure sampling from all host rock units, one random sample is drawn from each of the tsw33 and tsw36, three random samples from the tsw34, and 19 random samples from the tsw35. The Peclet numbers and fracture water film thicknesses selected here are used as inputs for the calculations performed in Section 6.5. A portion of the output for the sampled values are given in Table H-3. See Wang (2003 [DIRS 163234], SN-LBNL-SCI-236-V1, p. 100) and DTN: LB0307FMRADTRN.001 for the complete output.

The sequence of calculations is given here:

Column A: Rock unit.

Column B: Fracture cell name.

Column C: Matrix cell name.

Column D: Fracture Peclet number from Appendix G.

Column E: Matrix Peclet number from Appendix G.

Column F: Fracture water content from Appendix G.

Column G: Dimensionless invert depth from Appendix G.

Column H: Uniform random numbers generated by the Excel spreadsheet function RAND() and saved.

Column I: Convert cumulative probability in Column H to an integer between 1 and 25 for the tsw33, between 26 and 95 for the tsw34, between 96 and 428 for the tsw35 and between 429 and 433 for the tsw36. In Excel, this is

Irn= INT(1+25*Hrn) for the tsw33 in row 2

Irn= INT(26+95*Hrn) for the tsw34 in rows 3, 4, and 5

Irn= INT(96+428*Hrn) for the tsw35 in rows 6 through 24

Irn= INT(429+433*Hrn) for the tsw36 in row 25

Column J: Find selected rock type from Column A. In Excel, this is

Jrn= INDEX(A$2:A$434,$Irn)

Column K: Find selected Fracture Peclet number from Column D. In Excel, this is

Krn= INDEX(D$2:D$434,$Irn)

Column L: Find selected Matrix Peclet number from Column E. In Excel, this is

Lrn= INDEX(E$2:E$434,$Irn)

Column M: Find selected fracture water content from Column F. In Excel, this is

Mrn= INDEX(F$2:F$434,$Irn)

Column N: Find selected dimensionless invert depth from Column G. In Excel, this is

Nrn= INDEX(G$2:G$434,$Irn)

Values selected in columns K, L, and M are used as input for the calculations discussed in Section 6.5.

Table H-3. Sampled Parameter Sets for Mean Infiltration Scenarios

	A	B	C	D	E	F	G	H	I	J	K	L	M	N	O
1	Rock Unit	Fracture Cell Name	Matrix Cell Name	Fracture Peclet Number, Pe_{ef}	Matrix Peclet Number, Pe_m	Fracture Water Content, θ_f	Dimensionless Invert Depth, y_{dm}	Fixed Uniform Random Number	Uniform Random Integer ranging over cells in each rock unit	Selected Rock Type	Selected Fracture Peclet Number, Pe_{fe}	Selected Matrix Peclet Number, Pe_m	Selected Fracture Water Content, θ_f	Selected Dimensionless Invert Depth, y_{dm}	Case Number
2	tsw33	F012Bl76	M012Bl76	-1.01E+00	-4.18E-01	5.12E-04	5.91E-01	3.2628E-01	9	tsw33	-1.62E+02	-1.01E+00	3.58E-05	1.52E+00	1
3	tsw33	F012Bl78	M012Bl78	-1.26E+01	-3.93E+00	3.89E-04	1.68E-01	9.4126E-01	91	tsw34	-4.05E+01	-2.62E-02	4.27E-04	3.62E+00	2
4	tsw33	F012Cl72	M012Cl72	-3.18E+00	-3.63E+00	3.77E-04	1.53E+00	5.0552E-01	61	tsw34	-2.87E+00	-5.99E-03	4.18E-04	8.14E+00	3
5	tsw33	F012Cl74	M012Cl74	-9.90E+00	-3.22E+00	1.91E-04	5.72E-01	5.7828E-01	66	tsw34	-2.45E+00	-4.48E-03	6.15E-05	7.78E+00	4
6	tsw33	F012Cm70	M012Cm70	-3.49E+01	-7.02E+00	2.36E-05	4.08E-01	5.8022E-01	289	tsw35	-4.37E+01	-1.90E-02	5.84E-04	3.91E+00	5
7	tsw33	F012Dg58	M012Dg58	-1.45E+00	-5.34E-01	1.09E-04	9.23E-01	5.2025E-01	269	tsw35	-6.49E+00	-1.33E-02	2.23E-04	5.38E+00	6
8	tsw33	F012Dl68	M012Dl68	-2.93E+00	-8.25E-01	4.52E-05	1.78E+00	6.5149E-01	312	tsw35	-1.47E+00	-3.96E-02	4.51E-05	1.17E+00	7
9	tsw33	F012Dl70	M012Dl70	-1.70E+00	-1.92E+00	1.41E-04	9.50E-01	8.8356E-01	390	tsw35	-8.82E-01	-2.00E-02	7.78E-05	1.92E+00	8
10	tsw33	F012Dl71	M012Dl71	-1.62E+02	-1.01E+00	3.58E-05	1.52E+00	3.2712E-01	204	tsw35	-2.29E+01	-6.15E-02	1.57E-04	1.59E+00	9
11	tsw33	F012Dl75	M012Dl75	-4.60E+00	-2.55E+00	1.91E-04	2.57E-01	9.5806E-01	415	tsw35	-8.53E+00	-3.56E-02	5.23E-05	1.68E+00	10
12	tsw33	F012Dl77	M012Dl77	-2.14E+01	-1.10E+00	2.86E-05	1.74E+00	4.3343E-01	240	tsw35	-1.66E+00	-5.90E-03	5.62E-05	6.82E+00	11
13	tsw33	F012Dl79	M012Dl79	-4.16E+00	-3.87E+00	3.90E-04	2.83E-01	5.3805E-01	275	tsw35	-2.63E+00	-6.72E-03	9.60E-04	5.35E+00	12
14	tsw33	F012Ef89	M012Ef89	-7.51E+00	-1.88E-01	2.44E-04	2.15E+00	8.3590E-01	374	tsw35	-4.99E+00	-1.13E-02	1.19E-04	1.69E+00	13
15	tsw33	F012Eg 2	M012Eg 2	-2.36E+00	-2.51E-01	9.75E-05	6.91E-01	5.9247E-01	293	tsw35	-1.20E+02	-7.27E-03	7.44E-05	3.62E+00	14
16	tsw33	F012Eg14	M012Eg14	-3.40E+01	-9.55E-02	2.41E-04	1.54E+00	4.0651E-01	231	tsw35	-9.89E-01	-3.08E-02	4.39E-04	2.17E+00	15
17	tsw33	F012Eg25	M012Eg25	-2.93E+00	-3.67E-01	5.32E-05	1.01E+00	3.3043E-01	206	tsw35	-1.95E+00	-1.85E-02	1.10E-04	1.08E+00	16
18	tsw33	F012Eg36	M012Eg36	-1.89E+00	-1.28E-01	6.43E-05	1.19E+00	4.4509E-02	110	tsw35	-3.46E+01	-7.85E-03	6.74E-04	3.32E+00	17
19	tsw33	F012Eg47	M012Eg47	-6.39E+00	-8.81E-01	3.25E-04	4.93E-01	5.7180E-01	286	tsw35	-3.34E+00	-2.03E-02	5.61E-05	2.99E+00	18
20	tsw33	F012Eh 1	M012Eh 1	-6.48E+00	-1.03E+00	7.84E-05	4.68E-01	8.5478E-01	380	tsw35	-2.09E-01	-9.65E-03	1.17E-04	2.36E+00	19
21	tsw33	F012El73	M012El73	-8.11E+00	-7.44E-01	1.82E-04	1.23E+00	2.3670E-01	174	tsw35	-4.59E+00	-2.77E-02	6.28E-05	1.33E+00	20
22	tsw33	F012Fg26	M012Fg26	-4.82E+00	-9.99E-01	7.02E-05	3.94E-01	6.6134E-01	316	tsw35	-1.14E+01	-8.15E-03	6.06E-04	5.43E+00	21
23	tsw33	F012Fg59	M012Fg59	-1.51E+01	-7.32E-01	5.13E-05	5.69E-01	2.3843E-01	175	tsw35	-3.26E+00	-7.18E-03	8.70E-05	4.54E+00	22
24	tsw33	F012Fg70	M012Fg70	-2.45E+01	-2.08E+00	3.73E-04	3.68E-01	8.1817E-01	368	tsw35	-6.11E+00	-6.35E-02	1.29E-04	9.09E-01	23
25	tsw33	F012Fg80	M012Fg80	-2.30E+02	-6.47E-01	5.64E-04	3.49E+00	4.2699E-01	431	tsw36	-7.60E+00	-1.16E-02	1.28E-04	3.65E+00	24
26	tsw33	F012Fg90	M012Fg90	-4.66E+00	-4.61E-01	4.10E-05	6.50E-01								
27	tsw34	F0013g 3	M0013g 3	-3.10E-01	-3.67E-02	3.15E-04	4.94E+00								
28	tsw34	F0013g48	M0013g48	-2.47E+00	-6.35E-03	1.64E-04	4.58E+00								
29	tsw34	F0013g91	M0013g91	-2.50E+01	-1.65E-02	1.28E-04	4.34E+00								
30	tsw34	F0013h 2	M0013h 2	-3.93E+00	-5.10E-02	8.19E-05	4.01E+00								

Output-DTN: LB0307FMRADTRN.001.

APPENDIX I

DISTRIBUTIONS FOR MATRIX DIFFUSION AND MEASURED MATRIX DIFFUSION COEFFICIENTS

DISTRIBUTIONS FOR MATRIX DIFFUSION AND MEASURED MATRIX DIFFUSION COEFFICIENTS

This appendix provides additional information pertaining to Section 6.4.5 of the main text. Anion and cation distributions for matrix diffusion coefficients are sampled from a beta distribution, using the distribution statistics shown here:

Table I-1. Matrix Diffusion Distributions

Solute	Min (m^2/s)	Max (m^2/s)	Mean (m^2/s)	Std Dev (m^2/s)	Distribution Type
Anions	0	1.0 E-9	3.2 E-11	1.0 E-11	Beta
Cations	0	1.0 E-9	1.6 E-10	0.5 E-10	Beta

DTN: LA0003JC831362.001 [DIRS 149557].

The distributions are generated by sampling 1,000 values from each beta distribution. The sampling for the beta distribution uses the approximation for the inverse as given in Equation 26.5.22 of Abramowitz and Stegun (1972 [DIRS 103280]). This method requires the generation of a Gaussian random number. Gaussian random numbers are computed using the rational approximation for the inverse cumulative probability distribution for a Gaussian random variable, as given in Equation 26.2.23 of Abramowitz and Stegun (1972 [DIRS 103280]). See Scientific Notebook by Wang (2003 [DIRS 163234], SN-LBNL-SCI-236-V1, pp. 40–42) for a discussion of the generation of Gaussian random numbers. A portion of the output with the results for anions are given in Table I-2. See Wang (2003 [DIRS 163234], SN-LBNL-SCI-236-V1, p. 75) and Output-DTN: LB0307FMRADTRN.001 for the complete output. The sequence of calculations is given here:

Column A: Uniform random numbers generated by the Excel spreadsheet function RAND() and saved. These are the cumulative probabilities, p.

Column B: The normalized Gaussian random number corresponding to the cumulative probability in Column A.

Column C: The parameter λ in the beta inverse function is given by Abramowitz and Stegun (1972 [DIRS 103280], Equation 26.5.22)

$$\lambda = \frac{y_p^2 - 3}{6} \qquad \text{(Eq. I-1)}$$

where y_p is defined in Column B. In Excel, this is

Crn=(Brn^2-3)/6

Column D: The parameter *w* in the beta inverse function is given by Abramowitz and Stegun (1972 [DIRS 103280], Equation 26.5.22)

$$w = \frac{y_p (h+\lambda)^{\frac{1}{2}}}{h} - \left(\frac{1}{2b-1} - \frac{1}{2a-1}\right)\left(\lambda + \frac{5}{6} - \frac{2}{3h}\right) \quad \text{(Eq. I-2)}$$

In Excel, this is

Drn= (Brn*(($K$2+Crn)^0.5)/$K$2)-((2*$J$2-1)^(-1)-(2*$I$2-1)^(-1))*(Crn+(5/6)-2/(3*$K$2))

Column E: The beta random number, x_p, is given by Abramowitz and Stegun (1972 [DIRS 103280], Equation 26.5.22)

$$x_p \approx \frac{a}{a + be^{2w}} \quad \text{(Eq. I-3)}$$

In Excel, this is

Ern=$I$2/($I$2+$J$2*EXP(2*Drn))

Column F: Contains the ordered values computed in Column E.

Column G: Contains the value of the mean matrix diffusion coefficient, μ_{D_m}, from Table- I-1.

Column H: Contains the value of the matrix diffusion coefficient standard deviation, σ_{D_m}, from Table I-1.

Column I: The beta distribution parameter *a* is derived from Abramowitz and Stegun (1972 [DIRS 103280], Equation 26.1.33) (for detailed derivation, see Appendix K)

$$a = \mu_{D_m}\left[\frac{\mu_{D_m}(1-\mu_{D_m})}{\sigma_{D_m}^2} - 1\right] \quad \text{(Eq. I-4)}$$

In Excel, this is

I2=G2*((G2*(1-G2)/H2^2)-1)

Column J: The beta distribution parameter *b* is derived from Abramowitz and Stegun (1972 [DIRS 103280], Equation 26.1.33) (for detailed derivation, see Appendix K)

$$b = (1-\mu_{D_m})\left[\frac{\mu_{D_m}(1-\mu_{D_m})}{\sigma_{D_m}^2} - 1\right] \quad \text{(Eq. I-5)}$$

In Excel, this is

J2=(1-G2)*((G2*(1-G2)/H2^2)-1)

Column K: The parameter *h* in the beta inverse function is given by Abramowitz and Stegun (1972 [DIRS 103280], Equation 26.5.22)

$$h = 2\left(\frac{1}{2a-1}+\frac{1}{2b-1}\right)^{-1} \quad \text{(Eq. I-6)}$$

In Excel, this is

K2=2*((2*I2-1)^(-1)+(2*J2-1)^(-1))^(-1)

The Reimus et al. (2002 [DIRS 163008]) correlation is sampled according to the scheme outlined in Section 6.4.5 and Equations 6-52 through 6-56, which are shown here:

$$\log(D_m) = -3.49 + 1.38\theta_m + 0.165\log(k_w) \quad \text{(Eq. I-7)}$$

$$X = \log\left(\frac{D_0}{D_m}\right) \quad \text{(Eq. I-8)}$$

$$\mu_X = \log(D_0) - \overline{\log(D_m)} \quad \text{(Eq. I-9)}$$

$$Y = \ln(X) \quad \text{(Eq. I-10)}$$

$$\mu_Y = \ln(\mu_X) \quad \text{(Eq. I-11)}$$

Here, D_0 is a limiting value of D_m taken to be 10^{-9} m^2/s (see Table I-1). The sampling follows a lognormal distribution scheme for the variable *X*, in which the variable *Y* in Equation I-10 is normally distributed. This sampled variable is reduced to the matrix diffusion coefficient using Equations I-8 and I-10. Gaussian random numbers are computed using the rational approximation for the inverse cumulative probability distribution for a Gaussian random variable as given in Equation 26.2.23 of Abramowitz and Stegun (1972 [DIRS 103280]). See Scientific Notebook by Wang (2003 [DIRS 163234], SN-LBNL-SCI-236-V1, pp. 40–42) for a discussion of the generation of Gaussian random numbers. A portion of the output is shown in Table I-3. See Wang (2003 [DIRS 163234], SN-LBNL-SCI-236-V1, p. 76) and DTN: LB0307FMRADTRN.001 for the complete output.

Table I-2. Anion Matrix Diffusion Coefficient Distribution

	A	B	C	D	E	F	G	H	I	J	K
1	Fixed Uniform Random Number (P)	yP - normalized Gaussian random number	Lambda	w	x_P - Beta random number (Dm, m^2/s)	Ordered Distribution (Dm, m^2/s)	Mean Dm - m2/s	Standard deviation Dm m^2/s	a	b	h
2	5.7681E-01	1.9336E-01	-4.94E-01	4.73E-02	2.91E-11	9.49E-12	3.20E-11	1.00E-11	1.02E+01	3.20E+11	3.90E+01
3	1.5444E-02	-2.1589E+00	2.77E-01	-2.91E-01	5.73E-11	9.78E-12					
4	8.9037E-01	1.2287E+00	-2.48E-01	2.25E-01	2.04E-11	1.23E-11					
5	5.6024E-01	1.5127E-01	-4.96E-01	4.05E-02	2.95E-11	1.32E-11					
6	3.7359E-01	-3.2192E-01	-4.83E-01	-3.41E-02	3.43E-11	1.33E-11					
7	2.4730E-01	-6.8273E-01	-4.22E-01	-8.86E-02	3.82E-11	1.34E-11					
8	9.0546E-01	1.3135E+00	-2.12E-01	2.41E-01	1.98E-11	1.35E-11					
9	7.0270E-01	5.3178E-01	-4.53E-01	1.03E-01	2.60E-11	1.37E-11					
10	4.1033E-01	-2.2629E-01	-4.91E-01	-1.94E-02	3.33E-11	1.41E-11					
11	1.0581E-01	-1.2493E+00	-2.40E-01	-1.70E-01	4.50E-11	1.42E-11					
12	3.9859E-01	-2.5657E-01	-4.89E-01	-2.41E-02	3.36E-11	1.49E-11					
13	8.0209E-01	8.4894E-01	-3.80E-01	1.58E-01	2.33E-11	1.49E-11					
14	5.1719E-01	4.2995E-02	-5.00E-01	2.31E-02	3.06E-11	1.49E-11					
15	5.6921E-01	1.7402E-01	-4.95E-01	4.42E-02	2.93E-11	1.50E-11					
16	4.4208E-01	-1.4540E-01	-4.96E-01	-6.73E-03	3.24E-11	1.52E-11					
17	8.4520E-01	1.0160E+00	-3.28E-01	1.87E-01	2.20E-11	1.53E-11					
18	9.3388E-01	1.5056E+00	-1.22E-01	2.76E-01	1.84E-11	1.53E-11					
19	8.3627E-01	9.7919E-01	-3.40E-01	1.81E-01	2.23E-11	1.53E-11					
20	2.0787E-01	-8.1365E-01	-3.90E-01	-1.08E-01	3.97E-11	1.54E-11					
21	6.9208E-01	5.0136E-01	-4.58E-01	9.82E-02	2.63E-11	1.57E-11					
22	5.2997E-01	7.5015E-02	-4.99E-01	2.82E-02	3.02E-11	1.57E-11					
23	8.1050E-02	-1.3983E+00	-1.74E-01	-1.91E-01	4.68E-11	1.58E-11					
24	2.0226E-01	-8.3341E-01	-3.84E-01	-1.11E-01	3.99E-11	1.58E-11					
25	6.0195E-01	2.5798E-01	-4.89E-01	5.79E-02	2.85E-11	1.59E-11					
26	9.4478E-01	1.5966E+00	-7.52E-02	2.94E-01	1.78E-11	1.61E-11					
27	9.0122E-01	1.2887E+00	-2.23E-01	2.36E-01	1.99E-11	1.61E-11					
28	6.8250E-02	-1.4892E+00	-1.30E-01	-2.03E-01	4.80E-11	1.62E-11					
29	4.9429E-01	-1.4281E-02	-5.00E-01	1.40E-02	3.11E-11	1.63E-11					
30	5.9879E-01	2.4979E-01	-4.90E-01	5.65E-02	2.86E-11	1.63E-11					

Output-DTN: LB0307FMRADTRN.001.

The sequence of calculations is as follows:

Column A: Uniform random numbers generated by the Excel spreadsheet function RAND() and saved. These are the cumulative probabilities, p.

Column B: The normalized Gaussian random number corresponding to the cumulative probability in Column A.

Column C: The corresponding random value of Y is derived from the normalized Gaussian random variable through the normalization definition:

$$f = x_p \sigma_Y + \mu_Y \quad \text{(Eq. I-12)}$$

In Excel, this is

Crn=Brn*$I$2+$H$2

where μ_Y and σ_Y are defined as discussed below.

Column D: This column calculates the fracture frequency through the inverse of (Eq. I-11)

$$X = \exp(Y) \quad \text{(Eq. I-13)}$$

In Excel, this is

Drn=exp(Crn)

Column E: The matrix diffusion coefficient is obtained from a known value of X using Equation I-8. In Excel, this is

Ern=10^(-Drn-9) (Eq. I-14)

Column F: The cumulative probability based on rank. In Excel, this is

Frn=F(rn-1)+$F$2

and

F1=1/1001

Column G: The values from Column E in ascending order.

Column H: Contains the value of μ_Y (see below).

Column I: Contains the value of σ_Y (see below).

The mean value for the case shown in Figure 6-22 is equal to the log(D_m), which is equal to the logarithm of the square root of the product of the mean values from Table I-1. The standard deviation is then adjusted to provide a distribution with a spread representative of the anion and cation curves shown in Figure 6-22. The mean value for Y is then computed from Equations I-9 and I-11. The "high" and "low" cases shown in Figure 6-23 are computed using mean values for log(D_m) computed from Equation I-7, using the 5th and 95th percentile matrix water content and matrix effective permeability computed in the mean infiltration scenario from Appendix F and converting to m^2/s. The data shown in Figure 6-24 are from DTN: LA0003JC831362.001 [DIRS 149557] and from Reimus et al. (2002 [DIRS 163008]). Both data sets contain values of D_m for pertechnetate (technetium) and tritium. Data for bicarbonate diffusion come from Reimus et al. (2002 [DIRS 163008]). These data are combined and ordered to generate a cumulative probability distribution, where the cumulative probability is defined by the order number of the sequence divided by the number of samples plus 1.

Table I-3. Matrix Diffusion Coefficient Distribution using Reimus et al. (2002 [DIRS 163008]) Correlation

	A	B	C	D	E	F	G	H	I
1	Fixed Uniform Random Number (P)	x_P - normalized Gaussian random number	x - Gaussian random number	Transfor-mation to -9-logDm	Transfor-mation to Dm	Cumulative Probability	Ordered Dm for Reimus mean high	Trans-formed mean	Standard deviation
2	5.3281E-01	8.2139E-02	2.79E-01	1.32E+00	4.76E-11	9.99E-04	7.89E-13	2.54E-01	3.00E-01
3	4.6699E-01	-8.2631E-02	2.30E-01	1.26E+00	5.52E-11	2.00E-03	1.04E-12		
4	3.3136E-01	-4.3574E-01	1.24E-01	1.13E+00	7.38E-11	3.00E-03	1.34E-12		
5	9.3271E-01	1.4966E+00	7.03E-01	2.02E+00	9.53E-12	4.00E-03	1.42E-12		
6	6.3809E-01	3.5292E-01	3.60E-01	1.43E+00	3.68E-11	5.00E-03	1.61E-12		
7	8.6930E-01	1.1232E+00	5.91E-01	1.81E+00	1.56E-11	5.99E-03	1.63E-12		
8	4.5888E-01	-1.0301E-01	2.24E-01	1.25E+00	5.62E-11	6.99E-03	2.00E-12		
9	2.0184E-01	-8.3491E-01	4.02E-03	1.00E+00	9.91E-11	7.99E-03	2.09E-12		
10	8.4635E-01	1.0209E+00	5.61E-01	1.75E+00	1.77E-11	8.99E-03	2.42E-12		
11	5.7322E-01	1.8423E-01	3.10E-01	1.36E+00	4.33E-11	9.99E-03	2.43E-12		
12	3.3340E-01	-4.3010E-01	1.25E-01	1.13E+00	7.35E-11	1.10E-02	2.66E-12		
13	1.2658E-01	-1.1428E+00	-8.84E-02	9.15E-01	1.21E-10	1.20E-02	2.76E-12		
14	9.0245E-01	1.2958E+00	6.43E-01	1.90E+00	1.25E-11	1.30E-02	2.76E-12		
15	6.4196E-01	3.6326E-01	3.63E-01	1.44E+00	3.64E-11	1.40E-02	3.14E-12		
16	9.9078E-01	2.3570E+00	9.62E-01	2.62E+00	2.42E-12	1.50E-02	3.23E-12		
17	5.1764E-01	4.4122E-02	2.68E-01	1.31E+00	4.93E-11	1.60E-02	4.08E-12		
18	9.3863E-01	1.5437E+00	7.18E-01	2.05E+00	8.92E-12	1.70E-02	4.20E-12		
19	7.0570E-01	5.4049E-01	4.17E-01	1.52E+00	3.04E-11	1.80E-02	4.33E-12		
20	6.8929E-01	4.9342E-01	4.03E-01	1.50E+00	3.19E-11	1.90E-02	4.88E-12		
21	2.9941E-01	-5.2571E-01	9.68E-02	1.10E+00	7.91E-11	2.00E-02	4.97E-12		
22	4.4436E-01	-1.3961E-01	2.13E-01	1.24E+00	5.80E-11	2.10E-02	5.04E-12		
23	7.3649E-04	-3.1802E+00	-7.00E-01	4.97E-01	3.19E-10	2.20E-02	5.11E-12		
24	8.9592E-01	1.2588E+00	6.32E-01	1.88E+00	1.31E-11	2.30E-02	5.11E-12		
25	3.2285E-01	-4.5932E-01	1.17E-01	1.12E+00	7.52E-11	2.40E-02	5.20E-12		
26	7.2163E-01	5.8732E-01	4.31E-01	1.54E+00	2.90E-11	2.50E-02	5.45E-12		
27	9.9740E-01	2.7953E+00	1.09E+00	2.98E+00	1.04E-12	2.60E-02	5.50E-12		
28	6.8463E-01	4.8028E-01	3.99E-01	1.49E+00	3.24E-11	2.70E-02	5.52E-12		
29	7.1169E-01	5.5794E-01	4.22E-01	1.52E+00	2.99E-11	2.80E-02	5.89E-12		
30	7.9956E-01	8.3989E-01	5.06E-01	1.66E+00	2.19E-11	2.90E-02	6.01E-12		

Output-DTN: LB0307FMRADTRN.001.

INTENTIONALLY LEFT BLANK

APPENDIX J

EXAMPLE OF CALCULATION FOR FRACTURE-MATRIX PARTITIONING

EXAMPLE OF CALCULATION FOR FRACTURE-MATRIX PARTITIONING

This appendix provides additional information pertaining to Section 6.4.4 of the main text. The calculation tool used to solve Equations 40 through 44 is Mathcad V11. The implementation of Mathcad for nominal cases 1 with 1,024 points is given on the following pages.

NOMINAL CASE 1 - 1024

Values used for calculation

$Pe_{fe} := -1$ **Pe_{fe} is the fracture Peclet number**

$Pe_m := -0.004$ **Pe_m is the matrix Peclet number**

$\theta_f := 0.0001$ **θ_f is the fracture water content**

$y_{dm} := 4.00$ **y_{dm} is the dimensionless invert thickness**

$b_d := \theta_f$ **b_d is the dimensionless fracture water thickness**

$j_{max} := 1023$ **j_{max}+1 is the number of Fourier coefficients**

Distance coordinate along drift wall

$i := 0 .. j_{max}$ **i is reference number for the coordinates along the drift wall**

$j := 0 .. j_{max}$ **j is the reference number for the Fourier coefficients**

$x_{d_i} := \frac{i}{j_{max}}$ **x_{di} is the dimensionless distance along the drift wall**

Sample values for verification of x_{di}

$x_{d_0} = 0$ $x_{d_1} = 9.775 \times 10^{-4}$ $x_{d_2} = 1.955 \times 10^{-3}$ ..... $x_{d_{1022}} = 0.999$ $x_{d_{1023}} = 1$

Solution for Fourier coefficients

$$q_{d_i} := Pe_{fe} + 0.5\cdot\left(Pe_m - Pe_{fe}\right)\cdot\left(\Phi\left(x_{d_i} - b_d\right) - \Phi\left(b_d - x_{d_i}\right) + 1\right)$$ Eq. (29), (30), (31) from main

q_{di} is the dimensionless water flux profile at the invert-rock interface

Note that the Heaviside step function (Φ) is defined to be 1 at x=0. Therefore, the combination of step functions, 0.5(Φ(x)-Φ(–x)+1), is needed to make $q_{di} = 0.5*(Pe_{fe}+Pe_m)$ at $x_{di}=b_d$

Sample values for verification of q_d

$q_{d_0} = -1$ $q_{d_1} = -4\times 10^{-3}$ $q_{d_2} = -4\times 10^{-3}$ .... $q_{d_{1022}} = -4\times 10^{-3}$ $q_{d_{1023}} = -4\times 10^{-3}$

$$M_{i,j} := \Phi(-j)\cdot\left(1 - y_{md}\cdot q_{d_i}\right) + \Phi(j-1)\cdot\cos\left(j\cdot\pi\cdot x_{d_i}\right)\cdot\left(j\cdot\pi - q_{d_i}\cdot\tanh\left(y_{md}\cdot j\cdot\pi\right)\right)$$ Eq. (36) from main

$M_{i,j}$ is the coefficient matrix for A

Sample values for verification of $M_{i,j}$

$M_{0,0} = 5$ $M_{0,1} = 4.142$ .... $M_{0,1022} = 3.212\times 10^{3}$ $M_{0,1023} = 3.215\times 10^{3}$

$M_{1,0} = 1.016$ $M_{1,1} = 3.146$ .... $M_{1,1022} = -3.211\times 10^{3}$ $M_{1,1023} = -3.214\times 10^{3}$

$M_{2,0} = 1.016$ $M_{2,1} = 3.146$ .... $M_{2,1022} = 3.211\times 10^{3}$ $M_{2,1023} = 3.214\times 10^{3}$

. . .

. $M_{511,511} = -1.134\times 10^{3}$.

. .

$M_{1022,0} = 1.016$ $M_{1022,1} = -3.146$ .... $M_{1022,1022} = -3.211\times 10^{3}$ $M_{1022,1023} = 3.214\times 10^{3}$

$M_{1023,0} = 1.016$ $M_{1023,1} = -3.146$ .... $M_{1023,1022} = 3.211\times 10^{3}$ $M_{1023,1023} = -3.214\times 10^{3}$

$A := M^{-1} \cdot q_d$ From Eq. (35) in main

A is the vector of Fourier coefficients

Verification of matrix solution for Fourier coefficients, A. CheckA is a vector of the residuals for M*A-q_d

$CheckA := M \cdot A - q_d$

Plot of residuals for M*A-q_d

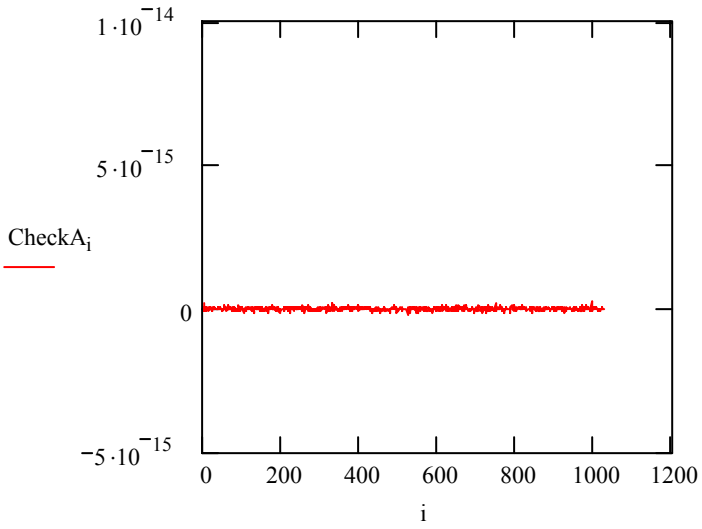

Calculations for cumulative dimensionless flux and flux ratio in fractures and matrix

$$F_{dfA} := Pe_{fe}\cdot\left[\theta_f\left(1 + A_0\cdot y_{md}\right) + \sum_{j=1}^{j_{max}} \frac{A_j}{j\cdot\pi}\cdot\tanh\left(j\cdot\pi\cdot y_{md}\right)\cdot\sin\left(j\cdot\pi\cdot b_d\right)\right]$$ Eq. (6-43) from main

$F_{dfA} = -9.801\times 10^{-5}$

F_{dfA} is the total dimensionless mass flux into the fracture at the drift wall on rock side of boundary

Partial sum for verification of F_{dfA}

$$CheckF_{dfA} := Pe_{fe}\cdot\left[\theta_f\left(1 + A_0\cdot y_{md}\right) + \sum_{j=1}^{8} \frac{A_j}{j\cdot\pi}\cdot\tanh\left(j\cdot\pi\cdot y_{md}\right)\cdot\sin\left(j\cdot\pi\cdot b_d\right)\right]$$

$A_0 = -4.407\times 10^{-3}$ $A_1 = -3.034\times 10^{-4}$ $A_2 = -1.518\times 10^{-4}$

$A_3 = -1.012\times 10^{-4}$ $A_4 = -7.591\times 10^{-5}$ $A_5 = -6.073\times 10^{-5}$

$A_6 = -5.061\times 10^{-5}$ $A_7 = -4.338\times 10^{-5}$ $A_8 = -3.796\times 10^{-5}$

$CheckF_{dfA} = -9.815\times 10^{-5}$

$$F_{dmA} := Pe_m\cdot\left[\left(1 - b_d\right)\cdot\left(1 + A_0\cdot y_{md}\right) - \sum_{j=1}^{j_{max}} \frac{A_j}{j\cdot\pi}\cdot\tanh\left(j\cdot\pi\cdot y_{md}\right)\cdot\sin\left(j\cdot\pi\cdot b_d\right)\right]$$ Eq. (6-44) from main

$F_{dmA} = -3.929\times 10^{-3}$

F_{dmA} is the total dimensionless mass flux into the matrix at the drift wall on rock side of boundary

Partial sum for verification of F_{dfA}

$$CheckF_{dmA} := Pe_m\cdot\left[\left(1 - b_d\right)\cdot\left(1 + A_0\cdot y_{md}\right) - \sum_{j=1}^{8} \frac{A_j}{j\cdot\pi}\cdot\tanh\left(j\cdot\pi\cdot y_{md}\right)\cdot\sin\left(j\cdot\pi\cdot b_d\right)\right]$$

$CheckF_{dmA} = -3.929\times 10^{-3}$

$$\frac{F_{dfA}}{F_{dmA} + F_{dfA}} = 0.02434$$

Dimensionless flux ratio on rock side of boundary

Eq. (6-41) from main

$$F_{dfD} := \theta_f \cdot A_0 + \sum_{j=1}^{j_{max}} A_j \cdot \sin\left(j \cdot \pi \cdot b_d\right)$$

F_{dfD} is the total dimensionless mass flux into the fracture at the drift wall on invert side of boundary

$$F_{dfD} = -9.745 \times 10^{-5}$$

Partial sum for verification of F_{dfD}

$$CheckF_{dfD} := \theta_f \cdot A_0 + \sum_{j=1}^{8} A_j \cdot \sin\left(j \cdot \pi \cdot b_d\right)$$

$$CheckF_{dfD} = -1.204 \times 10^{-6}$$

$$F_{dmD} := \left(1 - b_d\right) \cdot A_0 - \sum_{j=1}^{j_{max}} A_j \cdot \sin\left(j \cdot \pi \cdot b_d\right)$$

Eq. (6-42) from main

$$F_{dmD} = -4.309 \times 10^{-3}$$

F_{dmD} is the total dimensionless mass flux into the matrix at the drift wall on invert side of boundary

Partial sum for verification of F_{dmD}

$$CheckF_{dmD} := \left(1 - b_d\right) \cdot A_0 - \sum_{j=1}^{8} A_j \cdot \sin\left(j \cdot \pi \cdot b_d\right)$$

$$CheckF_{dmD} = -4.405 \times 10^{-3}$$

$$\frac{F_{dfD}}{F_{dmD} + F_{dfD}} = 0.02211$$

Dimensionless flux ratio on invert side of boundary

NOTE: The output of the calculation, which is the dimensionless flux ratio given above, is not affected by the evaluations from this point forward; these are presented to provide background information on the character of the solution.

Eq. (6-40) from main

$$C_{d_i} := A_0 \cdot y_{md} + \sum_{j=1}^{j_{max}} A_j \cdot \cos\left(j \cdot \pi \cdot x_{d_i}\right) \cdot \tanh\left(j \cdot \pi \cdot y_{md}\right)$$

C_{di} are the dimensionless concentrations at the invert-rock interface

$$CP(i) := 1 + C_{d_i}$$

CP(i) is the plotting variable for the unnormalized dimensionless concentration

$$XP(i) := x_{d_i}$$

XP(i) is the plotting variable for the dimensionless distance

Plot of the unnormalized dimensionless concentration (C/C_m) at the solution points for the Fourier coefficients

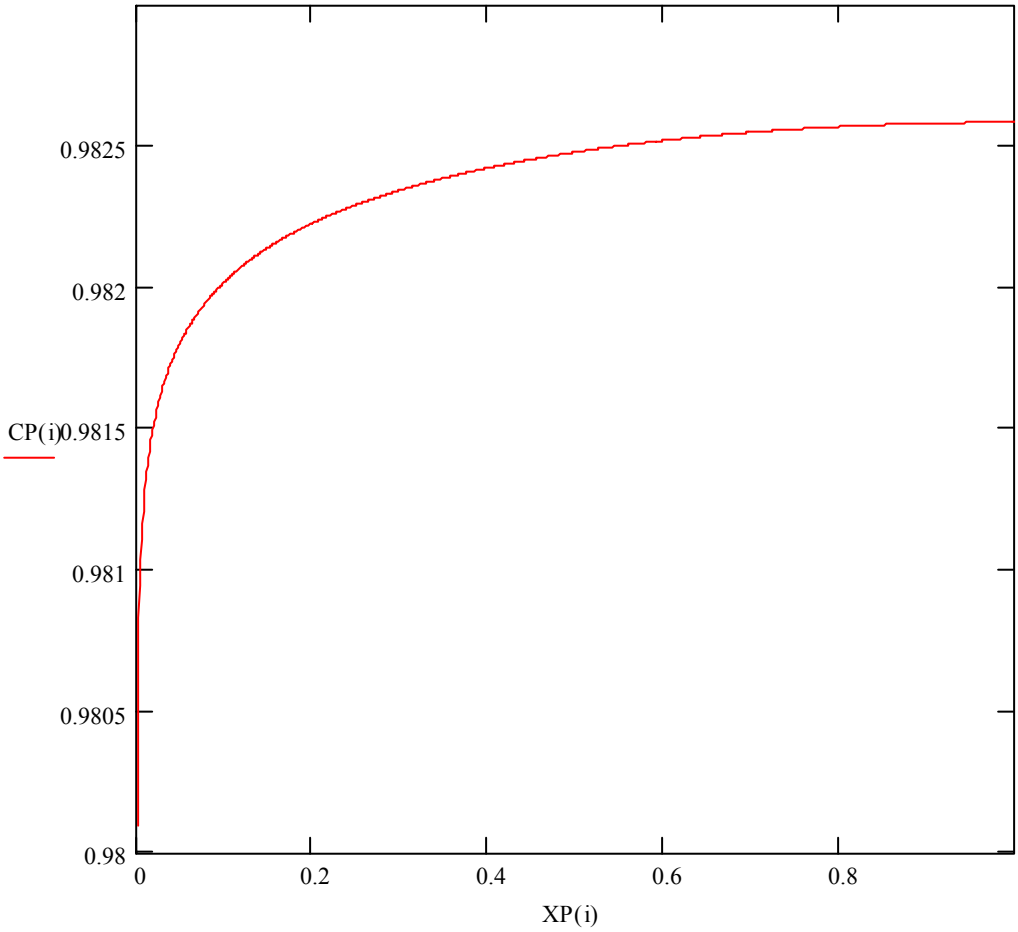

Behavior of local dimensionless mass flux at drift wall

$qC_i := q_{d_i} \cdot \left(C_{d_i} + 1 \right)$

Local dimensionless mass flux in rock at drift wall

$qCP(i) := -qC_i$

qCP(i) is the plotting variable for the negative of the local dimensionless advective mass flux in the rock at drift wall

$XP(i) := x_{d_i}$

XP(i) is the plotting variable for the dimensionless distance along the drift wall

Plot of negative of local dimensionless flux at the solution points for the Fourier coefficients

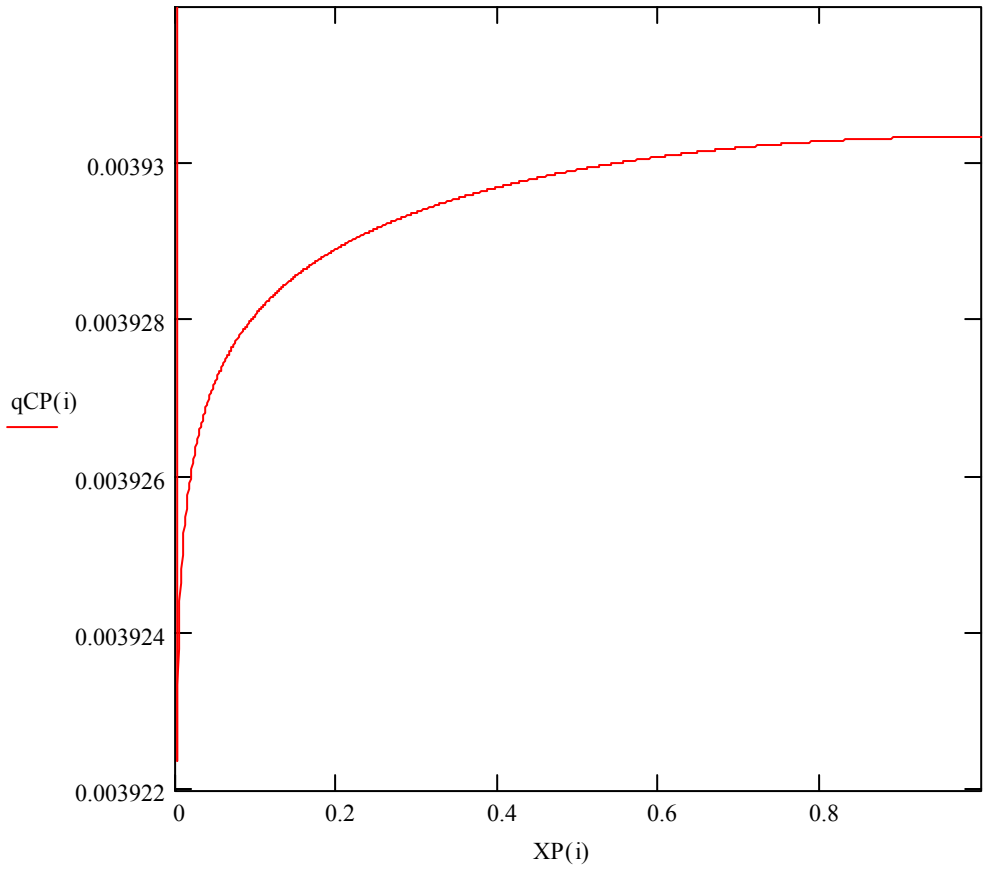

Output-DTN: LB0307FMRADTRN.001

Comparison of radionuclide flux in invert and rock at the drift wall at points not fixed in solution for the Fourier coefficients

$k_{max} := 4000$

$k := 0 .. k_{max}$ **k is the reference number for coordinates along the drift wall not fixed in the solution for the Fourier coefficients**

$x_{d_k} := \frac{k}{k_{max}}$ **x_{dk} are the coordinates along the drift wall not fixed in the solution for the Fourier coefficients**

$$q_{d_k} := Pe_{fe} + 0.5 \cdot \left(Pe_m - Pe_{fe}\right) \cdot \left(\Phi\left(x_{d_k} - b_d\right) - \Phi\left(b_d - x_{d_k}\right) + 1\right)$$

$$C_{d_k} := A_0 \cdot y_{md} + \sum_{j=1}^{j_{max}} A_j \cdot \cos\left(j \cdot \pi \cdot x_{d_k}\right) \cdot \tanh\left(j \cdot \pi \cdot y_{md}\right)$$ **Dimensionless local flux in rock at drift wall**

$$qC_k := q_{d_k} \cdot \left(C_{d_k} + 1\right)$$

$$dC_{d_k} := A_0 + \sum_{j=1}^{j_{max}} j \cdot \pi \cdot A_j \cdot \cos\left(j \cdot \pi \cdot x_{d_k}\right)$$ **Dimensionless local flux in invert at drift wall**

$qCP(k) := -qC_k$

qCP(k) is a plotting variable for the negative of the local dimensionless advective flux in the rock matrix plus the diffusive flux in the fracture at drift wall

$dCP(k) := -dC_{d_k}$

dCP(k) is a plotting variables for the negative of the local dimensionless diffusive flux in the invert at drift wall

$XP(k) := x_{d_k}$

XP(k) is a plotting variable for dimensionless distance

Comparison plot of flux in the invert and rock at the drift wall over the entire domain

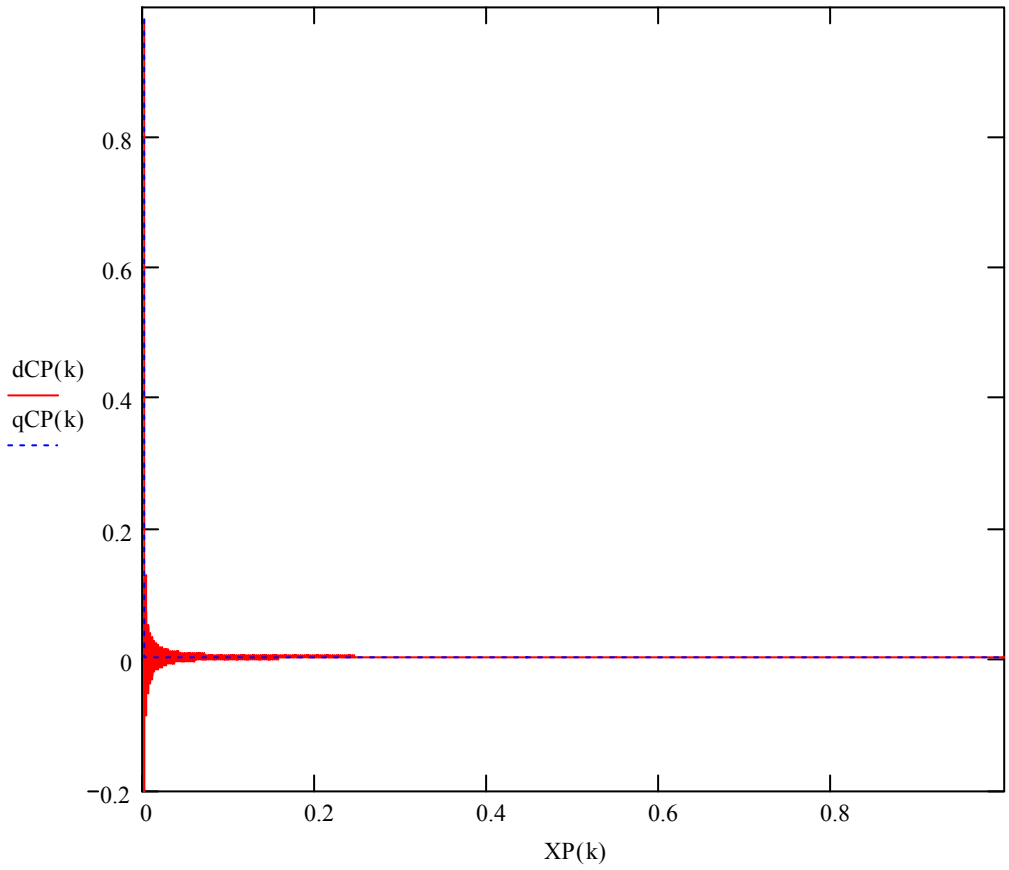

Output-DTN: LB0307FMRADTRN.001

Comparison plot of flux in the invert and rock at the drift wall over region near fracture

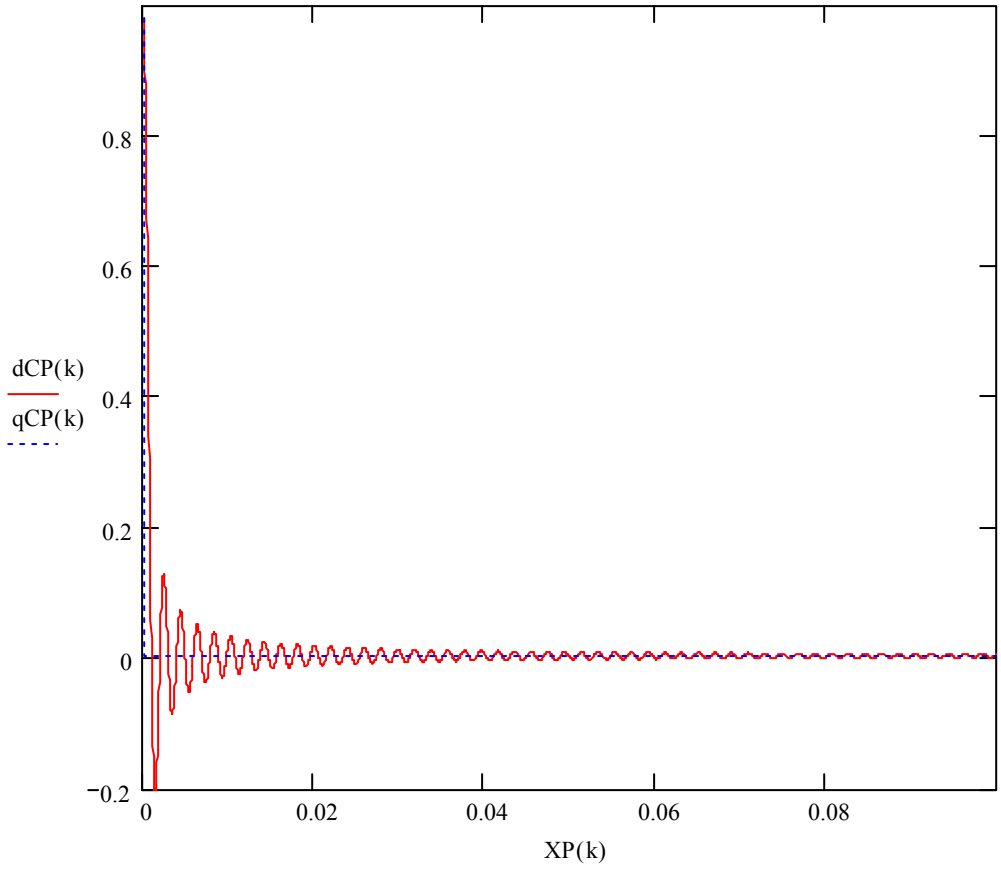

Output-DTN: LB0307FMRADTRN.001

Comparison plot of flux in the invert and rock at the drift wall - fracture close-up

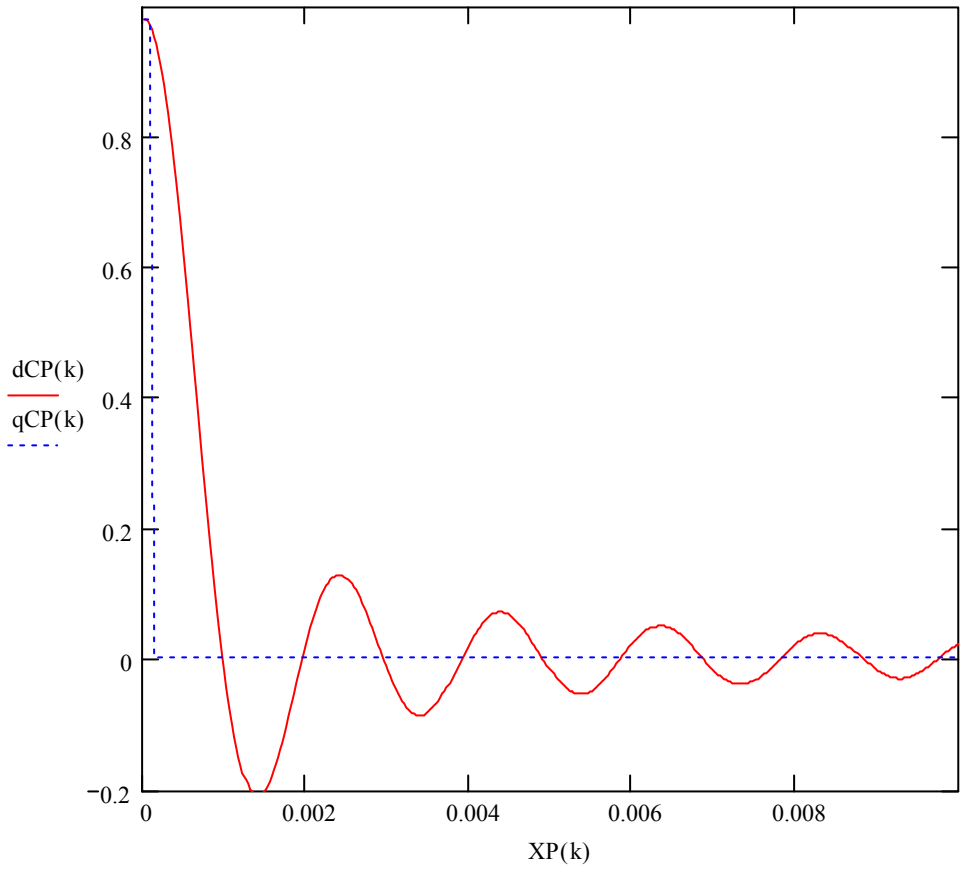

Output-DTN: LB0307FMRADTRN.001

Comparison of boundary condition results (drift wall) at intermediate x-coordinates to those used in the solution for the discrete transform coefficients

$$q_{d_k} := Pe_{fe} + 0.5\cdot\left(Pe_m - Pe_{fe}\right)\cdot\left(\Phi\left(x_{d_k} - b_d\right) - \Phi\left(b_d - x_{d_k}\right) + 1\right)$$

q_{dk} is the flux function

$$fa_k := \left[\sum_j \left[A_j\cdot\Phi(-j)\cdot\left(1 - y_{md}\cdot q_{d_k}\right) + A_j\cdot\Phi(j-1)\cdot\cos\left(j\cdot\pi\cdot x_{d_k}\right)\cdot\left(j\cdot\pi - q_{d_k}\cdot\tanh\left(j\cdot\pi\cdot y_{md}\right)\right)\right]\right]$$

fa_k is the series expansion of the flux function

Eq. (6-34) from main

$$q_{d_1} = -1$$

$XP(k) := x_{d_k}$ **XP(k) is a plotting variable for the dimensionless distance**

$QP(k) := q_{d_k}$ **QP(k) is a plotting variable for the flux function**

$FAP(k) := fa_k$ **FAP(k) is a plotting variable for series representation of the flux function**

Comparison of boundary condition results (drift wall) at intermediate x-coordinates to those used in the solution for the discrete transform coefficients over the entire domain.

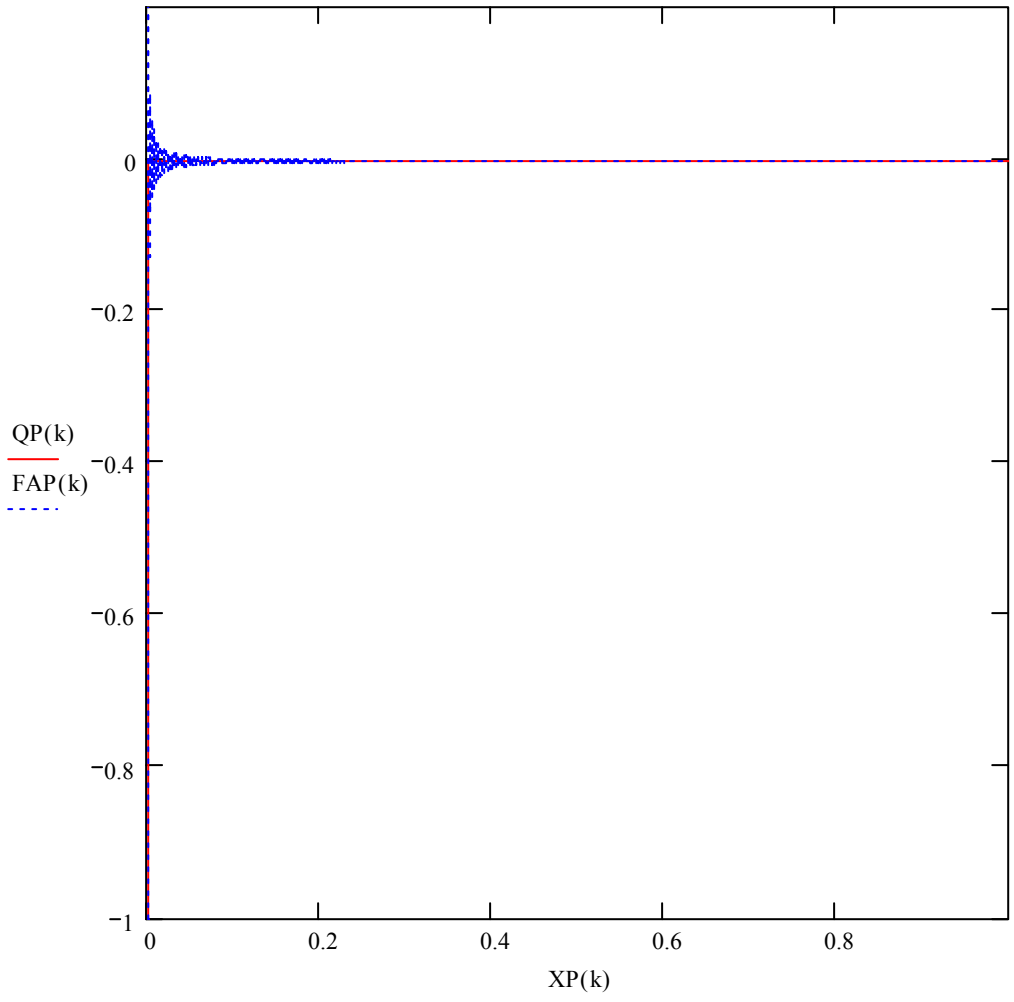

Output-DTN: LB0307FMRADTRN.001

Comparison of boundary condition results (drift wall) at intermediate x-coordinates to those used in the solution for the discrete transform coefficients over a region near the fracture.

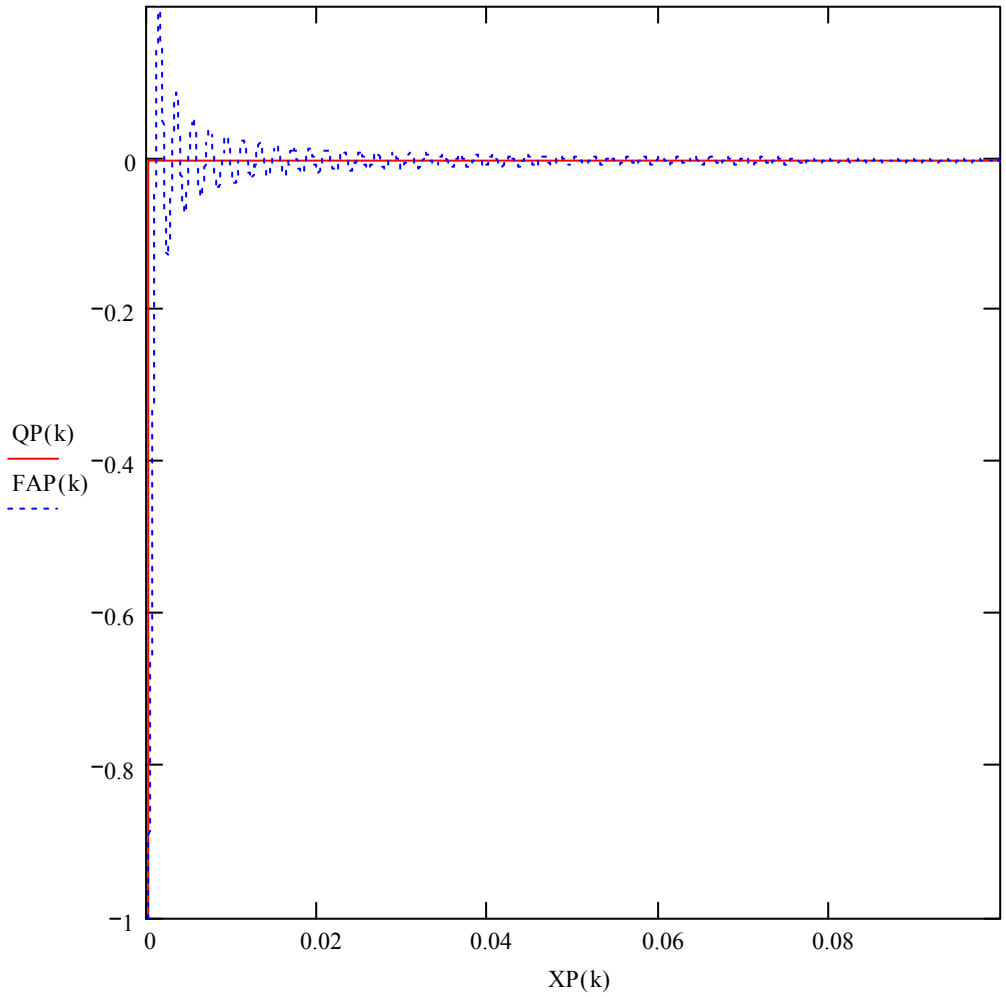

Output-DTN: LB0307FMRADTRN.001

Comparison of boundary condition results (drift wall) at intermediate x-coordinates to those used in the solution for the discrete transform coefficients - fracture close-up.

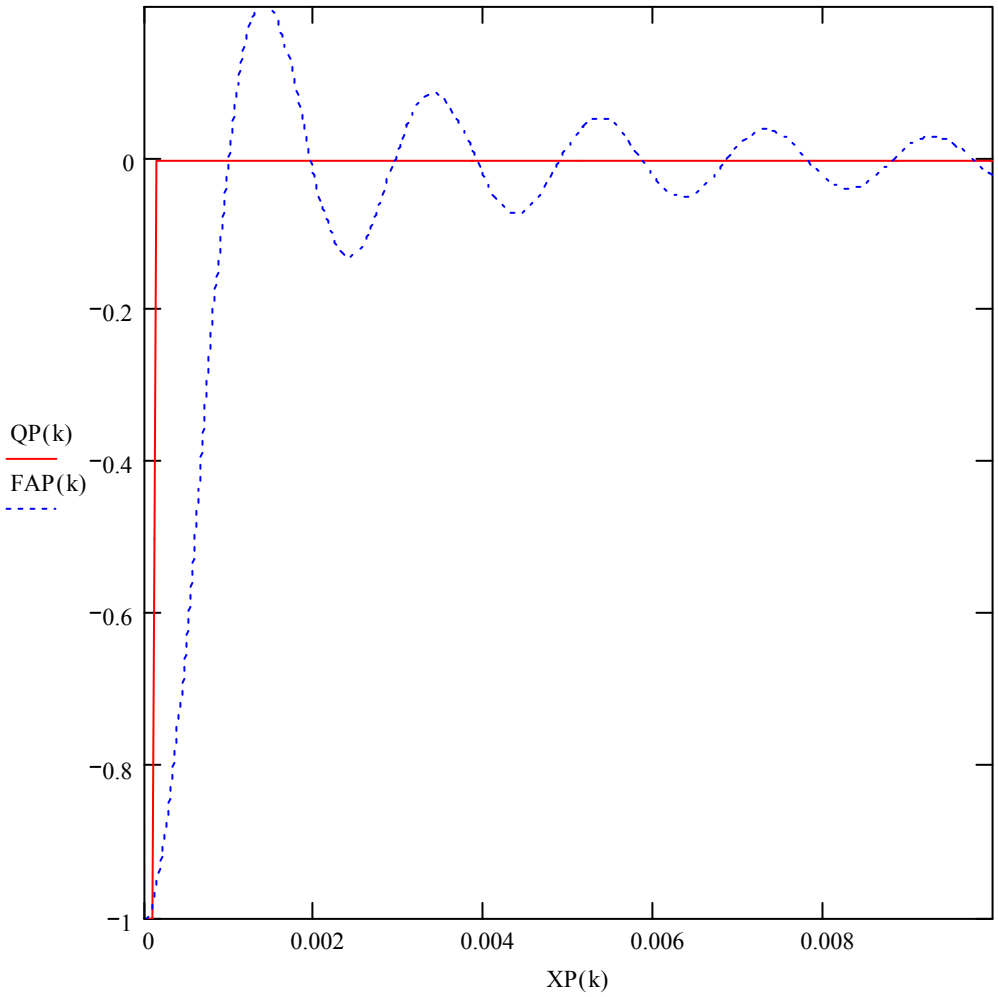

Output-DTN: LB0307FMRADTRN.001

APPENDIX K

SUPPLEMENTARY DERIVATIONS

SUPPLEMENTARY DERIVATIONS

This appendix provides additional information pertaining to Section 6.4.5 of the main text and Appendices A, D, and I.

The derivation of Equation 6-50 in the main text, starting from Equation 6-49,

$$F = \frac{S_{fna}^{\frac{1}{2}} \left[1 - \left(1 - S_{fna}^{\frac{1}{m}} \right)^m \right]^2}{S_{fn}^{\frac{1}{2}} \left[1 - \left(1 - S_{fn}^{\frac{1}{m}} \right)^m \right]^2} \qquad \text{(Eq. 6-49)}$$

and expanding the numerator for small $S_{fma}^{\frac{1}{m}}$ using the following first-order Taylor series expansion:

$(1-x)^m \approx 1 - mx$ where $x = S_{fma}^{\frac{1}{m}}$

Substitute this into the numerator of Equation 6-49 gives,

$$F = \frac{S_{fna}^{\frac{1}{2}} \left[1 - \left(1 - mS_{fma}^{\frac{1}{m}} \right) \right]^2}{S_{fn}^{\frac{1}{2}} \left[1 - \left(1 - S_{fn}^{\frac{1}{m}} \right)^m \right]^2} \qquad \text{(Eq. K-1)}$$

Reducing the numerator gives,

$$F = \frac{m^2 S_{fna}^{\frac{1}{2}+\frac{2}{m}}}{S_{fn}^{\frac{1}{2}} \left[1 - \left(1 - S_{fn}^{\frac{1}{m}} \right)^m \right]^2} \qquad \text{(Eq. K-2)}$$

Rearranging to solve for S_{fma} gives,

$$S_{fna}^{\frac{4+m}{2m}} = \frac{F}{m^2} S_{fn}^{\frac{1}{2}} \left[1 - \left(1 - S_{fn}^{\frac{1}{m}} \right)^m \right]^2 \qquad \text{(Eq. K-3)}$$

or

$$S_{fna} = \left[\left(\frac{F}{m^2} \right) S_{fn}^{\frac{1}{2}} \left\{ 1 - \left(1 - S_{fn}^{\frac{1}{m}} \right)^m \right\}^2 \right]^{\frac{2m}{4+m}} \qquad \text{(Eq. 6-50)}$$

Equations (A-1) and (A-2) in Appendix A are derived as follows:

Let Y be log-normal with mean μ_Y and standard deviation σ_Y and X is normal with mean μ_X and standard deviation σ_X; also $X = \ln(Y)$ or $Y = e^X$.

First, find $\overline{e^X}$ and $\overline{e^{2X}}$, or equivalently, $\overline{Y}$ and $\overline{Y^2}$.

$$\overline{e^X} = \int_{-\infty}^{\infty} \frac{e^X}{\sqrt{2\pi}\sigma_X} e^{-\frac{(X-\mu_X)^2}{2\sigma_X^2}} dX = e^{\mu_X + \frac{\sigma_X^2}{2}} \qquad \text{(Eq. K-4)}$$

$$\text{or } \mu_Y = e^{\mu_X + \frac{\sigma_X^2}{2}} \qquad \text{(Eq. K-5)}$$

and

$$\overline{e^{2X}} = \int_{-\infty}^{\infty} \frac{e^{2X}}{\sqrt{2\pi}\sigma_X} e^{-\frac{(X-\mu_X)^2}{2\sigma_X^2}} dX = e^{2\mu_X + 2\sigma_X^2} \qquad \text{(Eq XI-6)}$$

and because $\sigma_Y^2 = \overline{e^{2X}} - \overline{e^X}^2$, then,

$$\sigma_Y^2 = e^{2\mu_X + \sigma_X^2} \left(e^{\sigma_X^2} - 1 \right) = \mu_Y^2 \left(e^{\sigma_X^2} - 1 \right) \qquad \text{(Eq. K-7)}$$

Rearranging Equation (K-7) and solving for σ_X gives,

$$\sigma_X = \sqrt{\ln\left(1 + \frac{\sigma_Y^2}{\mu_Y^2} \right)} \qquad \text{(Eq. A-2)}$$

Rearranging Equation (K-5) and using Equation (A-2) to solve for μ_X gives,

$$\mu_X = \ln(\mu_Y) - \frac{1}{2}\ln\left(1 + \frac{\sigma_Y^2}{\mu_Y^2}\right) \quad \text{(Eq. A-1)}$$

The derivation of equations (D-4), (D-5), (I-4), and (I-5) from Abramowitz and Stegun (1972 [DIRS 103280], Equation 26.1.33) is shown here:

$$\text{mean} \equiv \mu = \frac{a}{a+b} \quad \text{(Eq. K-8)}$$

$$\text{variance} \equiv \sigma^2 = \frac{ab}{(a+b)^2(a+b+1)} \quad \text{(Eq. K-9)}$$

Solve equation (K-8) for *b*

$$b = a\left(\frac{1-\mu}{\mu}\right) \quad \text{(Eq. K-10)}$$

Also note from equation (K-8) that

$$a + b = \frac{a}{\mu} \quad \text{(Eq. K-11)}$$

Substitute equations (K-10) and (K-11) into equation (K-9) to give

$$\sigma^2 = \frac{a^2\left(\frac{1-\mu}{\mu}\right)}{\left(\frac{a}{\mu}\right)^2\left(\frac{a}{\mu}+1\right)} \quad \text{(Eq. K-12)}$$

Simplifying equation (K-12) gives

$$\sigma^2 = \frac{\mu(1-\mu)}{\left(\frac{a}{\mu}+1\right)} \quad \text{(Eq. K-13)}$$

Solving equation (K-13) for *a* gives

$$a = \mu\left[\frac{\mu(1-\mu)}{\sigma^2} - 1\right] \qquad \text{(Eq. D-4 and I-4)}$$

and substituting equation (D-4) for *a* in equation (K-10) gives

$$b = (1-\mu)\left[\frac{\mu(1-\mu)}{\sigma^2} - 1\right] \qquad \text{(Eq. D-5 and I-5)}$$

APPENDIX L

DEMONSTRATION OF EQUIVALENCE OF THE DISCRETE TRANSFORM SOLUTION AND FOURIER SERIES SOLUTION

DEMONSTRATION OF EQUIVALENCE OF THE DISCRETE TRANSFORM SOLUTION AND FOURIER SERIES SOLUTION

This appendix provides additional information pertaining to Section 6.4.3 of the main text.

Summary from Sections 6.4.2 and 6.4.3

The steady-state diffusion equation and four boundary conditions to be solved are given by equations (6-24) through (6-28) of the main text:

$$\nabla_d^2 C_d\left(x_d, y_d\right) = 0 \qquad \text{(Eq. 6-24)}$$

$$C_d\left(x_d, 0\right) = 0 \qquad \text{(Eq. 6-25)}$$

$$\frac{\partial C_d}{\partial x_d}\left(0, y_d\right) = 0 \qquad \text{(Eq. 6-26)}$$

$$\frac{\partial C_d}{\partial x_d}\left(1, y_d\right) = 0 \qquad \text{(Eq. 6-27)}$$

$$\frac{\partial C_d}{\partial y_d}\left(x_d, y_{md}\right) = q_d\left(x_d\right)\left(C_d\left(x_d, y_{md}\right) + 1\right) \qquad \text{(Eq. 6-28)}$$

A solution that satisfies Equation 6-24 and the boundary conditions, Equations 6-25 to 6-27 is

$$C_d\left(x_d, y_d\right) = B_0 y_d + \sum_{j=1}^{\infty} B_j \cos\left(j\pi x_d\right)\sinh\left(j\pi y_d\right) \qquad \text{(Eq. 6-33)}$$

which may be verified by direct substitution.

Substituting Equation 6-33 into Equation 6-28 gives

$$A_0\left(1 - q_d\left(x_d\right) y_{md}\right) + \sum_{j=1}^{\infty} A_j \cos\left(j\pi x_d\right)\left[j\pi - q_d\left(x_d\right)\tanh\left(j\pi y_{md}\right)\right] = q_d\left(x_d\right) \qquad \text{(Eq. 6-34)}$$

or

$$\sum_{j=0}^{\infty} M_{ij} A_j = q_{di} \qquad \text{(Eq. 6-35)}$$

where

$$M_{i0} = \left(1 - q_d\left(x_{di}\right) y_{md}\right) \quad \text{(Eq. 6-36)}$$

$$M_{ij} = \cos\left(j\pi x_{di}\right)\left[j\pi - q_d\left(x_{di}\right)\tanh\left(j\pi y_{md}\right)\right] \quad \text{for} \quad i > 0 \quad \text{(Eq. 6-37)}$$

$$q_{di} = q_d\left(x_{di}\right) \quad \text{(Eq. 6-38)}$$

$$A_j = B_j \cosh\left(j\pi y_{md}\right) \quad \text{(Eq. 6-39)}$$

The transformation from B_j to A_j is introduced to eliminate numerical difficulties in the evaluation of $\cosh\left(j\,\pi\, y_{md}\right)$ and $\sinh\left(j\,\pi\, y_{md}\right)$ for large j.

Explanation of Discrete Transform Solution Method

If a solution for A_j can be found that satisfies equation (6-35) at all points in the domain of the problem, then, in combination with equation (6-39) and equation (6-33) we have the exact solution to equations (6-24) through (6-28). Therefore, equation (6-35) represents a linear system of equations for A_j that can produce the exact solution in the limit as $j \to \infty$. An approximate solution may be derived by solving for A_j at a finite number of points and this solution converges as j increases.

Demonstration of Equivalence with Fourier Series

A test of the discrete transform solution method is given here for a problem in which the standard Fourier solution is also available. In this test, an analytical form for the concentration at the invert-rock boundary was assumed. That is, starting with equations (6-24) through (6-27), we then specify the concentration at the invert-rock interface, replacing the flux boundary condition in equation (6-28) with a concentration boundary condition. With this type of boundary condition, the solution may be obtained using standard Fourier methods. This solution was then substituted into equation (6-28) to derive a form for $q_d\left(x_d\right)$ that is consistent with the assumed concentration boundary condition. Therefore, we now have the identical problem with a flux-type boundary condition as given in equation (6-28). A series of values for $q_d\left(x_d\right)$ were then generated from the standard Fourier solution and used as input to the discrete transform solution method to solve equations (6-24) through (6-28). The resulting Fourier coefficients may be compared with those generated from the standard Fourier solution, and the concentration distribution at the invert-rock boundary may be compared with the assumed concentration distribution. The following presents the details of this comparison.

Given equations (6-33) and (6-39), we have,

$$C_d\left(x_d, y_{dm}\right) = A_0 y_{dm} + \sum_{j=1}^{\infty} A_j \cos\left(j\pi x_d\right)\tanh\left(j\pi y_{dm}\right) \quad \text{(Eq. 6-40)}$$

Assume the following form for the concentration distribution at the invert-rock interface:

$$C_d\left(x_d, y_{dm}\right) = K_1 + K_2\left[1 - \exp\left(-K_3 x_d\right)\right] \quad \text{(Eq. L-1)}$$

where K_1, K_2, and K_3 are constants.

For the Fourier cosine series,

$$C_d\left(x_d, y_{dm}\right) = \frac{a_0}{2} + \sum_{j=1}^{\infty} a_j \cos\left(jx\right) \quad \text{(Eq. L-2)}$$

where $x = \pi x_d$.

Fourier coefficients are obtained using the orthogonality properties of the cosine function,

$$a_0 = \frac{2}{\pi}\int_0^{\pi}\left\{K_1 + K_2\left[1 - \exp\left(\frac{-K_3}{\pi}x\right)\right]\right\}dx \quad \text{(Eq. L-3)}$$

$$a_j = \frac{2}{\pi}\int_0^{\pi}\left\{K_1 + K_2\left[1 - \exp\left(\frac{-K_3}{\pi}x\right)\right]\right\}\cos\left(jx\right)\,dx \quad \text{(Eq. L-4)}$$

giving the following results for the Fourier Coefficients:

$$a_0 = 2K_1 + 2K_2 - \frac{2K_2}{K_3}\left[1 - \exp\left(-K_3\right)\right] \quad \text{(Eq. L-5)}$$

$$a_j = \frac{-2K_2K_3}{K_3^2 + j^2\pi^2}\left[1 - \exp\left(-K_3\right)\cos\left(j\pi\right)\right] \quad \text{(Eq. L-6)}$$

Comparing Equations 6-40 and L-2 we find,

$$\frac{a_0}{2} = A_0 y_{dm} \quad \text{(Eq. L-7)}$$

$$a_j = A_j \tanh\left(j\pi y_{dm}\right) \quad \text{(Eq. L-8)}$$

Therefore,

$$A_0 = \frac{K_1}{y_{dm}} + \frac{K_2}{y_{dm}} - \frac{K_2}{K_3 y_{dm}}\left[1 - \exp\left(-K_3\right)\right] \quad \text{(Eq. L-9)}$$

$$A_j = \frac{-2K_2K_3}{K_3^2 + j^2\pi^2}\frac{\left[1 - \exp\left(-K_3\right)\cos\left(j\pi\right)\right]}{\tanh\left(j\pi y_{dm}\right)} \quad \text{(Eq. L-10)}$$

and expressions for B_j are derived using Equation 6-39 in combination with L-9 and L-10.

Substituting for B_j into equation (6-33) gives,

$$C_d(x_d, y_d) = \frac{K_1 y_d}{y_{dm}} + \frac{K_2 y_d}{y_{dm}} - \frac{K_2 y_d}{K_3 y_{dm}}\left[1 - \exp(-K_3)\right] - \sum_{j=1}^{\infty} \frac{2K_2 K_3}{K_3^2 + j^2\pi^2} \frac{\left[1 - \exp(-K_3)\cos(j\pi)\right]}{\sinh(j\pi y_{dm})} \cos(j\pi x_d)\sinh(j\pi y_d) \quad \text{(Eq. L-11)}$$

and

$$\frac{\partial C(x_d, y_d)}{\partial y_d} = \frac{K_1}{y_{dm}} + \frac{K_2}{y_{dm}} - \frac{K_2}{K_3 y_{dm}}\left[1 - \exp(-K_3)\right] - \sum_{j=1}^{\infty} \frac{2K_2 K_3 (j\pi)}{K_3^2 + j^2\pi^2} \frac{\left[1 - \exp(-K_3)\cos(j\pi)\right]}{\sinh(j\pi y_{dm})} \cos(j\pi x_d)\cosh(j\pi y_d) \quad \text{(Eq. L-12)}$$

Evaluating Equations L-11 and L-12 at $y_d = y_{dm}$ gives

$$C_d(x_d, y_{dm}) = K_1 + K_2 - \frac{K_2}{K_3}\left[1 - \exp(-K_3)\right] - \sum_{j=1}^{\infty} \frac{2K_2 K_3}{K_3^2 + j^2\pi^2}\left[1 - \exp(-K_3)\cos(j\pi)\right]\cos(j\pi x_d) \quad \text{(Eq. L-13)}$$

and

$$\frac{\partial C(x_d, y_{dm})}{\partial y_d} = \frac{K_1}{y_{dm}} + \frac{K_2}{y_{dm}} - \frac{K_2}{K_3 y_{dm}}\left[1 - \exp(-K_3)\right] - \sum_{j=1}^{\infty} \frac{2K_2 K_3 (j\pi)}{K_3^2 + j^2\pi^2} \frac{\left[1 - \exp(-K_3)\cos(j\pi)\right]}{\tanh(j\pi y_{dm})} \cos(j\pi x_d) \quad \text{(Eq. L-14)}$$

From equation (6-28)

$$q_d(x_d) = \frac{\dfrac{\partial C(x_d, y_{dm})}{\partial y_d}}{C_d(x_d, y_{dm}) + 1} \quad \text{(Eq. L-15)}$$

Substituting Equations L-13 and L-14 into Equation L-15 allows for the evaluation of $q_d(x_d)$.

Letting $K_1 = -0.02$, $K_2 = 0.0025$, and $K_3 = 10$, the concentration profile (Equation L-1) and Fourier representation of that concentration profile (Equation L-13) using 101 Fourier coefficients is plotted in Figure L-1 (note that C_d ranges from –1 to 0 and $C_d + 1$ is plotted):

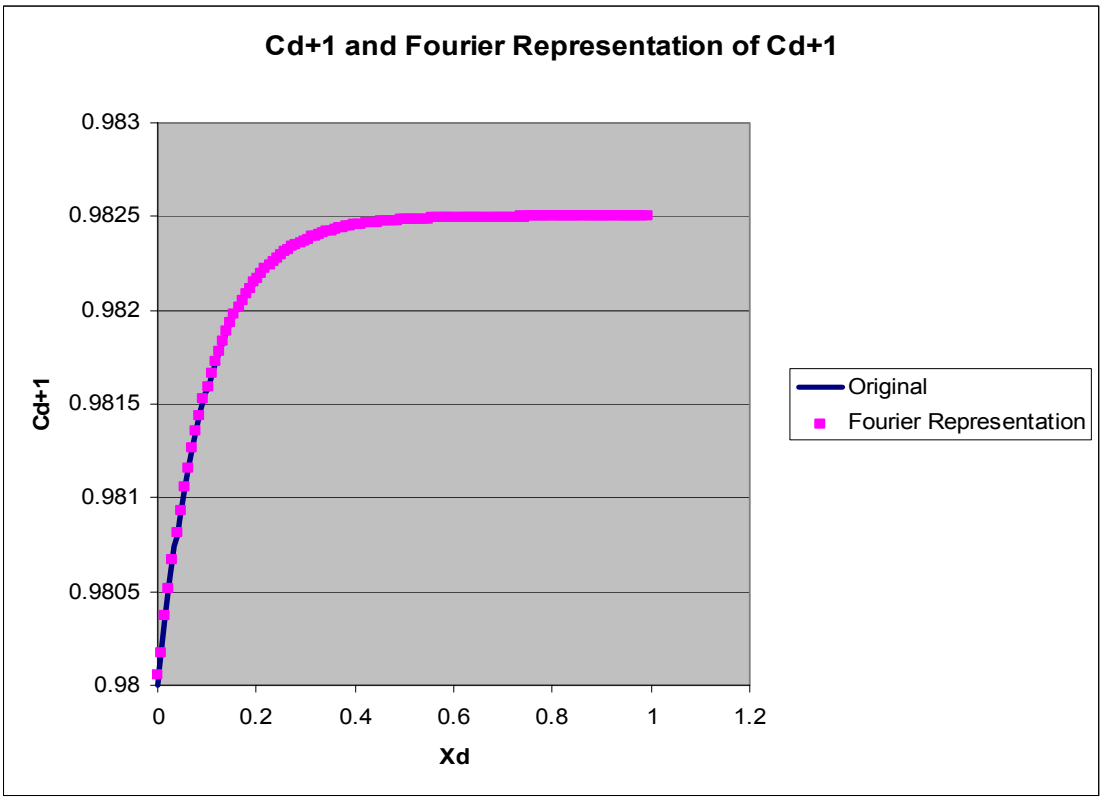

Output-DTN: LB0307FMRADTRN.001.

Figure L-1. Assumed Concentration Profile and its Fourier Representation

As expected, the Fourier decomposition may be used to reconstruct the function.

Using Equation L-15 to generate values of q_d, the discrete transform solution method was used to solve Equations 24 through 28. For this test case, 128 discrete transform coefficients were used in solution of Equation 6-35 for A_j. Fourier coefficients determined in Equations L-9 and L-10 are compared with the coefficients determined from the discrete transform solution method concentration as shown in Figure L-2.

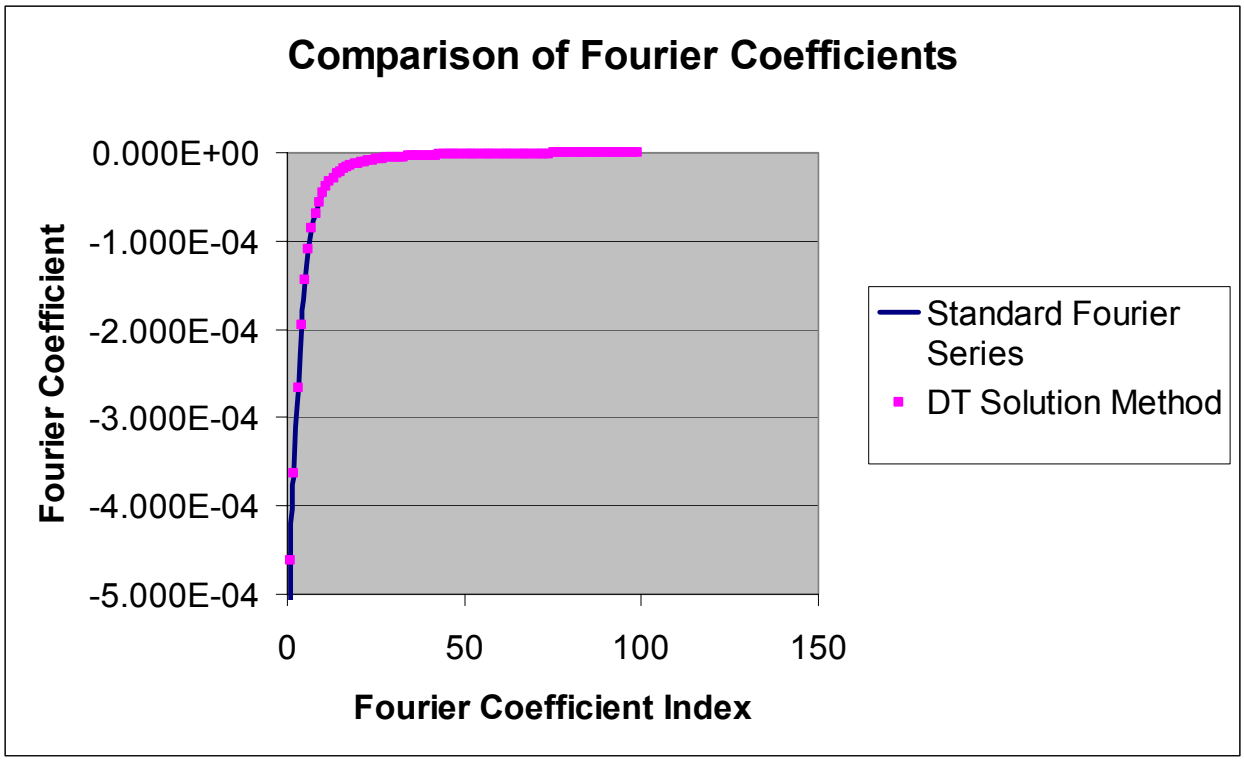

Output-DTN: LB0307FMRADTRN.001.

Figure L-2. Assumed Concentration Profile and its Fourier Representation

This shows that the original Fourier coefficients are closely approximated by the coefficients determined using the discrete transform solution method for the same problem. The coefficient for A_0 is not shown in this figure so that the scale of the figure may more clearly show the comparison for the remaining coefficients. For the original Fourier coefficients, A_0 = -0.004437 as compared with –0.004441 for the discrete transform solution method.

The discrete transform solution method was also used to determine the concentration at the invert-rock interface. The comparison between this concentration and the original concentration shown above is shown in Figure L-3.

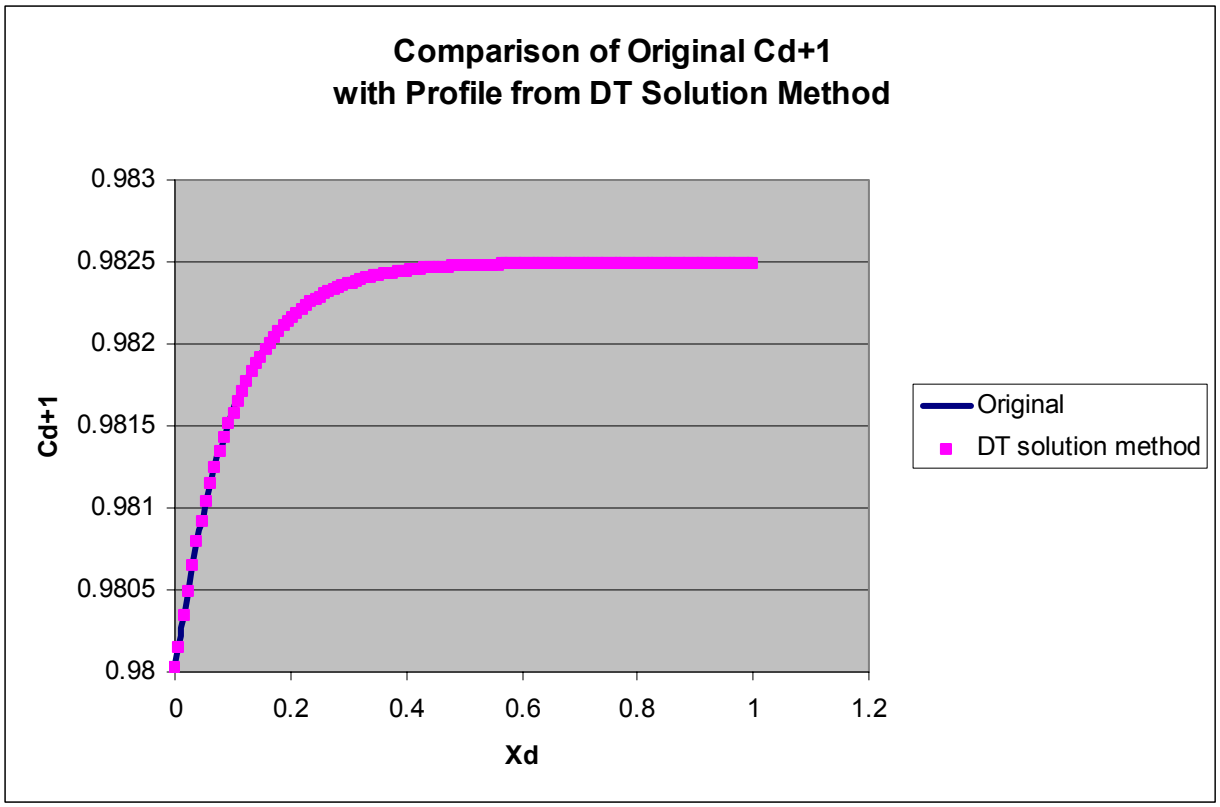

Output-DTN: LB0307FMRADTRN.001.

Figure L-3. Comparison of Assumed Profile and Computed Profile using DT Method

The root-mean-square relative error between the concentration curves is 1.3×10^{-5}. Therefore, the discrete transform solution method for Equations 24 through 28 results in a concentration distribution that is essentially identical with the original concentration distribution.

Excel Calculations for Fourier Solution

Equation L-13 is computed in excel using the following:

For the first Fourier coefficient (evaluated in cell B2), Equation L-9 in Excel is:

B2=0.25*($CY$1+$CZ$1-($CZ$1/$DA$1)*(1-EXP(-$DA$1)))

Where K1, K2, and K3 (see Equation L-1) are constants in cells CY1, CZ1, and DA1, respectively.

The remaining Fourier coefficients, in cells C2 through CX2, are computed from Equation L-10, which in Excel is:

COL2=(-2*$CZ$1*$DA$1/($DA$1^2+COL$1^2*PI()^2))*(1-EXP(-$DA$1)*COS(COL$1*PI()))/TANH(COL$1*PI()*4)

where COL is a generic designation for the column label.

The concentration at a given location is computed using Equation L-13. The cells B3 through B130 contain the dimensionless coordinate, x_d. Cells Crn through CXrn (where rn lies between 3 and 130) are the elements of the summation in Equation L-13 for each location, x_d, not including the common factor in the summation that is independent of the summation index. The Excel formula for the series elements is:

COLrn=(1-EXP(-
$DA$1)*COS(COL$1*PI()))*COS(COL$1*PI()*$Brn)/($DA1^2+COL1^2*PI()^2)

where rn is a generic designation for row number. A portion of the results using these formulas is shown in Table L-1. See Wang (2003 [DIRS 163234], SN-LBNL-SCI-236-V1, p. 75) and DTN: LB0307FMRADTRN.001 for the complete output.

Table L-1. Fourier Coefficients and Calculation of Concentration Profile

	A	B	C	D	E	F	G
1	j	0	1	2	3	4	5
2	**Fourier Coefficients**	-0.004437497	-0.00046	-0.000358462	-0.00026	-0.00019	-0.00014
3	**Dimensionless coordinate, Xd**	0	0.009102	0.007169243	0.005296	0.003877	0.002884
4		0.0078125	0.009099	0.007160607	0.005282	0.003858	0.002862
5		0.015625	0.009091	0.007134721	0.005239	0.003803	0.002798
6		0.0234375	0.009077	0.007091646	0.005167	0.00371	0.002691
7		0.03125	0.009058	0.007031488	0.005068	0.003582	0.002544

Output-DTN: LB0307FMRADTRN.001

The summation is carried out in cells CY3 through CY130 using the following formula:

CYrn=SUM(Crn:CXrn)

The common factor is multiplied by the summation results in cells CYrn and the constant in Equation L-13 is added. This is performed in CZ3 through CZ130 using the following formula:

CZrn=$CY$1+$CZ$1-($CZ$1/$DA$1)*(1-EXP(-$DA$1))-2*$CZ$1*$DA$1*CYrn

The value of Cd+1 is given by the values in CZrn plus 1 in column DB.

The calculation of Equation L-14 is also performed in Excel. This is done using a similar structure as for the series expression for Equation L-13 discussed above. Cells B135 through B262 contain the values of the dimensionless coordinate, x_d. Cells Crn through CXrn (where rn lies between 135 and 262) are the elements of the summation in Equation L-14 for each location, x_d, not including the common factor in the summation that is independent of the summation index. The Excel formula for the series elements is:

COLrn=(COL$134*PI())*(1-EXP(-$DA$1)*COS(COL$134*PI()))*COS(COL$134*PI()*$Brn)/(($DA$1^2+COL$134^2*PI()^2)*TANH(COL$134*PI()*4))

A portion of the results using these formulas is shown in Table L-2. See Wang (2003 [DIRS 163234], SN-LBNL-SCI-236-V1, p. 75) and DTN: LB0307FMRADTRN.001 for the complete output.

Table L-2. Calculation of Concentration Derivative with Respect to y_d

134	j		1	2	3	4	5
135	Dimensionless coordinate, Xd	0	0.028595	0.045045679	0.049915	0.048721	0.045304
136		0.0078125	0.028587	0.04499142	0.049779	0.048486	0.044963
137		0.015625	0.028561	0.044828772	0.049374	0.047785	0.043946
138		0.0234375	0.028518	0.044558128	0.048702	0.046623	0.042268
139		0.03125	0.028457	0.044180139	0.047765	0.045012	0.039954

Output-DTN: LB0307FMRADTRN.001

The summation is carried out in cells CY135 through CY262 using the following formula:

CYrn=SUM(Drn:CYrn)

The common factor is multiplied by the summation results in cells CYrn and the constant in Equation L-14 is added. This is performed in CZ135 through CZ262 using the following formula:

CZrn=0.25*$CY$1+0.25*$CZ$1-(0.25*$CZ$1/$DA$1)*(1-EXP(-$DA$1))-2*$CZ$1*$DA$1*CYrn

The dimensionless flux (q_d) profile is then computed from Equation L-15 using the following Excel formula:

DBrn=CZrn/DB(rn-132)

which gives the dimensionless flux at each coordinate x_d.

Mathcad Calculations for the Discrete Transform Method.

The discrete transform calculation discussed above was performed using Mathcad and is given on the following pages:

Solution Method Test Case

Values used for calculation

$y_{dm} := 4.00$ **y_{dm} is the dimensionless invert thickness**

$j_{max} := 127$ **$j_{max}+1$ is the number of Fourier coefficients**

Distance coordinate along drift wall

$i := 0 .. j_{max}$ **i is reference number for the coordinates along the drift wall**

$j := 0 .. j_{max}$ **j is the reference number for the Fourier coefficients**

$x_{d_i} := \frac{i}{j_{max}}$ **x_{di} is the dimensionless distance along the drift wall**

Sample values for verification of x_{di}

$x_{d_0} = 0$ $x_{d_1} = 7.874 \times 10^{-3}$ $x_{d_2} = 0.016$ ..... $x_{d_{126}} = 0.992$ $x_{d_{127}} = 1$

Solution for Fourier coefficients

$q_d :=$ 

qd is input from the Fourier solution, represented by the icon, and calculated from Equation L-15.

q_{di} is the dimensionless water flux profile at the invert-rock interface

DTN: LB0307FMRADTRN.001

Sample values for verification of q_d

$q_{d_0} = -0.06$ $q_{d_1} = -0.041$ $q_{d_2} = -0.023$ .... $q_{d_{126}} = -4.107 \times 10^{-3}$ $q_{d_{127}} = -4.026 \times 10^{-3}$

$$M_{i,j} := \Phi(-j)\cdot\left(1 - y_{md}\cdot q_{d_i}\right) + \Phi(j-1)\cdot\cos\left(j\cdot\pi\cdot x_{d_i}\right)\cdot\left(j\cdot\pi - q_{d_i}\cdot\tanh\left(y_{md}\cdot j\cdot\pi\right)\right)$$

$M_{i,j}$ is the coefficient matrix for A

Sample values for verification of $M_{i,j}$

$M_{0,0} = 1.242$ $M_{0,1} = 3.202$ .... $M_{0,126} = 395.901$ $M_{0,127} = 399.043$

$M_{1,0} = 1.166$ $M_{1,1} = 3.182$ .... $M_{1,126} = -395.761$ $M_{1,127} = -399.024$

$M_{2,0} = 1.09$ $M_{2,1} = 3.16$ .... $M_{2,126} = 395.379$ $M_{2,127} = 399.005$

. . .

. $M_{64,64} = 141.293$.

. .

$M_{126,0} = 1.016$ $M_{126,1} = -3.145$ .... $M_{126,126} = -395.724$ $M_{126,127} = 398.986$

$M_{127,0} = 1.016$ $M_{127,1} = -3.146$ .... $M_{127,126} = 395.845$ $M_{127,127} = -398.986$

$$A := M^{-1}\cdot q_d$$

A is the vector of Fourier coefficients

Verification of matrix solution for Fourier coefficients, A.
CheckA is a vector of the residuals for M*A-q_d

$$CheckA := M\cdot A - q_d$$

Plot of residuals for M*A-q_d

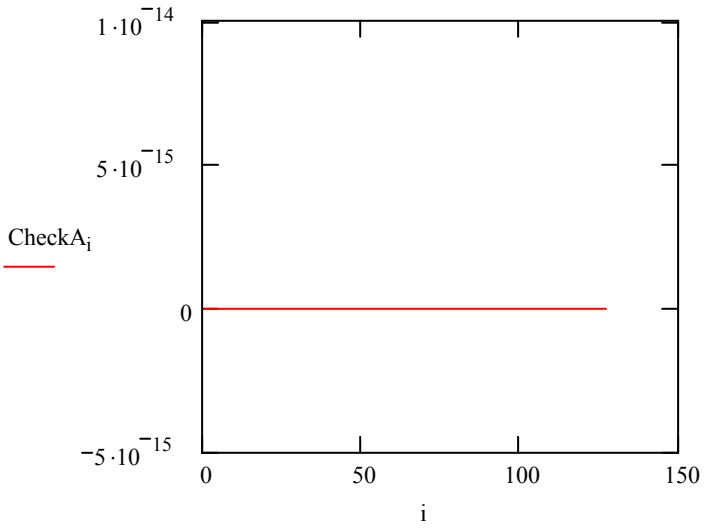

$$C_{d_i} := A_0 \cdot y_{md} + \sum_{j=1}^{j_{max}} A_j \cdot \cos\left(j \cdot \pi \cdot x_{d_i}\right) \cdot \tanh\left(j \cdot \pi \cdot y_{md}\right)$$

C_{di} are the dimensionless concentrations at the invert-rock interface

$$CP(i) := 1 + C_{d_i}$$

CP(i) is the plotting variable for the unnormalized dimensionless concentration

$$XP(i) := x_{d_i}$$

XP(i) is the plotting variable for the dimensionless distance

Plot of the unnormalized dimensionless concentration (C/C_m) at the solution points for the Fourier coefficients

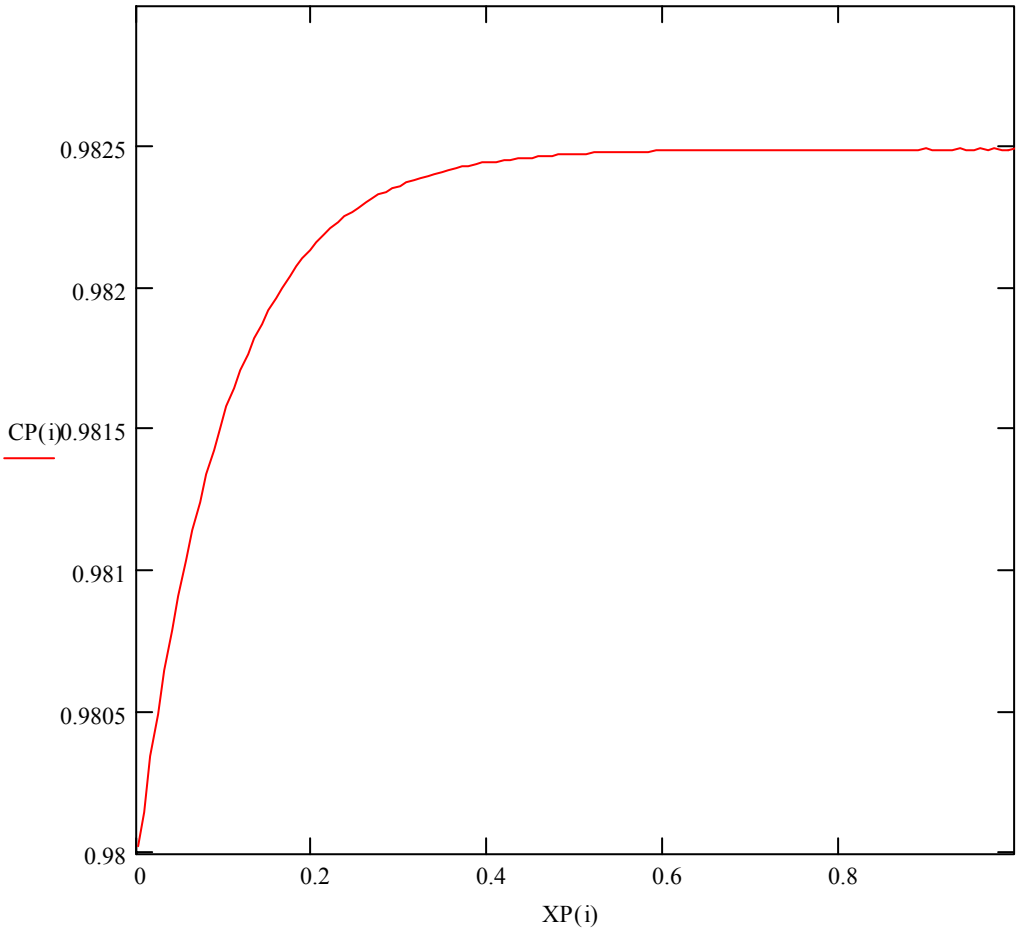

Output-DTN: LB0307FMRADTRN.001

Behavior of local dimensionless mass flux at drift wall

$qC_i := q_{d_i} \cdot \left(C_{d_i} + 1 \right)$

Local dimensionless mass flux in rock at drift wall

$qCP(i) := -qC_i$

qCP(i) is the plotting variable for the negative of the local dimensionless advective mass flux in the rock at drift wall

$XP(i) := x_{d_i}$

XP(i) is the plotting variable for the dimensionless distance along the drift wall

Plot of negative of local dimensionless flux at the solution points for the Fourier coefficients

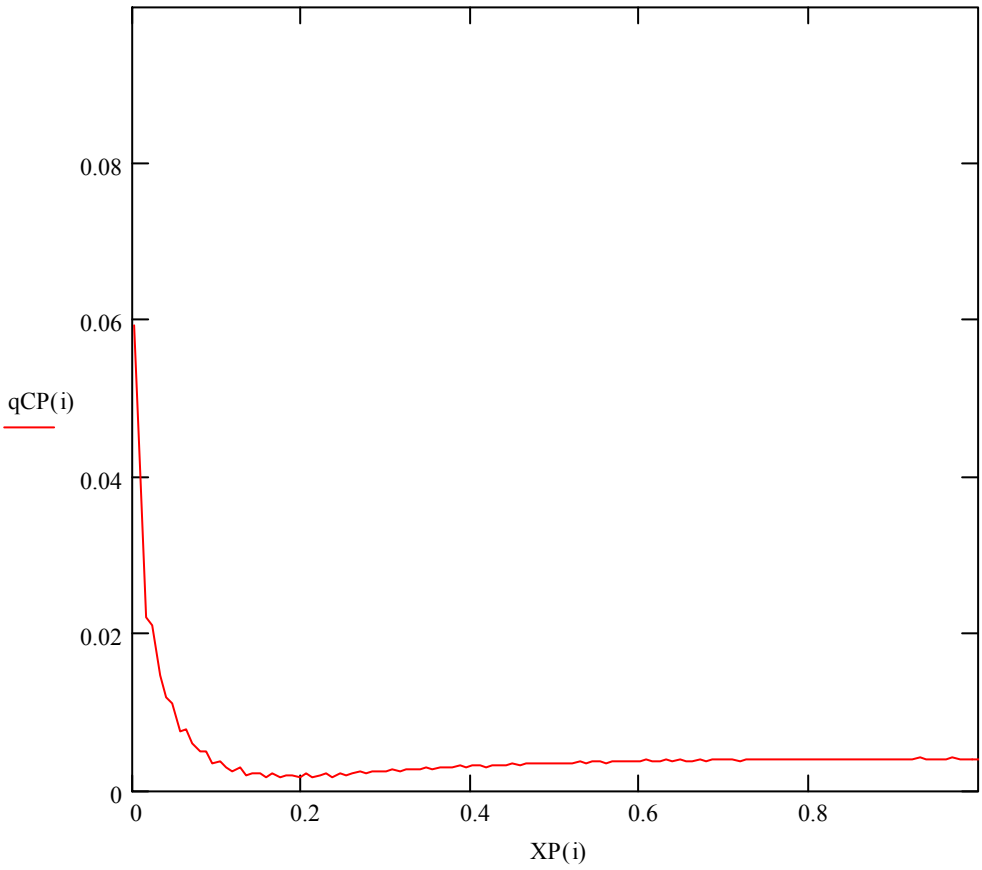

Output-DTN: LB0307FMRADTRN.001.